Crustal Evolution and Hydrothermal Gold Mineralization in the Katuma Block of the Paleoproterozoic Ubendian Belt, Tanzania

Dissertation

zur Erlangung des Doktorgrades

an der Mathematisch-Naturwissenschftiliches Fakultät

der Christian-Albrechts-Universität

zu Kiel

vorgelegt von

Emmanuel Owden Kazimoto

Kiel 2014

Crustal Evolution and Hydrothermal Gold Mineralization in the Katuma Block of the Paleoproterozoic Ubendian Belt, Tanzania

Dissertation

zur Erlangung des Doktorgrades

an der Mathematisch-Naturwissenschftiliches Fakultät

der Christian-Albrechts-Universität

zu Kiel

vorgelegt von

Emmanuel Owden Kazimoto

Kiel 2014

Gedruckt mit der Unterstützung des Deutschen Akademischen Austauschdienstes

Referent: Prof. Dr. Volker Schenk
Korrereferentin: Prof. Dr. Astrid Holzheid
Tad der mündlichen Prüfung: 1-7-2014
Zum Druck genehmigt

Der Dekan

Vorwort

Die vorliegende Arbeit wurde als monographische Dissertation verfasst, jedoch ist in den drei Kapiteln jeweils eine eigenständige Einleitung und Diskussion vorhanden. Für die einzelnen Kapitel wurde bewusst ein unabhängiger Aufbau gewählt, da diese losgelöst voneinander in internationalen Fachzeitschriften publiziert werden sollen. Daher finden sich in jedem Kapitel eine Einleitung, Diskussion und Literaturverzeichnis wieder, auch die Länge und etwaige Formatierungen sind in Hinblick auf die jeweiligen Vorgaben der Fachzeitschriften bewusst gewählt. Der Leser sei darauf hingewiesen, dass es durch den gewählten Aufbau zu Wiederholungen kommen kann und möge diesen Sachverhalt bei der Lektüre berücksichtigen.

Kiel, June 2014

Emmanuel Owden Kazimoto

Acknowledgements

I would like to thank the German Academic Exchange Programme (DAAD) and The Ministry of Education and Vocational Training of Tanzania (MOEVT) through the Tanzania Commission for Universities (TCU) for providing funds that facilitated my stay in Germany and enabled me to attain my PhD degree. I am also grateful to the University of Dar es Salaam for the financial support of my fieldworks through the Sida Earth Science Project.

The success of my PhD study was possible through the support from many people, who I may neither be able to mention in their totality nor express in words gratitude that would equal what they did to me. Here let me start with Prof. Dr. Volker Schenk, to whom I am indefinitely indebted first of all for accepting me to work together with him and the Department of Petrology here at the Institute of Geoscience in the Christian Albrecht University Kiel, I benefited a lot from his vast knowledge and experience in Petrology. Not only good supervision but also I learned a great deal from his well organised field excursions in different geologically interesting regions, for example, the Alps in northern Italy, the Ore Mountains in Germany, the Himalaya Mountains in India and Nepal, the Aravalli Craton in India and the great Semail ophiolite in Oman. I would also like to thank him and his wife, Prof. Dr. Dominique Lattard, for always making me feel like part of their family especially during sensitive times like festival seasons.

I am grateful to Prof. Dr. Astrid Holzheid for accepting to be a co-supervisor for my PhD project and therefore enabling me to pursue my doctorate degree here at Christian Albrecht University Kiel.

I would like to thank Dr. Peter Appel for being kind enough to teach and share with me his vast knowledge in Electron Probe Micro Analyser, mineral analyses and monazite dating technique. It would have not been possible to finish my doctorate degree without his skills.

My gratitude also goes to Dr. Petra Herms; first of all for being ready to teach and introduce me to fluid inclusions studies. I gained a great deal of knowledge from her vast experience on fluid inclusions studies. But also I am very appreciative for the advice or help she provided me on different matters that were concerning my personal life, for instance when my 20 ore samples were mysteriously lost. I am thankful to Dr. Peter Raase for being kind and

supportive officemate at the time we shared an office, I benefited a lot from his knowledge on microscopy and mineral identification.

I would also like to extend my thanks to Dr. Heidi Höfer of Goethe University in Frankfurt and Dr. Jasper Berndt-Gerdes of Münster University for allowing me to utilize their laboratories and for the technical assistance they provided me when I was using Scanning Electron Microscope and Laser Ablation Inductively Coupled Mass Spectrometer.

My grateful thanks are also extended to Dr. Sönke Brandt, who introduces me to pseudosection modelling using Theriak Domino software. Mr. Andreas Fehler is thanked for making a number of rock and polished thin sections, which were used in my PhD studies.

Words cannot express my gratitude to Mrs. Barbara Mader for her kindness and support that made my stay in Germany comfortable and memorable. Apart from being helpful in EPMA laboratory, Mrs. Mader has been very supportive to me and my family in different matters. I really appreciate.

I would also like to thank my colleagues: Tapabrato Sarkar, Julia Bial, Shreya Karmakar, Dr. Rauno Baase, Britta Jensen, Robert Seidel, William Schink, Daniel Weimer, Julia Immor, Rashid Benaouda and Dr. Erik Duesterhoeft, for their readiness to share their knowledge, discuss, help, listen and participate in social activities with me. It would have been very tough for me without them being there for me. I thank them very much.

Many thanks go to members of the Department of Geology of the University of Dar es salaam Tanzania for their different roles during my PhD studies. Dr. Nelson Boniface for introducing me to Prof. Dr. Volker Schenk and accompanying me during my fieldworks; Prof. Justinian R. Ikingura for his support during my first fieldwork to Mpanda; Prof. Makenya Maboko and Dr. Shukrani Manya are thanked for enabling me obtain funds for the Re-OS analyses and Dr. Isaac Marobhe and Mr. Claud John are thanked for accompanying me during my first fieldwork.

Last but not least, I would like to express my sincere thanks to my lovely wife Atuwene, son Caleb and daughter Candela. They had to go through difficult times without me for more than 42 months. I appreciate their patience, love and support in the course of my doctorate studies.

Contents

Vorwort iii

Acknowledgements v

Contents vii

List of Figures xi

List of Tables xv

Zusammenfassung xvii

Abstract xxi

Introduction xxiii

Study approach and analytical techniques xxiv

Outline of this study xxv

1. Neoarchean and Paleoproterozoic crust formation in the Ubendian Belt of Tanzania

Abstract 1

1. Introduction 2

2. Geological setting 3

2.1 Ubendian Belt 3

2.2 Katuma Block 4

3. Petrography 6

3.1 Metabasites and gabbronorites 6

3.2 Orthogneisses and granites 6

3.3 Metasedimentary rocks 7

4. Analytical methods 9

4.1 Geochemistry 9

4.2 U-Pb zircon LA-ICP-Mass Spectrometry 9

5. U–Pb zircon geochronology 10
5.1 Migmatitic orthogneiss and leucosome 11
5.2 Metabasite and gabbronorite 16
5.3 Granite, granodiorite and a granitic-gneiss 18
5.4 Metasedimentary rocks 21
6. Geochemistry 24
6.1 Element mobility 24
6.2 Metabasites and gabbronorites 25
6.3 Orthogneisses and granites 28
7. Discussion 29
7.1 Magmatic crustal forming events 29
7.2 Sedimentation age of the Ikulu Group 30
7.3 Age of metamorphic and deformational events in the Katuma Block 31
7.4 Petrogenesis of metabasites and gabbronorites 32
7.5 Petrogenesis of the Archean and Paleoproterozoic granitoids 37
7.6 Crustal evolution of the Katuma Block 38
8. Summary and conclusion 38
Acknowledgements 39
References 39

2. Granulite-facies metamorphic events in the northwestern Ubendian Belt of Tanzania

Abstract 45
1. Introduction 47
2. Geological background 47
2.1 Ubendian Belt 47
2.2 Katuma Block 48
3. Petrography and mineral chemistry 51
3.1 Analytical methods 51
3.2 Metabasites 51
3.3 Metapelites 55

4. Pressure-temperature conditions during different metamorphic events 56
4.1 Conventional geothermobarometry 57
4.2 Pseudosection modelling 58
5. Texturally controlled, in situ monazite dating 64
5.1 Monazite texture and chemistry 64
5.2 In situ U-Th-total Pb dating of monazite 66
6. Discussion 67
6.1 P-T evolution and timing of the granulite-facies metamorphism 67
6.2 Metamorphic events and crustal evolution in the Ubendian Belt 68
7. Conclusion 71
Acknowledgements 72
References 72

3. The age of Au-Cu-Pb bearing veins in the poly orogenic Ubendian Belt, Tanzania

Abstract 77
1. Introduction 78
2. Geological Setting 79
2.1 Ubendian Belt 79
2.2 Katuma Block 82
3. Analytical methods 83
4. Petrography and mineral chemistry 84
4.1 Ikulu metapelite 84
4.2 Calc-silicate rocks 86
4.3 Orthoamphibolite 86
4.4 Metamorphic evolution of the vein country rocks at Chemchem 86
5. Monazite in metapelite 88
5.1 Textures and chemistry 88
5.2 U-Th-total Pb monazite dating 92
6. Discussion 93
7. Summary and conclusions 94

Acknowledgments 95
References 95

Appendices 101
Chapter 1 101
Chapter 2 124
Chapter 3 137
Curriculum Vitae 141
Erklärung 143

List of Figures

Chapter 1

Fig. 1.1 (A) Geological map of the Ubendian Belt. (B) Lithological map of the Katuma Block.. 5

Fig. 1.2 Field pictures. 7

Fig. 1.3 Micrographs of Katuma metabasites, orthogneisses and granitoids.. 8

Fig. 1.4 Cathodoluminescence (CL) images of selected zircon grains from different rock types of the Katuma Block.. 12

Fig. 1.5 Concordia diagrams of zircon from the Katuma Block of the Ubendian Belt showing U-Pb isotope ratios and ages of migmatitic orthogneisses and a leucosomes and a diagram showing weighted mean $^{207}Pb/^{206}Pb$ age of a migmatitic orthogneiss. 15

Fig. 1.6 Diagrams showing weighted mean $^{207}Pb/^{206}Pb$ ages and concordia diagrams showing U-Pb isotope ratios and ages of orthogneiss, metabasites and gabbronorites of the Katuma Block. 17

Fig. 1.7 Diagrams showing weighted mean $^{207}Pb/^{206}Pb$ ages and concordia diagrams showing U-Pb isotope ratios and ages of granitoids and the granitic gneiss of the Katuma Block. 20

Fig. 1.8 Histogram showing $^{207}Pb/^{206}Pb$ ages of detrital zircon cores and concordia diagrams showing U-Pb ages of metamorphic zircon overgrowths from metasedimentary rocks of the Katuma Block. 23

Fig. 1.9 Classification and geochemical characteristics of the Katuma metabasites and orthogneisses. 26

Fig. 1.10 Primitive mantle (PM) normalized and (C) chondrite normalized spidergrams for metabasalts and gabbronorites.. 27

Fig. 1.11 Fenner diagrams: MgO versus selected major element oxides for gabbronorites and metabasites.. 27

Fig. 1.12 Primitive mantle (PM) normalize and chondrite normalized spidergrams.. 29

Fig. 1.13 Plots of La/Yb_{CN} versus Yb_{CN} and Sr/Y versus Y. 33

Fig. 1.14 Discrimination diagrams of Katuma metabasites and gabbronorites and their tectonic interpretation. 34

Fig. 1.15 REE modelling of melting of spinel lherzolite and decoupled fractional crystallization and assimilation (AFC).. 36

Fig. 1.16 Trace elements (ppm) versus Gd (ppm) diagrams for the Katuma metabasites and gabbros. 121

Fig. 1.17 Diagrams showing trace elements (ppm) versus Zr (ppm) or TiO_2 (wt. %) for the Katuma orthogneisses and granitoids..... 123

Chapter 2

Fig. 2.1 (a) Geological map of the Ubendian Belt. 49

Fig. 2.2 Photomicrographs, field photograph and backscatter images of metabasites and metapelites from the Katuma Block.. 53

Fig. 2.3 Composition of garnet in mafic granulite showing retrograde zoning profile in which X_{Mg} and X_{Prp} decreases and X_{Alm} increases rimwards. (b) Classification of ortho- and clinopyroxene in mafic granulite. (c and d) Composition of amphiboles in mafic granulites and amphibolites. (e and f) Zoning profiles of plagioclase in mafic granulites. 54

Fig. 2.4 (a) Composition of garnet porphyroblast in the Ikulu metapelite (b) Biotite compositions in the garnet-bearing (T18) and cordierite-bearing metapelite (T4) (c) Chemical compositions of muscovite in the metapelite. 56

Fig. 2.5 P-T pseudosection in the system Na_2O-CaO-FeO-MgO-Al_2O_3-SiO_2-TiO_2-H_2O for the mafic granulite T9-1-10.. 59

Fig. 2.6 P-T pseudosection in the system Na_2O-CaO-FeO-MgO-Al_2O_3-SiO_2-H_2O for mafic granulite T10-1-10.. 60

Fig. 2.7 P-T pseudosection in the system Na_2O-CaO-FeO-MgO-Al_2O_3-SiO_2-TiO_2-H_2O for the mafic granulite T26-3-10.. 62

Fig. 2.8 P-T pseudosection in the system Na_2O-CaO-K_2O-FeO-MgO-Al_2O_3-SiO_2-H_2O for the garnet-bearing metapelite T18-2-10.. 63

Fig. 2.9 Backscatter images of monazite grains from the Ikulu metapelites showing microtextures and the correlation of growth zones with the temporal evolution.. 65

Fig. 2.10 Chondrite-normalised rare earth elements and Y patterns of monazite from metapelites..... 66

Fig. 2.11 Plot of ((Th, U) + Si) *4 vs. ((REEs, Y) + P)*4 showing cheralite and huttonite vectors for monazite core and rim analyses of sample T18-2-10 and T4-11-10. 66

Fig. 2.12 Monazite age histograms: (a) Metamorphic ages of sample T18-2-10 (b) Metamorphic ages of sample T4-11-10. 67

Fig. 2.13 Geological sketches showing a model the most likely scenario for the geologic evolution of the northwestern Ubendian Belt of Tanzania. 70

Chapter 3

Fig. 3.1 (a) Regional geological map showing the geological setting of the Paleoproterozoic Ubendian Belt, its blocks and bordering belts. 80

Fig. 3.2 (a) Ikulu metapelite at Chemchem mine showing mafic bands (Bt-Sil) and felsic bands (Qz-Fsp). (b) K-feldspar alteration of Ikulu metapelite adjacent to the Au-Cu bearing veins at Chemchem mine. (c) Epidote-K-feldspar-sericite alteration of Ikulu metapelite adjacent to the Au-Cu-Pb bearing veins at Chemchem mine. (d) Chlorite-epidote-pyrite alteration of amphibolite adjacent to gold bearing vein. 81

Fig. 3.3 (a) A photo of ores from Singililwa Au-Cu mine. (b) Another type of ore primarily composed of quartz and sulfides (pyrite and chalcopyrite). 82

Fig. 3.4 Plane-polarized photomicrographs of various rock types from the Chemchem mine.... 85

Fig. 3.5 (a) Plot of Ti (per 11 oxygens) of biotite of the Ikulu metapelite hosting gold bearing veins. (b) Retrograde zoning in biotite of Ikulu metapelite. 87

Fig. 3.6 Microtextures of selected monazite grains (in backscattered electron images; a–e):..... 89

Fig. 3.7 Comparison of concentrations of various elements in hydrothermally altered monazite and unaltered monazite overgrowths. 90

Fig. 3.8 Plot of ((Th, U) + Si) *4 vs. ((REEs, Y) + P)*4 showing cheralite and huttonite vectors. 91

Fig. 3.9 Chondrite-normalized REE and Y patterns of the three types of monazite in the Chemchem metapelite. 91

Fig. 3.10 Age histograms. 92

List of Tables

Chapter 1

Table 1. Sample locations, protolith/metamorphic age, mineralogy and textural descriptions of the major rock types of the Katuma Block 101

Table 2. Description of zircon texture under cathodoluminescence (CL) images, interpretation of zircon growths and their corresponding age and the geologic interpretation 102

Table 3. LA-ICP-MS analyses for a meta-granodiorite (sample T1-17-10) 104

Table 4. LA-ICP-MS analyses for a paleosome of an orthogneiss (sample T14-3-10) 105

Table 5. LA-ICP-MS analyses for a leucosome of an orthogneiss (sample T14-1-10) 105

Table 6. LA-ICP-MS analyses for a granitic gneiss (sample T6-6-10) 107

Table 7. LA-ICP-MS analyses for a garnet amphibolite (sample T17-3-10) 107

Table 8. LA-ICP-MS analyses for a gabbronorite (sample T17-1-10) 108

Table 9. LA-ICP-MS analyses for a mafic granulite (sample T16-1-10) 109

Table 10. LA-ICP-MS analyses for an amphibolite (sample T19-1-10) 110

Table 11. LA-ICP-MS analyses for a granodiorite (sample T2a-2-10) 110

Table 12. LA-ICP-MS analyses for a Bt-granite (sample T2c-1-10) 111

Table 13. LA-ICP-MS analyses for a granitic gneiss (sample T19-3-10) 113

Table 14. LA-ICP-MS analyses for a calc-silicate rocks (sample T4-39-10) 113

Table 15. LA-ICP-MS analyses for a metapelite (sample T4-38-10) 114

Table 16. LA-ICP-MS analyses for a leucosome of a metapelite (sample T4-37-10) 117

Table 17. Geochemical composition of the Katuma metabasites; major elements are presented in wt. % and trace elements in ppm. 118

Table 18. Geochemical composition of the Katuma orthogneisses and granitoids; major elements are presented in wt. % and trace elements in ppm. 120

Chapter 2

Table 1 Sample locations and mineral assemblages of metabasites and metapelites of the Katuma Block..... 50

Table 2 Representative mineral chemical data for metabasites 124

Table 3 Representative mineral chemical data for metapelites..... 125

Table 4 Geothermobarometric results of metabasites and metapelites of Katuma Block 128

Table 5 Major elements composition of metabasites and one metapelite sample (T18-2-10)... 129

Table 6 Monazite core compositions and calculated U-Th-total Pb ages of a cordierite bearing metapelite (T4-11-10) 130

Table 7 Monazite rim compositions and calculated U-Th-total Pb ages of a cordierite bearing metapelite (T4-11-10) 131

Table 8 Monazite core compositions and calculated U-Th-total Pb ages of a garnet bearing metapelite (T18-2-10) 132

Table 9 ISM 4a Monazite rim compositions and calculated U-Th-total Pb ages of a garnet bearing metapelite (T18-2-10) 134

Chapter 3

Table 1 Representative electron microprobe analyses of different minerals in metapelite, calc-silicate rock and metabasite..... 137

Table 2 Electron microprobe analyses of unaltered monazite cores..... 138

Table 3 Electron microprobe analyses of unaltered monazite overgrowth zones..... 139

Table 4 Electron microprobe analyses of hydrothermally altered monazite..... 140

Zusammenfassung

Tief erodierte Orogene sind Regionen der kontinentalen Erdkruste, in denen regionalmetamorphe Gesteine vorkommen, die sich in der tiefen Kruste gebildet haben. Studien an solchen metamorphen Gürteln sind daher wichtig für das Verständnis von Prozessen, die in Wurzeln von Gebirgsgürteln stattfinden und zur Entschlüsselung von Krustenbildungsvorgängen und der Krustenentwicklung. In dieser Arbeit geht es um die Entschlüsselung der orogenen Entwicklung eines linearen paläoproterozoischen Gebirgsgürtels, dem Ubendian Belt von Tanzania, der unter anderem auch eines der ältesten in einem Gebirge aufgeschlossenen Eklogitvorkommen der Erde enthält.

Um die Bildung und Krustenentwicklung dieses linearen Ubendian Belts, sowie das Alter und die Entstehung der dortigen Lagerstätten an edlen und unedlen Metallen zu bestimmen, wurden die Gesteine des Katuma-Blocks des nordwestlichen Ubendian Belts geochemisch und petrologisch untersucht. Zudem wurde das Alter von Zirkon (U-Pb) und Monazit (U-Th-total Pb) unter Verwendung von Laser Ablation Inductively Coupled Plasma Massenspektrometrie beziehungsweise der Elektronenstrahlmikrosonde.

Interne Texturen der Zirkonkörner in Verbindung mit ihren U-Pb-Altern deuten darauf hin, dass die magmatische Bildung der Protolithe der Orthogneise und Metabasite des Katuma-Blocks hauptsächlich im Neoarchaikum (ca. 2.71–2.64 Ga), aber untergeordnet auch während des Paleoproterozoikums (2.05–1.94 Ga) stattfand. Diese zwei Perioden liegen etwa 600 Ma auseinander und werden als Stadien mit aktivem Kontinentalrand an der Grenze des Tansania Kratons interpretiert, wie aus der kalkalkalischen Zusammensetzung und den Spurenelementmustern der Metabasite und Orthogneise abgeleitet werden kann.

Die granulitfaziellen Säume in Metabasiten, bestehend aus Granat, Klinopyroxen, Quarz und Hornblende, welche magmatisch gewachsenen Orthopyroxen und Plagioklas ersetzen, lassen darauf schließen, dass die magmatischen Protolithe nach ihrer Bildung in der tiefen Kruste eine nahezu isobare Abkühlung während einer tektonisch ruhigen Phase (< 2.64 Ga) erlebten. Die detritischen Zirkonkörner aus den Metasedimenten liefern Alter von 2.64 bis 2.05 Ga, ähnlich den Bildungsaltern der Gesteine des Katuma-Blocks, was andeutet, dass der Katuma-Block

selbst die wahrscheinliche Quelle des Sediments war. Der Zeitraum der Sedimentation kann eingeschränkt werden durch das höchste Alter detritischer Zirkone bei ca. 2680 Ma und dem Alter der ersten Metamorphose der Sedimente bei ca. 1960 Ma. Dieses Ereignis wurde datiert durch das Alter von metamorphen Zirkon-Säumen und das von Monazit-Kernen. Die Phase der Sedimentation und der nahezu isobarer Abkühlung der Metabasite in der tieferen Kruste wird einem Stadium mit passivem Kontinentalrand des Tansania Kratons zwischen 2.65 und 2.05 Ga zugeordnet.

Im Gegensatz zur Art der post-magmatischen Abkühlung der archaischen Metamorphose der Metabasite, liefert das häufige Vorkommen von Sillimanit-Pseudomorphosen nach cm-großen Disthenkristallen in migmatitischen Metapeliten Beweise für zwei Stadien prograder Metamorphose verbunden mit paläoproterozoischer Krustenverdickung. Ein frühes Stadium der Metamorphose fand innerhalb des Disthen-Stabilitätsfeldes statt, wogegen der anschließende Metamorphose-Peak durch die Stabilität der Mineralparagenese Sillimanit-Granat/Cordierit-K-Feldspat charakterisiert wird. Pseudosection Modellierung der X_{Mg}-Verhältnisse für Granat zeigen, dass sich die Bildung der homogen zusammengesetzten Kerne von Granatporphyroblasten bei Bedingungen von 7 kbar und 770℃ ereignete, was vereinbar ist mit den Ergebnissen der GASP-Barometrie. Die Bildung von späten Plagioklas-Säumen um Granat in Metapeliten und die Abnahme von X_{Mg} der in den Rändern von Granatporphyroblasten, lassen auf eine nahezu isotherme Heraushebung nach der Peak-Metamorphose schließen und damit auf eine Krustenverdickung, die der Peak-Metamorphose vorangegangen sein muss.

Die U-Th-total Pb Monazit-Alter lassen vermuten, dass die Metapelite des Katuma-Blocks während des Paleoproterozoikums zwei verschiedene Metamorphoseereignisse bei ca. 1.96 Ga und 1.84 Ga durchlebten. Da zwei Wachstumszonen von Monazits (Kerne und Säume) sowohl bei Monazitkörnern in der Gesteinsmatrix als auch bei Einschlüssen in Granatporphyroblasten gefunden werden, muss das Granatwachstum während oder nach dem zweiten metamorphen Ereignis bei ca. 1840 Ma stattgefunden haben. Diese Interpretation ist wird unterstützt von der zunehmenden Verarmung an HREE und Y in den Monaziträndern, die auf ein gleichzeitiges Wachstum der Monazitsäume und der Granatporphyroblasten hinweist. Das zweite, hochgradige Ereignis bei ca. 1840 Ma steht somit in Verbindung mit der Entstehung des Ubendian Belts während der Kollision zwischen dem Tansania-Kraton und dem Bangweulu-Block. Das erste metamorphe Ereignis bei ca. 1960 Ma, welches sich ca. 120 Ma vor der Kollision ereignete, wird einer Metamorphose bei Disthen-Stabilität zugeschrieben, die während Akkretions-

Prozessen und damit verbundenem Kalk-alkalinem Magmatismus (2.05–1.94 Ga) entlang des aktiven Kontinentalrandes des Tansania-Kratons stattfand.

U-Th-total Pb-Datierung an hydrothermal alterierten Monazitkörnern von hydrothermal überprägten Metapeliten, welche die Au-Cu-Pb-haltigen Adern des Mpanda Mineral Field im Katuma Blocks enthalten, liefern ein mesoproterozoisches Alter (1171 ± 17 Ma). Dieses Alter stimmt überein mit der ersten amphibolit-aziellen Metamorphose von Metasedimenten im Wakole-Block, der nach Südwesten an den Katuma-Block angrenzt. Das ermittelte Alter liefert eine Verbindung zwischen der Metamorphose der Metasedimente im Wakole-Block und der Freisetzung hydrothermaler Fluide, welche für die Entstehung der Gold-Kupfer-Blei haltigen Adern des Katuma-Blocks verantwortlich sind.

Abstract

Orogenic belts are regions of the Earth's continental crust, in which regional metamorphic rocks occur that may have formed in the deep crust of an orogen. Studies of metamorphic belts are thus important to an understanding of processes that are taking place in roots of mountain belts.

In order to determine the formation and crustal evolution of the linear Paleoproterozoic Ubendian Belt in Tanzania and the age and origin of its precious-base metal deposits, the rocks in the Katuma Block of the northwestern Ubendian Belt were geochemically and petrologically investigated and their U-Pb zircon and U-Th-total Pb monazite ages determined using Laser Ablation Inductively Coupled Plasma Mass Spectrometer and an Electron Probe Micro Analyser, respectively.

Internal textures of the zircon grains in combination with their U-Pb ages indicate that the magmatic formation of the protoliths of the orthogneisses and metabasites of the Katuma Block occurred mostly in the Neoarchean (ca. 2.71–2.64 Ga) but also during the Paleoproterozoic (2.05–1.94 Ga). These two periods are separated for about 600 Ma and are interpreted as active continental margin stages at the border of the Tanzania Craton, as deduced by the calc-alkaline nature and trace element geochemistry of the metabasites and orthogneisses.

The granulite-facies corona assemblages in metabasites consisting of garnet, clinopyroxene, quartz and hornblende replacing magmatic orthopyroxene and plagioclase indicate that the magmatic protoliths experienced a near isobaric cooling after their intrusion into the deep crust during a tectonically quite period (< 2.64 Ga). The detrital zircon grains from the metasediments of the Katuma Block gave ages ranging between 2.64 and 2.05 Ga, similar to the magmatic formation ages of rocks of the Katuma Block, suggesting that the Katuma Block itself was most likely the source for the detritus. The time interval of sedimentation is constrained by the oldest age of the detrital zircon at about 2680 Ma and the age of the first metamorphism of the sediments at about 1960 Ma. This event is documented by the age of metamorphic zircon rims and that of monazite cores. The stage of sedimentation and the near isobaric cooling of the metabasites in the deep crust is ascribed to a passive continental margin stage of the Tanzania Craton between 2.65 and 2.05 Ga.

In contrast to the post-magmatic cooling nature of the Archean metamorphism of the metabasites, the common occurrence of sillimanite pseudomorphs after cm-sized kyanite crystals in migmatitic metapelites provides evidence for two stages of prograde metamorphism associated with Paleoproterozoic crustal thickening events. An early stage of metamorphism took place in the kyanite stability field whereas the subsequent peak metamorphism is characterised by the stability of the mineral assemblage sillimanite–garnet/cordierite–K-feldspar. Pseudosection modelling of the X_{Mg} ratios for garnet in combination with GASP barometry revealed that the formation of the compositionally homogenous cores of garnet porphyroblasts formed at conditions of about 7 kbar and 770 ℃. The formation of late-stage plagioclase coronas around garnet in metapelites and the decrease of X_{Mg} and of the spessartine component in rims of garnet porphyroblasts point to a near isothermal uplift after peak metamorphism and thus to a crustal thickening event that preceded the peak metamorphism.

The U-Th-total Pb monazite ages suggest that during the Paleoproterozoic time the Katuma metapelites experienced two separate metamorphic events at about 1.96 Ga and 1.84 Ga. As the two ages of monazite growth zones (cores and rims) are found in monazite grains of the rock matrix and in inclusions in garnet porphyroblasts, the garnet growth must have occurred during or after the second metamorphic event at 1840 Ma. This interpretation is in agreement with the increasing depletion of HREE and Y in the monazite rims indicating concurrent growth of the monazite rims and the garnet porphyroblasts. The second, high-grade event at ca. 1840 Ma is correlated with the formation of the Ubendian Belt during the collision between the Tanzania Craton and the Bangwelu Block. The first metamorphic event at ca. 1960 Ma that preceded the collision for about 120 Ma is attributed to the kyanite grade metamorphism during accretionary processes and associated calc-alkaline magmatism (2.05–1.94 Ga) along the active continental margin of the Tanzania Craton.

U-Th-total Pb dating of hydrothermally altered monazite grains from hydrothermally altered metapelites hosting the Au-Cu-Pb bearing veins of the Mpanda Mineral Field in the Katuma Block yielded a Mesoproterozoic age (1171 ± 17 Ma). This age coincides with the first, amphibolite grade metamorphism of metasediments in the Wakole Block adjoining the Katuma Block to the southwest. The obtained age provides a link between the metamorphism of the Wakole metasediments and the generation of hydrothermal fluids responsible for the formation of the gold-copper-lead bearing veins in the Katuma Block.

Introduction

The Ubendian Belt

The Ubendian Belt in the western Tanzania is a linear metamorphic belt consisting of deformed high grade metamorphic rocks and contains significant metallic resources like Cu, Au, Pb, Fe, Pd, Pt and REE (Evans et al., 2011; Lawley et al., 2013b; McConnell, 1950; Pinna et al., 2004). This belt formed in Paleoproterozoic time (2.1–1.8 Ga; Boniface et al. 2012; Lenoir et al. 1994) during the assembly of the global-scale supercontinent Columbia along collisional orogens (Zhao et al., 2002). Interestingly, the Ubendian Belt hosts Paleoproterozoic eclogites (1.88–1.86 Ga; Boniface et al., 2012), which are rarely preserved in other high grade metamorphic belts of that age, only known from a few localities (e.g. Nyong, Cameroon and Usagaran Belt, Tanazania; Möller et al., 1995; Schenk et al., 2006). These eclogites attest for oceanic lithosphere subduction preceding the continental collisions that led to the formation of the supercontinent Columbia. The Ubendian Belt therefore provides a suitable setting for studying the geodynamic evolution of a Paleoproterozoic orogen.

Despite a number of recent studies of rocks of the Ubendian Belt, its formation and geodynamic evolution is still not well understood and a comprehensive crustal evolution model of its formation is still lacking. Lenoir et al. (1994) proposed that the Ubendian Belt formed by the collisional event at about 2.1–2.0 Ga and was then affected by lateral displacements of the individual crustal blocks in this belt at about 1.86 Ga. Recent studies by Boniface and Schenk (2012) revealed eclogites of ca. 1.88–1.86 Ga in age reflecting an oceanic lithosphere subduction and a possible 1.86 Ga continent collision event. Lawley et al. (2013a) reported also the subduction related magmatism (ca. 1.96–1.88 Ga) in the southeastern Ubendian Belt that is younger than the assumed collisional event at ca. 2.1–2.0 Ga that was proposed by Lenoir et al. (1994). Therefore, the evolution of the Ubendian Belt and the general sequence of events during its evolution remained unclear. In order to resolve this problem, this study focuses on unravelling the crustal evolution of the Ubendian Belt.

In addition to the geologic history of the Ubendian Belt, the origin of the orogenic Au, Cu and Pb deposits (Goldfarb et al., 2001) in the northwestern Ubendian belt is also unclear.

Previous studies attributed the Paleoproterozoic orogenic formation of the belt to that of the deposits (Cahen et al., 1966; Nanyaro, 1989), however the subsequently reported ages for the formation of the deposits (1.66 Ga and 1.57 Ga) post-dated the Ubendian orogenic event (~ 2.1−1.8 Ga). Stendal et al. (2004) suggested contemporary intrusion of the carbonatite and the formation of the deposits in the Neoproterozoic. In addition, they proposed a genetic relationship between the two events, the carbonatite and the orogenic Au, Cu and Pb deposit formation. The recent recognition of Mesoproterozoic and Neoproterozoic orogenic events in the Ubendian Belt by Boniface et al. (2014) and Boniface and Schenk (2012) warrant speculations on the origin of these orogenic deposits. Therefore, this study used hydrothermally altered monazites of the deposits to date and to understand the orogenic formation of the deposits.

Study approach and analytical techniques

In order to unravel the crustal evolution of the Katuma Block and the origin of its precious and base metal mineralisation, fieldwork was conducted in the Mpanda area within the Katuma Block at different sites including those of artisanal and medium scale gold mines. Many rock samples of metabasites, orthogneisses, metasediments and granitoids were collected.

Geochemical data of metabasites, orthogneisses and granitoids were obtained by X-ray florescence spectrometry for major elements and ICP-MS as well as ICP-OES for trace elements. The geochemical data were used to deduce the petrogenetic history of magmatic protoliths of the rocks and the ancient tectonic setting of their magmatic formation.

Zircon grains were separated from metabasites, orthogneisses, granitoids and metasediments for LA-ICP-MS U-Pb dating. In addition, leucosomes from both migmatitic orthogneisses and metapelites were collected for dating of the migmatization events. In order to interprete the meaning of zircon ages, the internal textures of zircon grains were first studied in backscattered electron and cathodoluminescence images obtained by using a Secondary Electron Microscope (SEM). After the growth histories of the grains had been petrographically analysed, LA-ICP-MS analytical points were selected and the analyses were perfomed.

Metapelites and metabasites were preferred for petrological studies as these rocks preserved the metamorphic history by reaction textures and mineral zonations. Mineral chemical data of minerals of these rocks were obtained using an Electron Microprobe. The mineral chemical data were then used to estimate pressure and temperature conditions of the metamorphism from the composition of minerals that formed in equilibrium. To understand the metamorphic history of a

rock petrographic and mineral chemical data have been combined to perfom conventional thermobarometry. Pseudosection modelling using the THERIAK-DOMINO software was additionally applied and equilibrium assemblage diagrams for specific metapelites and metabasites have been calculated from which the conditions of metamorphism have been obtained.

In addition to zircon ages, monazite of metapelites was also dated using an electron microprobe. The U-Th-total Pb method provided the ages of metamorphic events. In situ texturally controlled monazite dating was preferred because the complex metamorphic pressure-temperature history was only obtained by linking the internal texture of metamorphic monazite grains and the texture of the rock forming minerals, in which the dated monazite occurs. Finally, hydrothermally altered monazites from hydrothermally altered metapelites hosting gold bearing veins were dated to obtain the age of the hydrothermal alteration and thus also the age of the mineralisation event.

Outline of this study

The results of this study are presented in three chapters, which are briefly described below.

Chapter 1 deals with unravelling the geologic evolution of the Katuma Block by examining internal textures of zircon grains and by determining their U-Pb ages. The ages of the magmatic crystallization of the protoliths, the age of deposition of clastic sediments on top of metamagmatic basement rocks and the ages metamorphic events of the different rock types were determined. In addition, geochemical data of selected metabasites, orthogneisses and granitoids is used to deduce their petrogenesis and ancient tectonic settings of their magmatic formation. This chapter provides new insights into magmatic and metamorphic events thatoccurred in the Neoarchean (2.71–2.64 Ga) and the Paleoproterozoic (2.05–1.94 Ga) continental margins of the Tanzania Craton. The Neoarchean events are correlated with those that formed greenstone belts in the Archean Tanzania Craton.

This chapter has been submitted to Precambrian Research.

Kazimoto, E.O., Schenk, V. and Berndt, J. (in review): Neoarchean and Paleoproterozoic crust formation in the Ubendian Belt of Tanzania: insights from zircon geochronology and geochemistry.

Chapter 2 deduces the age and nature of the metamorphic events recorded in metapelites and metabasites of the Katuma Block from petrological studies and from texturally controlled U-Th-total Pb microprobe dating of monazite in metapelites. The chapter proposes a first Neoarchean to Paleoproterozoic crustal evolution model for the Ubendian Belt, which includes all magmatic, sedimentation and metamorphic events and consists of four evolutionary stages: a Neoarchean active continental margin stage (ca. 2710–2640 Ma), a passive continental margin stage (ca. 2640–2050 Ma), a Paleoproterozoic active continental margin stage (ca. 2050 – 1880 Ma) and a final continent collisional stage (ca. 1880–1840 Ma) associated with the exhumation of eclogites.

This chapter has been submitted to Precambrian Research.

Kazimoto, E., Schenk, V. and Appel, P. (submitted): Granulite-facies metamorphic events in the northwestern Ubendian Belt of Tanzania: Implications for the Neoarchean to Paleoproterozoic crustal evolution.

Chapter 3 attempts to date a hydrothermal alteration event that associates with the Au-Cu-Pb mineralization in the Katuma Block by using Microprobe U-Th-total Pb monazite dating of the hydrothermally altered monazite grains from hydrothermally altered metapelites. The Mesoproterozoic age (≈ 1171 Ma) was obtained from these monazite grains. This Mesoproterozoic age is similar to the age of the first amphibolite grade metamorphism of metapelites of the tectonically adjoined Wakole Block to the southwest of the Katuma Block. In conclusion a Mesoproterozoic orogenic gold mineralization model is proposed for the formation of mineralization in the Katuma Block of the Ubendian Belt.

This chapter has been submitted to Contributions to Mineralogy and Petrology.

Kazimoto, E., Schenk, V. and Appel, P. (in review): The age of Au-Cu-Pb bearing veins in the poly-orogenic Ubendian Belt (Tanzania): U Th total Pb dating of hydrothermally altered monazite.

In summary the results of this thesis indicate that the northeastern Paleoproterozoic Ubendian Belt consists of Neoarchean and Paleoproterozoic protoliths, which were formed when the southwestern border of the Tanzania Craton represented an active continental margin. The rocks experienced their main metamorphic reworking during several Paleoproterozoic orogenic events. The formation of the associated Au-Cu-Pb vein deposits in the Katuma Block was the result of neither Paleoproterozoic nor Neoproterozoic mineralization events as proposed by previous authors (Nanyaro, 1989; Stendal et al., 2004), but is of Mesoproterozoic age.

References

Boniface, N., Schenk, V., 2012. Neoproterozoic eclogites in the Paleoproterozoic Ubendian Belt of Tanzania: Evidence for a Pan-African suture between the Bangweulu Block and the Tanzania Craton. Precambrian Research 208-211, 72-89.

Boniface, N., Schenk, V., Appel, P., 2012. Paleoproterozoic eclogites of MORB-type chemistry and three Proterozoic orogenic cycles in the Ubendian Belt (Tanzania): Evidence from monazite and zircon geochronology , and geochemistry. Precambrian Research 192-195, 16-33.

Boniface, N., Schenk, V., Appel, P., 2014. Mesoproterozoic high-grade metamorphism in pelitic rocks of the northwestern Ubendian Belt: Implication for the extension of the Kibaran intra-continental basins to Tanzania. Precambrian Research.

Cahen, L., Snelling, N.J., Delhal, J., Vail, J., 1966. The Geochronology and evolution of Africa.

Evans, D.M., Barrett, F.M., Prichard, H.M., Fisher, P.C., 2011. Platinum–palladium–gold mineralization in the Nkenja mafic–ultramafic body, Ubendian metamorphic belt, Tanzania. Mineralium Deposita 47, 175-196.

Goldfarb, R.J., Groves, D.I., Gardoll, S., 2001. Orogenic gold and geologic time: A global synthesis. Ore Geology Reviews 18, 1-75.

Lawley, C.J.M., Selby, D., Condon, D.J., Horstwood, M., Millar, I., Crowley, Q., Imber, J., 2013a. Lithogeochemistry, geochronology and geodynamic setting of the Lupa Terrane, Tanzania: Implications for the extent of the Archean Tanzanian Craton. Precambrian Research 231, 174-193.

Lawley, C.J.M., Selby, D., Condon, D.J., Imber, J., 2013b. Palaeoproterozoic orogenic gold style mineralization at the Southwestern Archaean Tanzanian cratonic margin, Lupa Goldfield, SW Tanzania: Implications from U–Pb titanite geochronology. Gondwana Research.

Lenoir, J.L., Liégeois, J.P., Theunissen, K., Klerkx, J., 1994. The Palaeoproterozoic Ubendian shear belt in Tanzania: geochronology and structure. Journal of African Earth 19, 169-184.

McConnell, R.B., 1950. Outline of the geology of Ufipa and Ubende.

Möller, A., Appel, P., Mezger, K., Schenk, V., 1995. Evidence for a 2 Ga subduction zone: eclogites in the Usagaran belt of Tanzania. Geological Society of America 23, 3-7.

Nanyaro, J.T., 1989. Proterozoic gold-base metal veins in the Mpanda mineral field, western Tanzania, Annalles Series in-8, Science Geologiques 97. Musée Royale de L'Afrique Centrale Tervuren, Belgium, p. 144.

Pinna, P., Muhongo, S., Mcharo, B.A., Legoff, E., Deschamps, Y., Ralay, F., Milesi, J.P., 2004. Geology and mineral map of Tanzania Scale 1:2000000. Bureau de Recherches Geologique et Minieres, France.

Schenk, V., Boniface, N., Loose, D., 2006. Paleoproterozoic subduction zones at the margins of the Tanzania and Congo Cratons: evidence from eclogites with MORB-type chemistry in the

Usagaran–Ubendian Belts of Tanzania and the Nyong complex of Cameroon. The Paleoproterozoic Record of the São Francisco Craton, 102-103.

Stendal, H., Frei, R., Muhongo, S., Rasmussen, T.M., Mnali, S.R., Petro, F., Brian Temu, E., 2004. Gold potential of the Mpanda Mineral Field, SW Tanzania: evaluation based on geological, lead isotopic and aeromagnetic data. Journal of African Earth Sciences 38, 437-447.

Zhao, G., Cawood, P.A., Wilde, S.A., Sun, M., 2002. Review of global 2.1–1.8 Ga orogens: implications for a pre-Rodinia supercontinent. Earth-Science Reviews 59, 125-162.

Chapter 1

Neoarchean and Paleoproterozoic crust formation in the Ubendian Belt of Tanzania: insights from zircon geochronology and geochemistry

Abstract

LA-ICP-MS U-Pb zircon geochronological and geochemical data of meta-igneous and metasedimentary rock types of the Katuma Block of the Paleoproterozoic Ubendian Belt in Tanzania are used to unravel the crustal evolution of this metalliferous terrain. The protoliths of the metabasites and orthogneisses previously considered to be Paleoproterozoic are in fact mostly Neoarchean in age (2713 ± 11 Ma to 2638 ± 5 Ma), from which the oldest rocks experienced their first metamorphism during the same Neoarchean orogenic cycle at ca. 2650 Ma. A second event of mafic magmatism (2021 ± 11 Ma) was concomitant with the migmatization of the Neoarchean orthogneisses and was succeeded by granitic intrusions at 1990–1940 Ma. All rocks of the Katuma Block experienced their main metamorphic reworking during several Paleoproterozoic orogenic events, which were recognized by dating of various metamorphic zircon growth zones and the age of magmatic events dated at ca. 2050, 1960 and 1880 Ma. The detritus of the high-grade metasedimentary rocks derived from Neoarchean (Katuma Block or Tanzania Craton?) and Paleoproterozoic provenances and the minimum age for the deposition is constrained by its first metamorphism at ca. 1960 Ma. The Neoarchean and Paleoproterozoic metabasites, gabbronorites and orthogneisses are sub-alkaline in composition displaying a REE and trace element geochemistry akin to those of rocks formed in modern-arc settings. On the basis of the geochemical data, the presence of eclogites, deformation and metamorphic ages, we suggest that in Paleoproterozoic time the Katuma Block was again at an active continental margin, below which a Paleoproterozoic oceanic lithosphere was subducting.

1. Introduction

When and how specific blocks of the earth's continental crust were formed is a persistent question that has interested geologist for a long time. One of the significances of understanding the formation and evolution of continental blocks is in the recognition that the genesis and regional to global distribution of large metallic deposits is related to crustal forming processes (Cooke et al., 2005; Groves et al., 2005). Since the evolution of crustal rocks has been significant for determining the controlling factors for the formation of large metallic deposits (Groves et al., 1995; Wang et al., 1998), crustal evolution studies provide a basis for formulating successful models for exploration of metallic deposit. The Paleoproterozoic Ubendian Belt in western Tanzania has been subdivided into eight crustal blocks, namely the Katuma, Wakole, Ubende, Ufipa, Mbozi, Lupa, Nyika and Upangwa blocks (Daly, 1988), among which the Lupa, Katuma and Upangwa blocks contain precious or/and base metal deposits (Fig. 1.1B). Previous studies suggested that the formation of the Ubendian Belt is related to different orogenic events, characterized by an initial collisional orogeny associated with granulite-facies metamorphism at ca. 2100–2025 Ma producing the E-W or WNW-ESE tectonic fabric of the rocks. This event was then followed by steep NW-SE lateral movements at ca. 1860 Ma (Daly, 1988; Lenoir et al., 1994). Conversely, recent studies have shown that the rocks in the Ubendian Belt experienced more than one orogenic cycle in Proterozoic time (Boniface and Schenk, 2012; Boniface et al., 2012). In addition, zircon dating of rocks in the Lupa Block showed that the protoliths of metagranites, which were previously considered to be Paleoproterozoic in age, are actually Neoarchean (~2.74 Ga) and were only reworked during the Paleoproterozoic (Lawley et al., 2013a). The same authors, in conjuction with regional seismic studies inferred that the Tanzania craton extends into the Ubendian Belt and suggested accretionary tectonics for the formation of the Ubendian Belt. Boniface and Schenk (2012) and Boniface et al. (2012) in their work on the Ubendian Belt eclogites recognized at least two Proterozoic suture zones in the Ubendian Belt: The Paleoproterozoic suture, which formed at ca. 1880 and 1860 Ma, manifested by the age of the eclogites of the Ubende Block, and a Neoproterozoic suture (ca. 590–520 Ma), which is recorded by younger eclogites of the Ufipa Block. These observations provide evidence for repeated collisional events along the suture between the Bangweulu Block in the southwest and the Tanzania Craton. In spite of the significance of the metal resources in the Katuma Block, the geodynamic setting and timing of its formation and evolution has been poorly studied. Existing geochronological data, which are mainly based on whole-rock Rb-Sr geochronology of the high-grade metamorphic rocks (Lenoir et al., 1994; Nanyaro, 1989), susceptible to resetting during metamorphism, are inadequate to understand the formation

history of the Katuma Block. In this study, we use LA-ICP-MS U-Pb zircon geochronology and geochemistry to deduce the formation history and evolution of the Katuma Block. Our data point out that most rocks of the Katuma Block were formed in a Neoarchean continental arc where they experienced also their first metamorphism. Later during the Paleoproterozoic, the block was intruded by mafic melts and granites and experienced several metamorphic events (at ca. 2650, 2050, 1960, and 1880 Ma).

2. Geological setting

2.1 Ubendian Belt

The Paleoproterozoic Ubendian Belt (Fig. 1.1) is a NW-SE trending metamorphic belt that separates the Archean Tanzania Craton at a length of about 500 km from the Karagwe-Ankolean Belt and the Bangwelu Block. To the southeast the Ubendian is bordered by the NE – SW striking Paleoproterozoic Usagaran Belt (Fig. 1.1). On its northern parts, the Ubendian Belt is overlain, with an unconformity, by Mesoproterozoic Karagwe Ankolean and the Bukoban sedimentary cover rocks. In recent studies, Lawley et al. (2013a) showed that early crustal forming events in the Lupa Block date back to Neoarchean time (2.74 Ga). Previous studies of the Ubendian Belt pointed to crustal forming events in the time between 2100 Ma and 1900 Ma, which mainly involved calc-alkaline felsic plutonism in the Nyika Block (Ring et al., 1997), Katuma and Ubende Block (Boniface, 2009) and Upangwa and Lupa Block (Lawley et al., 2013a; Lenoir et al., 1994; Manya, 2012). During this period the rocks in the Nyika Block experienced granulite-facies metamorphism (Ring et al., 1997). Eclogites with Mid Oceanic Ridge Basalt (MORB) chemistry in the Ubende Block yield SHRIMP U-Pb zircon ages of 1886 ± 16 Ma and 1866 ± 14 Ma, which represent a phases of subduction of oceanic crust and may represent the formation of a suture zone during Paleoproterozoic time (Boniface et al., 2012). Metapelites associated with these eclogites contain zircon and monazite recording an age of about 1830 Ma for a subsequent crustal thickening event in the Ubende Block (Boniface, 2009; Boniface et al., 2012). Similar ages have been reported for the emplacement of calc-alkaline granitoids and mafic rocks: 1846 ± 37 Ma for the Mpanda granite in the Katuma Block (Nanyaro, 1989), 1864 ± 32 Ma from a U-Pb zircon age of the Ufipa granite (Lenoir et al., 1994) and a SHRIMP U-Pb age of 1877 ± 20 Ma from magmatic zircon cores of the Ufipa eclogites (Boniface and Schenk, 2012). In addition to these Paleoproterozoic events, the rocks of the Wakole Block gave Mesoproterozoic metamorphic ages associated with a crustal thickening event (Boniface, 2009). Similar ages have also been found for rocks of the Ubende Block and

Lupa Blocks (Boniface et al., 2012; Lawley et al., 2013a). A Neoproterozoic to Cambrian suture zone at the northern border of the Ufipa Block contains eclogites with back-arc and island arc basalt (IAB) chemistry, which have been dated between about 590 Ma and 520 Ma (Boniface and Schenk, 2012). A Neoproterozoic–Paleozoic metamorphic overprint is also reported to occur ubiquitously in the rocks of the Ufipa and Ubende Blocks (Boniface and Schenk, 2012; Boniface et al., 2012). Ray, (1974) and Stendal et al (2004) obtained a whole rock Rb-Sr syenite crystallization age of 685 ± 62 Ma and a Pb-Pb model age for a carbonatite of 733 ± 33 Ma in the Lupa Block and Ubende Block, respectively. The latter provides evidence for a Neoproterozoic crustal extension phase prior to the Pan-African collisional event.

2.2 Katuma Block

The geology of the Katuma Block is presented in geological maps of the quarter degree sheets 152, 153, and 170 (Biyashev et al., 1977; Semyanov et al., 1977; Smirnov et al., 1970) (Fig. 1.1). A large part of the Katuma Block is extensively covered by Cenozoic alluvium and laterites (Fig. 1.1B). On its northern part, the block is covered by Meso- to Neoproterozoic terrigenous sediments of the Bukoban Supergroup that are separated from the basement by an unconformity (Semyanov et al., 1977). The basement rocks of the Katuma Block have been traditionally subdivided into two groups, of which the Katuma Group consists of migmatitic I-type orthogneisses (Hbl, Bt bearing) whereas the Ikulu group consists mainly of metasedimentary rocks, which include metapelites calc-silicate rocks, quartzite and marble (Biyashev et al., 1977; Semyanov et al., 1977; Smirnov et al., 1970). The rocks of the Ikulu Group overlie unconfomably those of the Katuma Group (Semyanov et al., 1977; Smirnov et al., 1970). The traditional subdivision of the Katuma rocks has to be questioned as the results of our zircon dating revealed that the Katuma Group includes metabasites and orthogneisses of Neoarchean and Paleoproterozoic age and should not be grouped together.

At the eastern part of the block, the orthogneisses occur together with ubiquitous amphibolites, mafic granulites and gabbronorites (Fig. 1.1B). Outcrops of amphibolites occur also in the western part of the Katuma Block adjacent to the Wakole Block (Fig. 1.1B, T19-1-10). The rocks of the Katuma Block were intruded by non-foliated to foliated granitoids that vary from biotite granite (leuco-granite), biotite-hornblende granite to granodiorite. Late E-W and NW-SW trending fractures cut the rocks of the Katuma Block and host carbonate-sulphide-quartz veins that are mineralized with Cu, Au and Pb (Fig. 1.2A). A summary of locations, protolith or metamorphic age, mineralogy and textural descriptions of major rock types of the Katuma Block is included as Table 1.

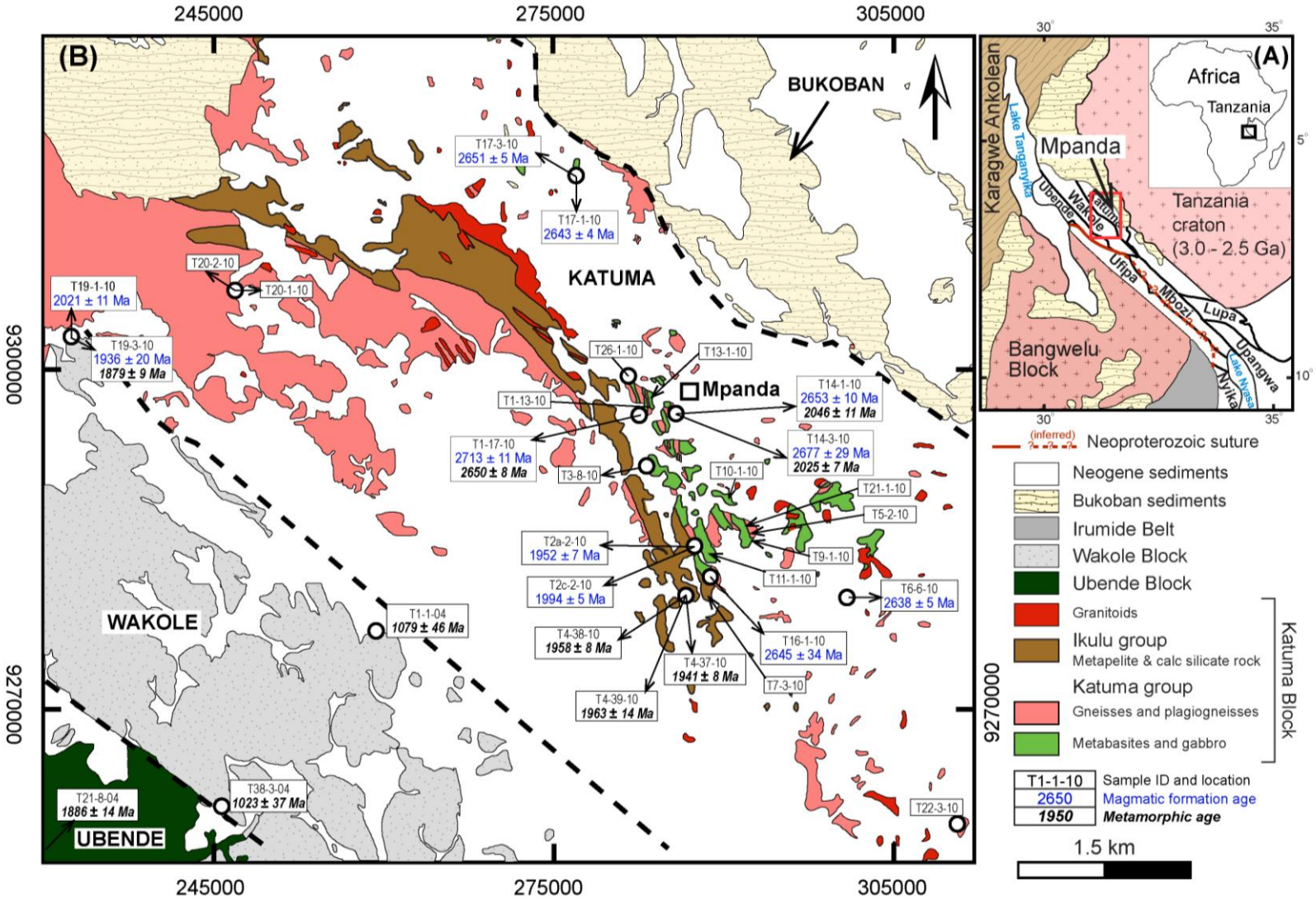

Fig. 1.1 (A) Geological map of the Ubendian Belt between the Tanzania Craton and the Bangweulu Block modified from Daly (1988); (B) Lithological map of the Katuma Block modified from Semyanov et al. (1977), Biyashev et al. (1977) and Smirnov et al. (1970) with magmatic formation and metamorphic ages, obtained in this study. The two ages of the Wakole metasedimentary rocks and one of the Ubende eclogite are from Boniface et al. (2014).

3. Petrography

3.1 Metabasites and gabbronorites

The mafic granulites are massive, greenish to dark gray in color, with mainly fine- to medium grain sizes (Fig. 1.2B). Mineral assemblages include plagioclase, ortho- and clinopyroxene, hornblende, garnet and locally biotite and pyrite. The unmetamorphic mafic rocks are gabbronorites. These rocks are massive, mainly with medium to coarse grain sizes and are composed of ortho- and clinopyroxene, plagioclase feldspar, ilmenite, pyrite, with or without biotite. Mafic minerals in both rock types are present in variable amounts between 65 and 50 vol. %. Quartz and ilmenite together are ≤ 5 vol %. Garnet in mafic granulites occurs as corona around ortho- and clinopyroxene (Fig. 1.3A).

Mafic granulites show different degrees of retrograde hydration, such that the rocks grade from granulites to amphibolites (Fig. 1.3B). Prograde mineral phases are partially replaced by hornblende, plagioclase and titanite as either late rims or symplectites. In parts, amphibolites have been further retrogressed to produce locally greenschist-facies assemblages: actinolite, epidote, chlorite, albite, titanite, quartz or/and carbonates. The gabbronorites crop out as small bodies in the Katuma Block and in places contain enclaves of garnet bearing amphibolites that are in sharp but irregular contact (Fig. 1.2C). The amphibolites also occur as small sub-conformable bodies with the enclosing gabbronoritic stocks (Semyanov et al., 1977).

3.2 Orthogneisses and granites

Orthogneisses and unfoliated granitoids cover a large part of the Katuma Block (Fig. 1.1). These rocks vary from coarse- to medium-grained, massive to gneissic and migmatitic in texture (Fig. 1.2D, 1.2E and 1.2F). The orthogneisses have mineralogical compositions similar to those of granites or granodiorites (e.g. Fig. 1.3C) with modal variations of their mafic minerals, which are mainly biotite and hornblende with or without ortho- and clinopyroxene. Ortho- and clinopyroxene, formed after biotite and hornblende, are found in melanosomes of the migmatitic orthogneisses (Fig. 1.3D). Locally the orthogneisses contain numerous mafic xenoliths (Fig. 1.2G and 1.2H), which were deformed together with their host orthogneisses (Fig. 1.2H). Veins originating from the leucosome cut some of these enclaves suggesting that the enclaves predate metamorphism and deformation. Unfoliated granitoids are mainly of two kinds: granite (leucocratic, biotite- and hornblende-biotite) and granodiorite (Fig. 1.3E and 1.3F).

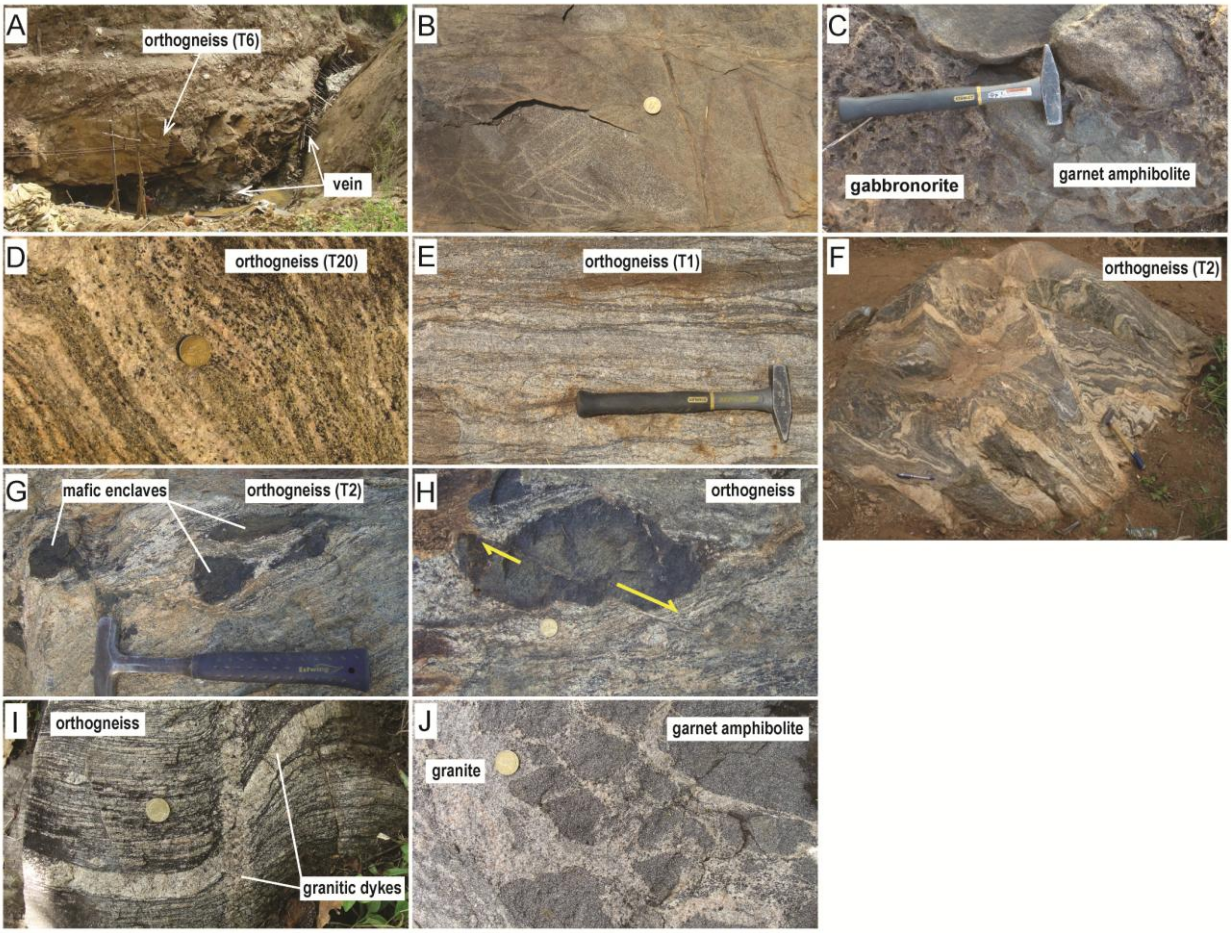

Fig. 1.2 Field pictures (A) A carbonate-quartz vein along a fracture zone cutting through a Neoarchean granite (T6-6-10). (B) An outcrop of a mafic granulite (T1-13-10) cut by numerous hydrothermal veinlets. (C) Garnet amphibolite xenoliths in a gabbronorite. (D) Foliated Hbl-Bt-granodiorite (T20-1-10). (E) Neoarchean foliated granodiorite (T1-17-10). (F) Migmatitic orthogneiss at Kapanda (T2-10). (G) Stretched mafic enclaves in Neoarchean orthogneisses of the Katuma Block (T2-10). (H) A microfault cuts both the mafic enclave and the host orthogneiss (T2-10). (I) Unfoliated granite dyke cutting a Neoarchean foliated granodiorite (T1-10), containing an earlier, deformed, near concordant dyke. (J) A contact between a brecciated garnet amphibolite and an unfoliated granite (T1-10).

Both granite types intrude the migmatitic orthogneisses and metabasites (Fig. 1.2I and 1.2J). The contact between granites and metabasites is sharp and marked either by brecciated fragments of metabasites in the granite or numerous enclaves within the granite (Fig. 1.2J). Different generations of granitic dykes can be seen cutting the orthogneisses (Fig. 1.2I).

3.3 Metasedimentary rocks

The Ikulu metasedimentary rocks exposed at Chemchem (Fig. 1.1B; T4-38-10), consist of metapelites and calc-silicate rocks. The metapelites contain K-feldspar, plagioclase, quartz, ilmenite, magnetite and pinite pseudomorphs after cordierite and sillimanite pseudomorphs after kyanite. To the north of Mpanda town, at Ibyambe Hills (T18-2-10), the metapelites consist of

garnet, sillimanite pseudomorphs after kyanite, K-feldspar, quartz, plagioclase, magnetite and ilmenite, but contain no cordierite. Calc-silicate rocks are foliated with diopside and quartz oriented parallel to the foliation. Only in thin-sections diopside, tremolite, zoisite, K-feldspar, muscovite, calcite and titanite can be recognized.

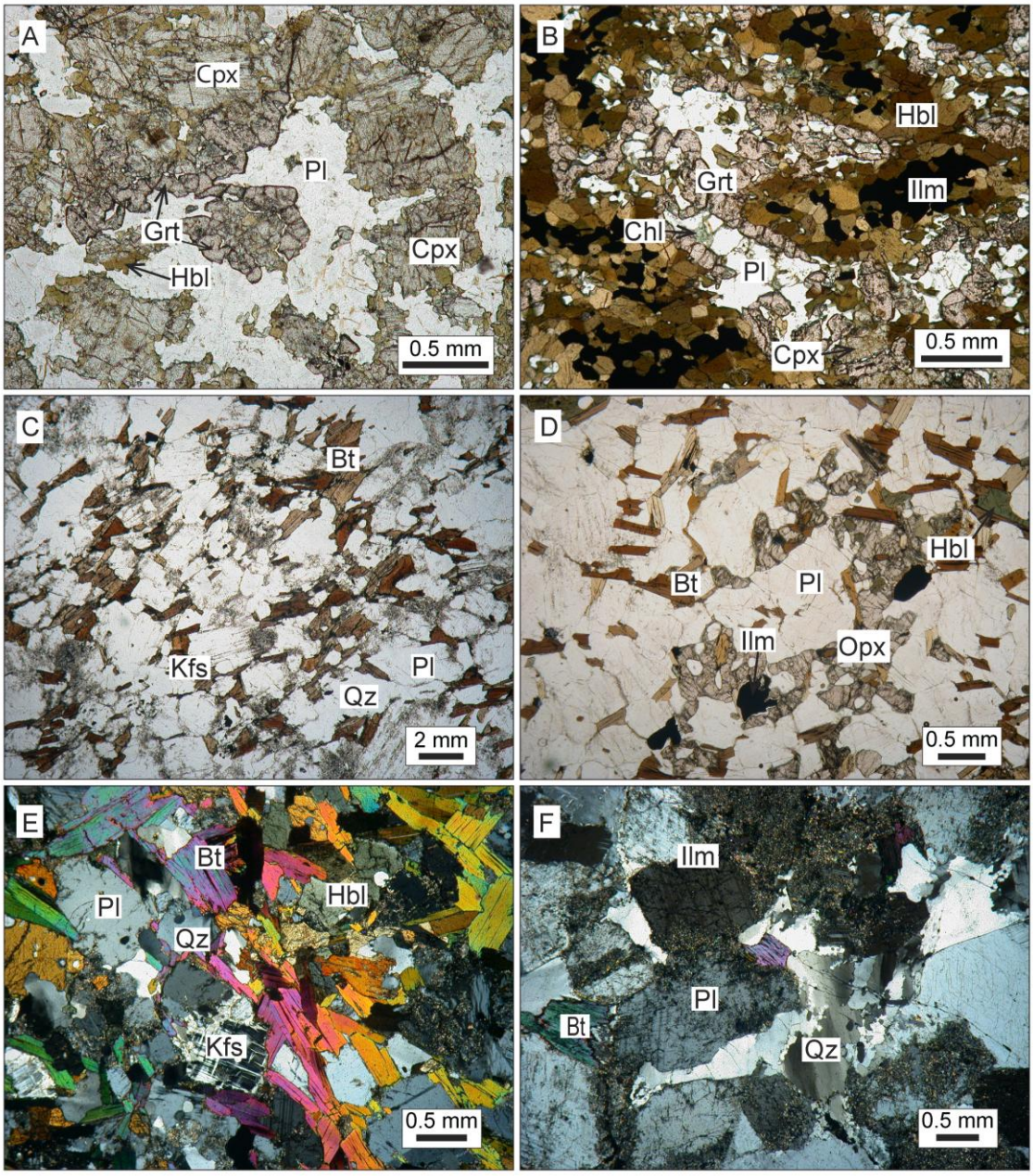

Fig. 1.3 Micrographs of Katuma metabasites, orthogneisses and granitoids. (A) Metabasites (T16-1-10) contains garnet (Grt) corona around clinopyroxene (Cpx), plagioclase (Pl), amphibole (Hbl). (B) Garnet amphibolite (T1-13-10) with the assemblage Hbl, Pl, Grt, Cpx, Qz and Ilm. (C) Meta-granodiorite (T1-17-10) consists mainly of Fsp, Qz and Bt. (D) Melanosome of Qz-monzonite (T7-2-10) contains Opx, Cpx, Hbl, Bt, Pl, Qz and Ilm. (E) Granodiorite (T2a-1-10) consists of Pl, Kfs, Qz, Hbl, Bt and Ilm. (F) Leucogranite (T2c-1-10) contains mainly Fsp, Qz, Bt and Ilm. Mineral abbreviations are from Whitney and Evans, (2009).

4. Analytical methods

4.1 Geochemistry

Texturally homogeneous fresh samples, which included twenty-three metabasites and thirteen orthogneisses and granitoids, have been analysed for major and trace elements. The samples were crushed using a screw press. Crushed samples were split into two halves and one of the halves was pulverised using an agate mill. For major element analyses, glass discs were prepared by melting a fusion of 0.6 g of a sample split together with 3.6 g lithium tetraborate ($Li_2B_4O_7$) and 2.0 g of ammonium nitrate on a five-stage OXIFLUX burner. Afterwards, the discs were analysed for major element oxides and trace element abundances using a Phillips PW 1400 X-ray fluorescence analyser at the University of Kiel. Loss on Ignition (LOI) was determined through calculating the weight difference between 2 g of a pulverised sample dried at 110°C and after ignition at 1000°C in a muffle furnace. Trace element, base and precious metal abundances of the samples were determined using Inductively Coupled Plasma Mass Spectrometry (ICP-MS) at the Acme Geochemical laboratories in Vancouver Canada. For a complete dissolution of all minerals including refractory minerals (e.g. zircon, rutile and chromite), 0.2 g of a sample split was fused with a Lithium metaborate / tetraborate flux to produce molten beads. Molten beads were then digested in 100 ml of 5% HNO_3 to produce an aliquot for trace element analyses. Precious and base metal concentrations were determined after 0.5 g of a sample was digested in Aqua Regia at 95 ^{o}C. Analytical accuracy and precision were evaluated using standards UB-N (serpentinite), BHVO-1 & -2 (basalt) and AN-G (anorthosite) for major elements, in-house standard STD SO-18 for trace elements, and in-house standard STD DS9 for precious and base metals. Precision for major and trace elements was better than 8 %, whereas the accuracy was between 1–3 % for major elements and better than 12 % for trace elements.

4.2 U-Pb zircon LA-ICP-Mass Spectrometry

Zircon mineral separation was achieved through crushing and pulverizing of samples to a grain size of ≤ 315 μm, magnetic separation using the Frantz isodynamic magnetic separator and heavy liquid separation. Zircon grains were handpicked under a binocular microscope, then mounted in epoxy and polished. For the study of grain-internal textures, cathodoluminescence (CL) and backscattered electron (BSE) images were taken by using a scanning electron microscope (SEM) at the Mineralogy Department at the Goethe University of Frankfurt. Points for analyses were selected away from fractures that occur in metamict zircons in order to avoid analyses with common Pb. The detailed procedure for the analysis of the U and Pb isotopic

composition of zircon is well described in Kooijman et al. (2012), and is briefly summarized here. U and Pb isotopic analyses of zircon were done at the Institute of Mineralogy University of Münster. The analytical instruments included a New Wave Research UP193HE ArF Excimer laser ablation system together with a Thermo Fisher Scientific sector field ICP–MS. Before the start of an analytical session, all selected zircon spots were pre-ablated three times using a 45 μm diameter laser beam. During the analyses a laser beam of 35 μm in diameter was preferentially used, although for the analysis of small zircon grains and thin zircon rim overgrowths a laser beam of 25 μm in diameter was occasionally applied. Two zircon reference materials were used: GJ-1 (Jackson et al., 2004) was the regular primary standard reference during the sessions and 91500 (Wiedenbeck et al., 1995) was utilized as an unknown to monitor precision and accuracy. The mean analytical uncertainties for single spot analyses on the 91500 reference standard zircon are 1.8% for $^{206}Pb/^{238}U$ and $^{207}Pb/^{235}U$ and 4.2 % for $^{207}Pb/^{206}Pb$. The weighted average $^{206}Pb/^{238}U$ and $^{207}Pb/^{206}Pb$ ages (n=29) are 1063 ± 5 Ma and 1063 ± 7 Ma and match within error the reported ID-TIMS ages of Wiedenbeck et al. (1995).

5. U–Pb zircon geochronology

Fourteen rock samples were selected for U-Pb zircon geochronology. These samples include 3 metabasites, 1 gabbronorite, 3 migmatitic orthogneisses, 2 granites and 1 granodiorite, 2 metasedimentary rocks and 2 leucosomes from a migmatitic orthogneiss and a metapelite (sample locations - Fig. 1.1). In this section, zircon textures, $^{207}Pb/^{206}Pb$ and U-Pb ages are used to determine the ages of the protoliths of metabasites and orthogneisses, of detrital zircon from metasedimentary rocks and the age of metamorphism. Zircon from the leucosomes was used to establish the age of migmatization of an Ikulu metapelite and a Katuma orthogneiss. The ages of these events were determined from concordant analyses of the zircon's core or overgrowth zones that most likely represent their crystallization ages.

The significance of ages determined from near concordant to discordant analyses from zircon core and overgrowth zones are discussed considering the possible Pb-loss at temperatures < 600 ºC in metamict zircon grains (Mezger and Krogstad, 1997). Moreover, the interpreted metamorphic ages were compared to and correlated with metamorphic ages determined from electron microprobe U-Th-total Pb monazite dating (ca. 1970 Ma and 1840 Ma; Kazimoto et al. in review; Kazimoto et al. in preparation). U-Pb isotope data tables are provided as Table 3–16. Representative CL images are given in Figure 1.4.

5.1 Migmatitic orthogneiss and leucosome

Four samples of the Katuma migmatitc orthogneisses were collected from three localities (Fig. 1.1): Mkamba Hill (T1-17-10), Nyakaliza (T14-3-10 and T14-1-10) and Singililwa (T6-6-10). These samples were selected in order to provide the age of their magmatic emplacement and metamorphism.

The granodioritic orthogneiss sample T1-17-10 is from the Mkwamba Hill near the abandoned Uruwira Au-Cu mine. Zircon grains from this sample range between 50 μm and 200 μm in size and vary from long prismatic to fairly stubby and rounded in shape (Fig. 1.4A). In cathodoluminescence images, zircon cores show concentric oscillatory zoning. Some zircon cores have resorbed irregular boundaries that are cut and surrounded by metamorphic overgrowths (Fig. 1.4A). Thirty-two (32) laser spots were made from 22 zircon grains. Among these spots 17 were made from zircon cores and 15 from rim overgrowths. Twelve analyses of zircon cores are concordant (100 ± 2 % concordance) with an apparent $^{207}Pb/^{206}Pb$ age range of 2740–2690 Ma (Fig. 1.5A) and an average weighted $^{207}Pb/^{206}Pb$ age of 2713 ± 11 Ma (MSWD = 3.5; Fig. 1.5B). Two analyses of zircon cores (T1-17-15-4 and T1-17-16-4) are near concordant and discordant (95.1 and 87.7 % concordance) with $^{207}Pb/^{206}Pb$ ages of 2646 ± 24 Ma and 2682 ± 21 Ma respectively, which suggests a possible Pb-loss of the zircon cores. Two further analyses of zircon cores (T1-17-1-4 and T1-17-12-4) possess significant common-Pb (1.3% and 1.7% $f206\%$) and thus gave imprecise low $^{207}Pb/^{206}Pb$ ages of 2234 ± 43 Ma and 2003 ± 61 Ma. One analysis of an inherited core (Table 3; T1-17-16-1) yielded a concordant $^{207}Pb/^{206}Pb$ age of 2805 ± 17 Ma.

Nine analyses of metamorphic rim overgrowths are concordant (100 ± 2 % concordance) and yielded a precise age of 2650 ± 8 Ma (MSWD 0.09; Fig. 1.5C). Five discordant analyses (Fig. 1.5D) yielded an upper intercept age of 2647 ± 53 Ma and a meaningless lower intercept age of -794 ± 2000 Ma (MSWD = 9.5; Fig. 1.5D). The upper intercept age is similar to that obtained from concordant rim analyses. Thus, the age of 2650 ± 8 Ma age is considered as the crystallization age of the zircon rim overgrowths, which is about 60 Ma younger than the age of the cores.

Two orthogneisses T14-3-10 and T14-1-10 were sampled at Nyakaliza Pb mine (artisanal), SW of Mpanda (Fig. 1.1). Sample T14-3-10 is a paleosome whereas T14-1-10 is a leucosome of an orthogneiss forming the host rock for the galena veins.

Fig. 1.4 Cathodoluminescence (CL) images of selected zircon grains from different rock types of the Katuma Block. The figures show different zircon textures: magmatic zircon cores with concentric oscillatory zoning (A-D, G-I), zircon rims overgrown during metamorphism (A-C, J-L) and late-stage magmatic re-crystallization of zircon (E). Spots on images represent areas of LA-ICP-MS analyses. For further explanation of the individual pictures see text.

Zircon grains in sample T14-3-10 are prismatic euhedral to subhedral. The grain sizes vary from < 200 µm to ≈ 400 µm. In CL images some zircon cores show concentric oscillatory magmatic zoning. Other grains have recrystallized zircon cores and show fracturing (Fig. 1.4B). The shape

of zircon cores are variable in characteristics, which include spherical, irregular and angular grains (Fig. 1.4B). The cores are surrounded by a metamorphic rim-overgrowth (Fig. 1.4B). Thirty-five ablations spots were made on 19 grains, including 15 spots of cores and 20 of rims. The most concordant core analyses (n=7; 100 ± 1 % concordance) yielded a $^{207}Pb/^{206}Pb$ age range of 2720–2640 Ma and a mean of 2677 ± 29 Ma (MSWD = 11.2). The large MSWD value reflects the large age range (80 Ma) of the core analyses. Four other concordant core analyses (T14-3-5-4, T14-3-7-4, T14-3-16-4 and T14-3-17-4; 100 ± 2 % concordance), yielded younger $^{207}Pb/^{206}Pb$ ages of 2597 ± 20 Ma, 2456 ± 18 Ma, 2439 ± 19 Ma and 2450 ± 18 Ma. These ages are similar to $^{207}Pb/^{206}Pb$ ages of slightly discordant points (e.g. T14-3-2-4, T14-3-12-4 and T14-3-19-4; 105 %, 94 %, 97 % concordance), thus suggesting a Pb-loss of these zircon cores or erroneously analyses due to laser probing of a zircon core together with parts of a rim overgrowths. Two further analyses (T14-3-12-4 and T14-3-13-4) contain significant common Pb (1.5 % *f*206%) and could not be used in age calculations. Concordant analyses of the metamorphically overgrown rims (n = 11; 100 ± 2 % concordance) yielded $^{207}Pb/^{206}Pb$ ages ranging between 2080 and 2002 Ma with a $^{207}Pb/^{206}Pb$ weighted mean age of 2032 ± 21 Ma (MSWD = 5.3). The large MSWD value reflects the scatter of $^{207}Pb/^{206}Pb$ ages for about 78 Ma. Excluding two analyses (out of the 11 points) with higher $^{207}Pb/^{206}Pb$ ages (≈ 2080 Ma) we obtained a precise U-Pb age of 2025 ± 8 Ma (MSWD = 0.04; Fig. 1.5E). Eight discordant analyses (93–96 % concordance) of zircon overgrowths gave an imprecise upper intercept age of 2643 ± 90 Ma and a lower intercept at 1758 ± 63 Ma (MSWD = 2.2; Fig. 1.5F), reflecting a crystallization age of the zircon rims at about 2650 Ma and most likely a Pb-loss event at about 1758 ± 63 Ma, which is within error to a 1840 Ma event obtained from monazite dating. One analysis (T14-3-12-7) of a zircon rim overgrowth was discarded from age calculations due to its high common-Pb (2.2 % f206%).

Zircon grains of an orthogneiss leucosome (T14-1-10; n=19) are similar in shape and size to those of the paleosome (T14-3-10), which are long prismatic and their sizes vary from < 200 μm to ≈ 400 μm. The grains have distinct cores surrounded by rim overgrowths (Fig. 1.4C). The majority of zircon cores have irregular, broken or resorbed margins and exhibit unzoned, recrystallized internal textures, but few cores show magmatic concentric oscillatory zoning (Fig. 1.4C). Zircon rim overgrowths are relatively large reaching up to 100 μm in width. Five concordant analyses (100 ± 1 % concordance) of zircon cores gave an U-Pb age of 2653 ± 10 Ma (MSWD = 0.5; Fig. 1.5G). This age is lower but within error similar to that of the zircon cores in the paleosome (2677 ± 29 Ma). Further eight concordant analyses of the cores

(98.3–101.1 % concordance; Table 5) yielded $^{207}Pb/^{206}Pb$ ages between 2620 and 2170 Ma. These ages are younger than those of the cores presented above (mean ≈ 2650 Ma), which could be a consequence of erroneously laser probing from parts of the rim overgrowths together with those of the core, although analyses points were carefully selected from CL images. Seven concordant analyses (100 ± 2 % concordance) of the rim overgrowths yielded a $^{207}Pb/^{206}Pb$ age range of 2070–2040 Ma and a weighted mean age of 2043 ± 18 Ma (MSWD = 1.5; Fig. 1.5H). These analyses gave a precise U-Pb age of 2045 ± 11 Ma (MSWD = 0.98), which is older but very similar to the crystallization age of the overgrowth zones in the paleosome. Four analyses of the zircon overgrowths zones are near concordant to discordant (concordance 82.4–104.2 %), indicating a Pb-loss. One analysis of an inherited core (T14-1-15-1) yielded a $^{207}Pb/^{206}Pb$ age of 2817 ± 27 Ma (Table 5). Three analyses of zircon cores and three of the overgrown rims have significant common-Pb (1.1–9.3 % $f206\%$), which could not be corrected using the Stacey-Kramer model and therefore were not included in Figure 1.5G and H.

A further granitic gneiss (T6-6-10), hosting gold bearing sulphide-carbonate-quartz veins, derives from the Singililwa Au-Cu mine situated southeast of Mpanda town. Zircon grains are in the size range 200 – 500μm, euhedral to subhedral and mainly prismatic in shape. Terminations of the grains are flat (Fig. 1.4D). Some grains are stubby (fairly equant) with small length to width ratios (1.5–2.0). In CL images, zircon grains show concentric oscillatory zonation that is interpreted to be of magmatic origin (Fig. 1.4D). Zircon cores vary from bright luminescent white (58–168 ppm) to dark gray non-luminiscent (328–525 ppm) zones. Forty-eight laser ablation spots were made in 20 zircon cores. Thirty-nine of these analyses yielded an weighted mean $^{207}Pb/^{206}Pb$ age of 2635 ± 8 Ma (MSWD = 6.5; Fig. 1.6A). The large MSWD value reflects the large scatter of $^{207}Pb/^{206}Pb$ ages (120 Ma). Selection of the most concordant analyses (100 ± 2 % concordance) that have $^{207}Pb/^{206}Pb$ ages close to that of the weighted mean age (≈ 2630 Ma) enabled the calculation of a precise U-Pb age of 2638 ± 5 Ma (MSWD = 0.14; Fig. 1.6B), which provides a good estimate of the magmatic crystallization age.

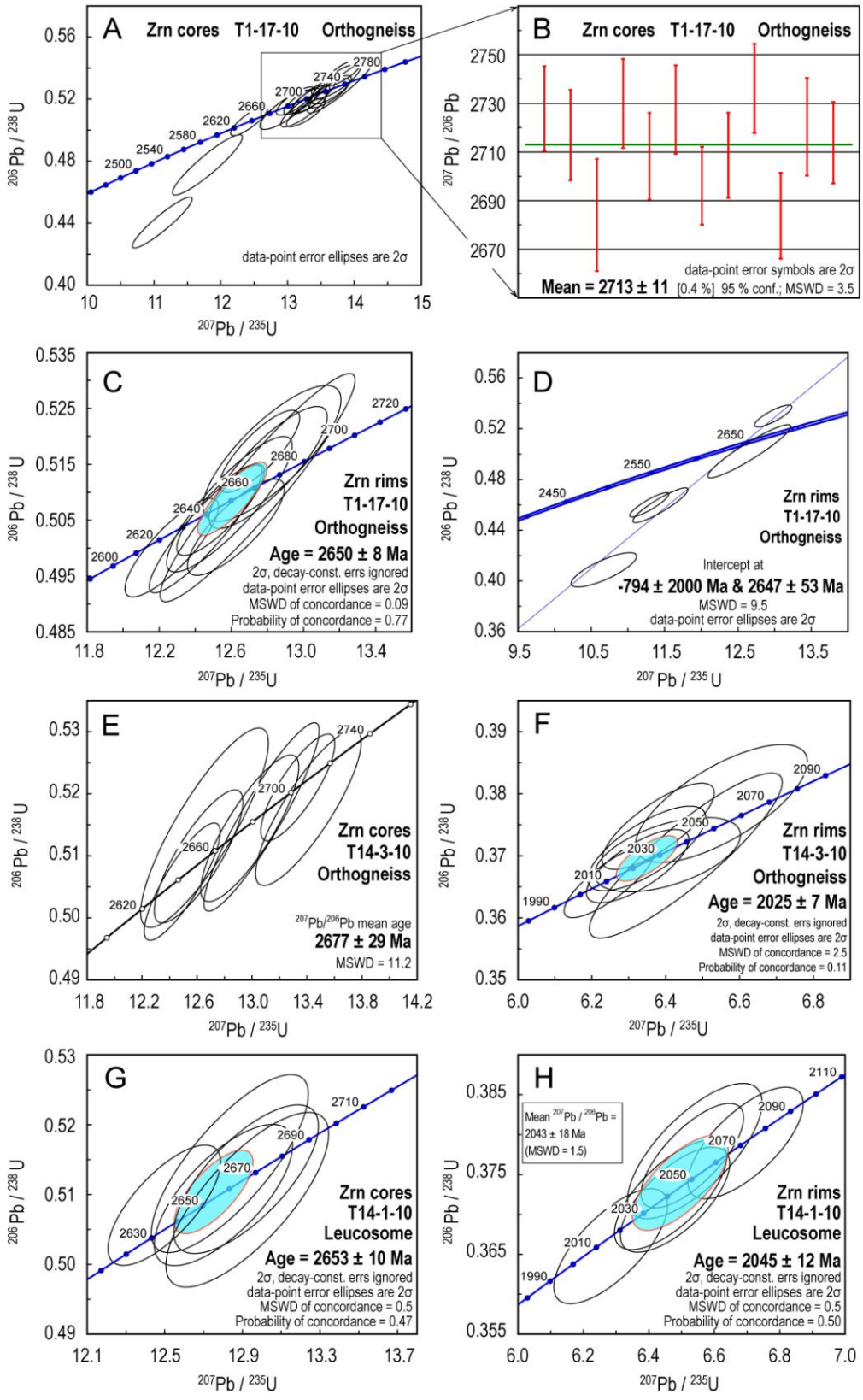

Fig. 1.5 Concordia diagrams of zircon from the Katuma Block of the Ubendian Belt showing U-Pb isotope ratios and ages of migmatitic orthogneisses and a leucosomes (A, C – H) and a diagram showing weighted mean $^{207}Pb/^{206}Pb$ age of a migmatitic orthogneiss (B; T1-17-10).

One zircon grain yielded two concordant analyses (T6-6-3-1 and T6-6-3-5; 100 ± 1% concordance) with a lower $^{207}Pb/^{206}Pb$ ages of 2573 ± 18 Ma and 2574 ± 27 Ma. Three concordant analyses (concordance 99.7% –102.1%) of overgrowth zones (T6-6-5-7, T6-6-20-7 and T6-6-20-8) have young $^{207}Pb/^{206}Pb$ ages of 1997 ± 22 Ma, 2033 ± 18 Ma and 2015 ± 19 Ma, respectively.

5.2 Metabasite and gabbronorite

One gabbronorite (T17-1-10) and an enclosed xenolith of a garnet amphibolite (T17-3-10; Fig. 1.2C), one mafic granulite (T16-1-10) and one amphibolite (T19-1-10) were analysed to date the age of the magmatic emplacements (for locations see Fig. 1.1B).The xenoliths in the gabbronorite contains medium to fine grained zircon grains (< 300 μm), which vary in morphology from prismatic to spherical grains, rarely with incomplete crystal faces and locally with concave embayments (Fig. 1.4E). The latter is suggestive of formation of zircon in interstitial spaces between early formed minerals in late-stage magmatic differentiates (Corfu et al., 2003). Few zircon grains contain mineral inclusions. In CL images, zircon grains show magmatic oscillatory zoning that is frequently disrupted by recrystallized zones (Fig. 1.4E). In some grains the irregular boundaries of cores are surrounded by non-luminescent rim overgrowths. Thirty-five ablation points were made on 23 zircon grains, both on zircon cores and recrystallized zones. Thirty-four concordant to near concordant analyses (100 ± 4 % concordance) yielded a $^{207}Pb/^{206}Pb$ weighted mean age of 2652 ± 8 Ma (MSWD = 2.3; Fig. 1.6C). The selection of the 26 most concordant analyses (100 ± 1 % concordance) yielded a precise U-Pb crystallization age of 2651 ± 5 Ma. The remaining points with slight discordance suggest a possible Pb-loss. One analysis has significant common-Pb (3.9 % *f*206%) and is not included in Figure 1.6C and D.

Zircon grains from the gabbronorite (T17-1-10) are coarse grained (ca. 500 μm) and prismatic with large length to width ratios (6:1). Cathodoluminescence images show broad oscillatory zones with bright luminescent inner zones (U = < 179 ppm) and dark non-luminescent outer zones (U = 238–524 ppm; Fig. 1.4F). Twenty-five ablation spots were made in 14 zircon grains. Twenty-four concordant to near concordant analyses (≥ 93–100 % concordance) yielded a $^{207}Pb/^{206}Pb$ weighted mean age of 2645 ± 5 Ma (MSWD = 1.8; Fig. 1.6E).

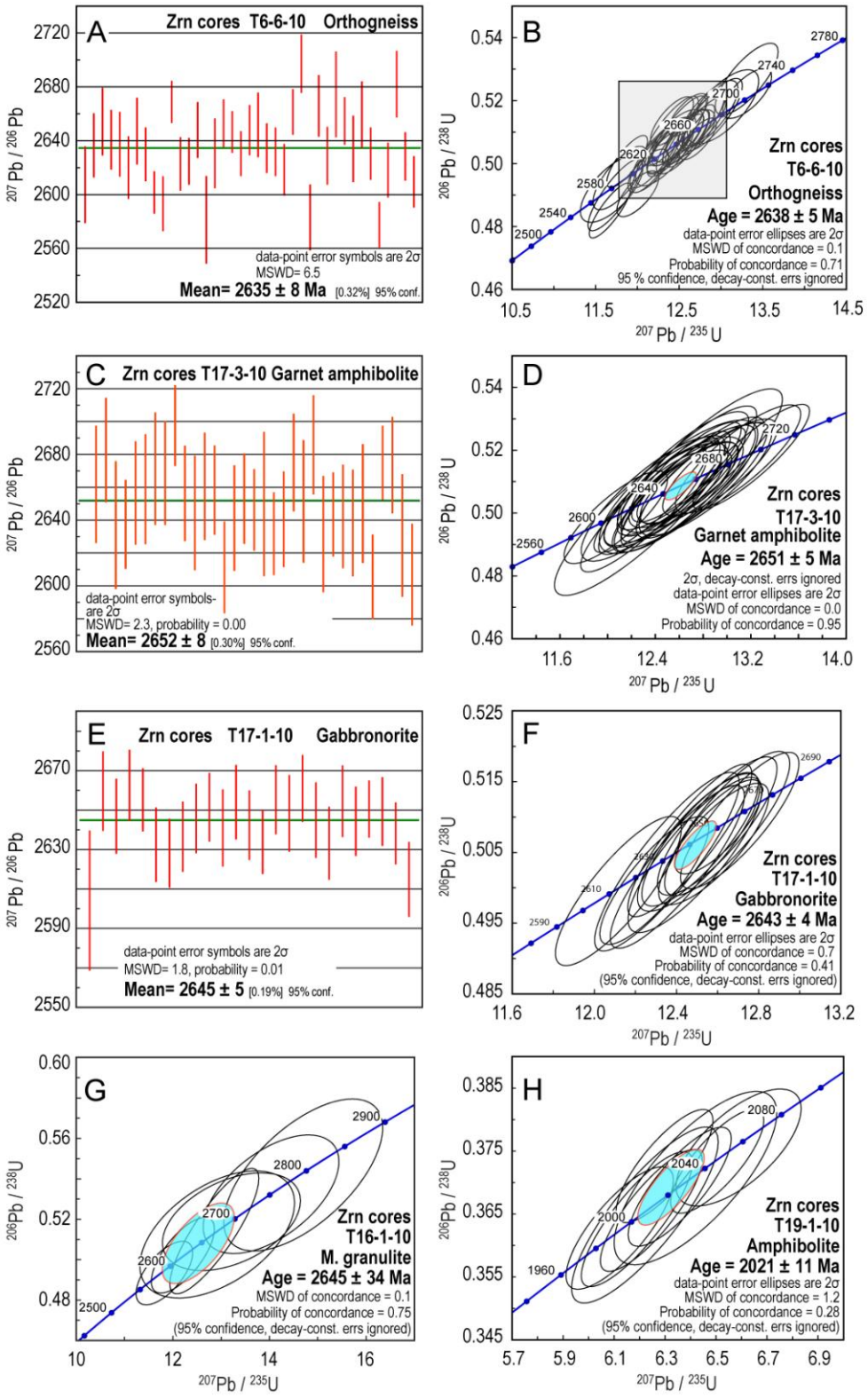

Fig. 1.6 Diagrams showing weighted mean $^{207}Pb/^{206}Pb$ ages (A, C and E) and concordia diagrams showing U-Pb isotope ratios and ages (B, D, F, G and H) of orthogneiss, metabasites and gabbronorites of the Katuma Block.

U-Pb age calculations of the 20 most concordant analyses (98–100 % concordance) yielded a precise crystallization age of 2643 ± 4 Ma (MSWD = 0.68) for the gabbronorite (Fig. 1.6D). This age is slightly younger or within the errors nearly identical to the age of its enclosed schistose garnet-amphibolite xenoliths (T17-3-10), which experienced their metamorphism prior to the intrusion of the Neoarchean gabbronorite. The remaining 5 slightly discordant analyses (87–95.3 % concordance) suggest a possible Pb-loss after crystallization.

A mafic granulite (T16-1-10) was taken from an outcrop near the Mpanda highway, south of Mpanda town (Fig. 1.1). Five zircon grains separated from this sample have grain sizes of < 200 μm, are prismatic in shape and show concentric magmatic zoning (Fig. 1.4G). Eleven ablation spots were made on the grains of which 7 are mostly concordant (concordance 99–104 %) and yielded a U-Pb age of 2645 ± 34 Ma (MSWD=0.1; Fig. 1.6G). Despite large uncertainties, the magmatic crystallization age of this mafic granulite is similar to the age obtained for magmatic crystallization of the orthogneisses (T6-6-10 and T14-3-10), the gabbronorite and its garnet amphibolite xenolith (T17-1-10 and T17-3-10). The remaining four analyses (T16-1-1-3, T16-1-2-4, T16-1-3-1 and T16-1-3-5) are discordant, suggesting a possible Pb-loss after the crystallization of these zircon grains.

An amphibolite (T19-1-10) was sampled to the west of Mpanda town at the boundary between the Katuma and the Wakole Block (Fig. 1.1). Only two zircon grains of about 200 μm in size could be separated from this sample. Thirteen analyses were made on the two zircon grains. Out of these, 10 concordant analyses (concordance 99–102 %) yielded an age of 2021 ± 11 Ma (MSWD = 1.15; Fig. 1.6H), which is interpreted as the crystallization age. Two discordant analyses (T19-1-1-5 and T19-1-3-4), one analysis that has high common Pb (T19-1-3-7; 1.2 % *f*206%) and one concordant analysis possessing large errors in U-Pb (T19-1-1-4) were not included in Figure 1.6H but gave similar $^{207}Pb/^{206}Pb$ ages of 1966 ± 25 Ma, 1914 ± 20 Ma, 1972 ± 28 Ma and 2013 ± 155 Ma.

5.3 Granite, granodiorite and a granitic-gneiss

Two major kinds of granitoids, granodiorites and biotite granites (leucogranite), intruded the Katuma orthogneisses, amphibolites and mafic granulites. Two samples from these unfoliated two granitoids types were selected to determine the age of their magmatic crystallization (biotite granite, T2c-1-10; granodiorite, T2a-2-10 at Kapanda mine). The magmatic and metamorphic age was determined from a muscovite-biotite granitic gneiss (T19-3-10), taken at the border between the Wakole and the Katuma Block; Fig. 1.1).

The granodiorite from the Kapanda artisanal mine (T2a-2-10) contains zircon grains that are subhedral and about 250 μm in size. They have small length to width ratios and shapes that vary from stubby, equant to spherical. The grains show concentric oscillatory magmatic zoning and only some have thin overgrowths that cut the growth zones of the cores (Fig. 1.4H). Twenty-seven spots were made from 14 zircon grains. Out of these analyses, the 17 most concordant analyses (100 ± 2 % concordance; one has 95 % concordance) yielded a weighted average $^{207}Pb/^{206}Pb$ age of 1963 ± 13 Ma (MSWD = 4.6; Fig. 1.7A). Concordant analyses (n = 12; 100 ± 2 % concordance) yielded a precise crystallization age of 1952 ± 7 Ma (MSWD = 1.9; Fig. 1.7B). Two further analyses (T2a-2-1-4 and T2a-2-14-5) are slightly discordant (95 % and 80% concordance), indicating a Pb-loss after their crystallization. Eight analyses of the 27 spots possessed significant common Pb (16.9–52.2 % *f*206%) and high U contents (709–5417 ppm), which possibly caused the metamictization of zircon grains and attributed to their high common Pb.

The biotite granite (T2c-1-10) crops out near to the granodiorite T2a-1-10 (Fig. 1.1). This rock contains coarse grained zircon (≤ 600 μm) (Fig. 1.4I), which shows magmatic growth zoning similar to those of magmatic crustal rocks (Corfu et al., 2003). The grains have small length to width ratios (1.5–2.0) and have short prismatic or ellipsoidal shapes. Twenty-one ablation points were made from 20 zircon grains, among which 16 concordant points (100 ± 2 % concordance) yielded a weighted mean $^{207}Pb/^{206}Pb$ age of 1989 ± 11 Ma (MSWD = 4.4; Fig. 1.7C). The large MSWD value reflects a scatter caused by three $^{207}Pb/^{206}Pb$ age outliers of concordant analyses (T2c-1-15-5, 1912 ± 24 Ma; T2c-1-16-4, 2022 ± 23 Ma; and T2c-1-18-4, 2019 ± 21 Ma). By excluding other three analyses out of the 16 concordant points because of their lower or higher $^{207}Pb/^{235}U$ and $^{206}Pb/^{238}U$ ages (T2c-1-10-4, T2c-1-15-4, T2c-1-15-5), it was possible to obtain a more precise U-Pb age of 1993 ± 6 Ma (MSWD = 1.3; Fig. 1.7D) for this granite. The remaining 5 out of the total 21 points are near concordant (94–106 % concordance) and yielded an upper intercept age of 1971 ± 13 Ma (MSWD = 2.2), which is similar within uncertainties to that of of the concordant points. The insignificant lower intercept age at 231 ± 490 Ma, reflects a later Pb-loss.

The muscovite-biotite granitic gneiss T19-3-10 (Fig. 1.1) has zircon grains of variable size, (≤ 200 μm) with different shapes and appearance compared to those of the other two Katuma granitoids (T2a-2-10 and T2c-1-10). The grains are long prismatic in shape with rounded terminations and have a large length to width ratio (3:1). In CL images (Fig. 1.4J and ISM 8), zircon cores are surrounded by very thin metamorphic rims.

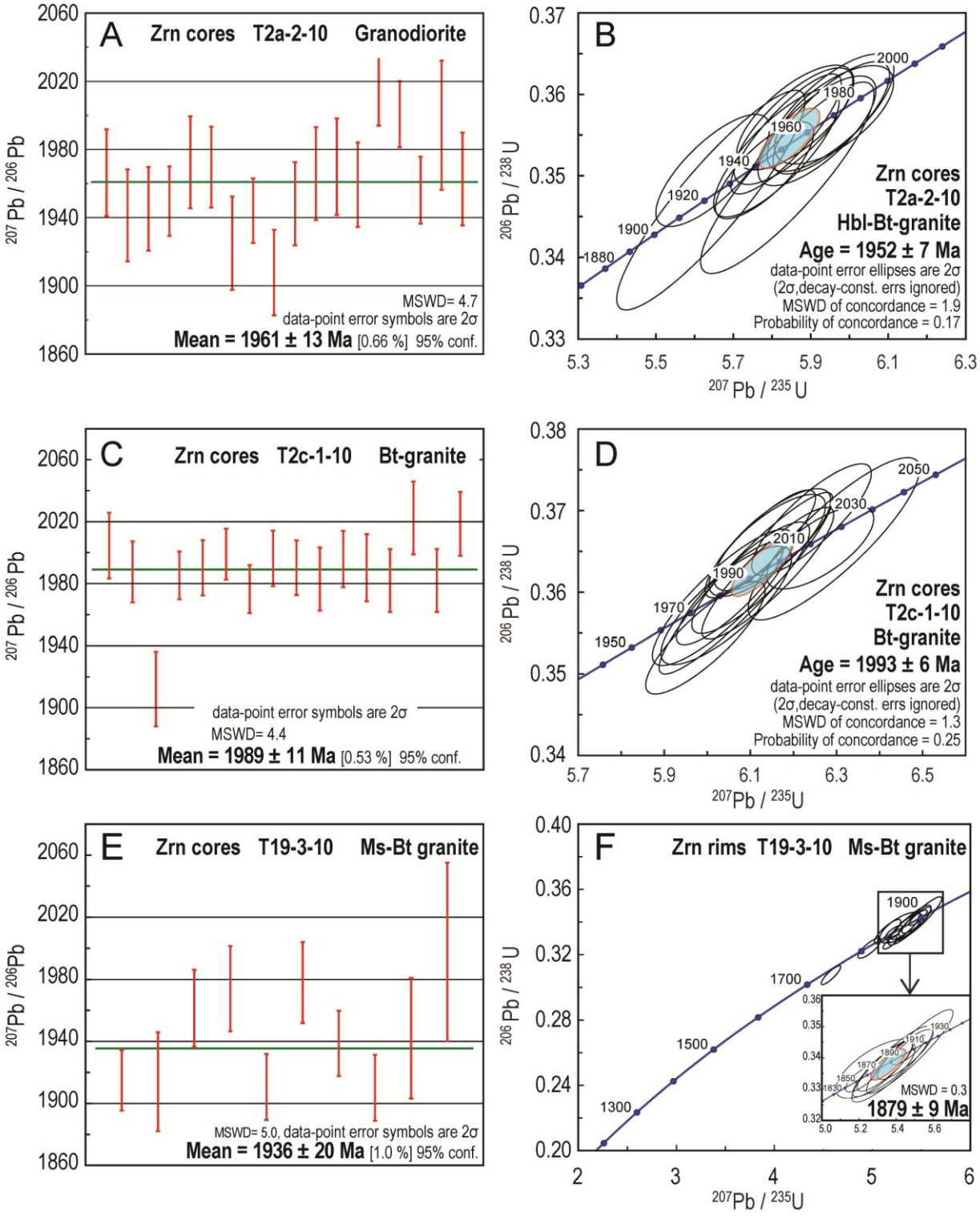

Fig. 1.7 Diagrams showing weighted mean $^{207}Pb/^{206}Pb$ ages (A, C and E) and concordia diagrams showing U-Pb isotope ratios and ages (B, D and F) of granitoids and the granitic gneiss of the Katuma Block.

The weak dark gray luminescent cores (mean U = 440 ppm) display narrow zoning similar to zircon of aplites (Corfu et al., 2003) and are interpreted to reflect magmatic growth. The rim overgrowths have gray tones of luminescence (mean U = 259 ppm). Twenty-eight ablation spots

were made on 23 zircon grains, among which 16 spots were of cores and 12 of rim overgrowths. Most analyses of zircon cores (n=10) are concordant (98–100 % concordance) and have a $^{207}Pb/^{206}Pb$ age range of 1910–1998 Ma with a weighted mean $^{207}Pb/^{206}Pb$ age of 1936 ± 20 Ma (MSWD = 5.0; Fig. 1.7E). This age is considered to represent the best crystallization age of the cores. Four cores analyses (T19-3-6-4, T19-3-13-4, T19-3-17-4 and T19-3-20-4) are discordant (concordance = 83.6%, 94.6 %, 95.4% and 109 %), indicating a Pb loss. Further 2 core analyses (T19-3-11-4 and T19-3-18-4) have high common Pb (1.1 and 3.2 % *f*206%) and could not be corrected using the Stacey-Kramer model, thus are not included in Figure 1.7E. Seven concordant rim analyses (concordance 99.9–100%) yielded an age of 1879 ± 9 Ma (MSWD = 0.34; Fig. 1.7F) that is considered as the precise age of the overgrowth zones. Other 4 rim analyses (T19-3-2-7, T19-3-8-7, T19-3-14-7 and T19-3-15-4) are concordant (100 ± 2 % concordance) but have lower $^{207}Pb/^{235}U$ and $^{206}Pb/^{238}U$ ages. These were included in U-Pb age calculations. It was not possible to obtain an U-Pb age for the rims.

5.4 Metasedimentary rocks

One calc-silicate (T4-39-10), one metapelite (T4-38-10) and one leucosome of a metapelite (T4-37-10) were selected rocks of the Ikulu group metasediments at the Chemchem Cu-Au abandoned mine (Fig. 1.1). The age of the metamorphic rims and the ages of the detrital zircon cores were determined.

The calc-silicate rock T4-39-10 (Fig. 1.1) was sampled from the Ikulu Hill. Zircon grains from this sample vary in size (50–300 μm) and shape. They are ellipsoidal or long to short prismatic and have rounded terminations. In CL images the grain cores are visible as ellipsoidal, broken fragments with rounded or irregular margins, which is consistent with their detrital origin (Fig. 1.4K). The growth zones of the detrital cores are truncated or surrounded by overgrowth zones (Fig. 1.4K). Twenty-nine zircon grains showing detrital cores and overgrown rims were analyzed. Concordant and near concordant analyses of detrital cores (n=13; 95–101 % concordance) yielded $^{207}Pb/^{206}Pb$ ages that range between 2640 and 2220 Ma (Fig. 1.8A). Eight analyses of the rims around detrital cores are concordant (97–102 % concordance) yielding a precise rim age of 1963 ± 14 Ma (MSWD = 0.0; Fig. 1.8B). In addition, one concordant analysis of a rim (T4-39-6-6) yielded a $^{207}Pb/^{206}Pb$ age of 1892 ± 54 Ma.

Zircon grains of the Ikulu metapelite T4-38-10 are prismatic in shape mainly < 200 μm in size and have rounded terminations. The cathodoluminescence images show grains cores and rim overgrowths. The majority of zircon cores vary from ellipsoidal to irregular in shape (Fig.

1.4L), which affirms their detrital origin. Detrital cores show various textures, which include oscillatory growth zoning and blurring of oscillatory growth zoning (Fig. 1.4L). These textural observations suggest either their magmatic or metamorphic origin. Overgrown rims around these detrital cores reach about 50 μm in thickness and may be internally zoned (Fig. 1.4L).

Sixty ablation spots were made on 38 zircon grains including 24 on detrital zircon cores and 36 on metamorphic rims. Nine analyses of detrital cores are concordant (100 ± 1 % concordance) and yielded $^{207}Pb/^{206}Pb$ ages between 2304 and 2066 Ma (Fig. 1.8C); 6 analyses of detrital cores are discordant, one of these analyses yielded an Archean $^{207}Pb/^{206}Pb$ age of 2678 ± 46 Ma (Fig. 1.4L). Ten analyses out of 24 of detrital cores have high common Pb (1.1–14.9 % *f*206%), their age dates were thus considered unreliable. Twenty-four out of 35 rim analyses are concordant to slightly discordant (89–103 % concordance) and yielded an upper and lower intercept age of 1985 ± 20 Ma and 614 ± 380 Ma (MSWD = 2.2; Fig. 1.8D), which reflects the age of the overgrowth zones at about 1985 Ma and a younger Pb-loss event. Eleven concordant rim analyses (100 ± 1 % concordances) yielded an U-Pb age of 1958 ± 8 Ma (MSWD = 0.16; Fig. 1.8E), which is considered as the best age of the metamorphic rims. The 11 remaining rim analyses had high common Pb (1.6–6.2% *f*206%) and were not included in Figure 1.8D and E.

A leucosome of the Ikulu metapelite T4-37-10 contains zircon grains, which are long to short prismatic and vary from subhedral to euhedral (Fig. 1.4M). Internal textures of the grains show oscillatory zoning. Some grains have cores that are surrounded by rim overgrowths. In both cores and rims 22 ablation spots were made on 11 zircon grains. Out of these 13 concordant analyses (100 ± 2 % concordance) gave an U-Pb age of 1941 ± 8 Ma (MSWD = 0.00; Fig. 1.8F), which is interpreted as the age of the zircon grains in the leucosome. The remaining nine analyses showed high common Pb and therefore were not included in Figure 1.8F.

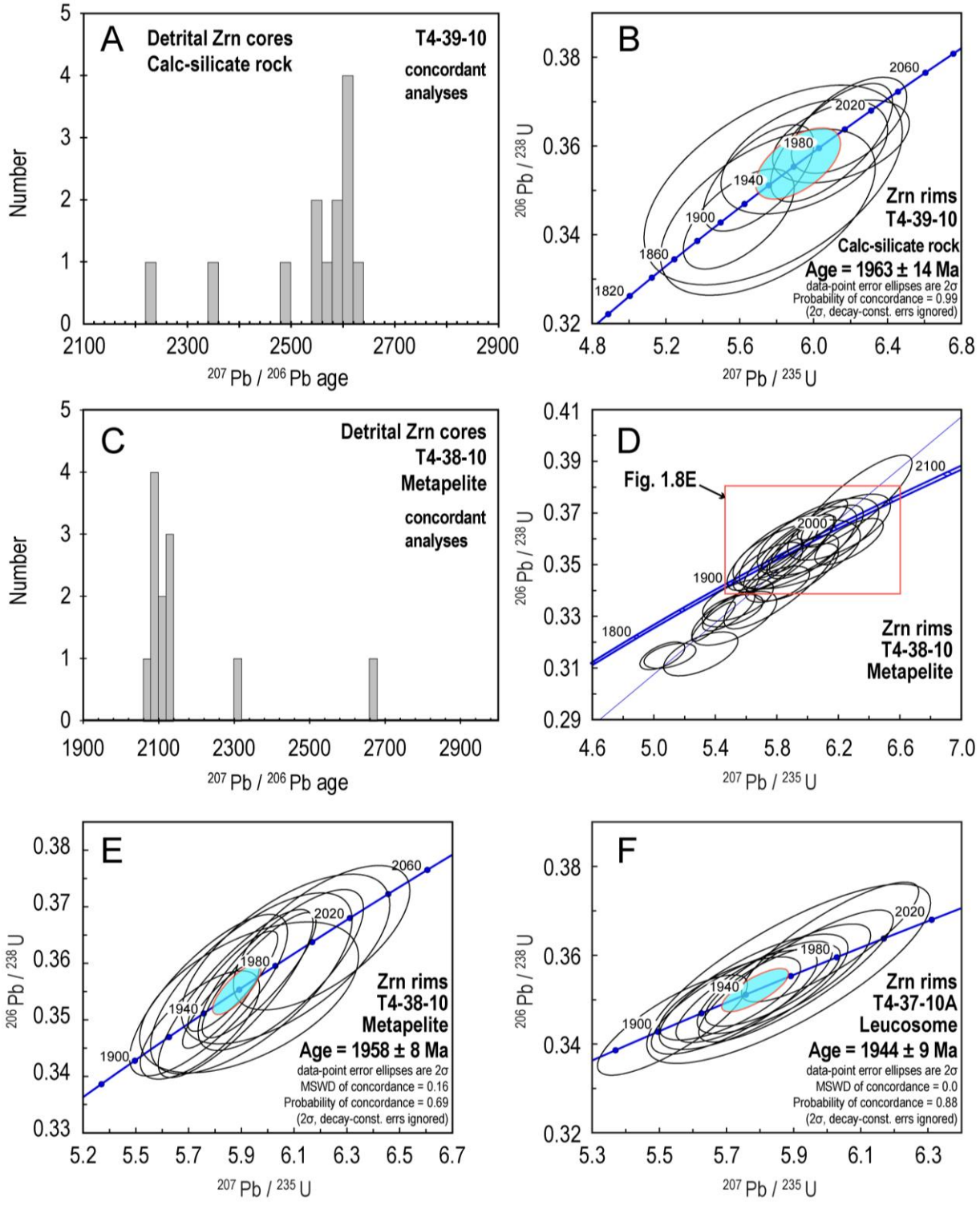

Fig. 1.8 (A and C) Histogram showing $^{207}Pb/^{206}Pb$ ages of detrital zircon cores. (B–F) Concordia diagrams showing U-Pb ages of metamorphic zircon overgrowths from metasedimentary rocks of the Katuma Block.

6. Geochemistry

Major and trace element abundances of metabasites, gabbronorites, granites and orthogneisses are used to deduce information about their petrogenesis and tectonic setting during the formation of their precursor.

6.1 Element mobility

Prior to the petrogenetic interpretation of major and trace element compositions of the rocks we will assess the degree of post-magmatic alteration and the suitability of major and trace element contents of the analysed Katuma metabasites, gabbronorites, orthogneisses and granitoids for unravelling their petrogenesis. Rocks that have been affected by retrograde low-grade chlorite, sericite and carbonate alteration through infiltration of hydrothermal fluids or by the late-stage formation of hydrous metamorphic minerals have a large loss on ignition (LOI > 3.5 wt. %) as defined by Manya (2004) and Polat and Hofmann (2003). All samples that have been selected for this study have LOI values below 2.0 wt. % reflecting the relatively little altered nature of our samples. The analysed metabasites and orthogneisses are not only poor in retrograde hydrous minerals but experience also during their prograde metamorphic history no strong hydration or dehydration processes: the metabasites obtained their granulite-facies mineralogy during isobaric cooling after the intrusion of the precursor melts into the deep crust and the orthogneisses still have their magmatic mineralogy.

To obtain information about the mobility of major and trace elements (e.g. LILE, HFSE and REE), we plotted the concentration of several of these elements against a relative immobile element, which is Gd for basic rocks and Zr or TiO_2 for felsic rocks and determined the square of correlation coefficient (R^2) (Polat and Hofmann, 2003). The bivarite graphs for the major elements oxides (K_2O, Na_2O, CaO, MgO, $Fe_2O_{3\,(T)}$) and trace elements (Rb, Ba, Th, La, Sr, Ta, Nb, Zr, Lu, Hf, Sm) are included Figure 1.16 and 1.17. For metabasites and gabbronorites (Fig. 1.16) the binary diagrams of Gd versus LILE and some major elements (K_2O, Na_2O and CaO) produce scattered points with low values of $R^2 \leq 0.3$, which suggests that these elements were most likely mobile during post-magmatic processes (Polat and Hofmann, 2003). The remaining elements show a good linear relationship with Gd ($R^2 > 0.56$) and suggest that they are not much affected by post-magmatitic processes and therefore suitable for petrogenetic studies. For orthogneisses (Fig. 1.17) the binary diagrams of Zr versus Na_2O, CaO, Rb and Sr have low R^2 values (< 0.3) and thus demonstrate their likely mobility, whereas Zr versus REE, HFSE (e.g. La, Ce and Hf) and Th show a good linear relationship with Zr (R^2 0.3–0.98).

TiO_2 versus Nb shows also good linear relationship (R^2 = 0.6), suggesting that it is not much affected by post-magmatitic processes. Therefore the interpretation of the geochemical data of the orthogneisses for petrogenetic consideration was done with caution, limited only to those elements that show least mobility during post-magmatic processes.

6.2 *Metabasites and gabbronorites*

Major and trace element compositions of metabasites and gabbronorites are presented in Table 17. The metabasites and gabbronorites are both classified as calk-alkaline on the basis of their Zr/Ti and Nb/Y and their Th to Co contents (Fig. 1.9A and B). The metabasites have SiO_2 contents between 43.5 and 56.0 wt. % (mean = 50.0 wt. %) whereas the gabbronorites between 51.0 and 53.5 wt. % (mean = 51.9 wt. %). In terms of Mg numbers, MgO, Ni and Cr concentrations, metabasites are more evolved compared to the gabbronorites. Gabbronorites have MgO contents of 7.0–16.4 wt. % and metabasites of 3.2–13.4 wt. %. Magnesium numbers (Mg # = $MgO/(MgO + FeO_{total})$ for the gabbronorites are uniform at 0.65 (except one sample at 0.35), whereas metabasites have lower Mg numbers of 0.2–0.6 (mean = 0.3). The gabbronorites have higher Ni (2110 ppm) and Cr (ca. 180 ppm) concentrations than the metabasites (mean 200 ppm Ni; mean 28 ppm Cr). The Al_2O_3 concentration is low in both metabasites (ca. 14.0 wt. %) and gabbronorites (9.0 wt. %). The TiO_2 concentrations (mean = 1.66 wt. %) of both rock types are similar to those of mid oceanic ridge basalts or island arc basalts (IAB) but lower than those of intra plate basalts (IPB) (e.g. Fig. 1.10A and B). With the exception of CaO and Al_2O_3 concentrations in metabasites and K_2O and Fe_2O_3 in the gabbronorites, major elements show antipathetic relationships with MgO (Fig. 1.11).

The contents of trace elements including the rare earth elements (REE) are akin to those of basaltic rocks formed in modern arc settings (Fig. 1.10A, B and C; Kelemen et al. 2003; Perfit et al. 1980). Both groups of rocks show enriched large ion lithophile element (LILE) abundances over primitive mantle. Large ion lithophile element contents of the rocks are variable but generally higher than those of the High Field Strength Elements (HFSE), which are depleted displaying Nb-Ta and Ti troughs (Fig. 1.10B).

Chondrite normalized (CN) rare earth element abundances of gabbronorites and metabasites show REE patterns, in which light REE are relatively enriched over middle- and heavy-REE (Fig. 1.10C). The metabasites and gabbronorites have $(La/Yb)_{CN}$ values, which range between 1.7 and 17.3 (mean = 5.5) and between 5.6 and 8.3 (mean = 6.7) respectively. The heavy REE display flat patterns similar to those of arc lavas, which formed from partial melting of spinel peridotite (Fig. 1.10C).

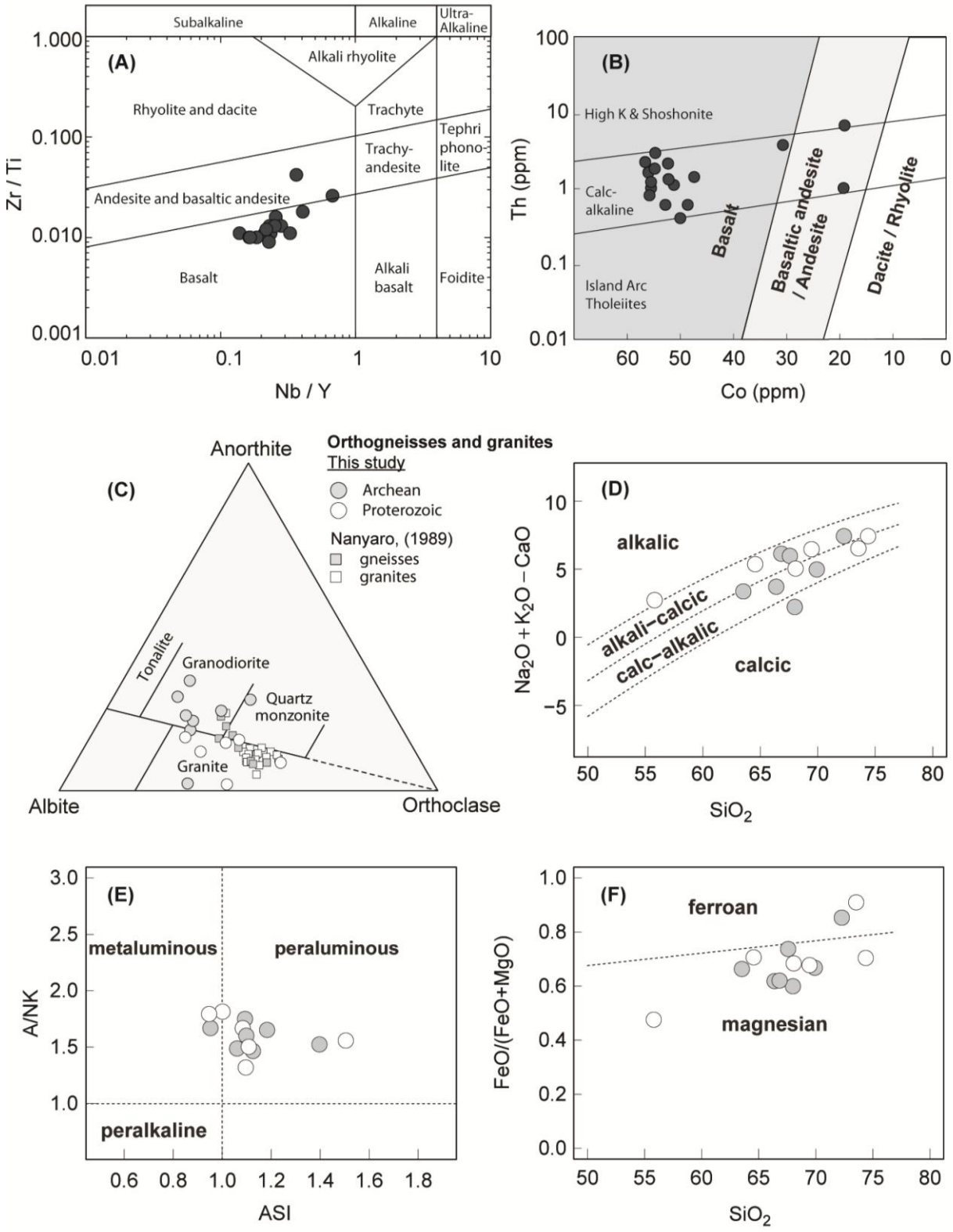

Fig. 1.9 Classification and geochemical characteristics of the Katuma metabasites and orthogneisses: (A) Zr/Ti versus Nb/Y classification (Pearce, 1996) of Katuma metabasites as subalkaline basalts. (B) Th versus Co classification (Hastie et al., 2007) of Katuma metabasalts as calc-alkaline basalts. (C) Normative feldspar classification (O'Connor, 1965) of Katuma orthogneisses as granodiorite (Archean) and granite (Paleoproterozoic). (D, E and F) Classification as metaluminous to peraluminous, magnesian and calc-alkalic to alkali-calcic granitoids, similar to granitoids that form in active continental margins (Cordilleran; Frost et al., 2001).

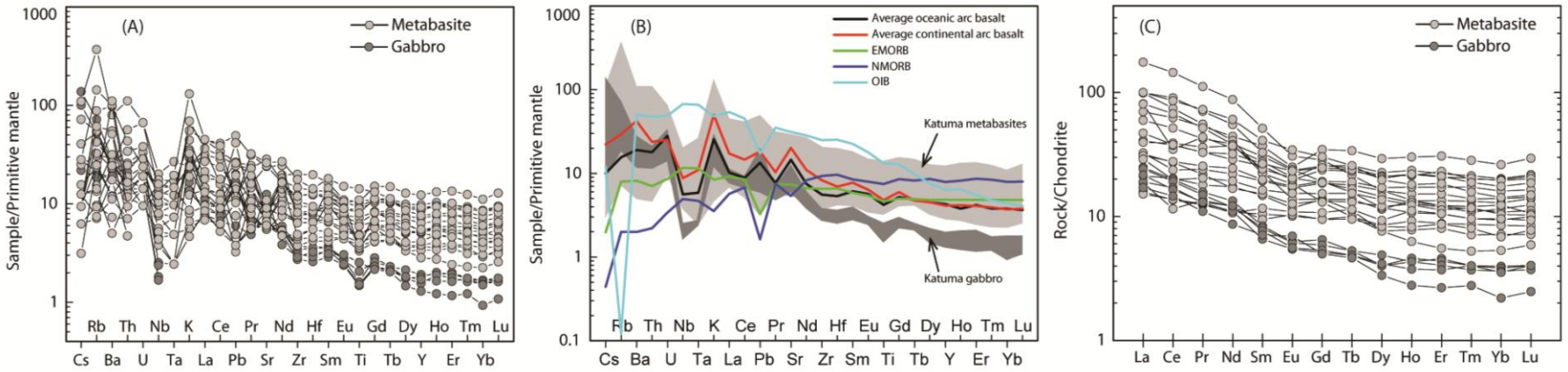

Fig. 1.10 (A, B) Primitive mantle (PM) normalized and (C) chondrite normalized spidergrams for metabasalts and gabbronorites. The PM and chondrite values are from Sun and McDonough, (1989). (A) Trace element patterns are similar to those of volcanic rocks in a volcanic arc setting. (B) The spidergrams of the Katuma metabasites and gabbronorites resemble those of average oceanic- and continental arc basalts.

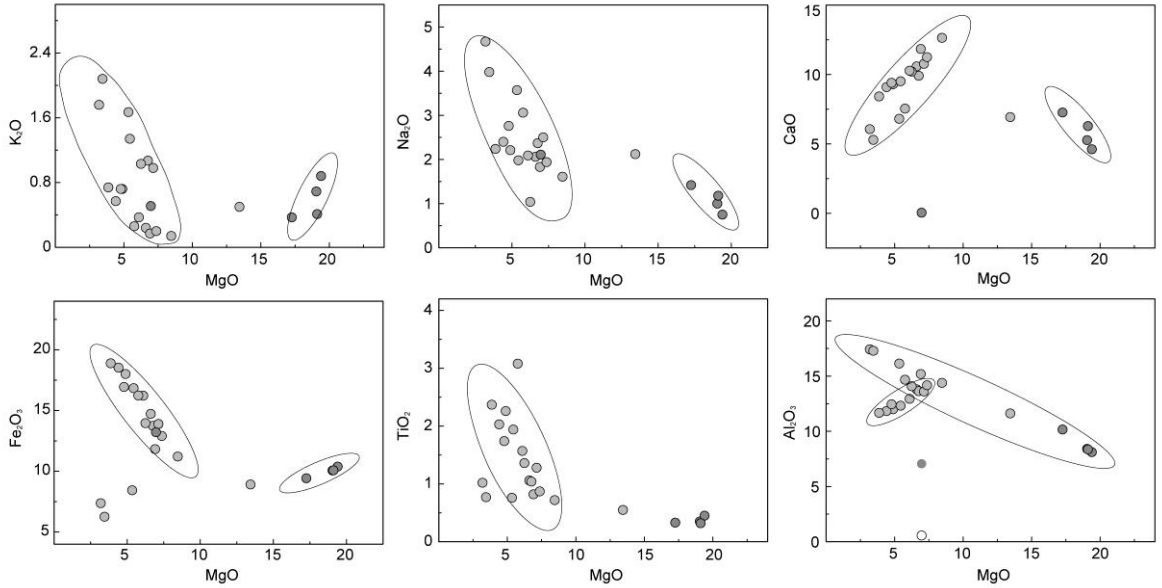

Fig. 1.11 Fenner diagrams: MgO versus selected major element oxides for gabbronorites and metabasites. Dark grey spots represent gabbronorites and light grey spots metabasites. The majority of major elements show a negative correlation with MgO, only CaO and Al_2O_3 in metabasites and FeO and K_2O in gabbronorites show positive correlations.

The europium anomaly $(Eu/Eu)_{CN}$ calculated as $(Eu_{CN}/(Sm.Gd)_{CN})^{0.5}$ (CN-chondrite normalized) is mostly moderately negative in metabasites and gabbronorites (mean = 0.9), with the exception of four samples (T7-3-10, T10-1-10, T16-1-10 and T17-1-10), which show slight positive Eu-anomalies.

6.3 Orthogneisses and granites

Major and trace element compositions of orthogneisses and granitoids are presented in Table 4. On the basis of crystallization ages, the orthogneisses and granitoids are subdivided into two groups: Archean and Paleoproterozoic granitoids. Hence, in this section the orthogneisses and granitoids will be referred to either Paleoproterozoic or Neoarchean granitoids. All the granitoids have SiO_2 contents between 55 and 74 wt. % (mean = 68 wt. %) and are classified mainly as granodiorite and quartz monzonite (Neoarchean) and granite and granodiorite (Paleoproterozoic) on the basis of their normative feldspars (Fig. 1.9C). The sodium contents of the granitoids range between 2.6 and 5.2 wt. %, therefore the rocks have low K_2O/Na_2O (0.5 – 2.1) and are classified as calc-alkalic to alkali-calcic granitoids (Fig. 1.9D). The Archean granitoids have a narrow range of Al_2O_3 contents of 15.2–15.9 wt. % whereas the Proterozoic ones have a larger Al_2O_3 range (12.7–19.6 wt. %). Most granitoids are classified as peraluminous (few as metaluminous; Fig. 1.9E). The granitoids have Fe-numbers mainly between 0.3 and 0.8 (Fe #=FeO_T/FeO_T+MgO) and low ferromagnesian contents (Fe_2O_3, MgO, MnO and TiO_2) of 1.2–4.9 wt. %, thus they are classified as magnesian in the Fe # versus SiO_2 diagram (Fig. 1.9F). Except for the two Paleoproterozoic granitoids (sample T2-10-10 and T19-3-10), the Archean granitoids have higher Cr and Sr concentrations than the Paleoproterozoic granitoids: Cr (93 ppm vs 42 ppm) and Sr (355 ppm vs 288 ppm). The Sr/Y value is greater in Paleoproterozoic granitoids (ca. 75) than in Neoarchean granitoids (ca. 59). Both rocks show fractionated REE patterns (Fig. 1.12) whereby the Paleoproterozoic granitoids have a higher mean La/Yb_{CN} (15–240) than the Archean granitoids (La/Yb_{CN} (10–200). In the diagrams of $(La/Yb)_{CN}$ versus Yb_{CN} and Sr/Y versus Y the granitoids are classified as adakite or Archean TTG (Fig. 1.13A and C).

In primitive mantle normalized spider diagrams, all granitoids are displaying patterns that are similar to those of rocks formed in modern arc settings (Fig. 1.12A, C and E). The patterns are characterized by negative anomalies of Nb, Ta and Ti and are depleted in HREE compared to LREE or LILE. In the plots of Th/Hf – Ta/Hf and Th/Ta – Yb (Fig. 1.13B and D) as proposed by Schandl and Gorton (2002), the Katuma Neaorchean and Paleoproterozoic granitoids plot

into the fields of high Th/Hf and Th/Ta values and thus are classified as granitoids of continental arc margins.

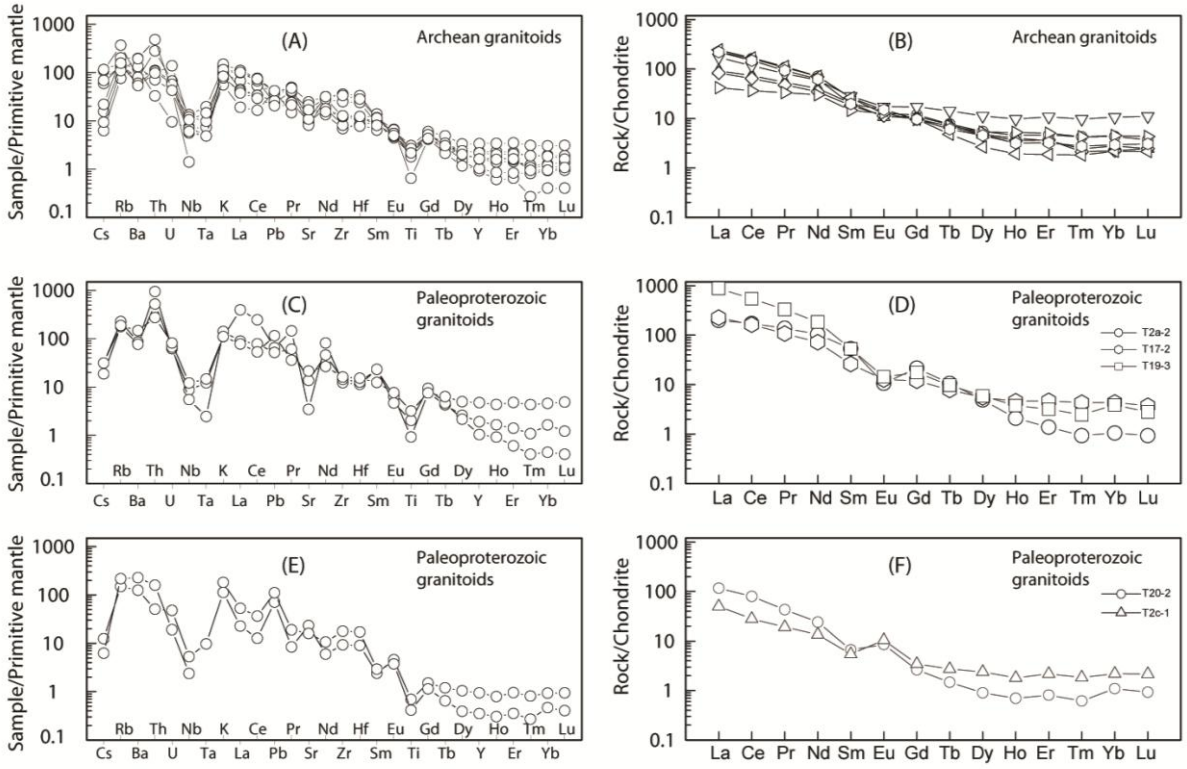

Fig. 1.12 Primitive mantle (PM) normalized (A, C and E) and chondrite normalized (B, D and F) spidergrams. The PM and chondrite values are from Sun and McDonough (1989). Trace element spidergrams of the Katuma orthogneisses and granites are similar to patterns of rocks of arc-settings.

7. Discussion

7.1 *Magmatic crustal forming events*

In this study we aim to deduce the formation history and evolution of the Paleoproterozoic Katuma Block in the Ubendian Belt on the basis of the geochemistry of meta-igneous rocks and the zircon geochronology of meta-igneous and metasedimentary rocks.

As orogenic belts are the geodynamic settings where juvenile mantle melts are added to pre-existing crust or where tectonic accretions occur (e.g. of islands arcs or oceanic plateaus), one may expect that the Ubendian Belt may represent the locus where similar processes of continental crust formation may have operated during the Paleoproterozoic orogenic cycle. However, our geochronological data show that most magmatic formation ages of the Katuma metabasites and orthogneisses are Neoarchean (~ 2710–2640 Ma) and thus predate the Paleoproterozoic Ubendian orogeny. These formation ages are similar to U-Pb zircon ages reported for the magmatic formation of some granite-greenstone belts of the Tanzania Craton,

(e.g. the Kilimafedha Greenstone Belt, 2700–2640 Ma; Wirth, 2004; the Musoma-Mara Greenstone Belt, 2760–2650; Chamberlain and Tosdal, 2007; Manya et al., 2006; Mtoro et al., 2009; and the Sukumaland Greenstone Belt, 2700–2640 Ma; (Borg and Krogh, 1999; Chamberlain and Tosdal, 2007; Sanislav et al., 2014). Similar U-Pb or U-Th-Pb zircon ages were also found for the protoliths in the reworked margins of the Tanzania Craton within the East African Orogen (Johnson et al., 2003; Sommer et al., 2005; Tenczer et al., 2006, 2013; Vogt et al., 2006) and the Paleoproterozoic Usagaran Belt (Möller et al., 1995; Reddy et al., 2003; Thomas et al., 2013). A recent study by Sanislav et al. (2014) suggested three periods of crustal growth of the Tanzania Craton at 2850–2800 Ma, 2770–2730 Ma and 2700–2620 Ma and attributed the major growth of the craton to the last period (2700–2620 Ma). The Neoarchean magmatism in the Katuma Block conforms to this last period of crustal growth, allowing the Neoarchean Katuma Block to be considered as part of the Tanzania Craton.

Our data also indicate that there was a second period of mafic and felsic magmatism that is Paleoproterozoic in age (2020–1940 Ma) reflecting addition of mantle material to the crust in the Katuma Block during the Ubendian orogeny. The field crosscutting relationship between the Paleoproterozoic rocks and the Neoarchean rocks (e.g. Fig 1.2I and J) also affirms for this crustal growth stage. The Paleoproterozoic magmatic events obtained for the Katuma Block are broadly concurrent to the ones in the other blocks of the Ubendian Belt ~ 2090–1930 Ma (Lawley et al., 2013a; Lenoir et al., 1994; Ring et al., 1997). The detection of metamagmatic rocks of two different ages, i.e. Neoarchean and Paleoproterozoic, questions the traditional grouping of the metamagmatic rocks of the Katuma Block into one group, the Katuma Group, though they represent the metamagmatic basement for the unconformably overlying metasedimentary Ikulu Group.

7.2 Sedimentation age of the Ikulu Group

The metasediments, of the Katuma Bock (Ikulu group) consisting of metapelites, calc-silicate, quartzites and marbles, contain detrital zircons that are 2680–2050 Ma in age and are thus similar to magmatic crystallization ages found in the Katuma Block and the Tanzania Craton (Pinna et al., 2004). This suggests that the Katuma Block itself or the Tanzania Craton may represent the likely detrital source areas for the clastic sediments. The rock association of very thick (> 1.3–1.5 km; Semyanov et al., 1977) clastic and carbonaceous sediments points to a shelf or an epicontinental environment. The lower age limit for the sedimentation is constrained by the age of the first metamorphism of the metasediments at ~ 1960 Ma (Fig. 1.8B and E). The

association of metabasites and orthogneisses may represent higher-grade equivalents to the granite-greenstone association of the central and northern Tanzania Craton.

7.3 Age of metamorphic and deformational events in the Katuma Block

The metamorphic grade of rocks exposed in the Katuma Block is mostly of granulite- or upper amphibolite-facies grade and is a result of several metamorphic events of Neoarchean and Paleoproterozoic age. However, in this paper we only want to discuss the ages of high-grade metamorphic events that we obtained from dating of metamorphically overgrown rims on zircon grains. The metamorphic P-T paths and results of texturally controlled monazite dating will be published elsewhere (Kazimoto et al., in preparation). Evidence for Neoarchean reworking of Katuma rocks are sparse but the oscillatory zoned magmatic zircon grains of the oldest Neoarchean metagranodiorite (T1-17-10; ca. 2710 Ma) show metamorphic rims and recrystallisation zones that are 60 Ma younger (2650 Ma) than the magmatic crystallisation of the cores. This Neoarchean metamorphic event at 2650 Ma is further firmly documented by schistose xenoliths of garnet amphibolites included in an unmetamorphosed gabbronorite dated at 2643 ± 4 Ma. In contrast to the sparse evidences for a Neoarchean metamorphism, there are many zircon ages indicating several high-grade metamorphic events of Paleoproterozoic age.

U-Pb zircon ages of a migmatitic orthogneiss and a leucosome (T14-3-10 and T14-1-10) revealed a migmatization event at about 2050–2030 Ma (Fig 1.2E and H; Table 2). Although these ages are older than recently published ages for the metamorphism in other blocks of the Ubendian Belt (Boniface et al., 2012; Lawley et al., 2013a), the ages are similar to the age of a granulite-facies metamorphic event that was attributed to the onset of the Paleoproterozoic collision in the Ubende, Ufipa and Nyika Blocks (Cahen et al., 1966; Lenoir et al., 1994; McConnell, 1950; McConnell, 1969; Ring et al., 1997). The age of the metamorphic growth zones around Neoarchean magmatic zircon grains and the common Pb loss of both magmatic zircon grains of metabasites and orthogneisses indicate Paleoproterozoic reworking of Neoarchean rocks. Thus, the Paleoproterozoic evolution of the Katuma Block is similar to that of other reworked margins of the Tanzania Craton (Johnson et al., 2003; Lawley et al., 2013a; Möller et al., 1998; Reddy et al., 2003; Sommer et al., 2005; Tenczer et al., 2006, 2013; Thomas et al., 2013; Vogt et al., 2006).

Zircon grains from two metasedimentary Ikulu samples and a leucosome of a Ikulu metapelitic migmatite record metamorphic ages of about 1960–1940 Ma (Fig 1.8B, E and F), indicating a concurrent metamorphism of the metapelites in the Katuma Block and the granitic

intrusions, deformation, greenschist-facies metamorphism and the gold mineralization in the Lupa Block (Lawley et al., 2013a; Lawley et al., 2013b; Lawley et al., 2013c). The crosscutting relationship between gneissic Neoarchean granitoids (~ 2710–2650 Ma) and unfoliated Paleoproterozoic granites (1990–1960 Ma) dates a deformation of the Katuma rocks between 2650 Ma and 1960 Ma (Fig. 1.2I).

Besides the 1960–1940 Ma high-grade event in the Ikulu metapelites there is also evidence for an even younger high-grade metamorphism at 1880–1840 Ma the obtained from metamorphic zircon rims, which is in agreement with the age of overgrowth zones in monazite (Kazimoto et al. in review; Kazimoto et al., in preparation). Metamorphic overgrowths on zircon grains of a Paleoproterozoic Ms-Bt-granitic gneiss (dated at 1940 Ma; T19-3-10), collected near the border between the Katuma and the Wakole Block record a younger Paleoproterozoic metamorphic age of about 1880 Ma. This younger metamorphic age and discordant zircon grains of the Neoarchean metamagmatic rocks suggest a younger Pb loss event after 1960 Ma.

Post-Paleoproterozoic metamorphic reworking of rocks (Mesoproterozoic and Neoproterozoic) documented by previous authors for the Wakole, Ubende, Ufipa and Lupa blocks of the Ubendian Belt (Boniface and Schenk, 2012; Boniface et al., 2012, 2014; Lawley et al., 2013a) is missing from our geochronological work on the Katuma Block. However, dating of a hydrothermal alteration associated with the gold mineralization event in the Katuma Block (U-Th-total Pb monazite dating) revealed a Mesoproterozoic age (~1170 Ma), which could mean that deformation and metamorphic reworking of blocks adjoining to the Katuma Block liberated metalliferous fluids that percolated into structural weaknesses of the Katuma rocks and caused both hydrothermal alterations and gold mineralization.

7.4 Petrogenesis of metabasites and gabbronorites

The geodynamic setting of rock formation in the Ubendian Belt, which occurred in Neoarchean and Paleoproterozoic time, can best be deduced from the trace element geochemistry of metabasites, granitoids and felsic orthogneisses. Like basalts of modern arcs, the Katuma metabasites and gabbronorites are enriched in incompatible elements (e.g. K, Rb, Ba, Th, LREE) and depleted in HFSE (TiO_2, Y, Nb, and Ta). This can be explained by the process of fluxing of fluids or melts rich in incompatible elements to the mantle wedge at subduction zones and subsequent partial melting of the modified peridotite and/or the subducting plate. High Th abundances of the metabasites and gabbronorites distinguish these rocks from basalts of other

settings as the high Th content is contributed from both the subducted oceanic and the overlying continental crust. High Th/Yb, Nb/Yb and Ta/Yb (Fig. 1.14A and B) are therefore good indicators of a Th input (Pearce, 2008) and allow to classify the metabasites and gabbronorites as continental arc rocks (Fig. 1.14A and B). The high Zr concentrations in metabasites and gabbronorites (ca.115 ppm and 35 ppm) are above the average Zr content of primitive oceanic- or continental-arc basalts (Kelemen et al., 2003) but less than average Zr content in OIB or WPB (Sun and McDonough, 1989), indicating that the earth's crust was involved in the formation of the precursor melts.

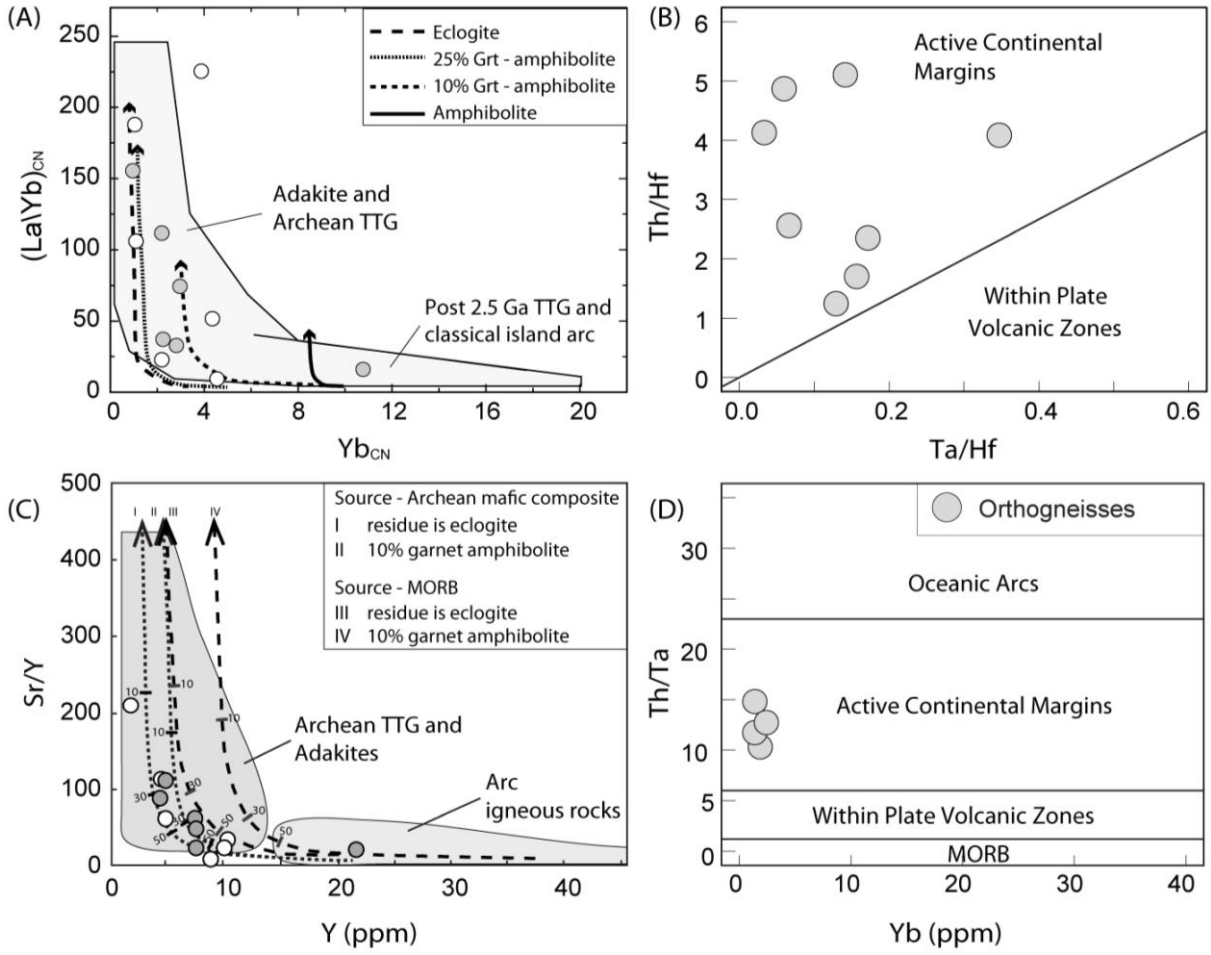

Fig. 1.13 (A) and (C) plots of La/Yb_{CN} versus Yb_{CN} and Sr/Y versus Y after Drummond and Defant, (1990) and Martin (1999). Katuma orthogneisses are similar to Archean TTG or modern adakites, which are formed by partial melting of Archean mafic sources. (B) and (D) Discrimination between granitoids using plots of Ta/Hf – Th/Hf and Yb – Th/Ta (Schandl and Gorton, 2002) and their tectonic interpretation: The Katuma orthogneisses are plotting in the field of granites formed at active continental margins.

The HFSE ratios (Zr/Y, Nb/Y, Nb/Th and Zr/Nb), remain unchanged during AFC processes and allow to identify the mantle sources for basalts (Condie, 2003, 2005a; Weaver, 1991). The Katuma metabasites and gabbronorites have low Nb/Th falling into the fields of arc basalts that were formed from a source similar to primitive mantle that has been modified by either subduction or crustal components and evolved towards an enriched mantle (EN) (Fig. 1.14C and D). The low Ni and Cr contents and the negative correlation of major element oxides against MgO (except for CaO and partly Al_2O_3) suggest that fractionation of olivine, pyroxenes and amphibole was involved in the petrogenesis of the Katuma mafic rocks.

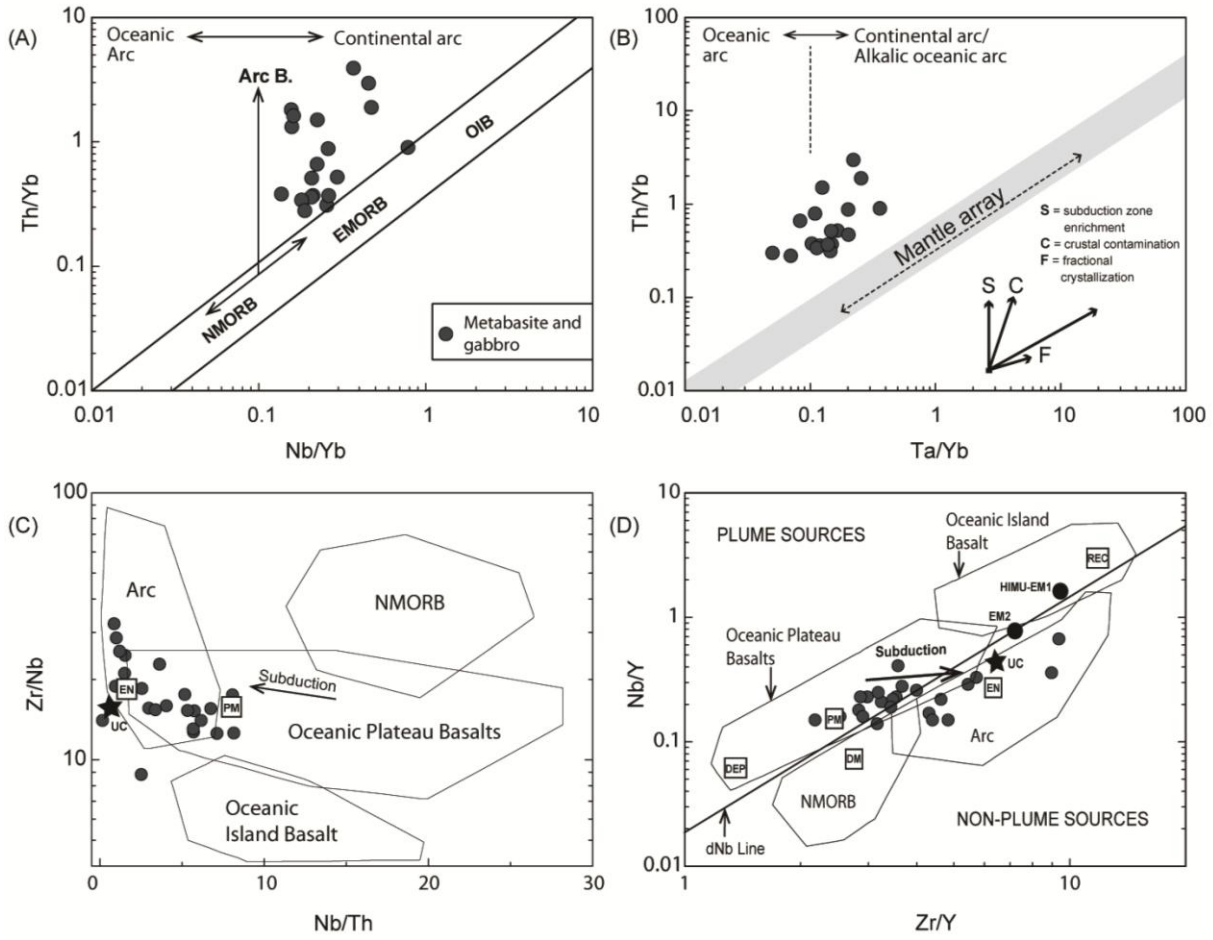

Fig. 1.14 (A), (B) Discrimination diagrams of Katuma metabasites and gabbronorites and their tectonic interpretation, diagrams after Pearce (1983, 2008). Katuma metabasites and gabbronorites have high Th/Yb values (above those of Mid Oceanic Ridge basalts or the mantle array). A high Th input from subduction fluids/melts and crustal contamination attributes to high Th/Yb values. (C) and (D) show different HFSE ratios (fields) of basalts from different tectonic settings and their mantle components modified from Condie (2005a). The HFSE ratios of the Katuma metabasites and gabbronorites plot into the fields of arc basalts and oceanic plateau basalts, which suggests an origin from primitive mantle that has been modified by a subduction fluid component and the upper crust.

Modelling of REE patterns of metabasites are aimed to support our interpretation that the Katuma metabasites and gabbronorites formed from melts deriving from a mantle that has a composition similar to that of a primitive mantle and that these melts experienced fractionation and crustal assimilation. We applied non-modal melting of a primitive mantle following an approach used by Lawley et al. (2013a) using the melting equation of Shaw (1970). Furthermore, modelling the REE composition of the melts during decoupled fractional crystallization and assimilation (FCA) was achieved using the program "FC-AFC-FCA modeller" (Ersoy and Helvacı, 2010). We selected the compositional values of the primitive mantle from Sun & McDonough (1989), mineral/matrix partition coefficients from McKenzie and O'Nions (1991), and mineral modes and melt-modes for spinel lherzolite from Kinzler (1997). For the modelling of the crustal assimilation, values of the bulk continental crust, the lower and upper crust are those of Taylor and McLennan (1995).

The results of the modelling are presented in chondrite-normalized REE diagrams (Fig. 1.15A, B and C). They show that the REE patterns of the metabasites can be explained by variable degrees (1–30 %) of partial melting of a primitive spinel lherzolite combined with mineral fractionation and assimilation: according to the modelling, the melts experienced different extents of fractionation of olivine, pyroxenes, magnetite, ilmenite and amphibole (Fig. 1.15A and B), and assimilated either lower continental crust (LC) or upper continental crust (UC) or both (bulk continental crust – BCC). The gabbronorites display REE patterns at very low concentrations (Fig. 1.15A) and can only be reproduced by modelling with very high degrees (60%) of partial melting of spinel lherzolite in combination with assimilation of UC material and little mineral (amphibole and garnet) fractionation (Fig. 1.15C). Partial melting of spinel peridotite combined with fractionation and assimilation are also involved to produce trace element patterns of modern arc magmas Murphy (2007) and Kelemen et al., (2003).

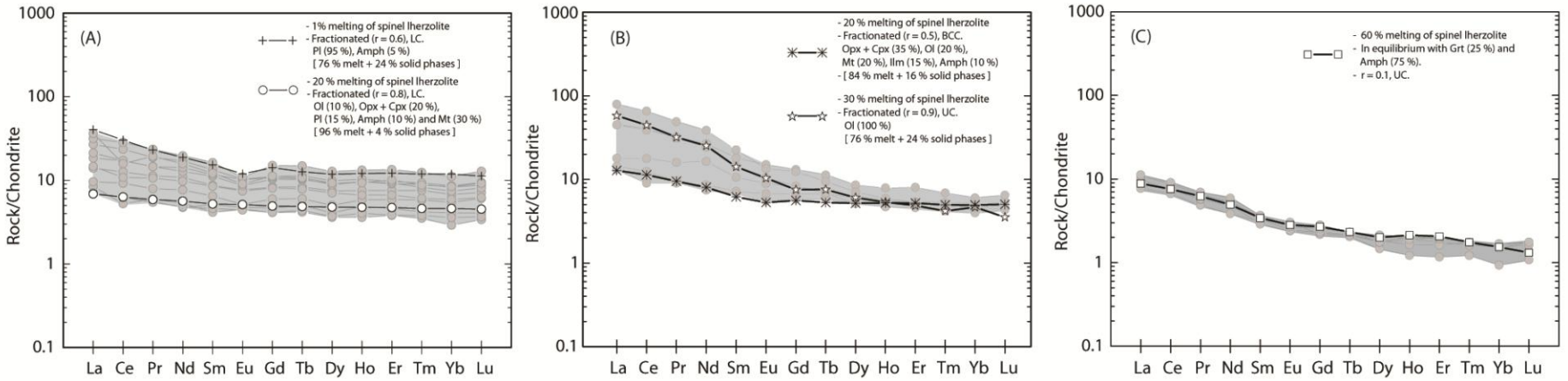

Fig. 1.15 (A), (B), (C) REE modelling of melting of spinel lherzolite and decoupled fractional crystallization and assimilation (AFC). REE patterns of metabasites and gabbronorites can be explained by various degrees of partial melting (1-30%), fractionation and crustal assimilation. Chondrite normalizing values are from Sun and McDonough (1989) [r = relative ratio of assimilated material to crystallized material; Ol – olivine, Opx – orthopyroxene, Cpx – clinopyroxene, Amph – amphibole, Grt – garnet, Pl – plagioclase, Mt – magnetite and Ilm – ilmenite].

7.5 Petrogenesis of the Archean and Paleoproterozoic granitoids

The use of the chemical composition of evolved rocks, like the orthogneisses of the Katuma Block, for identifying the geodynamic setting of melt formation is not straight forward as that of mafic rocks. The geochemistry of granitoids may reflect the geochemistry of precursor crustal rocks, if they are formed by partial melting of the crust, or the progress of AFC processes may mask the original chemical composition of the primitive melt and thus destroying the signature for identification of the source.

Like for the metabasites and gabbronorites, major element characteristics (Fig. 1.9D-F), trace element patterns (Fig. 1.13A-F) and diagrams of Th/Ta versus Yb and Th/Hf versus Ta/Hf (Fig. 1.13B and D) of the Katuma granitoids indicate their formation at an active continental margin. However, the lack of isotopic information of the granitoids (e.g. Sr, Nd and Hf) limits the identifiction if the granitoids represent juvenile active continental margin melts. Therefore, several possible petrogenetic origins have to be considered.

Yttrium, ytterbium and strontium contents of the Katuma granitoids are similar to those of Archean TTG or adakites and the rocks show resemblance to experimentally derived melts formed after partial melting of Archean mafic composites with 10–25% garnet or to a melt with an eclogitic residue (Fig. 1.13A and C; Drummond and Defant, 1990; Martin et al., 2005). The adakitic signature (low Y and Yb and moderate to high Sr/Y and $(La/Yb)_{CN}$) as also observed in our rocks is thought (first model) to be attained by interaction of slab melts with mantle wedge peridotite or through fractional crystallization (Kay, 1978; Kay and Kay, 2002; Moyen, 2009; Richards and Kerrich, 2007). However, the low Mg# and the low Ni and Cr contents of the rocks do not support an interaction of slab melts with a mantle peridotite, rather alludes for an origin from older evolved crustal rocks.

Therefore the second petrogenetic model is that the granitoids with adakite-like chemical compositions are derived from partial melting of older garnet bearing mafic rocks (Fig. 1.13A and C). The presence of mafic xenoliths (Fig. 1.2G and H) and inherited zircon grains with $^{207}Pb/^{206}Pb$ ages of 2805 ± 17 Ma and 2817 ± 27 Ma in the Katuma granitoids (e.g. T1-17-10 and T14-1-10) is in agreement with this interpretation.

A third possible origin of adakite-like melts is by fractional crystallization of a mafic magma (Moyen, 2009; Richards and Kerrich, 2007). However, to produce voluminous adakite-like melts that form the widespread granitoids of the Katuma Block would require the presence of voluminous restite mafic rocks that are co-magmatic with the Katuma granitoids. However, these have not been found. In addition, the similarities in concentrations of REE and LILE of the

Katuma metabasites to those of the granitoids (Fig. 1.10 and 1.12) excludes the mafic rocks as the likely source of the evolved granitoids.

In conclusion, the crustal melting scenario provides the most likely explanation for the origin of the Katuma adakite-like granitoids, which is in agreement that most TTGs are considered to be formed by partial melting of older rocks in the middle or lower crust (Condie, 2005b; Hoffmann et al., 2011). The Neoarchean and Paleoproterozoic mafic magmas in the Katuma Block could have provided the necessary heat that is required to generate adakite-like magmas.

7.6 Crustal evolution of the Katuma Block

U-Pb zircon geochronology of Katuma rocks revealed two magmatic crustal forming events, the Neoarchean (2710–2640 Ma) and the Paleoproterozoic (2020–1940 Ma). The Neoarchean event can be attributed to the Neoarchean crustal growth of the Tanzania Craton along an active continental margin, whereas the Paleoproterozoic crust formation is attributed to the Ubendian event. Dating of metamorphic zircon rims indicate that the Neoarchean and the Paleoproterozoic magmatic events were both associated with metamorphism. However, whereas most rocks of the Katuma Block formed in the Neoarchean, the main metamorphic reworking occurred during two major periods in Paleoproterozoic time (~ 2050–1940 Ma and ~ 1880–1840 Ma). The obtained Paleoproterozoic metamorphic ages can be subdivided and attributed to two different stages separated by about 60 Ma. The first stage (2050–1940 Ma) correlates with the age of mafic and granitic magmatism in the Katuma Block and with deformation and gold mineralisation in the Lupa Block (Lawley et al., 2013c). The second stage (1880–1840 Ma), which correlates with emplacement of calc-alaline granitoids (Lenoir et al., 1994), the second gold mineralisation event in the Lupa Block (Lawley et al., 2013c), the eclogite formation of ocean floor basalts in the adjoining Ubende Block and collision leading to the uplift of the eclogites (Boniface et al., 2012).

The similarity in age, lithological composition and paleotectonic setting during rock formation between the Katuma Block and the Neoarchean greenstone belts of the Tanzania Craton most likely explain their shared potential for metallic deposits.

8. Summary and conclusion

Zircon ages in combination with geochemical data of mafic rocks of the Katuma Block in the Paleoproterozoic Ubendian Belt indicate that the rocks formed at continental margins mainly in the Neoarchean (2.71–2.64 Ga) but also in the Paleoproterozoic (2.02–1.94 Ga). The trace

element geochemistry indicates that that the mafic rocks formed in a similar manner as magmatic rocks in modern continental arcs, i.e. by hydrous partial melting of a modified primitive mantle combined with fractionation and contamination of the melts through the overlying continental crust during their ascent. The first Archean metamorphic event in the Katuma Block is recorded only by zircon and was dated at about 2650 Ga. This event was succeeded by a Paleoproterozoic magmatic crustal forming event at ca. 2050–1940 Ga.

The detrital zircon grains of the Katuma metasediments suggest that the Neoarchean Katuma Block or Tanzania Craton were the most likely source for the sediment, that were deposited prior to their first metamorphism at ca. 1960 Ga. The similarity of ages of the youngest Paleoproterozoic metamorphism at ca. 1.88–1.84 Ma Ma and the similar metamorphic age of MORB-type eclogites of the adjoining Ubende Block suggests that the Katuma Block was affected by a collision event that led to exhumation of the Paleoproterozoic eclogites.

Acknowledgements

This work was supported through funds from the Ministry of Education and Vocational Training of Tanzania (MOEVT), German Academic Exchange Service (DAAD) and the Department of Geology of the University of Dar es Salaam, Tanzania (through the Sida Earth Science Project). We are grateful to Nelson Boniface for his support during the fieldwork. We would like to thank Andreas Fehler for making of rock thin sections. Christopher J. M. Lawley assisted with chemical modelling. Christopher J. M. Lawley and Gregor Borg critically reviewed an earlier version that led to improvements of this manuscript.

References

Biyashev, M., Pentelkov, V., Emelyanov, S., Chuklanov, B., Stepnov, E., Matrenitzky, T., Novikov, A., 1977. Sitalike: Geological Map Quarter Degree Sheet 170. Geological Survey of Tanzania, Dodoma.

Boniface, N., 2009. Eburnean, Kibaran and Pan-African metamorphic events in the Ubendian belt of Tanzania: Zircon and Monazite geochronology, Department of Geosciences. University of Kiel, Kiel, p. 110.

Boniface, N., Schenk, V., 2012. Neoproterozoic eclogites in the Paleoproterozoic Ubendian Belt of Tanzania: Evidence for a Pan-African suture between the Bangweulu Block and the Tanzania Craton. Precambrian Research 208-211, 72-89.

Boniface, N., Schenk, V., Appel, P., 2012. Paleoproterozoic eclogites of MORB–type chemistry and three Proterozoic orogenic cycles in the Ubendian Belt (Tanzania): Evidence from

monazite and zircon geochronology , and geochemistry. Precambrian Research 192–195, 16–33.

Boniface, N., Schenk, V., Appel, P., 2014. Mesoproterozoic high-grade metamorphism in pelitic rocks of the northwestern Ubendian Belt: Implication for the extension of the Kibaran intra-continental basins to Tanzania. Precambrian research.

Borg, G., Krogh, T., 1999. Isotopic age data of single zircons from the Archaean Sukumaland Greenstone Belt , Tanzania. Journal of African Earth Sciences 29, 301-312.

Cahen, L., Snelling, N.J., Delhal, J., Vail, J., 1966. The Geochronology and evolution of Africa.

Condie, K.C., 1989. Geochemical changes in basalts and andesites across the Archean-Proterozoic boundary: Identification and significance. Lithos 23, 1-18.

Condie, K.C., 2003. Incompatible element ratios in oceanic basalts and komatiites: Tracking deep mantle sources and continental growth rates with time. Geological Society, London, Special Publications 4, 1-28.

Condie, K.C., 2005a. High field strength element ratios in Archean basalts: a window to evolving sources of mantle plumes? Lithos 79, 491-504.

Condie, K.C., 2005b. TTGs and adakites: are they both slab melts? Lithos 80, 33-44.

Cooke, D.R., Hollings, P., Walshe, J.L., 2005. Giant porphyry deposits: characteristics, distribution, and tectonic controls. Economic Geology 100, 801-818.

Corfu, F., Hanchar, J.M., Hoskin, P.W.O., Kinny, P., 2003. Atlas of zircon textures. Reviews in Mineralogy, 469-499.

Daly, M.C., 1988. Crustal Shear Zones in Central Africa: a kinematic approach to Proterozoic Tectonics. Episodes 11, 5-11.

Drummond, M.S., Defant, M.J., 1990. A model for trondhjemite-tonalite-dacite genesis and crustal growth via slab melting: Archean to modern comparisons. Journal of Geophysical Research 95, 503-521.

Ersoy, Y., Helvacı, C., 2010. FC–AFC–FCA and mixing modeler: A Microsoft® Excel© spreadsheet program for modeling geochemical differentiation of magma by crystal fractionation, crustal assimilation and mixing. Computers & Geosciences 36, 383-390.

Frost, R.B., Barnes, C.G., Collins, W.J., Arculus, R.J., Ellis, D.J., Frost, C.D., 2001. A geochemical classification for granitic rocks. Journal of Petrology 42, 2033-2048.

Groves, D.I., Ridley, J.R., Bloem, E.M.J., Gebre-Mariam, M., Hagemann, S.G., Hronsky, J.M.a., Knight, J.T., McNaughton, N.J., Ojala, J., Vielreicher, R.M., McCuaig, T.C., Holyland, P.W., 1995. Lode-gold deposits of the Yilgarn block: products of Late Archaean crustal-scale overpressured hydrothermal systems. Geological Society, London, Special Publications 95, 155-172.

Groves, D.I., Vielreicher, R.M., Goldfarb, R.J., Condie, K.C., 2005. Controls on the heterogeneous distribution of mineral deposits through time. Geological Society, London, Special Publications 248, 71-101.

Hastie, A.R., Kerr, A.C., Pearce, J.A., Mitchell, S.F., 2007. Classification of Altered Volcanic Island Arc Rocks using Immobile Trace Elements: Development of the Th Co Discrimination Diagram. Journal of Petrology 48, 2341-2357.

Hoffmann, E.J., Münker, C., Næraa, T., Rosing, M.T., Herwartz, D., Garbe-Schönberg, D., Svahnberg, H., 2011. Mechanisms of Archean crust formation inferred from high-precision HFSE systematics in TTGs. Geochimica et Cosmochimica Acta 75, 4157-4178.

Jackson, S.E., Pearson, N.J., Griffin, W.L., Belousova, E.A., 2004. The application of laser ablation-inductively coupled plasma-mass spectrometry to in situ U–Pb zircon geochronology. Chemical Geology 211, 47-69.

Johnson, S.P., Cutten, H.N.C., Muhongo, S., De-Waele, B., 2003. Neoarchaean magmatism and metamorphism of the western granulites in the central domain of the Mozambique belt, Tanzania: U–Pb shrimp geochronology and PT estimates. Tectonophysics 375, 125-145.

Kay, R., 1978. Aleutian magnesian andesites: melts from subducted Pacific Ocean crust. Journal of Volcanology and Geothermal Research 4, 117-132.

Kay, R., Kay, S., 2002. Andean Adakites: Three Ways to Make Them. Acta Petrologica Sinica 18, 303-311.

Kazimoto, E.O., Schenk, V., Appel, P., in preparation. Granulite-facies metamorphic events in the northeastern Ubendian Belt of Tanzania: Implications for the Neoarchean to Paleoproterozoic crustal evolution.

Kazimoto, E.O., Schenk, V., Appel, P., in review. The age of Au-Cu-Pb bearing veins in the poly orogenic Ubendian Belt (Tanzania): U Th total Pb dating of hydrothermally altered monazite. Contributions to Mineralogy and Petrology.

Keith, M., 2001. Evidence for a plate tectonics debate. Earth-Science Reviews 55, 235-336.

Kelemen, P.B., Hanghøj, K., Greene, A.R., 2003. One view of the geochemistry of subduction-related magmatic arcs, with an emphasis on primitive andesite and lower crust. Treatise on geochemistry 3, 293-659.

Kinzler, R.J., 1997. Melting of mantle peridotite at pressures approaching the spinel to garnet transition: Application to mid-ocean ridge basalt petrogenesis. Journal of Geophysical Research 102, 853-874.

Kooijman, E., Berndt, J., Mezger, K., 2012. U-Pb dating of zircon by laser ablation ICP-MS: recent improvements and new insights. European Journal of Mineralogy 24, 5-21.

Kröner, A., Hegner, E., Collins, A.S., Windley, B.F., Brewer, T.S., Razakamanana, T., Pidgeon, R.T., 2000. Age and magmatic history of the Antananarivo Block, central Madagascar, as derived from zircon geochronology and Nd isotopic systematics. American Journal of Science 300, 251-288.

Lawley, C.J.M., Selby, D., Condon, D.J., Horstwood, M., Millar, I., Crowley, Q., Imber, J., 2013a. Lithogeochemistry, geochronology and geodynamic setting of the Lupa Terrane, Tanzania: Implications for the extent of the Archean Tanzanian Craton. Precambrian Research 231, 174-193.

Lawley, C.J.M., Selby, D., Condon, D.J., Imber, J., 2013b. Palaeoproterozoic orogenic gold style mineralization at the Southwestern Archaean Tanzanian cratonic margin, Lupa Goldfield, SW Tanzania: Implications from U–Pb titanite geochronology. Gondwana Research.

Lawley, C.J.M., Selby, D., Imber, J., 2013c. Re-Os Molybdenite, Pyrite and Chalcopyrite Geochronology, Lupa Goldfield, Southwestern Tanzania: Tracing Metallogenic Time Scales at Midcrustal Shear Zones Hosting Orogenic Au Deposits. Economic Geology 108, 1591-1613.

Lenoir, J.L., Liégeois, J.P., Theunissen, K., Klerkx, J., 1994. The Palaeoproterozoic Ubendian shear belt in Tanzania: geochronology and structure. Journal of African Earth 19, 169-184.

Manya, S., 2004. Geochemistry and petrogenesis of volcanic rocks of the Neoarchaean Sukumaland Greenstone Belt, northwestern Tanzania. Journal of African Earth Sciences 40, 269-279.

Manya, S., 2012. SHRIMP zircon U-Pb dating of the mafic and felsic intrusive rocks of the Saza area in the Lupa goldfields, southwestern Tanzania: Implication for gold mineralization. Natural Science 04, 724-730.

Martin, H., 1999. Adakitic magmas: modern analogues of Archaean granitoids. Lithos 46, 411-429.

McConnell, R.B., 1950. Outline of the geology of Ufipa and Ubende.

McConnell, R.B., 1969. The association of granites with zones of stress and shearing. Geological Society of America Bulletin 80, 115-120.

Mezger, K., Krogstad, E.J., 1997. Interpretation of discordant U-Pb zircon ages: An evaluation. Journal of Metamorphic Geology 15, 127-140.

Möller, A., Appel, P., Mezger, K., Schenk, V., 1995. Evidence for a 2 Ga subduction zone: eclogites in the Usagaran belt of Tanzania. Geological Society of America 23, 3-7.

Möller, A., Mezger, K., Schenk, V., 1998. Crustal age domains and the evolution of the continental crust in the Mozambique Belt of Tanzania: combined Sm–Nd, Rb–Sr, and Pb–Pb isotopic evidence. Journal of Petrology 39, 749-783.

Moyen, J.-F., 2009. High Sr/Y and La/Yb ratios: the meaning of the “adakitic signature”. Lithos 112, 556-574.

Murphy, B.J., 2007. Igneous Rock Associations 8. Arc Magmatism II: Geo-chemical and Isotopic Characteristics. Geoscience Canada 34.

Nanyaro, J.T., 1989. Proterozoic gold-base metal veins in the Mpanda mineral field, western Tanzania, Annalles Series in-8, Science Geologiques 97. Musée Royale de L’Afrique Centrale Tervuren, Belgium, p. 144.

O’Connor, J.T., 1965. A classification for quartz-rich igneous rocks based on feldspar ratios. US Geologial Survey Research, 525, 79-84.

Pearce, J.A., 1983. Role of sub-continental lithosphere in magma genesis at active continental margins, in: Hawkesworth, C.J., Norry, M.J. (Eds.), Continental Basalts and Mantle Xenoliths, Shiva Nantwich, pp. 230-249.

Pearce, J.A., 1996. A user's guide to basalt discrimination diagrams, in: Wyman, D.A. (Ed.), Trace element geochemistry of volcanic rocks: Applications for massive sulphide exploration. Geological Association of Canada, pp. 79-113.

Pearce, J.A., 2008. Geochemical fingerprinting of oceanic basalts with applications to ophiolite classification and the search for Archean oceanic crust. Lithos 100, 14-48.

Perfit, M.R., Gust, D.A., Bence, A.E., Arculus, R.J., Taylor, S.R., 1980. Chemical characteristics of island-arc basalts: implications for mantle sources. Chemical Geology 30, 227-256.

Pinna, P., Muhongo, S., Mcharo, B.A., 2004. Geology and mineral map of Tanzania.

Polat, A., Hofmann, A.W., 2003. Alteration and geochemical patterns in the 3.7–3.8 Ga Isua greenstone belt, West Greenland. Precambrian Research 126, 197-218.

Ray, G.E., 1974. The structural and metamorphic geology of northern Malawi. Journal of the Geological Society 130, 427-440.

Reddy, S.M., Collins, A.S., Mruma, A.H., 2003. Complex high-strain deformation in the Usagaran Orogen, Tanzania: structural setting of Palaeoproterozoic eclogites. Tectonophysics 375, 101-123.

Richards, J.P., Kerrich, R., 2007. Special paper: adakite-like rocks: their diverse origins and questionable role in metallogenesis. Economic Geology 102, 537-576.

Ring, U., Kröner, A., Toulkeridis, T., 1997. Palaeoproterozoic granulite-facies metamorphism and granitoid intrusions in the Ubendian-Usagaran Orogen of northern Malawi, east-central Africa. Precambrian Research 85, 27-51.

Sanislav, I.V., Wormald, R.J., Dirks, P.H.G.M., Blenkinsop, T.G., Salamba, L., Joseph, D., 2014. Zircon U–Pb ages and Lu–Hf isotope systematics from late-tectonic granites, Geita Greenstone Belt: Implications for crustal growth of the Tanzania Craton. Precambrian Research 242, 187-204.

Schandl, E.S., Gorton, M.P., 2002. Application of high field strength elements to discriminate tectonic settings in VMS environments. Economic Geology 97, 629-642.

Semyanov, A., Kireev, A., Doronkin, I., Gavrilov, G., Matrenitzky, T., Novicov, A.G., 1977. Mpanda: Geological Map Quarter Degree Sheet 153. Geological Survey of Tanzania, Dodoma.

Shaw, D.M., 1970. Trace element fractionation during anatexis. Geochimica et Cosmochimica Acta 34, 237-243.

Smirnov, V., Shulyatin, O., Tolochko, V., Zhukov, S., Mwakisunga, M., Matrenitzky, T., 1970. Katuma: Geological Map Quarter Degree Sheet 152. Ministry of Energy and Minerals.

Sommer, H., Kröner, A., Muhongo, S., Hauzenberger, C.A., 2005. SHRIMP zircon ages for post-Usagaran granitoid and rhyolitic rocks from the Palaeoproterozoic terrain of southwestern Tanzania. South African Journal of Geology 108, 447-463.

Stendal, H., Frei, R., Muhongo, S., Rasmussen, T.M., Mnali, S.R., Petro, F., Brian Temu, E., 2004. Gold potential of the Mpanda Mineral Field, SW Tanzania: evaluation based on geological, lead isotopic and aeromagnetic data. Journal of African Earth Sciences 38, 437-447.

Sun, S.S., McDonough, W.F., 1989. Chemical and isotopic systematics of oceanic basalts: implications for mantle composition and processes. Geological Society, London, Special Publications 42, 313-345.

Taylor, S.R., McLennan, S.M., 1995. The geochemical evolution of the continental crust. Reviews of Geophysics 33, 241.

Tenczer, V., Hauzenberger, C.A., Fritz, H., Hoinkes, G., Muhongo, S., Klötzli, U., 2013. Crustal age domains and metamorphic reworking of the deep crust in Northern-Central Tanzania: a U/Pb zircon and monazite age study. Mineralogy and Petrology 5, 679-707

Tenczer, V., Hauzenberger, C.A., Fritz, H., Whitehouse, M.J., Mogessie, A., Wallbrecher, E., Muhongo, S., Hoinkes, G., 2006. Anorthosites in the Eastern Granulites of Tanzania—New SIMS zircon U–Pb age data, petrography and geochemistry. Precambrian Research 148, 85-114.

Thomas, R.J., Roberts, N.M.W., Jacobs, J., Bushi, A.M., Horstwood, M.S.A., Mruma, A.H., 2013. Structural and geochronological constraints on the evolution of the eastern margin of the Tanzania Craton in the Mpwapwa area, central Tanzania. Precambrian Research 224, 671-689.

Vogt, M., Kröner, A., Poller, U., Sommer, H., Muhongo, S., Wingate, M.T.D., 2006. Archaean and Palaeoproterozoic gneisses reworked during a Neoproterozoic (Pan-African) high-grade event in the Mozambique belt of East Africa: Structural relationships and zircon ages from the Kidatu area, central Tanzania. Journal of African Earth Sciences 45, 139-155.

Wang, L.G., Qiu, Y.M., McNaughton, N.J., Groves, D.I., Luo, Z.K., Huang, J.Z., Miao, L.C., Liu, Y.K., 1998. Constraints on crustal evolution and gold metallogeny in the Northwestern Jiaodong Peninsula, China, from SHRIMP U–Pb zircon studies of granitoids. Ore Geology Reviews 13, 275-291.

Weaver, B.L., 1991. The origin of ocean island basalt end-member compositions: trace element and isotopic constraints. Earth and Planetary Science Letters 104, 381-397.

Whitney, D.L., Evans, B.W., 2009. Abbreviations for names of rock-forming minerals. American Mineralogist 95, 185-187.

Wiedenbeck, M., Alle, P., Corfu, F., Griffin, W.L., Meier, M., Oberli, F., Quadt, A.V., Roddick, J.C., Spiegel, W., Von Quadt, A., 1995. Three natural zircon standards for U-Th-Pb, Lu-Hf, trace element and REE analyses. Geostandards Newsletter 19, 1-23.

Chapter 2

Granulite-facies metamorphic events in the northwestern Ubendian Belt of Tanzania: Implications for the Neoarchean to Paleoproterozoic crustal evolution

Abstract

We present a geological evolution model for the Paleoproterozoic Ubendian Belt. This model is deduced from the metamorphic histories of metasediments and metamafites combined with crust formation ages and metamorphic ages obtained from different rock types of the Katuma Block (NW Ubendian Belt).

Geothermobarometry and pseudosection modelling of metabasites indicate that the granulite-facies coronas containing garnet-clinopyroxene-quartz-hornblende formed at about 8.9–6.5 kbar and 790–700 °C. The formation of the corona textures is attributed to the post magmatic cooling history in the deep crust following their intrusion at about 2.65 Ga. This period correlates with the age of deposition of sediments in the Katuma Block, as deduced from the age of detrital zircon grains. The metamorphic P-T path of these sediments contrasts with that of the Archean mafic rocks. The common occurrence of sillimanite pseudomorphs after cm-sized kyanite crystals in migmatitic metapelites provides evidence that an early stage of metamorphism took place in the kyanite stability field whereas the subsequent peak metamorphism was characterised by the stability of the mineral assemblage sillimanite-garnet/cordierite-K-feldspar. Modelling of the X_{Mg} ratios of compositionally homogenous cores of garnet porphyroblasts together with GASP barometry suggest peak P-T conditions of about 7 kbar and 770 °C. The formation of plagioclase coronas around garnet in metapelites, the decrease in X_{Mg} and an increase of the spessartine fraction in rims of garnet porphyroblasts point to a near isothermal uplift after peak metamorphism.

Texturally controlled in situ U-Th-total Pb microprobe dating of monazite in metapelites resulted in two ages for metamorphic events. The monazite of the two dated samples is mostly complex and patchy zoned. The cores record ages of 1957 ± 10 Ma and 1967 ± 16 Ma, whereas the rims give ages of 1837 ± 6 Ma and 1848 ± 16 Ma. As the two ages of monazite growth

zones (core and rims) are found in monazite of the rock matrix and in monazite inclusions of garnet porphyroblasts, we conclude that garnet growth occurred during or after the second metamorphic event at 1840 Ma. This interpretation is in agreement with the depletion of HREE and Y in the monazite rims. We correlate the second, high-grade event with the collisional stage between the Tanzania Craton and the Bangwelu Block. The first event that preceded the collision for about 120 Ma is attributed to the kyanite grade metamorphism during accretionary processes and associated calc-alkaline magmatism along the continental margin of the Tanzania Craton.

Our new model proposes that the geologic history of rocks in the Ubendian Belt began in Neoarchean (2.7–2.6 Ga) during a magmatic formation phase in an active continental margin setting. Then followed a Neoarchean–Paleoproterozoic (2.65–2.05 Ga) stage tectonically inactive, passive continental margin subsequently there was again a protracted period of subduction (2.05–1.84 Ga) at an active continental margin associated with magmatic additions and metamorphic events during tectonic accretions. The collisional stage at 1.84 Ga most likely was responsible for the obduction and exposure of 1880–1860 Ma MORB type eclogites in the Ubendian Belt.

1. Introduction

The Ubendian Belt in SW Tanzania forms a linear belt that was traditionally interpreted to be formed entirely during the Paleoproterozoic (Lenoir et al., 1994; McConnell, 1969; Ring et al., 1997). However, recent studies showed that this belt was affected, at least in parts, also by Mesoproterozoic and Neoproterozoic orogenic events (Boniface and Schenk, 2012; Boniface et al., 2014). Despite the wealth of new petrological and age data that have been obtained in the course of these new studies, it was not possible to develop an evolutionary model for the Paleoproterozoic period of the Ubendian Belt. This unsatisfactory situation was due to the dearth of magmatic protolith ages, the missing knowledge about the number, nature and ages of metamorphic events and the lack of information about the duration and timing of sediments deposition recorded by detrital zircon. To develop an evolutionary model for the Paleoproterozoic Ubendian Belt we studied the metamorphic histories of metasediments and metamafites in the northeastern part of the belt by petrological methods and in situ U-Th-total Pb monazite dating. Combining these new data with those of previous (Boniface et al., 2012) and concomitant studies on the geochemistry and zircon geochronology of the metamagmatites (Kazimoto et al., in review-b), we develop an evolutionary model for the Paleoproterozoic orogenic cycle including the age and nature of the pre-existing continental crust that was involved in the formation of the Ubendian Belt.

2. Geological background

2.1 Ubendian Belt

The Ubendian Belt is a NW-SE trending metamorphic belt that borders the Tanzania Craton on its southwest side and separates the craton from the Bangweulu Block and the Irumide Belt to the southwest (Fig. 2.1a). Like the Paleoproterozoic and Neoproterozoic metamorphic belts of the eastern margin of the Tanzania Craton, the Ubendian Belt also consists in part of Neoarchean rocks that have been overprinted by younger metamorphic events (Kazimoto et al., in review-b; Lawley et al., 2013a). In this way the Ubendian Belt can be seen as a cratonic margin that has been reworked and received additions of new crustal material during the amalgamation of the Paleoproterozoic supercontinent Columbia between 2.1 and 1.8 Ga. The Ubendian Belt has been subdivided into eight lithologically distinct blocks (Fig. 2.1a), which are separated by NW-SE striking ductile shear zones (Daly, 1988). Previous authors subdivided the geodynamic evolution of this belt into two stages: an initial stage at 2.1–2.0 Ga characterised by arc magmatism, granulite-facies metamorphism and a late-stage deformation that was associated

with greenschist-facies overprint (Lawley et al., 2013a; Lenoir et al., 1994; Ring et al., 1997) and a second stage at 1.9–1.8 Ga characterised eclogite formation (Boniface et al., 2012), magmatism and amphibolite- to granulite-facies metamorphism and deformation (Lawley et al., 2013c; Lenoir et al., 1994). The latter events led to orogenic gold mineralisation in the Lupa Block (Lawley et al., 2013a; Lawley et al., 2013b; Lawley et al., 2013c). In addition to Paleoproterozoic tectonothermal activities, Boniface et al. (2012) and Boniface et al. (2014) recognized a Mesoproterozoic amphibolite grade crustal thickening event in the Wakole Block of the northwestern Ubendian Belt (Fig. 2.1) and a Mesoproterozoic metamorphic overprint of the Ubende Block. The Neoproterozoic eclogites recognized in the northern Ufipa Block reflect a Pan-African subduction event (0.59–0.52 Ga) between the Tanzania craton and the Bangweulu Block (Boniface and Schenk, 2012).

2.2 Katuma Block

The rocks of the Katuma Block of the northwestern Ubendian belt (Fig. 2.1b), have been subdivided into two groups (Semyanov et al., 1977; Smirnov et al., 1970): the Katuma Group consisting primarily of metabasites, gabbronorites, meta-granites and meta-granodiorites, and the Ikulu Group consisting mainly of metasediments (Fig. 2.1b). The rocks of the Katuma Group formed mainly during Neoarchean time (2.71–2.64 Ga) and during the Paleoproterozoic time (2.02–1.94 Ga; Kazimoto et al., in review). The recognition of two timely widely separated magmatic phases in the Katuma Group makes the traditional grouping of the rocks questionable. The age of a Neoarchean metamorphism is slightly older (2650 ± 8 Ma) than the crystallization of an unmetamorphosed gabbronorite (2643 ± 4 Ma) enclosing blocks of schistose garnet amphibolite (> metre scale). The detritus of the Ikulu metasediments derived from Neoarchean (≈ 2.64 Ga) and Paleoproterozoic (2.0 Ga) provenances, similar in age to that of rocks of the Katuma Group. The minimum deposition age of these sediments is constrained by their first metamorphic event at about 1.96 Ga, associated with the intrusion of calc-alkaline granites (1.99–1.94 Ga; Kazimoto et al., in review-b). The nature of the metamorphism of the two lithological groups is still enigmatic. In the north, the rocks of both groups are overlain by a Neo- to Mesoproterozoic and a Cenozoic sedimentary cover (Fig. 2.1b). All the rocks are cut by E-W and NW-SE trending fracture and shear zones, which host Mesoproterozoic hydrothermal Au-Cu-Pb bearing quartz-siderite-barite-sulphide veins. The hydrothermal event correlates with the Mesoproterozoic crustal thickening event at about 1.2 Ga (Kazimoto et al., in review-a).

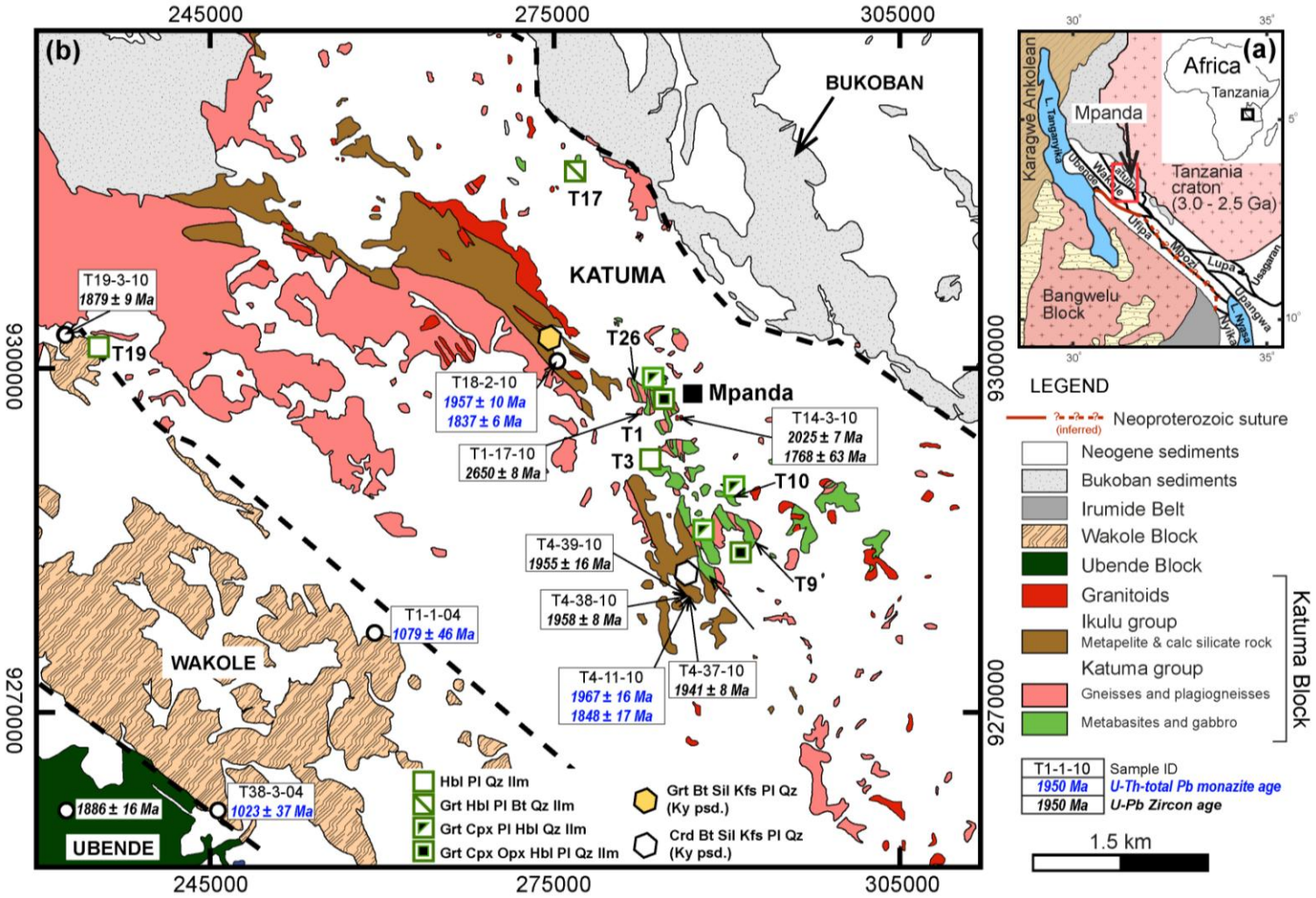

Fig. 2.1 (a) Geological map of the Ubendian Belt, modified from Daly (1988). The Ubendian Belt is located between the Tanzania Craton and the Bangweulu Block (b) Lithological map of the Katuma Block, modified from Biyashev et al. (1977), Semyanov et al. (1977b) and Smirnov et al. (1970), with metamorphic mineral assemblages and U-Th-total Pb monazite metamorphic ages obtained in this study. U-Pb zircon ages are from Kazimoto et. al. (in review) and the two ages of the Wakole metasedimentary rocks are from Boniface et. al. (2014) and one of the Ubende eclogite is from Boniface et al. (Boniface et al., 2012).

Table 1 Sample locations and mineral assemblages of metabasites and metapelites of the Katuma Block.

	Mineral assemblage																							
	Opx	Cpx	Hbl	Act	Grt	Bt	Pl	Kfs	Sil	Qz	Ilm	Mt	Pinite	Spn	Chl	Rt	Ep	Ser/Ms	Carb	Scp	Zrn	Mnz	Location	Easting (km)	Northing (km)
Metabasites																									
T1-12-10		x	[x]	?	[x]		x			x	x				[x]	x	[x]	[x]	[x]	[x]			Mkwamba		
T1-13-10		x	[x]		[x]		x			x	x			[x]	?								Mkwamba	283.7	929.6
T1-16-10	(o)	x	x		[x]	x	x	[x]		x	x												Mkwamba		
T2-9-10			x	?			x			x					[x]		[x]	[x]					Kapanda	286.9	928.5
T3-8-10			x				x				x				[x]	x	[x]	[x]	[x]				D-reef	283.6	929.1
T6-5-10			x	?		x	x				x			x		x	[x]	[x]					Singililwa	300.2	928.0
T9-1-10	(o)	x	[x]	[x]	x		x			x	x				x								Mpanda	292.5	928.5
T10-1-10		x	x		x		x			x	x												Mpanda	289.9	928.8
T11-1-10		x	x	x			x				x			x		x	x	x	x				Mpanda	288.0	928.4
T13-3-10		x	x	?	x		x			x	x				x								Mpanda	283.5	929.7
T14-2-10			x			x	x				x			x	x		x	x	x				Nyakaliza	284.8	929.7
T16-1-10	(o)	x	x		x		x			x	x												Mpanda	324.2	928.4
T17-3-10			x		x	x	x			x	x			x							x		Mpanda	276.7	931.8
T26-1-10		x	x		x		x			x	x			x	x	x	x						Lufuti	281.7	929.9
T26-3-10	(o)	x	x		x		x			x	x			x	x	x							Lufuti		
Metapelites																									
T18-1-10						x	x	x	x, k	x	ac				[x]			[x]			ac	ac	Ibyambe	275581	9299980
T18-2-10					x	x, (b)	x, (p)	x	x, k	x	ac				[x]			[x]			ac	ac	Ibyambe		
T4-7-10						x	x	x	x, k	x	ac, [x]	[x]	c		[x]		[x]	[x]	[x]		ac	ac	Chemchem	288391	9280264
T4-11-10						x	x	x	x, k	x	ac, [x]	[x]	c		[x]		[x]	[x]	[x]		ac	ac	Chemchem		

x, major phase; ac, accessory phase; [x] retrograde phase; (o), Opx inclusion in Cpx; (b), Bt inclusion in Grt; (p) Pl inclusion in Grt; k, Sil pseudomorphs after Ky; c: pinite pseudomorphs after Crd;

3. Petrography and mineral chemistry

3.1 Analytical methods

Mineral compositions were determined using a JEOL Superprobe JXA-8900R electron probe analyser at the University of Kiel equipped with five wavelength-dispersive spectrometers (WDS). The mineral analyses, except for that of monazite, were performed using an accelerating voltage of 15 kV and a probe current ranging between 15 nA and 20 nA. Synthetic and natural mineral standards were used for calibration, and the CITZAF method of Armstrong (1995) was used for matrix correction. The monazite composition was determined following similar procedures described by Braun and Appel (2006), Jöns et al. (2006) and Jöns and Schenk (2011), which are briefly summarised here. An accelerating voltage of 20 kV and a probe current of 60 or 80 nA were used during the analyses. The microprobe was calibrated using standards that included thorianite for Th, crocoite for Pb, synthetic uranium-bearing glasses for U, wollastonite for Si and Ca, corundum for Al and rare earth element orthophosphates of the Smithsonian Institute (Jarosewich and Boatner, 1991) for REE, Y and P. The composition of the REE orthophosphates standards were carefully determined considering their Pb content (see Donovan et al. 2003). Corrections from the matrix analyses were performed using the JEOL ZAF program. Counting times for Pb were between 2 and 4 minutes on the peak and similar times on the background, depending on the intensities. The Pb Mb lines, Th Ma lines and U Mb lines (considering interference from Y Mg) were used. More details about the analytical protocol and the background approximation for Pb are given at http://www.ifg.uni-kiel.de/1202.html. The quality of the data was controlled using an internal monazite standard that included monazite from southeast Madagascar, which is homogenous in composition and was dated using the U-Pb method and a Sm-Nd monazite-biotite-garnet-zircon isochron to an age of 542 ± 2 Ma and 542 ± 11 Ma, respectively (Paquette et al., 1994) and recently by A. Möller (per. comm.) with TIMS at an age of 560 ± 1 Ma. Analyses that contain significant apparent Al were rejected to avoid artefacts from secondary fluorescence that may occur if analytical points are near to grain boundaries. The chemical monazite ages and their errors were calculated using the "Comb error" (http://www.ifg.uni-kiel.de/339.html) and "AgeFinder" software (Appel, 2010).

3.2 Metabasites

Metabasites are omnipresent in the eastern part of the Katuma Block (Fig. 2.1b), where they occur together with orthogneisses. The rocks are greenish to dark grey, massive and primarily

fine- to medium grained. The mineral assemblages (Table 1) include plagioclase, ortho- and clinopyroxene, hornblende, garnet and accessory biotite and pyrite. Accessory minerals are ilmenite, titanite and zircon. The mafic minerals are present in variable amounts between 50 and 65 vol. %. The metabasites display various degrees of amphibolite-facies retrogression, in which the peak metamorphic minerals are partially replaced by hornblende, plagioclase, quartz and titanite as either late rims or symplectites. In places, the metabasites experienced greenschist-facies retrogression as displayed by the formation of actinolite, epidote, chlorite, albite, titanite, quartz or/and carbonates. Representative analyses of minerals of metabasites are presented in Table 2.

Garnet is present as rims together with quartz around ortho- and clinopyroxene and as aggregates consisting of anhedral to subhedral grains (Fig. 2.2a, b and c) that are porphyroblastic in places and contain inclusions of quartz, plagioclase, ilmenite and hornblende. The garnet coronas display an increase in X_{Alm} and continuous decrease of X_{Mg}, X_{Prp} and X_{Grs} towards the rims (Fig. 2.3a). The range of compositions are X_{Alm} = 0.69–0.50, X_{Prp} = 0.4–0.1, X_{Grs} = 0.29–0.24, $X_{Sps} \approx 0.02$ and X_{Mg} = 0.3–0.1. Two types of clinopyroxene were recognised: one type is pale green to brownish in colour, subhedral to anhedral, frequently interlocking with plagioclase that makes ophitic to subophitic textures. The other type is darker green and its grains, in places, form an intergranular texture with amphibole. By using the classification scheme of Morimoto et al. (1988), the green to brownish clinopyroxene is classified as augite (Fig. 2.3b) with compositional ranges of X_{En}= 0.24–0.71, X_{Fs}= 0.44, X_{Wo}=0.23–0.45, X_{Na} = 0.01–0.15 and X_{Mg} = 0.35–0.75. The green clinopyroxene is classified as diopside (Fig. 2.3b) with compositional ranges of X_{En}= 0.29–0.41, X_{Fs}= 0.12–0.26, X_{Wo} = 0.45–0.48, X_{Na} = 0.01–0.05 and X_{Mg} = 0.52–0.77. The orthopyroxene, which is present as relicts in diopside, has compositional ranges of X_{En}= 0.36–0.59, X_{Fs} = 0.40–62, X_{Wo} = 0.52–1.91, X_{Al} = 0.02–0.07 and X_{Mg} = 0.37–0.60. The amphiboles form rims around clinopyroxene (Fig. 2.2a, c and d) and are present as late-stage symplectites together with clinopyroxene, plagioclase and/or quartz. According to the classification scheme of Leake et al. (1997), the amphiboles are mainly pargasite, ferropargasite, magnesiohornblende, ferrohornblende, tschermakite ferro-tschermakite and edenite. Actinolite is a late stage formation (Fig. 2.3c and d). The titanium contents in these amphiboles range between 0.26 apfu and 0.08 apfu, with higher values in the mafic granulites and garnet-amphibolites, but lower values in the amphibolites.

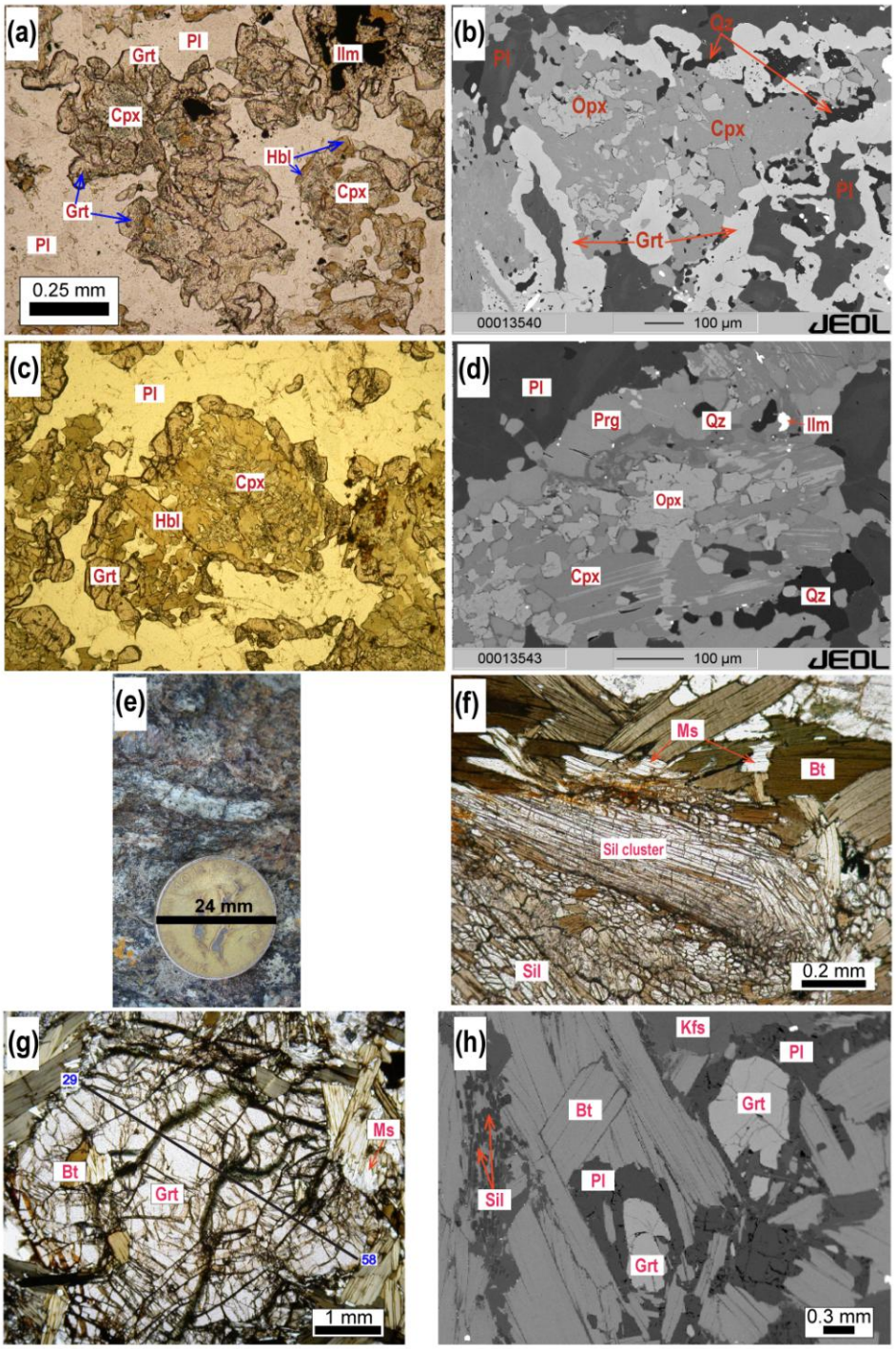

Fig. 2.2 Photomicrographs, field photograph and backscatter images of metabasite and metapelite from the Katuma Block. Mineral abbreviations are from Whitney and Evans (2009). (a) Replacement of ortho- and clinopyroxene and plagioclase by garnet coronas and hornblende in mafic granulite (sample T9-1-10) (b) A BSE image showing replacement of garnet and quartz forming coronas around ortho- and clinopyroxene (sample T9-1-10) (c) Replacement of clinopyroxene and plagioclase by garnet coronas and hornblende in mafic granulite (sample T10-1-10) (d) Formation of ilmenite, amphibole and quartz after plagioclase, ortho- and clinopyroxene in a mafic granulite (sample T26-3-10) (e) Prismatic sillimanite pseudomorphs after kyanite in Ikulu metapelite (location T4-11-10) (f) Microphotograph of sillimanite pseudomorphs after kyanite showing sillimanite cluster surrounded by biotite (T18-2-10) (g) Garnet porphyroblast with biotite inclusions in the garnet-bearing metapelite (h) BSE image showing a plagioclase corona around garnet in metapelite (T18-2-10).

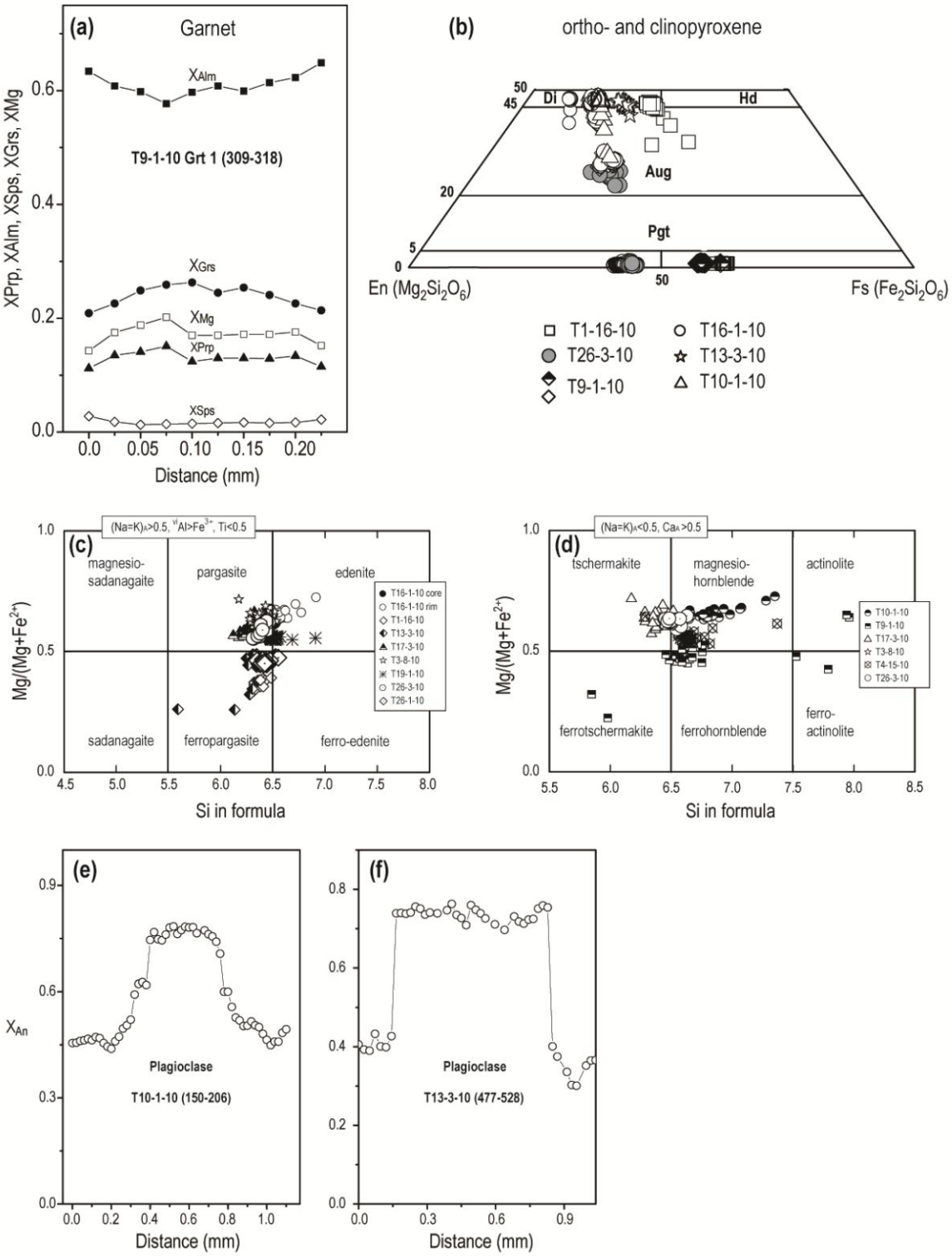

Fig. 2.3 (a) Composition of garnet in mafic granulite showing retrograde zoning profile in which X_{Mg} and X_{Prp} decreases and X_{Alm} increases rimwards. (b) Classification of ortho- and clinopyroxene in mafic granulite; magmatic clinopyroxene is augite, whereas metamorphic clinopyroxene is diopside. (c and d) Composition of amphiboles in mafic granulites and amphibolites, formula calculated on the basis of 23 oxygens. (e and f) Zoning profiles of plagioclase in mafic granulite showing magmatic cores ($X_{An} > 0.6$) and metamorphic rims ($X_{An} < 0.6$).

.

Plagioclase forms laths displaying strong compositional zoning (Fig. 2.3e and f); some crystals occur enclosed in or interlocked with clinopyroxene, which is interpreted to reflect a preserved magmatic texture. The anorthite fraction of plagioclase in the amphibolites ranges between 15% and 57%. The high X_{An} cores (An_{50-85}) of mafic granulite are interpreted to be relicts of the magmatic plagioclase, whereas low X_{An} rims (An_{30-62}), surrounding the cores with an abrupt compositional change, are interpreted to be of metamorphic origin (Fig. 2.3e and f).

3.3 Metapelites

Samples of the aluminous metapelites have been collected at two localities. One to the north of Mpanda town at Ibyambe hills (T18-2-10; Fig. 2.1) containing garnet-biotite-sillimanite-K-feldpar and another derives from the south of Mpanda town at Chemchem hill (T4-11-10; Fig. 2.1) containing cordierite instead of garnet that is totally pinitised. The Ikulu migmatitic metapelites are gneissic in texture with an assemblage (Table 1) of biotite, sillimanite, plagioclase, K-feldspar, only small amounts of quartz and porphyroblastic garnet (T18-2-10) or pinite pseudomorphs after cordierite instead of garnet (T4-11-10).

The accessory minerals include ilmenite, magnetite, zircon and monazite, whereas the retrograde minerals include muscovite. Sillimanite is present in clusters forming pseudomorphs after kyanite. The original form of the later is often still preserved as 2–3 cm long prismatic grains (Fig. 2.2e and f). Garnet forms ellipsoidal porphyroblasts up to 5 mm in diameter (Fig. 2.2g) that contain biotite, plagioclase, sillimanite and monazite as inclusions. Biotite is also present in the matrix and forms, in parts, flakes that are intergrown with sillimanite. Biotite in both cordierite bearing and garnet bearing metapelites displays retrograde exsolution of ilmenite along its rims. K-feldspar in the garnet bearing metapelite is present as perthitic microcline that may be surrounded by albite rims formed from the perthitic exsolutions, whereas in the cordierite bearing metapelite the K-feldspar shows sericitization. Late-stage muscovite forms small flakes along grain boundaries of biotite and sillimanite (Fig. 2.2f and g).

Representative analyses of the minerals are presented in Table 3. Garnet cores are homogenous (Fig. 2.4a) and have compositional ranges of X_{Mg} = 0.1–0.2, X_{Alm} = 0.65–0.72, X_{Prp} = 0.08–0.18, X_{Grs} = 0.01–0.03 and X_{Sps} = 0.1–0.24. Garnet grains display retrograde re-equilibration only along the rims showing increasing X_{Fe} (≈ 0.20 mm; Fig. 2.4a). The increase in spessartine component in the outermost rim most likely indicates resorption of garnet and biotite formation at the expense of garnet during retrogression. Both the matrix plagioclase and

plagioclase inclusions in garnet have a composition of $An_{20-23}Ab_{75-83}Or_{0-6}$. The K-feldspar composition is in the range of $Or_{82-100}Ab_{28-0}$, whereas its exsolution lamellae have composition of $Ab_{84-100}Or_{14-0}$. The X_{Mg} of biotite has lower values in the garnet-bearing metapelite than in the cordierite-bearing metapelite (Fig. 2.4b). The preserved titanium concentrations in biotite range from 0.15 pfu to 0.35 pfu. Ti contents and the X_{Mg} ratios are similar to those of biotite of the sillimanite-staurolite and kyanite-staurolite metamorphic zones in New England (Fig. 2.4b; Robinson et al., 1982; Spear, 1995). Nevertheless, owing to the generally strong retrograde exsolution of ilmenite these mineral chemical data reflect only minimum metamorphic conditions. The late-stage Muscovite contains 3.0–3.07 Si apfu and 0.17–0.22 (Mg+Fe) apfu, not following the phengite substitution line (Fig. 2.4c). In the garnet bearing sample quartz is nearly absent, but mainly preserved as spherical inclusions in feldspars.

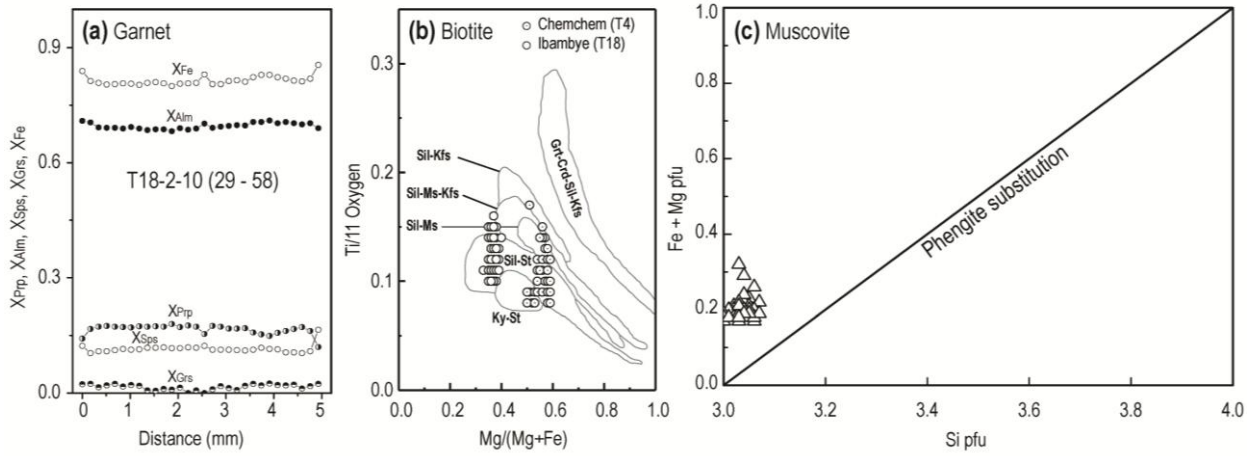

Fig. 2.4 (a) Composition of garnet porphyroblast in the Ikulu metapelite depicting homogenous core compositions with narrow retrograde rims (< 0.5 mm: low X_{Prp} and high X_{Alm}) (b) Biotite compositions in the garnet-bearing (T18) and cordierite-bearing metapelite (T4) (c) Chemical compositions of muscovite in the metapelite; low Si contents of muscovite plot away from the phengite substitution line.

4. Pressure-temperature conditions during different metamorphic events

The metabasites and metapelites of the Katuma Block are suitable to allow estimates of the pressure and temperature conditions of their formation. However, it has to be kept in mind that the rocks of the Katuma Block were formed in Neoarchean and in Paleoproterozoic times and the mineral assemblages preserved in the rocks may not have been formed during the same orogenic cycle but have to be attributed to different metamorphic events, which have to be resolved in connection with textural controlled dating of monazite.

On the basis of the described petrographic observations we obtain critical information for the P-T conditions and evolution. At both localities, where metapelites have been sampled, north and south of Mpanda town, the Grt-Sil-Bt gneisses and Crd-Sil-Bt gneisses contain sillimanite pseudomorphs after kyanite (Fig. 2.2e and f), indicating that in both areas kyanite was stable during an early stage. However, at a later stage at higher temperatures sillimanite became stable either with garnet (north of Mpanda) or with cordierite (south of Mpanda). During this stage anatectic melts have formed in both garnet and cordierite bearing assemblages. In contrast, in mafic granulites the most striking petrographic feature is the development of garnet and hornblende or clinopyroxene coronas between orthopyroxene and plagioclase, which usually are interpreted as a texture related to retrograde near isobaric cooling at elevated pressures (e.g. Schenk, 1984). For further constraining the pressure-temperature conditions for the formation of the different assemblages we applied conventional geothermobarometry as well as pseudosection modelling.

4.1 Conventional geothermobarometry

The presence of ortho- and clinopyroxene, garnet, plagioclase, quartz, hornblende and minor biotite in the metabasites provides a basis for estimating both the peak and the retrograde pressure-temperature (P-T) conditions. The calibrations of Ellis and Green (1979) and Powell (1985) for Fe-Mg partitioning between co-existing garnet-clinopyroxene and the Fe-Mg distribution between garnet-hornblende (Graham and Powell, 1984; Perchuk et al., 1985)(1984b), were used as thermometers. The calibrations of Eckert et al. (1991) and Newton and Perkins (1982) for the garnet-plagioclase-clinopyroxene/orthopyroxene-quartz equilibrium (GADS and GAES) were applied for pressure estimates of the mafic granulites. The garnet-plagioclase-hornblende barometer (Kohn and Spear, 1990) was used for pressure estimates of the amphibolites. All P-T estimates were performed without correcting for ferric iron and using the core compositions with the highest X_{Mg} for garnet and high Ti concentrations in the case of hornblende. The P-T estimates are summarised in Table 4. The mafic granulites yielded pressure estimates in the range of 6.7–8.9 kbar and temperature estimates in the range of 630 – 750 °C for the corona forming event. The P-T estimates for the amphibolites using the Hbl-Grt-Pl-Qz barometer and Hbl-Grt thermometer gave values in the range of 6.8–8.7 kbar and 640–790 °C, respectively.

The estimates of the peak metamorphic conditions for the metapelites were not straightforward because of the dearth of minerals that can be used for thermometry. The

retrogression of biotite, even visible in the form of Fe-Ti oxide exsolutions, limited the use of the Fe-Mg distribution between biotite and garnet for temperature estimates. The presence of compositionally homogenous plagioclase feldspars that are in equilibrium with garnet porphyroblasts provided a means to estimate pressure conditions (GASP) only at a particular temperature condition. At the assumed temperature of 770 °C (cf. section 4.2), the obtained pressure are in the range of 6.1 to 7.1 kbar (Table 4).

4.2 Pseudosection modelling

To obtain the thermobarometric information and to determine the P-T evolution metapelites and metabasites, several pseudosections (Fig. 2.5, 2.6, 2.7 and 2.8) were calculated using the THERIAK-DOMINO software (De-Capitani and Petrakakis, 2010) and the internally consistent datasets of Holland and Powell (1998) and Berman (1988), files tcdb55c2d (THERMOCALC v. 3.25) and jun92. The activity models used in the Holland and Powell (1998) dataset (tcdb55c2p) are those of Baldwin et al. (2005) for feldspar, White et al. (2007) for garnet (tc 325) and biotite, Coggon and Holland (2002) for white mica, and Holland and Powell (1998) for cordierite. The mineral assemblages of the metapelites and metabasites are presented in Table 1, and the major element compositions are presented in Table 5. The H_2O concentrations were derived from the values of loss on ignition, which, prior to their use, were checked using thermodynamic modelling of the equilibrium assemblage in diagrams of temperature versus H_2O. All of the applied values of H_2O produced the observed assemblages of the rocks.

Mafic granulite T9-1-10

The P-T pseudosection calculated for the mafic granulite T9-1-10 consists of di-, tri-, and quadri-variant fields in a pressure range of 5.5–9.0 kbar and a temperature range of 600–800 °C (Fig. 2.5). The assemblage of this mafic granulite is represented in the di-variant field of Ilm + Opx + Grt + Cpx + Pl + Prg + aQz + H_2O, with the exception of the late-stage amphibole, which occurs in the sample as ferrohornblende instead of pargasite. The disparity in amphibole is most likely due to the inadequacy of amphibole activity models in the Jun92 dataset of Berman (1988), which is limited to pargasite, tschermakite and tremolite. The X_{Mg}-isopleths of garnet that co-exists with pargasite on the low temperature side of the amphibole-out line are more temperature dependent than those on the high temperature side of this line, which are both pressure and temperature dependent as are those of the X_{An} of plagioclase (Fig. 2.5). The

maximum X_{Mg} values in garnet cores (0.2) and the X_{An} of the metamorphic plagioclase (0.51) provide a P-T estimate of 7.8 kbar and 700 ℃ for their equilibriation. These P-T conditions are in the tri-variant field of Ilm + Opx + Grt + Cpx + Pl + aQz + H_2O, which is characterised by the reaction Opx + Cpx_1 + Pl = Grt + Cpx_2 + Qz, consistent with the textural features of garnet-clinopyroxene corona around orthopyroxene (Fig. 2.2a and b). The rimward decrease in X_{Mg} of garnet and the decrease of X_{An} of the metamorphic plagioclase correspond to the isopleths of X_{Mg} of garnet and X_{An} of plagioclase that are crossed with falling temperatures (Fig. 2.5). The inferred near isobaric cooling path crosses the pargasite-forming reaction Opx + Cpx + Pl + Qz = Grt + Prg + Qz and may be manifested in the sample by the replacement of orthopyroxene, clinopyroxene and plagioclase by ferrohornblende, garnet and quartz (Fig. 2.2a and b).

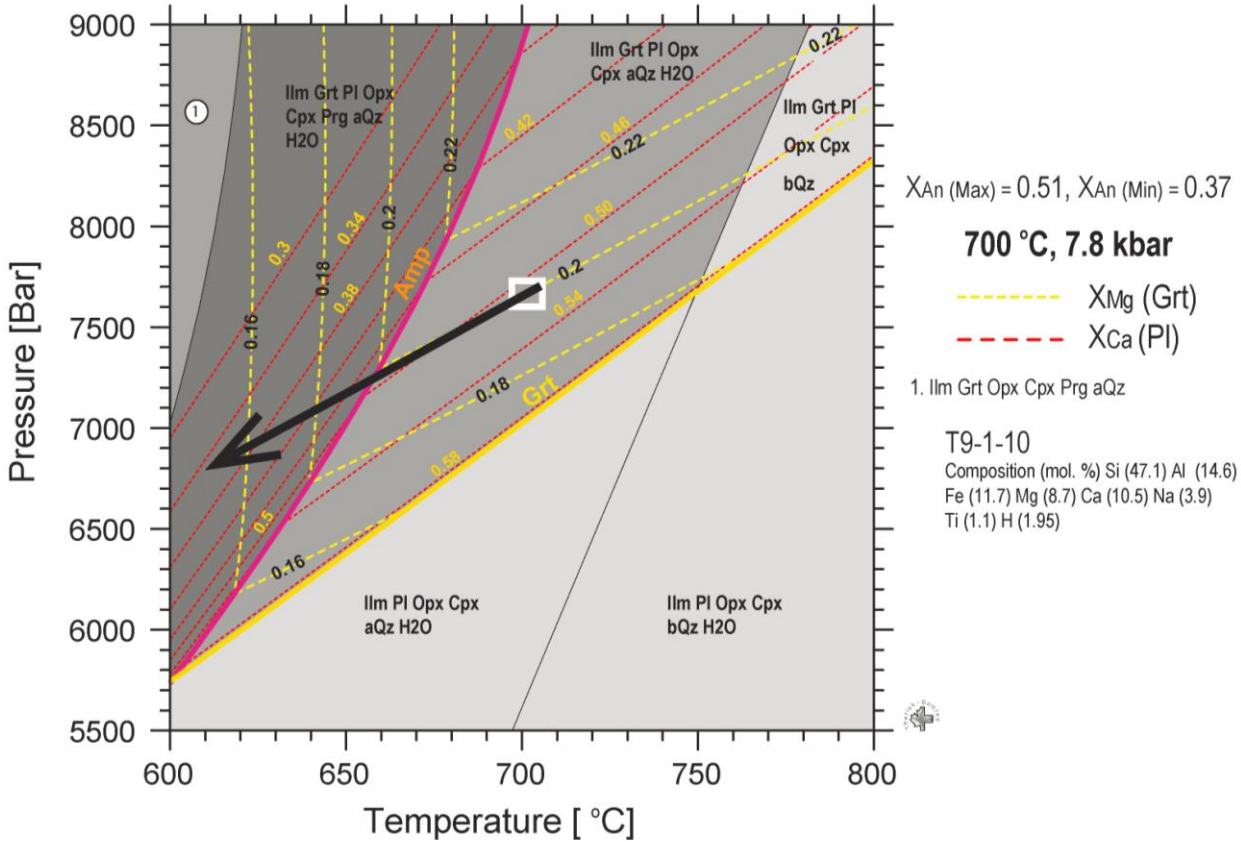

Fig. 2.5 P-T pseudosection in the system Na_2O-CaO-FeO-MgO-Al_2O_3-SiO_2-TiO_2-H_2O for the mafic granulite T9-1-10. Dark gray, medium gray and light gray shading represent di-, tri-, and quadri-variant fields, respectively. The Pseudosection is overlain with isopleths of X_{Mg} (yellow dashed lines) and X_{Ca} (red dashed lines), yellow and pink bold lines represent garnet-in and amphibole-in line. White box represents P-T conditions determined from isopleths of X_{Mg} and X_{Ca}. The black arrow represents the P-T path.

Mafic granulite T10-1-10

The pseudosection for the mafic granulite T10-1-10 is dominated by tri- and quadri-variant fields and minor di- and quini-variant fields shown in a P-T diagram ranging from 7.5 to 9 kbar and from 600 to 800 °C (Fig. 2.6). The equilibrium assemblage is represented by a very broad tri-variant field of Grt + Pl + Cpx + Prg + aQz + H_2O that is limited at 7.5–9 kbar and temperatures above 600 to 740 °C (depending on pressure) by a small di-variant field with the assemblage Grt + Pl + Opx + Cpx + Prg + aQz + H_2O.

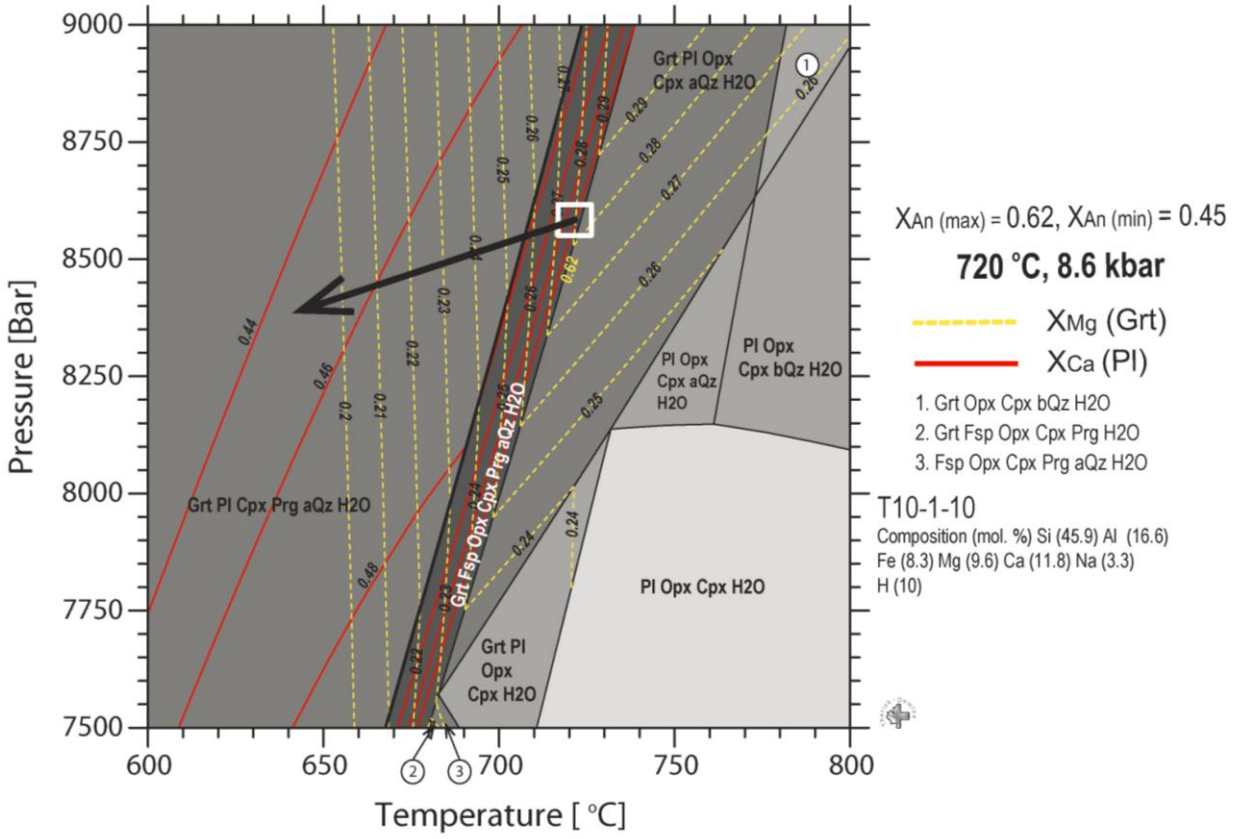

Fig. 2.6 P-T pseudosection in the system Na_2O-CaO-FeO-MgO-Al_2O_3-SiO_2-H_2O for mafic granulite T10-1-10. Increasingly dark grey tones of the fields correspond to the increase in variance of the fields (di-, tri-, quadri- and quini-variant fields). Pseudosection is overlain with isopleths of X_{Mg} (yellow dashed lines) and X_{Ca} (red lines), white box represents P-T conditions determined from isopleths of X_{Mg} and X_{Ca} and black line represents the deduced P-T path.

The few small relicts of orthopyroxene in this sample indicates that the earliest preserved metamorphic stage was in the narrow divariant field of Grt + Pl + Opx + Cpx + Prg + aQz + H_2O. As in the case of the pseudosection for the mafc granulite T9-1-10, pargasite is predicted as the stable amphibole instead of magnesiohornblende due to inadequacy of the applied amphibole activity models. The modelled isopleths of the X_{Mg} values in garnet are strongly temperature dependent in the tri- and divariant field mentioned above, whereas those of X_{An} in

plagioclase are pressure and temperature dependent (Fig. 2.6). Thus, the maximum X_{Mg} of the garnet core values and the maximum X_{An} of the coexisting inner part of the metamorphic plagioclase value constrain the P-T conditions to 8.6 kbar and 720 °C. The rimward decrease of X_{Mg} ratios in garnet and X_{An} in plagioclase (Fig. 2.3e) suggests that the garnet cores, their rims and the metamorphic plagioclase grew during near isobaric cooling. The small orthopyroxene relicts in this sample, the presence of garnet coronas around clinopyroxene and the replacement of clinopyroxene by hornblende (Fig. 2c) are consistent with the crossing of the Opx-out reaction line Pl + Opx + H_2O = Grt + Cpx + Hbl + Qz (Fig. 2.6).

Mafic granulite T26-3-10

The pseudosection for sample T26-3-10 consists of di-, tri-, quadri- and quini-variant fields shown in a digram for the P-T range of 8.2–9.2 kbar and 680–740 °C (Fig. 2.7). The equilibrium assemblage consists of garnet, ortho- and clinopyroxene, amphibole (pargasite), plagioclase feldspar, quartz and ilmenite and is represented in the broad corresponding di-variant field (low T part in Fig. 2.7). This field is limited towards higher temperatures by the replacement of ilmenite and rutile. The X_{Mg} isopleths of garnet are strongly temperature dependent in both the ilmenite and the rutile bearing divariant fields. The X_{An} isopleths of plagioclase are pressure and temperature dependent. Using the X_{Mg} of the garnet core (0.28) and the X_{An} of the metamorphic plagioclase rim (0.51), a peak pressure of about 8.9 kbar and a temperature of 725 °C is obtained (Fig. 2.7). This P-T point is located near an amphibole-in line that marks the beginning of the reaction Opx + Pl + H_2O = Grt + Cpx + Prg + Qz, which is consistent with the reaction textures observed in this mafic granulite, in which magmatic ortho- and clinopyroxene (augite) is replaced by metamorphic clinopyoxene (diopside), garnet, quartz and pargasite (similar to textures in Fig. 2.2a and d). Like in the pseudosections for the mafic granulites T9-1-10 and T10-1-10, the decreases of the calculated X_{Mg} ratios and the X_{An} towards lower P-T conditions correspond to the rimward decreases of X_{Mg} in garnet of the sample (ca. 0.25) and the decrease of X_{An} of the plagioclase (0.40). These decreases depict a near isobaric cooling path for this mafic granulite, which crosses a reaction line at which rutile is replaced by ilmenite. The absence of rutile in the assemblage suggests that all rutile was completely consumed in this reaction to form ilmenite.

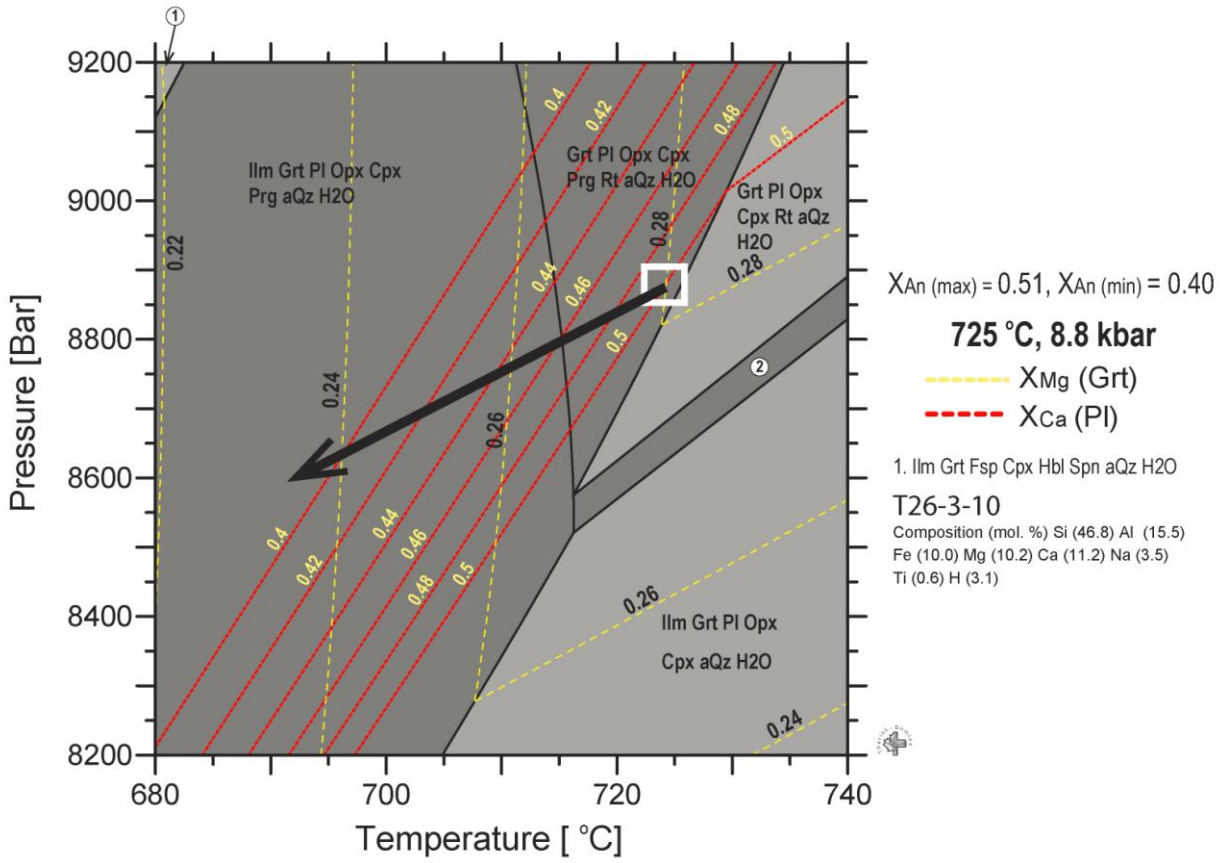

Fig. 2.7 P-T pseudosection in the system Na_2O-CaO-FeO-MgO-Al_2O_3-SiO_2-TiO_2-H_2O for the mafic granulite T26-3-10. Variance of the fields is depicted as in Figure 6. Pseudosection is overlain with isopleths of X_{Mg} (yellow dashed lines) and X_{Ca} (red dashed lines), white box represents the P-T conditions determined from the isopleths of X_{Mg} and X_{Ca} . The black arrow represents the P-T path.

Garnet-bearing metapelite T18-2-10

The pseudosection for the garnet-bearing metapelite is characterised by di-, tri-, quadri- and quini-variant fields at pressures of 3–7 kbar and temperatures of 550-850 °C. The mineral assemblage of the garnet-bearing metapelite is depicted in the quadri-variant field of Pl + Sa + Grt + Bt + melt + Sil, which occurs at pressures, above 5–7 kbar and a temperature range of 730–820 °C (Fig. 2.8). The isopleths for X_{Mg}, X_{Alm} and X_{Sps} of garnet are calculated given in the equilibrium assemblage diagram. The X_{Mg} in the garnet core of T18-2-10 (0.20; Fig. 2.8) result in a P-T estimate of about 6 kbar and 790 °C. Biotite, plagioclase and sillimanite inclusions in garnet together with sillimanite pseudomorphs after kyanite (Fig. 2.2e and g) suggest that, during the prograde evolution the metapelite experienced conditions in the kyanite stability field. The conditions then evolved towards the stability of the quadri-variant field of Pl + Sa + Grt + Bt + Sil + Ms + Qz and the quadri-variant field of Pl + Sa + Grt + Bt + Sil + Qz + melt (Fig. 2.8). These observations document a P-T path with heating. The cooling and

decompression phase of this metapelite is documented by the decrease of X_{Mg}, X_{Alm} and X_{Sps} values in garnet rims (0.11, 0.65 and 0.1; Fig. 2.8) and the formation of retrograde muscovite replacing biotite and sillimanite (Fig. 2.2f and g), which corresponds to a cooling path through the quadri -variant field of Pl + Sa + Grt + Bt + Sil + Qz + melt, crossing a Ms formation line to the quadri-variant field of Pl + Sa + Grt + Bt + Sil + Ms + Qz (Fig. 2.8). The late-stage plagioclase corona around garnet is in agreement with isothermal decompression after peak metamorphism. Pressure estimates for the plagioclase-corona forming stage with garnet rim compositions and the plagioclase of the corona result in about 6 kbar, which is about 1 kbar below the peak pressure (Fig. 2.8; GASP, Koziol and Newton, 1988).

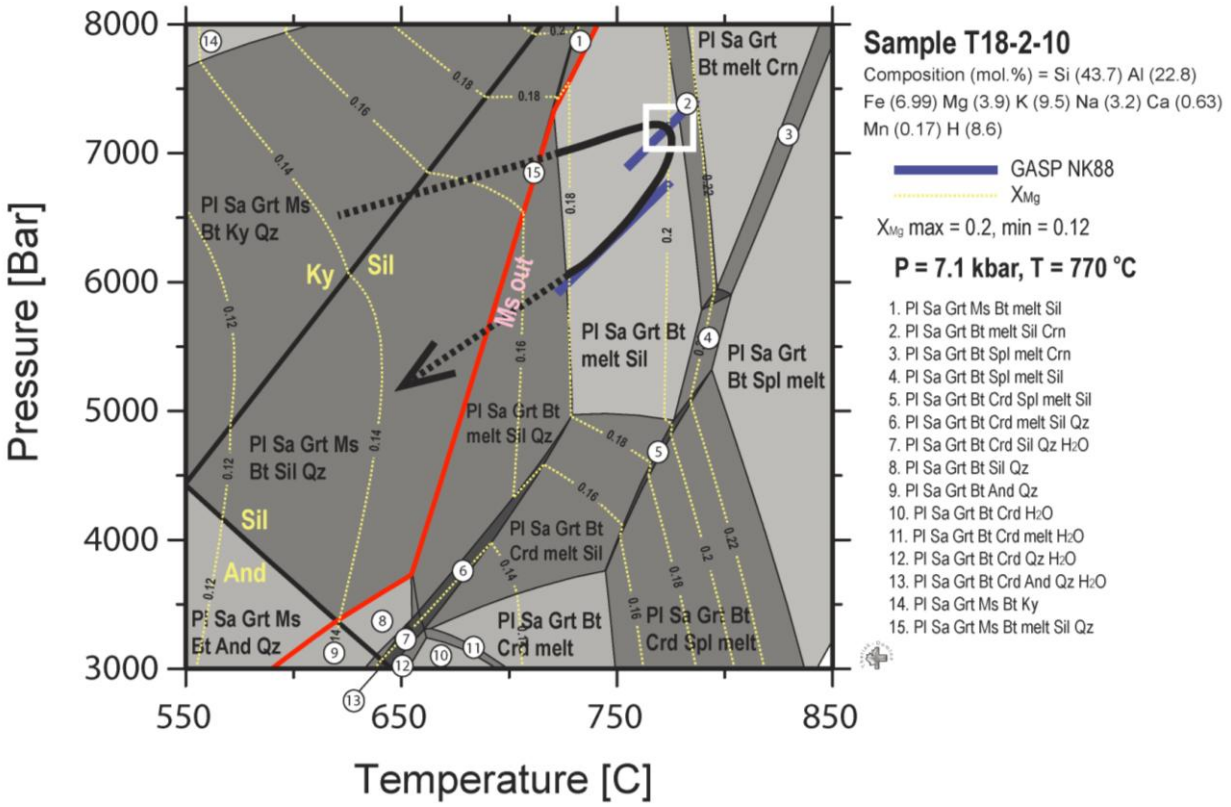

Fig. 2.8 P-T pseudosection in the system Na_2O-CaO-K_2O-FeO-MgO-Al_2O_3-SiO_2-H_2O for the garnet-bearing metapelite T18-2-10. Increasingly dark grey tones of the fields correspond to the increase in variance of the fields (tri-, quadri- and quini- variant fields). Pseudosection is overlain with isopleths of X_{Mg} (yellow dashed lines), black bold lines represent kyanite-sillimanite and andalusite-sillimanite transitions, red line represents the muscovite-out line, purple lines are GASP (grossular-aluminosilicate-silica-anorthite; KN 88 - Koziol and Newton, 1988) lines. The white box represents the P-T conditions determined from isopleths of X_{Mg} and the GASP lines. Black solid/dashed arrow represents the P-T path.

5. Texturally controlled, in situ monazite dating

The in situ analysis of monazite for U, Th and total Pb dating using an electron microprobe was performed to date the metamorphic evolution by linking the geochronological data with the internal texture of a single monazite grains and the texture of the rock forming minerals, in which the dated monazite occurs, i.e. as inclusions in garnet or as matrix grains. Two metapelite samples, the cordierite bearing metapelite (T4-11-10) and the garnet bearing metapelite (T18-2-10), were selected for the texturally controlled in situ monazite dating.

5.1 Monazite texture and chemistry

The internal textures of monazite grains are similar in both samples and are independent of their textural setting (inclusion in garnet and matrix). However, the textures are better preserved in the garnet bearing rock (T18-2-10) due to some hydrothermal alteration at the Chemchem locality of the cordierite-sillimanite-kfeldspar-biotite-bearing sample (T4-11-10).

The monazite grains (15 to 250 μm) have dark cores in BSE images that are partially replaced by lighter coloured patches that developed with convex grain boundaries into the darker zones (Fig. 2.9b, c, d, f). These patchy textured cores are surrounded by concentrically zoned rims, which are in most cases light coloured in BSE images (Fig. 2.9b, d and f) but sometimes also quite dark gray (Fig. 2.9a and c). This pattern represents a complex zoning. The mineral chemical data from the different types of monazite grains are presented in Table 6–9.

The monazite grains are present as accessory minerals in the matrix or as inclusions in other minerals (e.g. garnet) in the metapelites. Monazite grains from the matrix and those of garnet inclusions exhibit characteristic enrichments in light rare earth elements (LREE) over heavy rare earth elements and Y (HREEs; Fig. 2.10a and b). The overgrown rims of the monazite grains tend to contain lower amounts of HREE and Y compared to the cores (Fig. 2.10a and b). All the monazite patterns exhibit Eu anomalies (Fig. 10a and b). In the plot of (Th+U+Si)*4 versus (REE+Y+P)*4 (Fig. 2.11), the chemical composition of the monazite cores is characterized by a varying cheralite substitution, whereas the overgrown rims spread between the huttonite and cheralite substitution vectors, suggesting effects of both substitutions in the overgrowths by fluid related processes (e.g. Harlov et al., 2011).

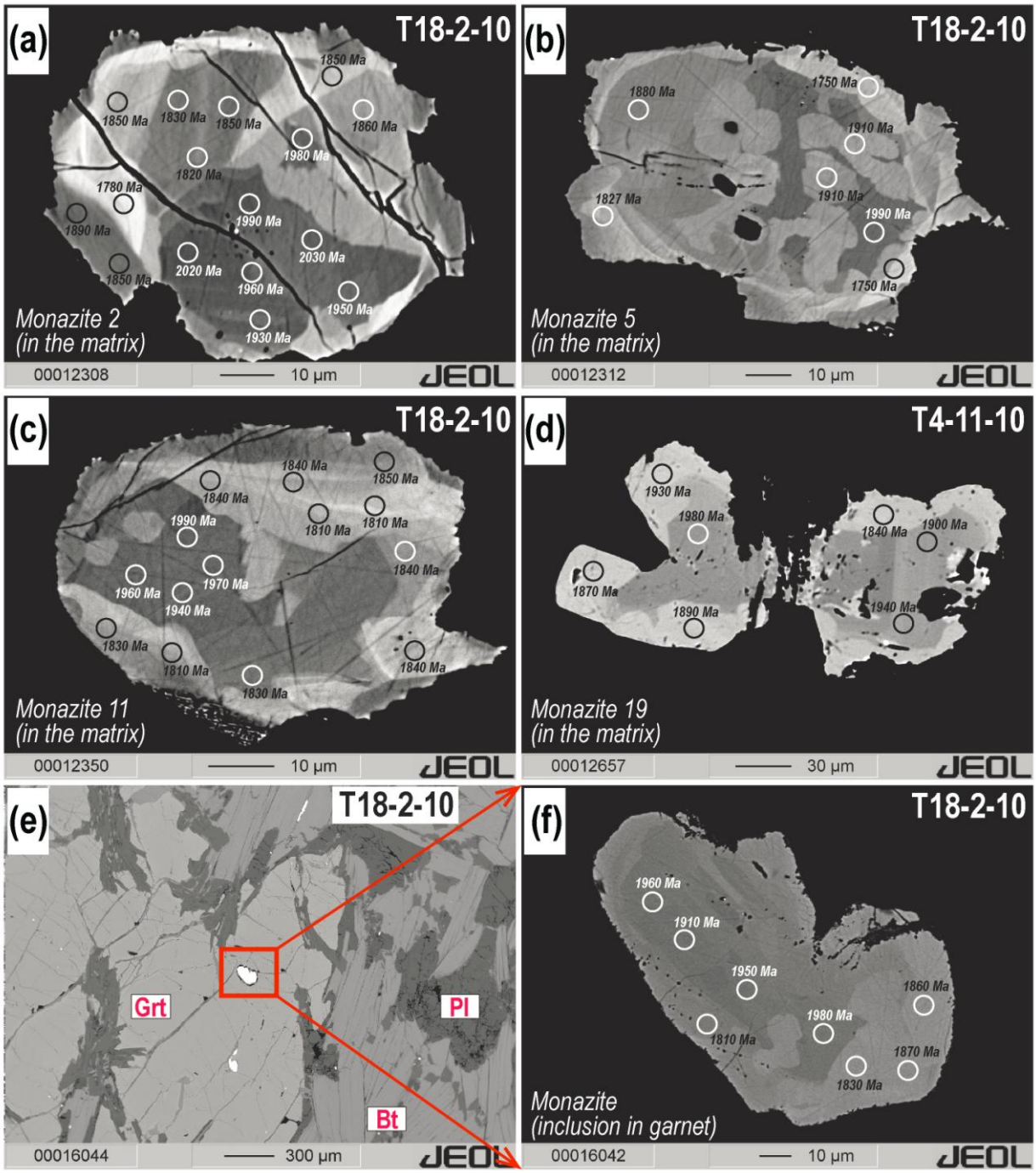

Fig. 2.9 Backscatter images of monazite grains from the Ikulu metapelites showing microtextures and the correlation of growth zones with the temporal evolution. (a – d) Complex, simple and patchy zoned monazite from the metapelite matrix (e) BSE image of garnet from a metapelite with monazite inclusions (e.g., bright white grain in red box) (f) Monazite inclusion in garnet showing both simple and patchy zoning.

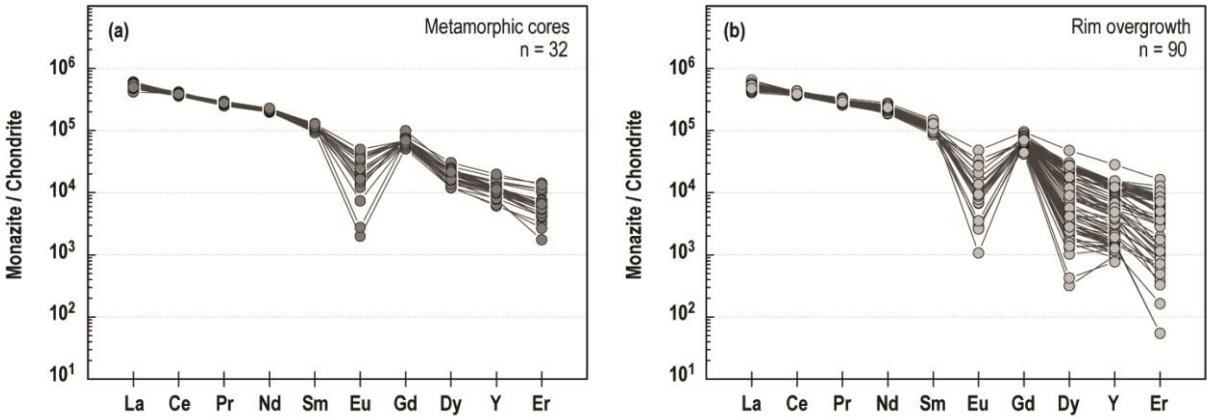

Fig. 2.10 Chondrite-normalised rare earth elements and Y patterns of monazite from metapelites; whereas LREE and Eu patterns in monazite cores and overgrown rims are similar, overgrown rims are relatively depleted in HREEs and Y compared to that in the cores.

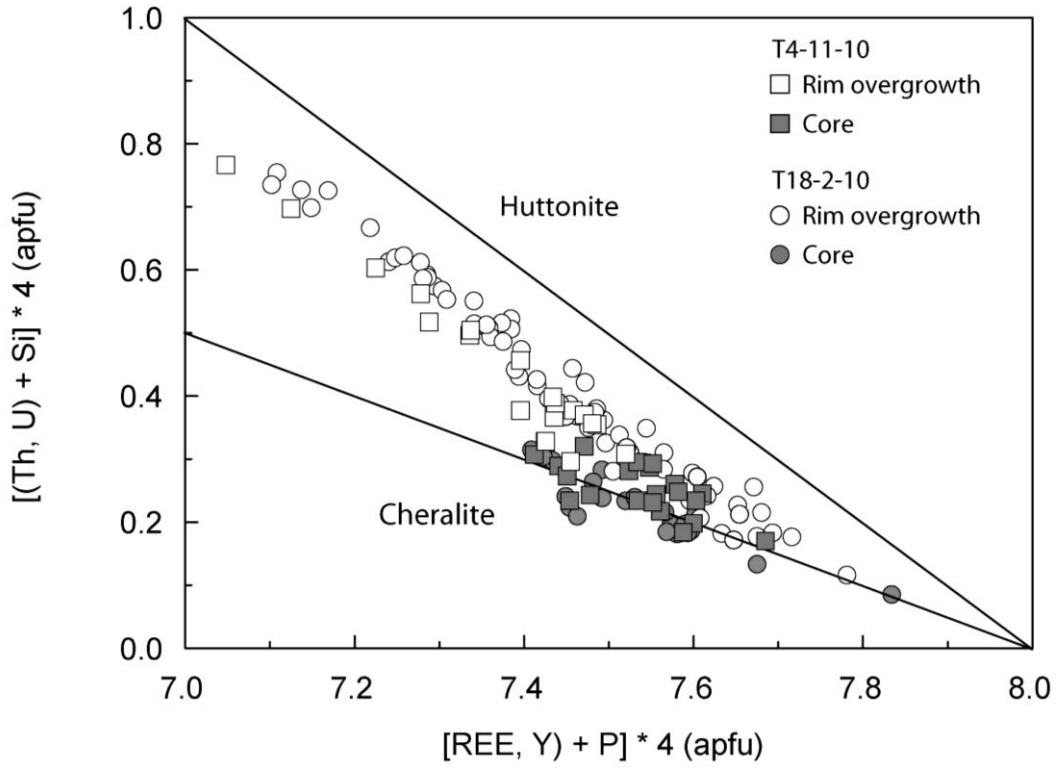

Fig. 2.11 Plot of ((Th, U) + Si) *4 vs. ((REEs, Y) + P)*4 showing cheralite and huttonite vectors for monazite core and rim analyses of sample T18-2-10 and T4-11-10.

5.2 In situ U-Th-total Pb dating of monazite

Dating of the core domains of monazite grains in the matrix and of inclusions in garnet yielded apparent ages in the range of 2030–1910 Ma and those of the overgrown rims in the range

1890–1790 Ma (Fig. 2.9a-f), which are more than 100 Ma younger than those of the core domains. For the core domains of the monazite grains in the garnet bearing sample (T18-2-10) the dating yielded weighted mean ages of 1957 ± 10 Ma, whereas the overgrown rims yielded an age of 1837 ± 6 Ma (Fig. 2.12a). Similarly, the cores of the cordierite bearing sample gave an age of 1967 ± 16 Ma and the rims of 1848 ± 17 Ma (Fig. 2.12b). This means that the core and rim ages of both metapelite samples are identical within errors and that the sediments in the Katuma Block experienced two metamorphic events that were separated by about 120 Ma.

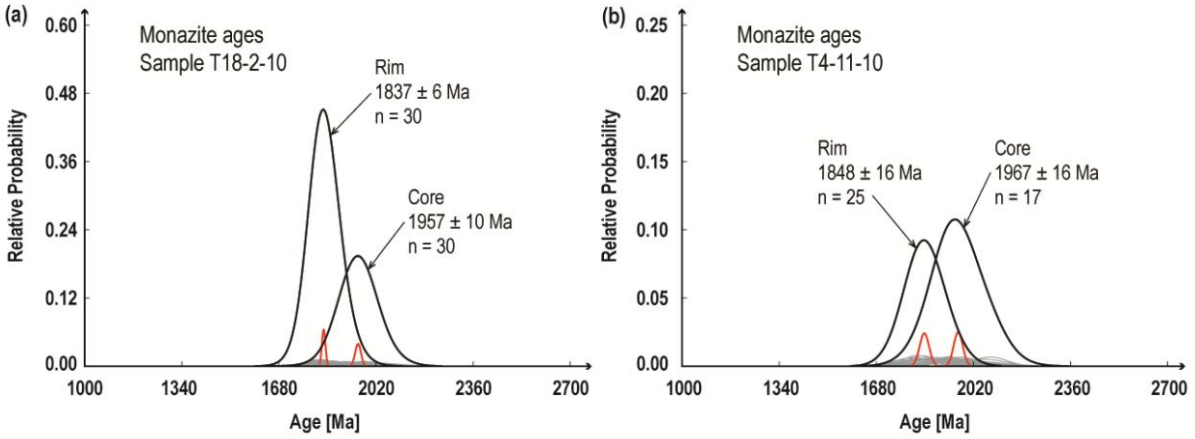

Fig. 2.12 Monazite age histograms: the tall black curves are summative curves of the dates of each age population, and the red curves are the weighted mean ages (2σ error) of the age populations. (a) Metamorphic ages of sample T18-2-10 (b) Metamorphic ages of sample T4-11-10.

6. Discussion

6.1 P-T evolution and timing of the granulite-facies metamorphism in the Katuma Block

In this paper we have presented petrological data of metabasites and of metapelites of the Katuma Block, which record contrasting P-T evolutions. Metamorphic monazite ages have only been obtained from metapelitic rocks showing two metamorphic events in Paleoproterozoic time, whereas for the metamorphism of the mafic rocks no age data are available due to the lack of monazite and as zircon of the mafic rocks did not show overgrown metamorphic rims (Kazimoto et al., in review-b). The correlation of the contrasting petrological P-T data with the radiometric ages is not straight forward, as additional U-Pb zircon ages that are available for the rocks of the Katuma Block indicate that this block experienced four metamorphic events in Archean and Paleoproterozoic times (Kazimoto et al., in review-b). Thermobarometric calculations and pseudosection modelling of the metabasites indicate that the granulite-facies reactions textures replacing the magmatic mineral assemblages occurred at 8.9–6.5 kbar and

790–700 °C. The replacement of the magmatic orthopyroxene and plagioclase by coronas containing garnet-clinopyroxene-quartz-hornblende document a near-isobaric cooling path in the deep crust. In the absence of a preserved prograde metamorphic evolution in the mineralogy of the rocks we ascribe the granulite-facies corona forming stage to the post-magmatic cooling after the intrusion of mafic melts into the deep crust. As the magmatic crystallization ages of the zircon grains in these rocks are about 2.65 Ga, the metamorphic mineral assemblages may have developed in late Archean or early Proterozoic time.

In metapelites, the common occurrence of cm-sized prismatic sillimanite pseudomorphs after kyanite provides evidence for two stages of the metamorphic evolution. The early stage occurred in the P-T stability field of kyanite, whereas the subsequent peak-metamorphism was associated with anatexis and is characterised by the development of Grt-Sil-Kfs and Crd-Sil-Kfs bearing assemblages. The strong pressure decrease after peak metamorphism points to a crustal collisional event preceding the isothermal uplift. Without the information of radiometric ages obtained by texturally controlled monazite dating the petrological data could easily be interpreted to reflect a single phase clockwise P-T evolution during a collisonal event. However, the two ages obtained from monazite grains of these rocks are separated by about 120Ma and therefore cannot be correlated with a single clockwise P-T path. As the two growth zones of monazite grains that preserved the two ages, at about 1960 Ma and 1840 Ma, occur in the rock matrix and as inclusions in garnet porphyroblasts, garnet should have grown during or after the second growth phase of the monazite grains. This interpretation is supported by the stronger depletion of Y and HREE in the overgrown rims compared to the cores (Fig. 2.10a and b), reflecting their growth in equilibrium with garnet (Foster and Parrish, 2003; Spear and Pyle, 2002). The growth of the core zones that do not show the strong Y and HREE depletion are tentatively attributed to the kyanite stage of the metamorphic evolution, when garnet was absent or present in only small amounts.

6.2 Metamorphic events and crustal evolution in the Ubendian Belt

The petrologically identified contrasting P-T evolutions for the Neoarchean metabasites and the overlying metasediments and the new monazite ages of the metamorphic events will be combined with already published zircon ages and geochemical data (Kazimoto et al., in review) to develop a geodynamic evolution model for the NW Ubendian Belt (Fig. 13). The recorded evolution of rocks in the Katuma Block began in the Neoarchean (2.71 and 2.64 Ga) by their magmatic formation in an active continental margin setting (Tanzania Craton) as evidenced by

the trace element characteristics of metabasites and orthogneisses of the Katuma Block (Kazimoto et al., in review). Metamorphic rims overgrown on zircon grains of the oldest orthogneiss (≈ 2.71 Ga) suggest that this period was also associated with a metamorphism of older magmatic rocks at ca. 2650 Ma, most likely related to the heat released from the magmas into this active continental margin (Fig. 13A; Harley, 1989; Lucassen and Franz, 1996). This Neoarchean metamorphic event (ca. 2650 Ma) is further documented by schistose xenoliths of garnet amphibolites included in an unmetamorphosed gabbronorite dated at 2643 ± 4 Ma. Detrital zircon cores in metasediments (calc-silicate rocks and metapelites), provide ages between 2680 Ma and 2050 Ma, indicating that sedimentation of the Ikulu sediments followed the Neoarchean magmatic crust formation period (Kazimoto et al., in review). The lower age limit for the sedimentation is constrained by the age of the first metamorphism of the metasediments at about 1970 Ma and by the youngest detrital cores at 2050 Ma (Fig. 13B). The similarity of U-Pb ages obtained from detrital zircon of the metasediments and the zircon from orthogneisses and metabasites implies that the magmatic rocks of the Katuma Block could well be the source of the sediments. The isobaric cooling deduced from reaction textures in the Neoarchean Katuma metabasites reflect a time of geodynamic quiescence, which we attribute to a passive continental margin stage, when the Ikulu sediments were deposited on the passive continental margin (2.65–2.05Ga; Fig 13B).

A younger phase of calc-alkaline magmatism including metabasites and granitoids has been dated between 2020 Ma and 1940 Ma (Kazimoto et al., in review). This magmatic period was concomitant to deformation and migmatization of the Neoarchean Katuma orthogneisses dated at about 2050–2030 Ma (U-Pb zircon in leucosome) and unfoliated granitoids dykes (~ 1990–1950 Ma) that cut the migmatites. Deformation and granulite metamorphism at about 2100–2000 Ma was already recognized by Cahen et. al. (1966), McConnell (1969), Lenoir et al. (1994b) and Ring et al. (1997), who interpreted the event as the onset of the Ubendian orogeny. In our model, we attribute this event to an active continental margin stage (Fig. 13C). U-Pb ages of metamorphic growth zones on zircon grains of metasediments dates the metamorphism of the precursor sediments at about 1960–1940 Ma culminating with migmatization (Kazimoto et al., in review). This age is in agreement with monazite ages of about 1960 Ma reported in this study. Similar ages of metamorphism (2050–1940 Ma) have been reported elsewhere in the Ubendian Belt (Boniface, 2009b; Boniface et al., 2012; Lawley et al., 2013c; Lawley et al., 2013d; Ring et al., 1997), which points to a common geodynamic evolution in an active continental margin setting during the formation of the Ubendian Belt.

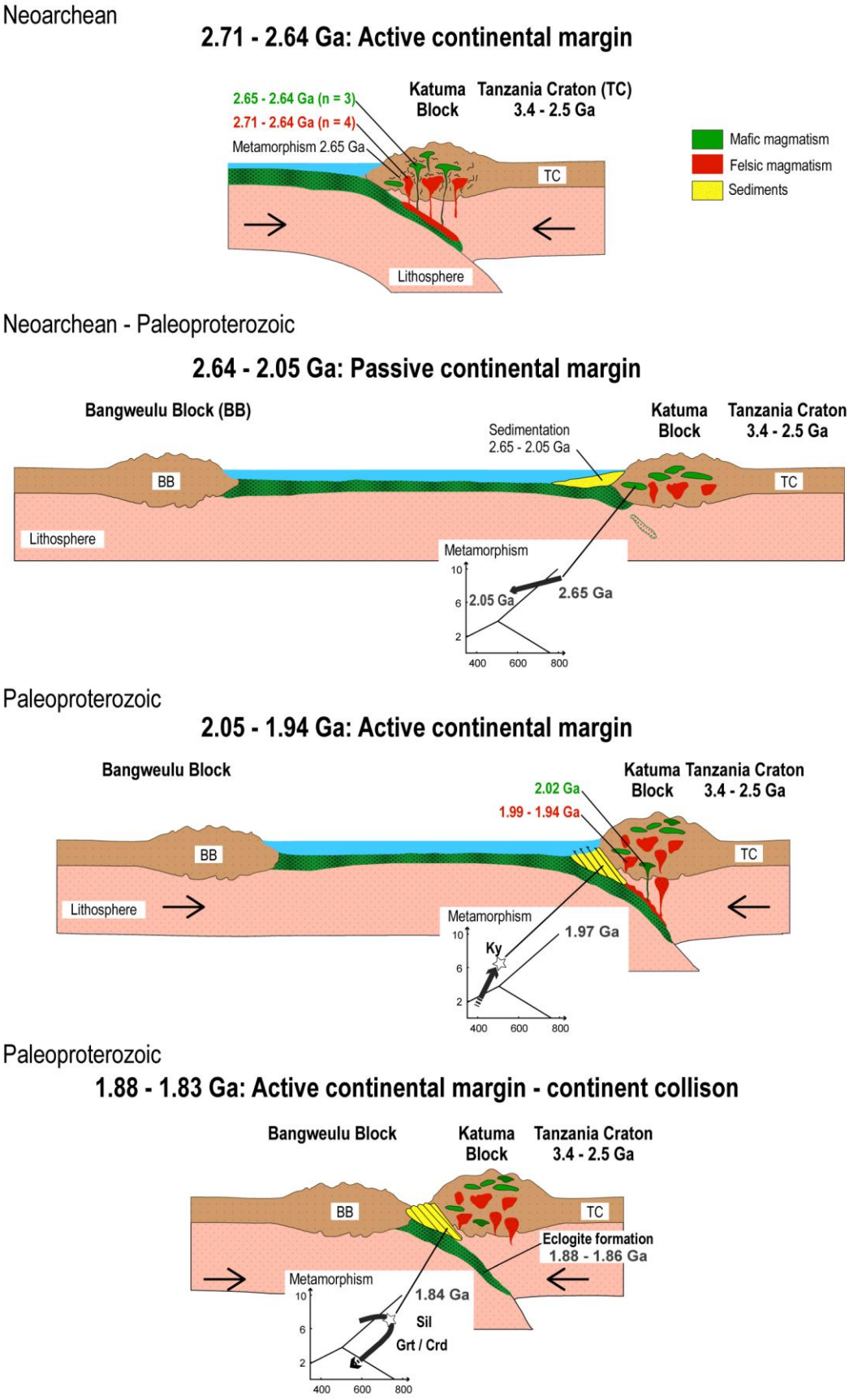

Fig. 2.13 Geological sketches showing a model the most likely scenario for the geologic evolution of the northwestern Ubendian Belt of Tanzania.

The relatively young Ms-Bt granite (1940 Ma) with a gneissic fabric containing zircon grains with metamorphic overgrowths indicate that at 1880 Ma pre-existing older Paleoproterozoic rocks were metamorphosed (Kazimoto et al., in review). This metamorphic event is also attested by Pb-loss recognized in Neoarchean and Paleoproterozoic magmatic zircon grains of metabasites and orthogneisses. The age of about 1840 Ma found in the outer rims of monazite grains included in metapelitic garnet porphyroblasts dates a crustal thickening event. This crustal thickening post dates the formation of MORB-type eclogites in the northern Ubendian Belt at ca. 1880–1860 Ma (Boniface et al., 2012). Similar metamorphic ages (ca. 1840–1810 Ma) for a crustal thickening event have already been reported elsewhere in the Ubendian belt for high-grade metamorphism (Boniface, 2009b; Boniface et al., 2012).

7. Conclusion

In this paper we have presented a first detailed model of the geological evolution of the linear Paleoproterozoic Ubendian Belt situated between the Archean Tanzania Craton and the Bangwelu Block. The model includes Neoarchean crust formation and several Paleoproterozoic metamorphic events.

The Ubendian Belt contains Neoarchean magmatic rocks formed about 2.74–2.64 Ga ago (Kazimoto et al., in review-b; Lawley et al., 2013a), forming an active continental margin of the Tanzania Craton, which is evidenced by the geochemical similarities of the Neoarchean Ubendian rocks and those of present magmatic arcs. The heat released from the Archean arc magmas caused a first metamorphism of the crust at about 2650 Ma.

The granulite-facies corona assemblages in metabasites consisting of garnet, clinopyroxene, hornblende and quartz replacing magmatic orthopyroxene and plagioclase suggest a tectonically quite period, during which the rocks cooled under near isobaric conditions subsequent to their magmatic formation. This period is interpreted as a passive continental margin stage during which the sediments of the Katuma Block, displaying detrital zircon ages of 2640–2050 Ma, have been deposited.

U-Pb magmatic zircon crystallization ages of mafic and felsic calc-alkaline rocks (2050–1940 Ma) reflect a second period of intense magmatic activity related to oceanic lithosphere subduction at an again active continental margin. This active continental margin stage is also recorded by a protracted period of metamorphism and deformation between 2050

Ma and 1840 Ma, indicating that subduction of oceanic crust at this margin lasted for about 200Ma.

The final collision and crustal thickening at about 1840 Ma between the Bangweulu and the Katuma Block led to the crystallization of sillimanite, cordierite and garnet porphyroblasts in metapelites at about 1840 Ma as indicated by the age of monazite inclusions in garnet porphyroblasts. This event also was responsible for the exhumation of 1880–1860 Ma eclogites representing the subducted ocean crust.

Acknowledgements

This work was supported by funds from the Ministry of Education and Vocational Training of Tanzania (MOEVT) and the German Academic Exchange Service (DAAD). We are grateful to the University of Dar es Salaam for financial support of the fieldwork through the Sida Earth Science Project. We would like to thank Andreas Fehler and Barbara Mader for their support during the thin sections preparations and microprobe analyses.

References

Appel, P., 2010. “AgeFinder”: A Mac OS X computer program to evaluate electron microprobe data of monazite for chemical age dating. Computers & Geosciences 36, 559-563.

Armstrong, J.T., 1995. CITZAF: A package of correction programs for the quantitative electron microbeam X-ray analysis of thick polished materials, thin films, and particles. Microbeam analysis-Deerfield Beach- 4, 177-200.

Baldwin, J.A., Powell, R., Brown, M., Moraes, R., Fuck, R.A., 2005. Modelling of mineral equilibria in ultrahigh-temperature metamorphic rocks from the Anápolis-Itauçu Complex, central Brazil. Journal of Metamorphic Geology 23, 511-531.

Berman, R.G., 1988. Internally-consistent thermodynamic data for minerals in the system Na2O-K2O-CaO-MgO-FeO-Fe2O3-Al2O3-SiO2-TiO2-H2O-CO2. Journal of Petrology 29, 445-522.

Biyashev, M., Pentelkov, V., Emelyanov, S., Chuklanov, B., Stepnov, E., Matrenitzky, T., Novikov, A., 1977. Sitalike: Geological Map Quarter Degree Sheet 170. Geological Survey of Tanzania, Dodoma.

Boniface, N., 2009. Eburnean, Kibaran and Pan-African metamorphic events in the Ubendian belt of Tanzania: Zircon and Monazite geochronology, Department of Geosciences. University of Kiel, Kiel, p. 110.

Boniface, N., Schenk, V., 2012. Neoproterozoic eclogites in the Paleoproterozoic Ubendian Belt of Tanzania: Evidence for a Pan-African suture between the Bangweulu Block and the Tanzania Craton. Precambrian Research 208-211, 72-89.

Boniface, N., Schenk, V., Appel, P., 2012. Paleoproterozoic eclogites of MORB-type chemistry and three Proterozoic orogenic cycles in the Ubendian Belt (Tanzania): Evidence from monazite and zircon geochronology , and geochemistry. Precambrian Research 192-195, 16-33.

Boniface, N., Schenk, V., Appel, P., 2014. Mesoproterozoic high-grade metamorphism in pelitic rocks of the northwestern Ubendian Belt: Implication for the extension of the Kibaran intra-continental basins to Tanzania. Precambrian research.

Braun, I., Appel, P., 2006. U-Th-total Pb dating of monazite from orthogneisses and their ultra-high temperature metapelitic enclaves: implications for the multistage tectonic evolution of the Madurai Block, southern India. European Journal of Mineralogy 18, 415-427.

Cahen, L., Snelling, N.J., Delhal, J., Vail, J., 1966. The Geochronology and evolution of Africa.

Coggon, R., Holland, T.J.B., 2002. Mixing properties of phengitic micas and revised garnet-phengite thermobarometers. Journal of Metamorphic Geology 20, 683-696.

Coulson, I., Dipple, G.M., Raudsepp, M., 2001. Evolution of HF and HCl activity in magmatic volatiles of the gold-mineralized Emerald Lake pluton, Yukon Territory, Canada. Mineralium Deposita 36, 594-606.

Daly, M.C., 1988. Crustal Shear Zones in Central Africa: a kinematic approach to Proterozoic Tectonics. Episodes 11, 5-11.

De-Capitani, C., Petrakakis, K., 2010. The computation of equilibrium assemblage diagrams with Theriak/Domino software. American Mineralogist 95, 1006-1016.

Delvaux, D., 2001. Karoo rifting in western Tanzania: precursor of Gondwana breakup. Geology and paleontology of Gondwana in honor of Helmut Wopfner, 111-125.

Eckert, J.O., Newton, R.C., Kleppa, O.J., 1991. The H of reaction and recalibration of garnet-pyroxene-plagioclase-quartz geobarometers in the CMAS system by solution calorimetry. American Mineralogist 76, 148-160.

Ellis, D.J., Green, D.H., 1979. An experimental study of the effect of Ca upon garnet-clinopyroxene Fe-Mg exchange equilibria. Contributions to Mineralogy and Petrology 22, 13-22.

Foster, G., Parrish, R.R., 2003. Metamorphic monazite and the generation of P-T-t paths. Geological Society, London, Special Publications 220, 25-47.

Graham, C.M., Powell, R., 1984. A garnet-hornblende geothermometer : calibration, testing, and application to the Pelona Schist, Southern California. Journal of Metamorphic Geology 2, 13-31.

Harley, S.L., 1989. The origins of granulites: a metamorphic perspective. Geological Magazine 126, 215-247.

Harlov, D.E., Wirth, R., Hetherington, C.J., 2010. Fluid-mediated partial alteration in monazite: the role of coupled dissolution–reprecipitation in element redistribution and mass transfer. Contributions to Mineralogy and Petrology 162, 329-348.

Holland, T.J.B., Powell, R., 1998. An internally consistent thermodynamic data set for phases of petrological interest. Journal of metamorphic Geology, 309-343.

Jarosewich, E., Boatner, L.A., 1991. Rare-Earth-Elements Reference Samples for Electron Microprobe analysis. Geostandards Newsletter 15, 397-399.

Jöns, N., Schenk, V., 2011. The ultrahigh temperature granulites of southern Madagascar in a polymetamorphic context: implications for the amalgamation of the Gondwana supercontinent. European Journal of Mineralogy 23, 127-156.

Jöns, N., Schenk, V., Appel, P., Razakamanana, T., 2006. Two-stage metamorphic evolution of the Bemarivo Belt of northern Madagascar: constraints from reaction textures and in situ monazite dating. Journal of Metamorphic Geology 24, 329-347.

Kazimoto, E.O., Schenk, V., Appel, P., in review-a. The age of Au-Cu-Pb bearing veins in the poly orogenic Ubendian Belt (Tanzania): U Th total Pb dating of hydrothermally altered monazite. Contributions to Mineralogy and Petrology.

Kazimoto, E.O., Schenk, V., Berndt, J., in review-b. Neoarchean crust formation in the Paleoproterozoic Ubendian Belt, Tanzania: insights from zircon geochronology and geochemistry. Precambrian Research.

Kohn, M.J., Spear, F.S., 1990. Two new geobarometers for garnet amphibolites, with applications to southeastern Vermont. American Mineralogist 75, 89-96.

Koziol, A.M., Newton, R.C., 1988. Redetermination of the anorthite breakdown reaction and improvement of the geobarometer. American Mineralogist 73, 216-223.

Large, R.R., Allen, R.L., Blake, M.D., Herrmann, W., 2001. Hydrothermal alteration and volatile element halos for the Rosebery K lens volcanic-hosted massive sulfide deposit, western Tasmania. Economic Geology 96, 1055-1072.

Lawley, C.J.M., Selby, D., Condon, D.J., Horstwood, M., Millar, I., Crowley, Q., Imber, J., 2013a. Lithogeochemistry, geochronology and geodynamic setting of the Lupa Terrane, Tanzania: Implications for the extent of the Archean Tanzanian Craton. Precambrian Research 231, 174-193.

Lawley, C.J.M., Selby, D., Condon, D.J., Imber, J., 2013b. Palaeoproterozoic orogenic gold style mineralization at the Southwestern Archaean Tanzanian cratonic margin, Lupa Goldfield, SW Tanzania: Implications from U–Pb titanite geochronology. Gondwana Research.

Lawley, C.J.M., Selby, D., Imber, J., 2013c. Re-Os Molybdenite, Pyrite and Chalcopyrite Geochronology, Lupa Goldfield, Southwestern Tanzania: Tracing Metallogenic Time Scales at Midcrustal Shear Zones Hosting Orogenic Au Deposits. Economic Geology 108, 1591-1613.

Leake, B.E., Woolley, A.R., Arps, C.E.S., Birch, W.D., Hawthorne, F.C., Kato, A., Kisch, H.J., Gurion, B., Krivovichev, V.G., Laird, J., Mandarino, J.A., Maresch, W.V., Nickel, E.H., Rock, N.M.S.N.M.S., Schumacher, J.C., Smith, D.C., Stephenson, N.C.N., Ungaretti, L., Whittaker, E.J.W., Youzhi, G., Gilbert, M.C., Grice, J.D., Linthout, K., Nicholaus, M.S., 1997. Nomenclature of amphiboles; report of the Subcommittee on Amphiboles of the

International Mineralogical Association Commission on new minerals and mineral names. The Canadian Mineralogist 35, 219-246.

Lenoir, J.L., Liegeois, J.P., Theunissen, K., Klerkx, J., Liégeois, J.P., 1994. The Palaeoproterozoic Ubendian shear belt in Tanzania: geochronology and structure. Journal of African Earth 19, 169-184.

Lucassen, F., Franz, G., 1996. Magmatic arc metamorphism: petrology and temperature history of metabasic rocks in the Coastal Cordillera of northern Chile. Journal of metamorphic Geology 14, 249-265.

Maloof, T.L., Baker, T., Thompson, J.F.H., 2001. The Dublin Gulch intrusion-hosted gold deposit, Tombstone plutonic suite, Yukon Territory, Canada. Mineralium Deposita 36, 583-593.

McConnell, R.B., 1969. The association of granites with zones of stress and shearing. Geological Society of America Bulletin 80, 115-120.

Morimoto, N., Faries, J., Ferguson, A.K., Ginzburg, I.V., Ross, M., Seifert, F.A., Zussman, J., Aoki, K., Gottardi, G., Fabries, J., Gizburg, I.V., 1988. Nomenclature of pyroxenes. Mineralogy and Petrology 39, 55-76.

Newton, R.C., Perkins, D., 1982. Thermodynamic calibration of geobarometers based on the assemblages garnet-plagioclase-orthopyroxene (clinopyroxene)-quartz. American Mineralogist 67, 203-222.

Perchuk, L.L., Aranovich, L.Y., Podlesskii, K.K., Lavrant'Eva, I.V., Gerasimov, V.Y., Fed'Kin, V.V., Kitsul, V.I., Karsakov, L.P., Berdnikov, N.V., 1985. Precambrian granulites of the Aldan shield, eastern Siberia, USSR. Journal of Metamorphic Geology 3, 265-310.

Powell, R., 1985. Regression diagnostics and robust regression in geothermometer/geobarometer calibration: the garnet-clinopyroxene geothermometer revisited. Journal of Metamorphic Geology 3, 231-243.

Ring, U., Kröner, A., Toulkeridis, T., 1997. Palaeoproterozoic granulite-facies metamorphism and granitoid intrusions in the Ubendian-Usagaran Orogen of northern Malawi, east-central Africa. Precambrian Research 85, 27-51.

Schenk, V., 1984. Petrology of felsic granulites, metapelites, metabasics, ultramafics, and metacarbonates from Southern Calabria (Italy): prograde metamorphism, uplift and cooling of a former lower crust. Journal of Petrology 25, 255-298.

Semyanov, A., Kireev, A., Doronkin, I., Gavrilov, G., Matrenitzky, T., Novicov, A.G., 1977. Mpanda: Geological Map Quarter Degree Sheet 153. Geological Survey of Tanzania, Dodoma.

Smirnov, V., Shulyatin, O., Tolochko, V., Zhukov, S., Mwakisunga, M., Matrenitzky, T., 1970. Katuma: Geological Map Quarter Degree Sheet 152. Ministry of Energy and Minerals.

Spear, F.S., Pyle, J.M., 2002. Apatite, Monazite, and Xenotime in Metamorphic Rocks. Reviews in Mineralogy and Geochemistry 48, 293-335.

Wan, B., Hegner, E., Zhang, L., Rocholl, A., Chen, Z., Huayingwu, Chen, F., Wu, H., 2009. Rb-Sr geochronology of chalcopyrite from the Chehugou porphyry Mo-Cu deposit (Northeast China) and geochemical constraints on the origin of hosting granites. Economic Geology 104, 351-363.

White, R.W., Powell, R., Holland, T.J.B., 2007. Progress relating to calculation of partial melting equilibria for metapelites. Journal of Metamorphic Geology 25, 511-527.

Chapter 3

The age of Au-Cu-Pb bearing veins in the poly orogenic Ubendian Belt (Tanzania): U-Th-total Pb dating of hydrothermally altered monazite

Abstract

The age of gold-copper-lead mineralization in the Katuma Block of the Ubendian Belt remains controversial because of the lack of radiometric ages that correlate with the age of tectonothermal events of this poly-orogenic belt. Previous studies reported whole rock and mineral Pb-Pb ages ranging between 1660 Ma and 720 Ma. In this study, we report U-Th-total Pb ages of monazite from hydrothermally altered metapelites that host the Au-Cu-Pb bearing veins. Three types of chemically and texturally distinct monazite grains or zones of grains were identified: monazite cores, which yielded a metamorphic age of 1938 ± 11 Ma (n=40), corresponding to known ages of a regional metamorphic event, deformation and granitic plutonism in the belt; metamorphic overgrowths that date a subsequent metamorphic event at 1827 ± 10 Ma (n=44) that postdates known eclogite metamorphism (at ca. 1880 Ma) in the belt; hydrothermally altered monazite, representing the third type of monazite, constrain the age of a hydrothermal alteration event at 1171 ± 17 Ma (n=19). This Mesoproterozoic age of the hydrothermal alteration coincides with the first amphibolite grade metamorphism of metasediments in the Wakole Block, which adjoins with a tectonic contact the vein bearing Katuma Block to the southwest. The obtained distinct monazite ages not only constrain the ages of metamorphic events in the Ubendian Belt, but also provide a link between the metamorphism of the Wakole metasediments and the generation of the hydrothermal fluids responsible for the formation of the gold copper lead veins in the Katuma Block.

1. Introduction

Despite many attempts and its importance in exploration dating of hydrothermal gold mineralization in orogenic belts is still a challenge due to the scarcity of minerals formed during mineralization that are suitable for dating. Additional difficulties for dating arise from the fact that mineralized zones are formed by multiple episodes of mineralization and post-depositional hydrothermal alterations; this results in a wide range of scattering dates. Attempts to date mineralization events using hydrothermally altered minerals of the adjoining country rocks may also result in ambiguous, mixed ages due to incomplete resetting of the applied isotopic systems. The geochronological methods used to date mineralization include $^{40}Ar/^{39}Ar$ dating of hydrothermal minerals (e.g., adularia, biotite, K-feldspar and white mica) and mica inclusion in hydrothermal sulfides (Phillips and Miller 2006), Re-Os dating of sulfide minerals (e.g., molybdenite, arsenopyrite, pyrite and chalcopyrite) associated with gold mineralization (Arne et al. 2001; Lawley et al. 2013b; Selby et al. 2002; Stein 2001), Pb-Pb dating of hydrothermal sulfides (Frei and Pettke 1996) and U-Pb and Pb-Pb dating of hydrothermally formed zircon and monazite (Davis et al. 1994; Hu et al. 2004; Kerrich and Kyser 1994; Rasmussen et al. 2006; Vielreicher et al. 2003).

Knowledge of the age of mineralization or of a hydrothermal event is a prerequisite to understanding its relation to the tectonic, magmatic or metamorphic events during an orogenic cycle. The formation of hydrothermal deposits is often coeval with the accretion of tectonic terranes and therefore, on a global scale, is often related to the amalgamation of supercontinents (Barley and Groves 1992; Kerrich and Cassidy 1994). In addition to this coeval mineralization, Kerrich and Cassidy (1994) noted that some vein deposits are up to 250 Ma younger than the primary orogenic events and seem not to be related to the orogenic evolution. The different age relationships between the mineralization and the orogenic evolution have been referred to as “early gold” and “late gold” models.

The Paleoproterozoic Ubendian Belt contains two orogenic gold deposits (Goldfarb et al. 2001): one in the Lupa Block (Lawley et al. 2013c; Lawley et al. 2013b; Lawley et al. 2013d) and a second the Mpanda mineral field in the Katuma Block (Fig. 3.1a & b). Attempts to date the Mpanda gold mineralization with the Pb-Pb method used galena, chalcopyrite, pyrite and Cu-Au oxidized ores, which resulted in a wide range of ages between 1660 Ma and 720 Ma (Cahen et al. 1966; Nanyaro 1989; Stendal et al. 2004). This range indicates that the mineralization in Mpanda cannot be regarded as an “early gold” mineralization with respect to the Paleoproterozoic orogenic evolution of the belt. Stendal et al. (2004), first classified this mineralization event as late gold of post-Paleoproterozoic age, using the Pb-Pb isotope

compositions of whole rocks and sulfides. According to these authors, the mineralization was contemporaneous with the emplacement of a alkali granite and the Sangu-Ikola carbonatite (ca. 720 Ma) within the Ubendian Belt.

In recent studies, it has been recognized that the Ubendian Belt, which was formerly interpreted as an entirely Paleoproterozoic Belt (Daly 1988; Lenoir et al. 1994), was affected by three orogenic cycles: the Paleoproterozoic Ubendian, the Mesoproterozoic Kibaran and the Neoproterozoic Pan-African events (Boniface and Schenk 2012; Boniface 2009; Boniface et al. 2012). These events did not affect the entire Ubendian Belt with the same intensity but were, in part, localized. For example, the Mesoproterozoic event affected only the northern parts of the belt north of a Neoproterozoic suture (Boniface 2009; Boniface et al. 2012). In view of these new findings, the interpretation of the origin of the Mpanda gold mineralization, its age and its correlation with the complex orogenic evolution of the Ubendian Belt warrants re-evaluation.

In the present study we dated a mineral that formed or recrystallized during the hydrothermal mineralization event. We employed electron microprobe U-Th-total Pb dating of hydrothermally altered monazite present in hydrothermally altered metapelites, which host the gold bearing veins. The ages of the hydrothermal veins obtained in this study are in accordance with reported ages of the first metamorphism of the precursor pelitic sediments of the adjoining Wakole Block. This result suggests that the gold mineralization in the Katuma Block occurred during the Mesoproterozoic Kibaran orogeny and lends support to an ‘early gold’ orogenic deposit model. Moreover, our study demonstrates the successful use of hydrothermally altered monazite in dating a metallic hydrothermal mineralization.

2. Geological Setting

2.1 Ubendian Belt

The Paleoproterozoic Ubendian Belt is a NW-SE trending metamorphic belt located along the southwest margin of the Archean Tanzania Craton, separating the craton from the Bangweulu Block and the Mesoproterozoic Irumide Belt to the southwest. The northern part of the belt is unconformably overlain by metamorphosed to unmetamorphosed sedimentary rocks of the Mesoproterozoic Karagwe-Ankolean Belt and the Meso- to Neoproterozoic Bukoban Supergroup (Fig. 3.1a). The belt has been subdivided into eight lithologically distinct blocks, namely the Ubende, Wakole, Katuma, Ufipa, Mbozi, Lupa, Upangwa and Nyika Blocks (Fig. 3.1a), which are separated by NW–SE trending zones of mylonite, ultra-mylonite and gouge that exhibit a dextral sense of shear (Daly 1988).

The Ubendian Belt is associated with a complex structural and metamorphic history that spans from the Paleoproterozoic to the Neogene; therefore, the belt has been considered to be a crustal zone of a persistent structural weakness (Boven et al. 1999; Kilembe and Rosendahl 1992; Lenoir et al. 1994; Theunissen et al. 1996; Delvaux et al. 2012).

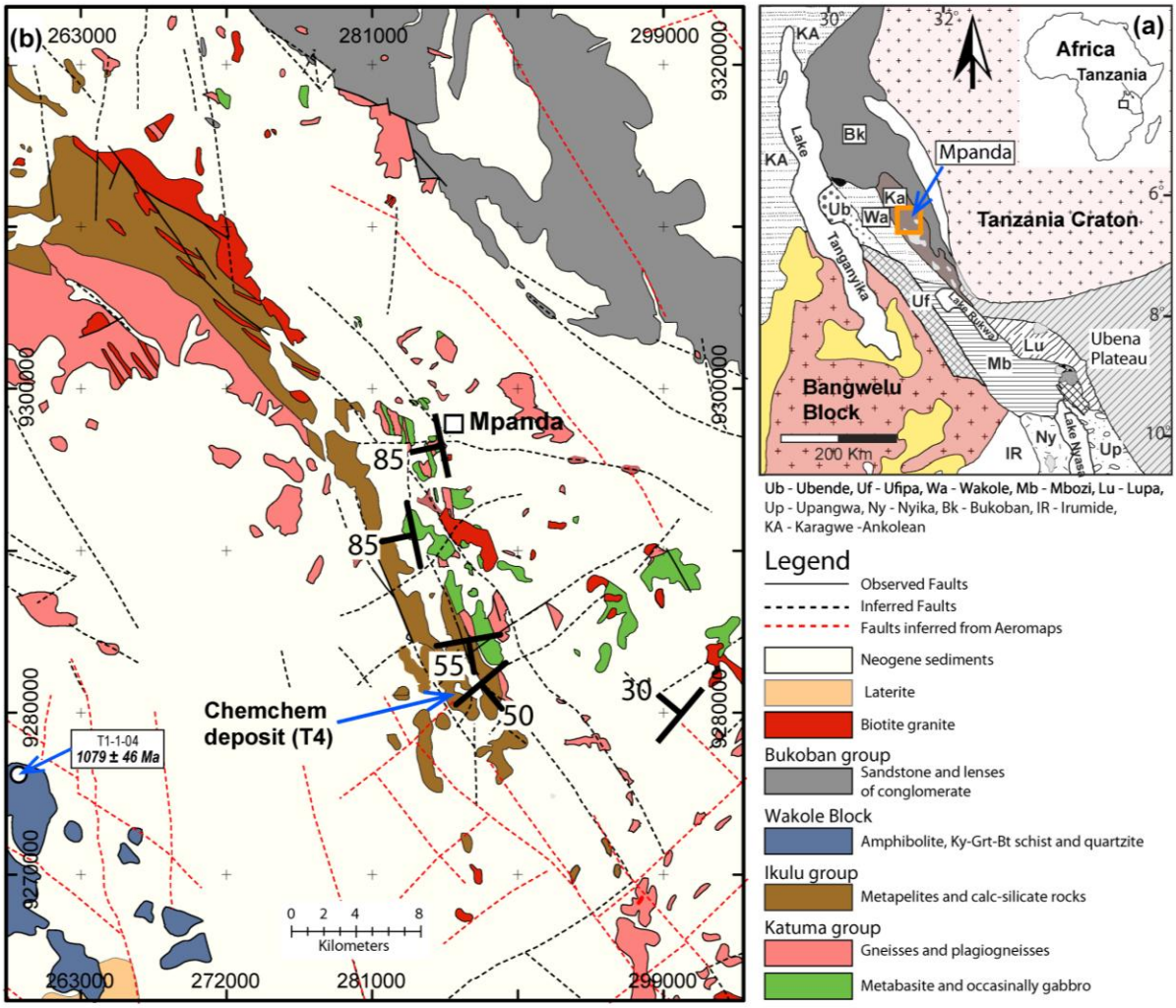

Fig. 3.1 (a) Regional geological map showing the geological setting of the Paleoproterozoic Ubendian Belt, its blocks and bordering belts (modified after Pohl, 1994 and Daly, 1988). (b) Geological map of Katuma Block modified after Biyashev et al., (1977), Semyanov et al. (1977) and Smirnov et al. (1973).

The early Paleoproterozoic tectono-thermal events have been assigned to two separate stages. The first stage (~ 2.1–2.0 Ga) is characterized by felsic and mafic magmatism and granulite facies metamorphism that was locally, along shear zones, followed by a greenschist facies overprint and an E-W striking tectonic rock fabric (Lawley et al. 2013c; Lawley et al. 2013d; Lenoir et al. 1994; Ring et al. 1997). The second stage (1.9–1.83 Ma) is associated with the formation of MORB-type eclogites, besides amphibolites and granulites, NW-SE block-

bounding shear zones and an orogenic gold deposit in the Lupa Block (Boniface et al. 2012; Lenoir et al. 1994; Lawley et al. 2013b; Lawley et al. 2013a). The Mesoproterozoic tectono-thermal events were recorded by zircon and monazite in the rocks of the blocks located in the northern part of the Ubendian Belt (Katuma, Ubende and Wakole Blocks) (Boniface 2009; Boniface et al. 2012). Only in the Wakole Block both zircon and monazite indicate that the metasediments were first metamorphosed during Mesoproterozoic events (1170 and 1010 Ma) due to crustal thickening (Boniface 2009).

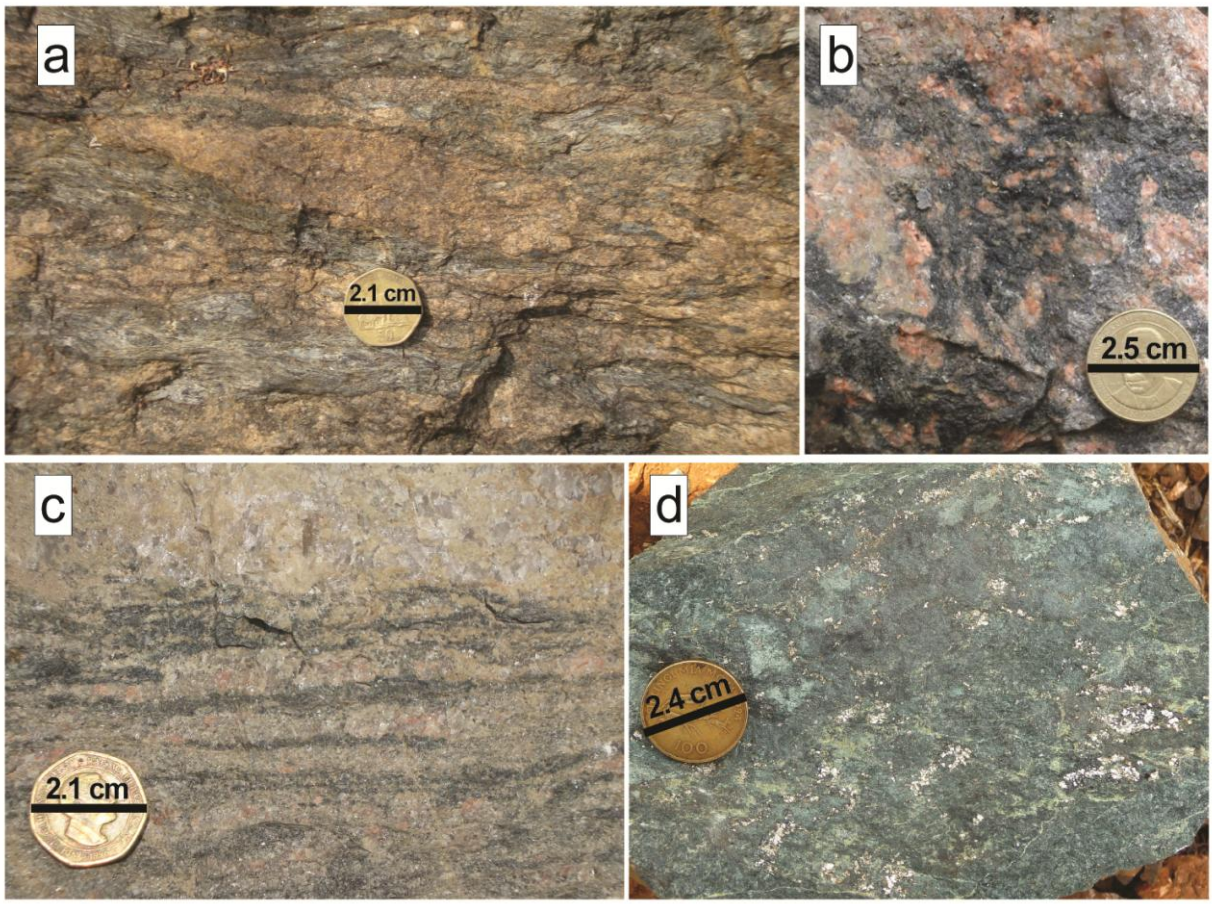

Fig. 3.2 (a) Ikulu metapelite at Chemchem mine showing mafic bands (Bt-Sil) and felsic bands (Qz-Fsp). (b) K-feldspar alteration of Ikulu metapelite adjacent to the Au-Cu bearing veins at Chemchem mine. (c) Epidote-K-feldspar-sericite alteration of Ikulu metapelite adjacent to the Au-Cu-Pb bearing veins at Chemchem mine. (d) Chlorite-epidote-pyrite alteration of amphibolite adjacent to gold bearing vein.

The eclogites with volcanic-arc type chemistry preserved in the Ufipa Block mark the location of a Neoproterozoic suture zone (ca. 590 – 520 Ma) that formed due to the amalgamation of the Gondwana supercontinent, when the Ubendian Belt was the site of volcanic-arc accretion and suturing between the Bangwelu Block and the Tanzania Craton (Boniface and Schenk 2012). The northwestern faults of the East African Rift along the Ubendian Belt suggest a young rift

related reactivation of the older Precambrian zones of weakness (Kilembe and Rosendahl 1992; Theunissen et al. 1996).

2.2 Katuma Block

The Katuma Block is located on the northern margin of the Ubendian Belt and is bounded by the Archean Tanzania Craton in the northeast, and the Wakole Block in the southwest (Fig 3.1a). The rocks in this block are divided into two groups (Fig 3.1b). The Katuma Group, for which a thickness of about 3.5 km has been estimated, is mainly composed of schistose to migmatitic orthogneisses and metabasites that are locally associated with gabbros. The Ikulu Group, which is thinner (ca. 1.4 km), unconformably overlies the Katuma Group and is composed mainly of metasedimentary rocks (Semyanov et al. 1977). Gold bearing veins cut the rocks of the Katuma and the Ikulu Group and are associated with hydrothermal alteration of the adjoining rocks, which include the formation of hydrothermal chlorite, sericite, epidote, quartz, calcite and K-feldspar (Fig. 3.2b-d). Near the gold bearing veins the host rocks are intensely silicified, sericitized and chloritized. The veins are composed of siderite, barite, quartz, K-feldspar and sulfides (primarily pyrite and chalcopyrite or/and galena), and the gold is primarily hosted in pyrite and chalcopyrite (Fig. 3.3a and b).

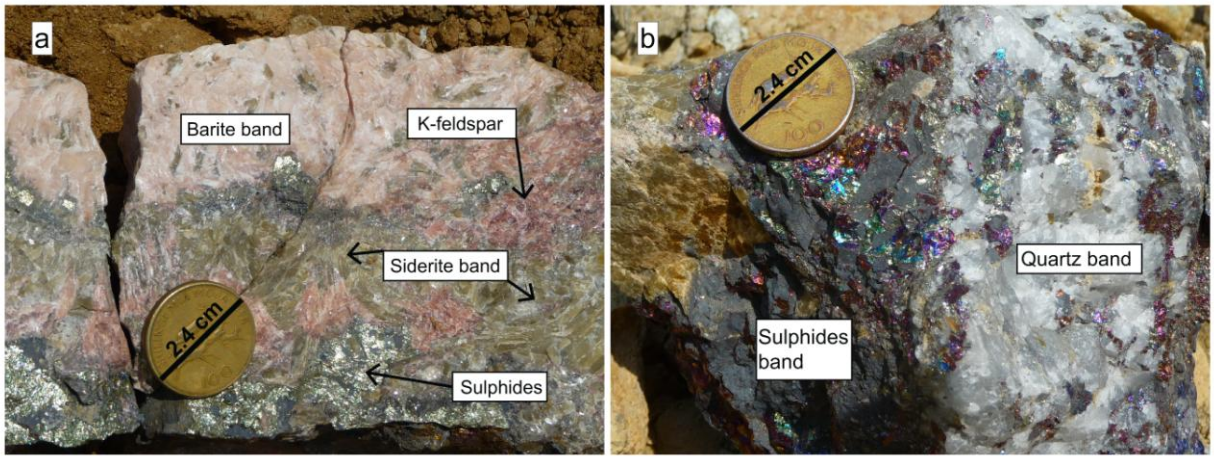

Fig. 3.3 (a) A photo of ores from Singililwa Au-Cu mine that consist of barite, K-feldspar, siderite and pyrite. (b) Another type of ore primarily composed of quartz and sulfides (pyrite and chalcopyrite).

The veins display two major orientational trends: parallel to the strike of the rocks (NW–SE) and nearly perpendicular to the strike (NE–SW and E–W) (Fig. 3.1b). The NW–SE shear and fracture zones are thought to have formed during the latest Paleoproterozoic Ubendian tectonic event (ca. 1.80 Ga; Stendal et al. 2004; Lenoir et al. 1994), whereas the E-W trending veins are

associated with the early Paleoproterozoic event (ca. 2.1–2.0 Ga) and the Neoproterozoic reactivation (Stendal et al. 2004). An interpretation of aeromagnetic data indicates primarily a structural control of the mineralized veins along the NW–SE border between the Katuma and Ikulu Group (Stendal et al. 2004)

3. Analytical methods

Samples of the Ikulu metapelites were collected adjacent to the Au-Cu-Pb bearing vein in the Chemchem Cu-Au abandoned mine in Mpanda (Fig. 3.1b). The mineral analyses and in-situ U-Th-total Pb monazite dating were performed using a JEOL Superprobe JXA-8900R Electron Probe Microanalyzer at the Institute of Geoscience of the University of Kiel. For biotite, plagioclase, amphiboles, epidote, zoisite, muscovite and chlorite analysis, analyses were performed using an accelerating voltage of 15 kV and a probe current of 15 nA or 20 nA. Synthetic and natural mineral standards were used and the CITZAF method of Armstrong (1995) was used for matrix correction. Except for minor differences in the values of accelerating potential and probe current, the in situ U-Th-total Pb monazite dating was performed using procedures similar to those described by Braun and Appel (2006) and Jöns et al. (2006). The U-Th-total Pb composition of the monazite was determined using an accelerating voltage of 20 kV and a probe current of 60 or 80 nA. The microprobe was calibrated for P, REE and Y using the synthetic REE orthophosphate standards of the Smithsonian Institute (Jarosewich and Boatner 1991). The composition of these standards were carefully determined considering their Pb content (see Donovan et al. 2003). For Th, Pb, U, Si, Ca and Al analysis, the microprobe was calibrated using thorianite, crocoite, synthetic U-bearing glasses, wollastonite and corundum, respectively. The JEOL ZAF program was used for matrix correction. Counting times for Pb are between 2 and 4 minutes on the peak and similar times on the background, depending on the intensities. The Pb Mb lines, Th Ma lines and U Mb lines (considering interference from Y Mg) were used. More details about the analytical Protocol and the background approximation for Pb are given at http://www.ifg.uni-kiel.de/1202.html. The quality of the data was controlled by repeated analyses of internal monazite standards from southeast Madagascar (kindly provided by Michael Raith, Bonn). These standards are homogenous in composition and were dated using cogenetic zircon using the U-Pb method, which resulted in an age of 542 ± 2 Ma. Samarium-neodymium (Sm-Nd) dating of monazite-biotite-garnet-zircon from the same rocks gave an isochron of 542 ± 11 Ma (Paquette et al. 1994). Analyses with significant apparent Al contents were rejected to avoid artifacts from secondary fluorescence that may occur if analytical points are too close to grain boundaries. The chemical ages of the monazite together with their

uncertainties were then calculated using the "Comb-error" and "AgeFinder" software programs (Appel 2010, 2013)

4. Petrography and mineral chemistry

4.1 Ikulu metapelite

Ikulu metapelites containing the dated hydrothermal altered monazite are gneissic to migmatitic in texture (Fig. 3.2a) and contain assemblages of biotite, sillimanite, plagioclase, quartz and K-feldspar. The biotite and sillimanite are primarily present in the melanosomes, and quartz, plagioclase and K-feldspar are primarily present in the leucosomes. Under the microscope, the biotite is green to brownish green and is surrounded by retrograde exsolution of ilmenite along its rims. The sillimanite is present in clusters, which are interpreted to form pseudomorphs after kyanite, or occurs intergrown with biotite. It is often surrounded by pinite pseudomorphs after cordierite (Fig. 3.4a and b). Minor minerals include zircon, monazite, ilmenite and magnetite that formed after ilmenite. The zircon and monazite grains are surrounded by pleochroic haloes in the pinite, supporting the interpretation that the pinite is really formed after cordierite (Fig. 3.4b). The metapelite adjacent to the gold bearing veins was affected by hydrothermal alteration of primary minerals, which includes chloritization of biotite, sericitization of plagioclase and sillimanite and the formation of epidote (Fig. 3.2).

Representative mineral analyses are presented in Table 1. The biotite in the metapelite exhibits X_{Fe} ratios of 0.44–058 (X_{Fe}=Fe/(Mg+Fe)). The titanium contents in biotite vary between 0.02 apfu along the rims to 0.15 apfu in the cores (Fig. 3.5a). Relict plagioclase is oligoclase containing an average X_{An} of 0.30. The hydrothermal sericite is muscovite and the chlorite is ripidolite and pynochlorite (Table 1).

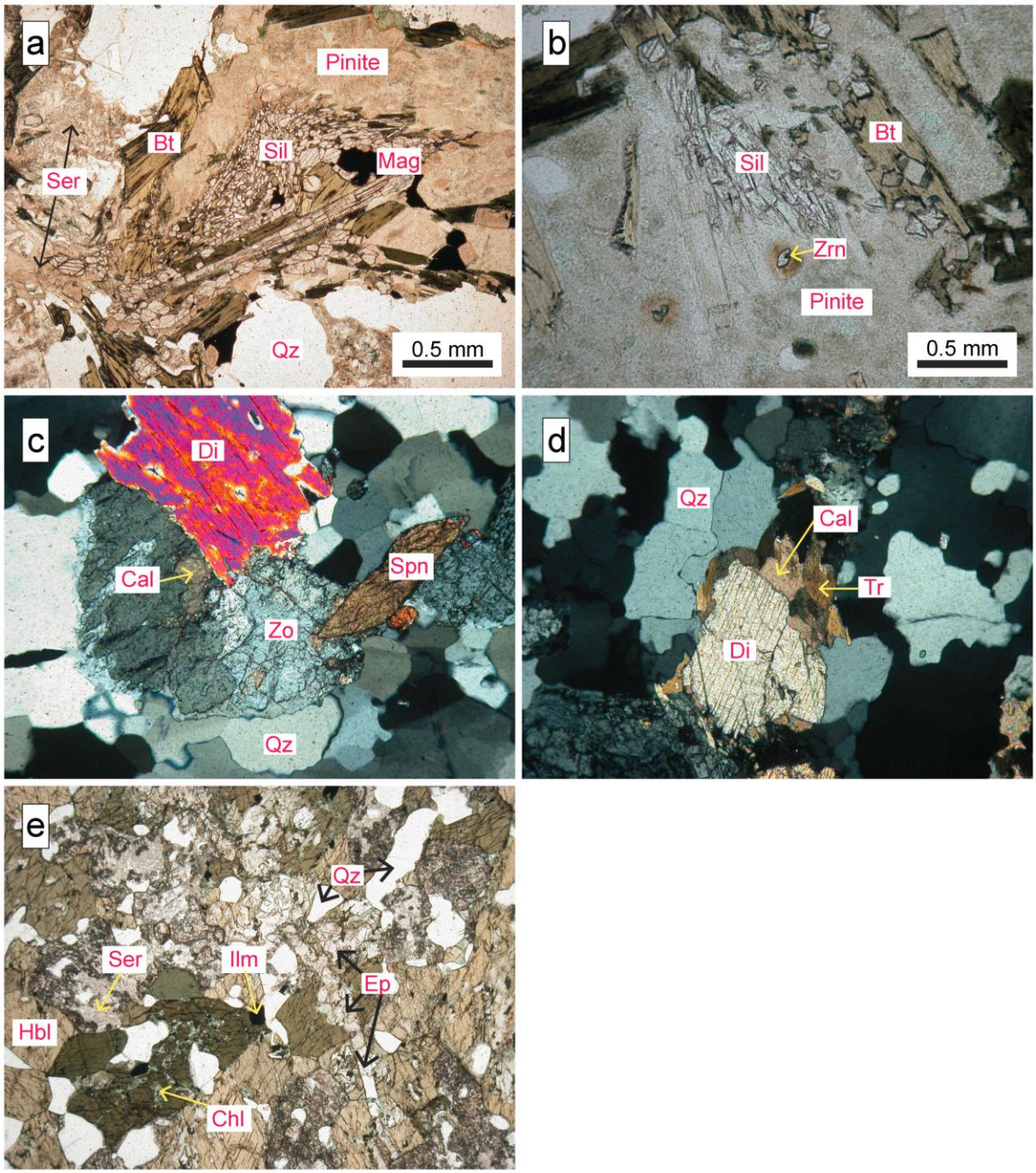

Fig. 3.4 Plane-polarized photomicrographs of various rock types from the Chemchem mine (a and b). Photomicrograph of the metapelite showing sillimanite cluster and biotite surrounded by pinite pseudomorph after cordierite and (b) zircon grains surrounded by pleochroic halos within the pinite. (c and d) Photomicrograph of the calc-silicate rock showing diopside (Di) and quartz (Qz) partly replaced by tremolite (Tr), calcite (Cal), zoisite (Zo) and titanite (Ttn). (E) Photomicrograph of the metabasite depicting an assemblage of hornblende (Hbl), plagioclase (Pl), ilmenite (Ilm) and quartz (Qz) replaced by chlorite (Chl), sericite (ser) and epidote (Ep).

4.2 Calc-silicate rocks

Calc-silicate rocks crop out together with the metapelites. These rocks are rich in quartz- (≈ 75 vol. %) and diopside. Under the microscope an assemblage of diopside, quartz and K-feldspar is partially replaced by a retrograde assemblage of tremolite, zoisite, muscovite and calcite. The zoisite is symplectitic intergrown with muscovite, albite and, in places, with calcite (Fig. 3.4c and d). Tremolite has an Al content of 0.51–0.04 apfu (Table 1) and is present as late-stage rims around diopside together with calcite. Additional minerals include titanite and zircon (Fig. 3.4c and d).

4.3 Orthoamphibolite

Orthoamphibolites are present near the Ikulu metapelites. This rock type contains hornblende, plagioclase and ilmenite. The hornblende is magnesiohornblende (X_{Mg} = 0.56) varying from olive green to brownish green and containing a mean TiO_2 content of about 1.0 wt. % (0.1–0.13 Ti apfu.), 6.63 apfu Si and 0.47 apfu Al^{vi}. The plagioclase is labradorite (X_{An} = 0.53–0.57) and in part has been affected by later formation of sericite and epidote. Metabasites are discordantly cut by epidote-chlorite micro-veins and the rocks next to the veins have been affected by hydrothermal alteration forming sericite, chlorite, epidote and calcite (Fig. 3.4e).

4.4 Metamorphic evolution of the vein country rocks at Chemchem

The mineralogy of the country rock of the Au-Cu-Pb veins reflects different stages of the metamorphic evolution prior to its hydrothermal alteration. These different evolutionary stages may also be recorded by the different internal growth zones and alteration textures of the monazite. The use of mineral chemistry data in determining the peak pressure and temperature conditions of metamorphism of the Ikulu metapelites at Chemchem is limited by the retrogression and hydrothermal alteration of its primary mineralogy, which led to the situation that cordierite is never preserved. However, the common occurrence of cm-sized prismatic pseudomorphs of silimanite after kyanite is clear evidence that the early stage of the evolution took place in the kyanite stability field. The peak conditions are characterized by the formation of anatectic leucosomes and the stability of cordierite, sillimanite and K-feldspar. This suggests that the metapelites were subjected to high-grade metamorphic conditions, which is in accordance with the observations of sillimanite, K-feldspar and cordierite bearing assemblages commonly found in metapelites of the upper amphibolite to granulite facies (e.g. Blümel and Schreyer, 1977).

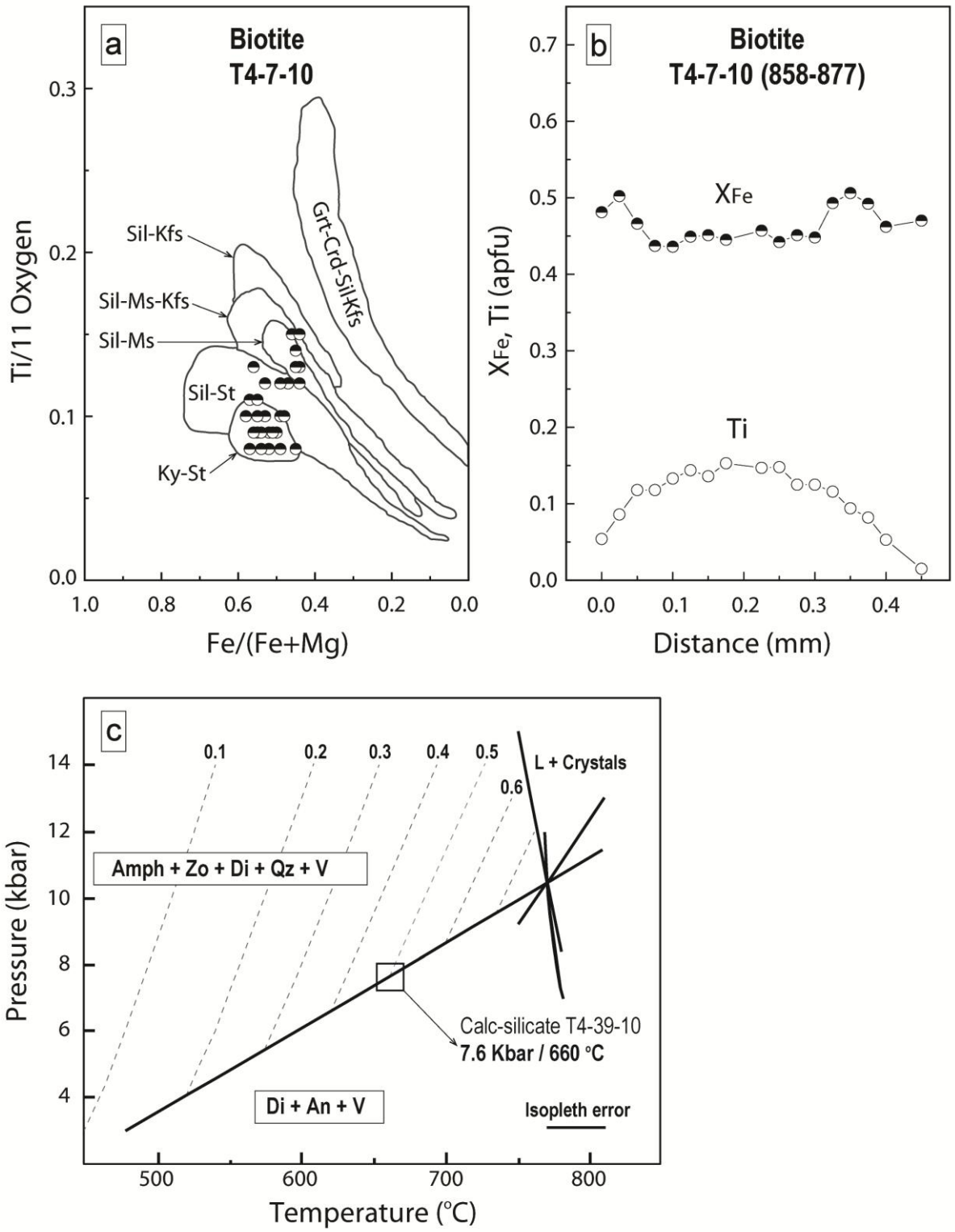

Fig. 3.5 (a) Plot of Ti (per 11 oxygens) of biotite of the Ikulu metapelite hosting gold bearing veins. The fields are compositions of biotite from metamorphic zones of northern England (Robinson et al., 1982; and Spear 1995). (b) Retrograde zoning in biotite of Ikulu metapelite (note low Ti values along the rims of biotite compared to the core).

The Ti-content and X_{Fe} values of biotite in metapelites are similar to those of biotite in kyanite-staurolite, sillimanite-staurolite and sillimanite-muscovite grades of metapelites in western Maine (USA; Fig. 3.5a; Robinson et al., 1982 and Spear 1995). However, due to the strong retrograde exsolution of ilmenite these mineral chemical data reflect only minimum metamorphic conditions. The influence of the retrogression on the Ti-content is seen in the strong decrease of the Ti-contents towards the rims of single biotite grains (Fig. 3.5b).

The hornblende-plagioclase thermometry of Holland and Blundy (1994) requires that the Si content of the hornblende is less than 7.8 pfu and the plagioclase X_{An} is less than 92. Amphiboles and plagioclase in the clinopyroxene bearing amphibolite of the present study meet those requirements. Estimates of the temperature using hornblende-plagioclase thermometry result in a temperature of amphibolite formation between 730 and 750°C. Retrograde formation of tremolite–zoisite–quartz from diopside and plagioclase in calc-silicate rocks and the maximum Al-content of cores (0.51 pfu) of the late-stage tremolite are consistent with the formation of this retrograde assemblage at temperature and pressure conditions of about > 650 °C and 7.6 kbar (Fig. 3.5c; Quirion and Jenkins, 1998).

In summary, the textures and mineralogy of the hydrothermally altered metapelitic country rocks of the Au-Cu-Pb veins give evidence of two metamorphic stages during the prograde evolution, of which the first stage was in the kyanite stability field, whereas the peak metamorphism reached anatectic temperatures in the stability field of the assemblage sillimanite–cordierite–biotite–K-feldspar. Estimates of peak temperatures of about 750℃ for this assemblage are in agreement with hornblende-plagioclase thermometry of a clinopyroxene-bearing amphibolite. Aluminum contents in late-stage tremolite of calc-silicates indicate partial retrograde re-equilibriation below 660℃ at 7.6 kbar. The penetrative pinitization of cordierite must have occurred under greenschist to sub-greenschist facies conditions.

5. Monazite in metapelite

5.1 Textures and chemistry

Monazite is present in the matrix of the metapelites together with altered feldspars, pinite, sillimanite, biotite and quartz. In the altered metapelites all minerals including monazite were affected to different degrees by hydrothermal alteration. Backscatter electron images (BSE) of unaltered monazite grains show dark gray cores that display various zoning patterns (concentric and patchy; Fig. 3.6a and b) and are surrounded by bright, light gray to white overgrowths (Fig. 3.6a and b).

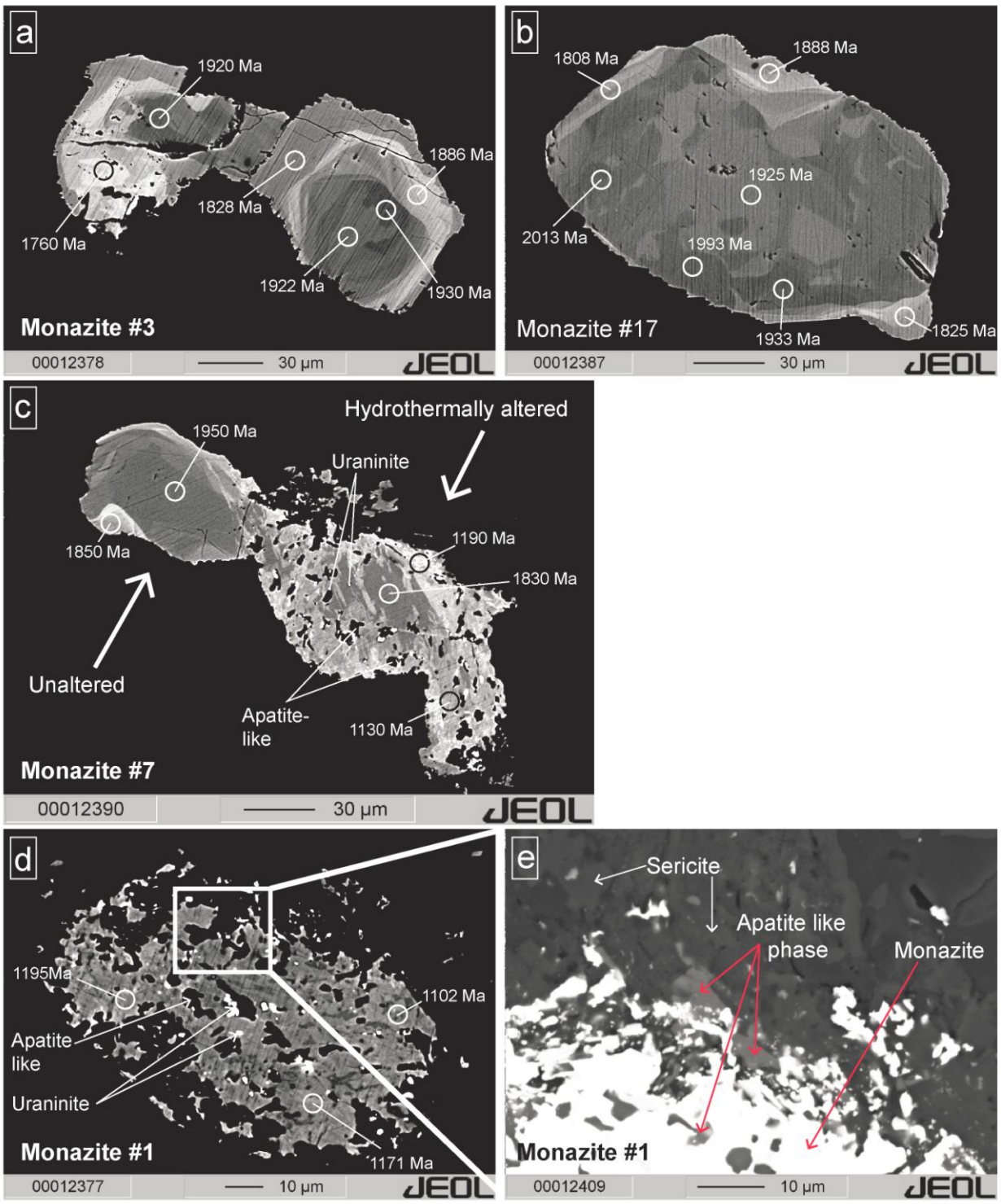

Fig. 3.6 Microtextures of selected monazite grains (in backscattered electron images; a – e): most metamorphic monazite grains display concentric (a) and patchy (b) zoning with overgrowths surrounding cores. The hydrothermal altered monazite grains (c and d) are brighter than the metamorphic monazite (C) and contain inclusions of apatite and uraninite. (e) Large area of monazite displaying hydrothermally altered monazite, sericite and apatite.

The hydrothermally altered monazite is generally distinguishable from unaltered grains by its poikilitic texture and the bright and light gray colour in BSE images (Fig. 3.6c, d and e). These

altered grains include dark gray relicts of older monazite, bright white spots of uraninite and elongated black inclusions (Fig. 3.6c, d and e), which are rich in Ca and PO_4 and thus appear to be similar to apatite (cf. Poitrasson et al., 2000).

The mineral chemistry data from the different types of monazite grains are presented in Tables 2, 3 and 4. The altered and unaltered monazite grains exhibit different mineral chemistries. Compared to the chemistry of average unaltered overgrowth zones, the hydrothermally altered monazite has slightly higher Eu concentrations and is depleted in Y, U, Pb, Th, Er, Dy and Ca (Fig. 3.7). The Si levels in the altered monazite are variable, i.e., slightly higher or lower than that of the unaltered monazite, whereas the P and light rare earth elements (LREEs: La, Ce, Pr and Nd) are present at similar concentrations in both the altered and unaltered monazite (Fig. 3.7).

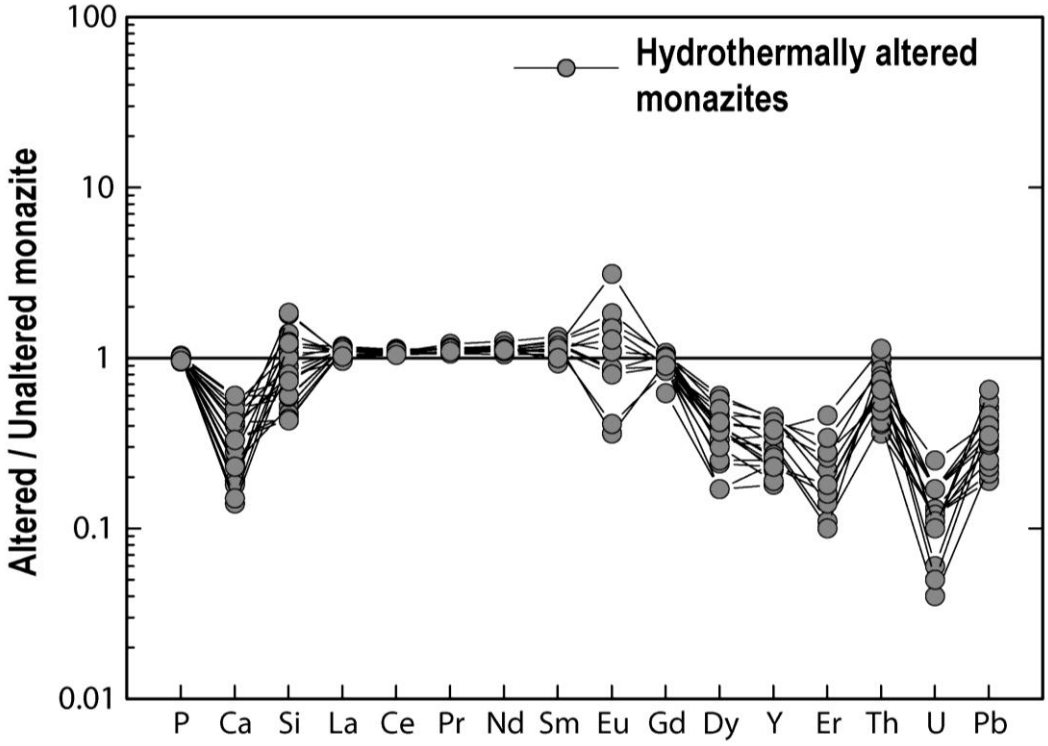

Fig. 3.7 Comparison of concentrations of various elements in hydrothermally altered monazite and unaltered monazite overgrowths: HREEs, U, Pb, Ca and Th are depleted in hydrothermally altered monazite compared to unaltered overgrowths, Eu is variable in hydrothermally altered monazite and P and LREE concentrations are similar in hydrothermally altered and unaltered monazite.

In the plot of (Th+U+Si)*4 versus (REE+Y+P)*4 (Fig. 3.8), the unaltered monazite cores are characterized by cheralite substitution, whereas the unaltered monazite overgrowths plot between the huttonite and cheralite substitution vectors, suggesting effects of both substitutions on the unaltered overgrowths. In contrast, only the huttonite substitution vector is important in

the hydrothermally altered monazite. The REE concentrations in the unaltered monazite cores and overgrown zones, exhibit similar chondrite normalized REE patterns (Fig. 3.9a and b). The patterns of LREE are similar in all the three types of monazite grains. The altered monazite displays relatively depleted heavy rare earth element patterns (HREEs: Dy and Er) compared to those of the unaltered monazite (Fig. 3.9a and b).

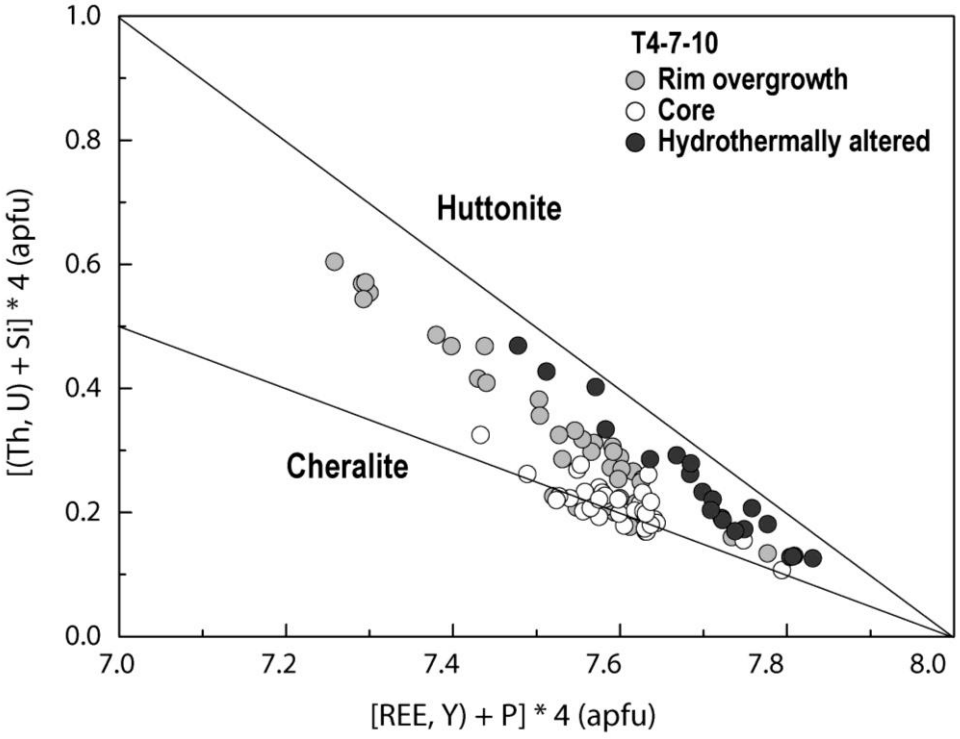

Fig. 3.8 Plot of ((Th, U) + Si) *4 vs. ((REEs, Y) + P)*4 showing cheralite and huttonite vectors.

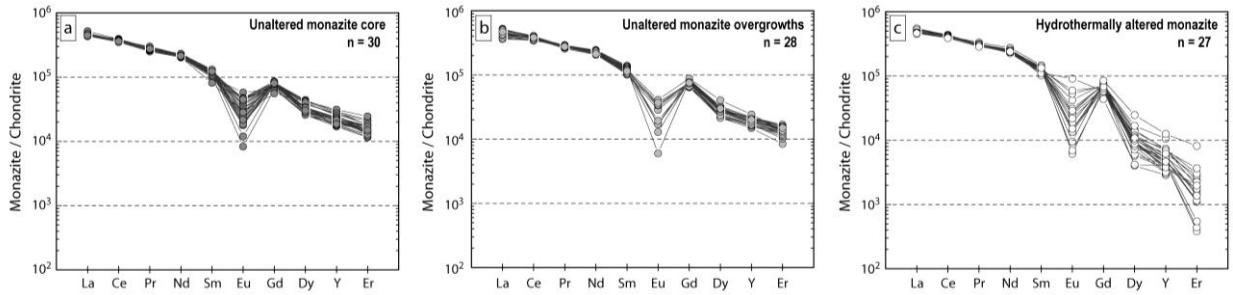

Fig. 3.9 Chondrite-normalized REE and Y patterns of the three types of monazite in the Chemchem metapelite; the normalizing values are from McDonough and Sun (1995).

5.2 U-Th-total Pb monazite dating

Analyses of U, Th and total Pb concentrations in monazite were obtained from the hydrothermally altered metapelitic sample (T4-7-10). The results of 84 points of unaltered and 19 points of hydrothermally altered monazite were used to calculate the ages of the different monazite grains and growth zones. The resulting histograms are presented in Figure 3.10. The three texturally and compositionally distinct monazite generations yielded three different weighted mean ages. The unaltered monazite cores have an age of 1938 ± 11 Ma and the unaltered overgrowth zone an age of 1827 ± 10 Ma. The hydrothermally altered monazite yielded a much younger age of 1171 ± 17 Ma (Fig. 3.10).

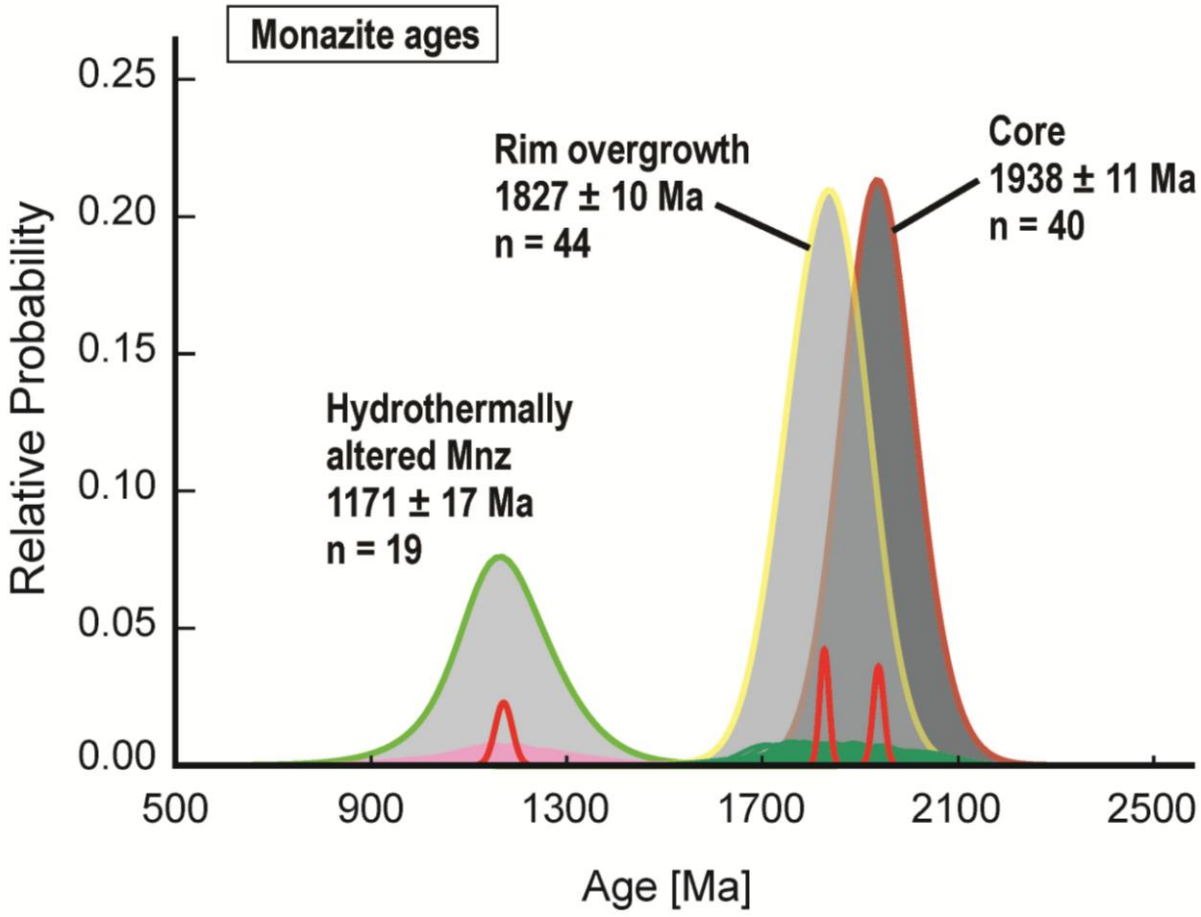

Fig. 3.10 Age histograms: the tall curves (red, yellow and green) are sum curves for the date of each age population, and the short curves (red) are curves for the weighted mean age (2σ error) of the age populations.

6. Discussion

As the Ubendian Belt was affected by three orogenic events during the Paleoproterozoic, Mesoproterozoic and Neoproterozoic (Boniface 2009; Boniface et al. 2012; Boniface and Schenk 2012), we aimed to evaluate the possible role of these three events in the formation of the Mpanda Au-Cu-Pb mineralization. Our dating of the unaltered monazite cores and overgrowth zones in high-grade metapelites, which show concentric growth zones and patchy zoning due to dissolution-precipitation processes, yielded two metamorphic ages at about 1940 Ma and at 1830 Ma. These two ages fall into the Paleoproterozoic orogenic cycle. The textures of the rock forming minerals of the metapelites also indicate two stages during the prograde evolution: an early stage in the kyanite stability field and a younger stage in the sillimanite–cordierite–biotite–K-feldspar stability field. Although it was not possible to perform texturally controlled dating of the two metamorphic stages (due to the absence of true kyanite relicts), we tentatively correlate the two Paleoproterozoic monazite ages with the kyanite stage (1940 Ma) and the sillimanite–cordierite stage (1830 Ma), respectively.

The older metamorphic age (ca. 1940 Ma) is similar to reported metamorphic zircon and monazite ages in different blocks of the Ubendian Belt (Boniface et al. 2012; Kazimoto et al., in review; Lawley et al., 2013c; Lawley et al., 2013d). Also the younger metamorphic monazite age (ca. 1830 Ma) found in the Chemchem metapelite, has already been recognized in the Ufipa and Ubende Blocks (Boniface et al. 2012). It postdates the formation of MORB type eclogites (ca. 1880 Ma) of the Ubende Block (Boniface et al. 2012). Unlike the prograde metamorphic monazite, the hydrothermally altered monazite is only found in metapelite samples bordering the gold bearing veins (Fig. 3.6c, d and e).

Our interpretation that the poikilitic, inclusion-rich monazite grains have been formed by hydrothermal fluids is in agreement with experimental results of Ayers and Watson (1991) and Ayers et al. (2004) who showed that P, T and pH has a strong influence on the solubility of monazite in hydrothermal fluids. The lowest solubility is at neutral pH-values but is increasing towards acidic and towards alkaline conditions as well. This indicates that monazite may dissolve in acidic hydrothermal fluids that causes sericitization of rocks (Poitrasson et al. 2000). Since sericitization, of e.g. feldspars, leads to increasing pH values of the hydrothermal fluid (Gruner 1944) new monazite may precipitate together with sericite from the neutral or less acidic fluid. Besides this dissolution-precipitation mechanism also cation exchange between the existing monazite and the hydrothermal fluids may lead to the formation of a new isotopically reset hydrothermal monazite. The cation exchange may follow the known cheralite ($2REE^{3+} = Th^{4+} + Ca^{2+}$) and huttonite ($REE^{3+} + P^{5+} = Th^{4+} + Si^{4+}$) substitutions. In addition to these

hydrothermal recrystallization mechanisms of monazite Poitrasson et al. (2000) described also different replacements of monazite grains by other minerals as a apatite-like phase, allanite or pyrite. From these different mechanisms the apatite-like replacement occurred also in the Chemchem altered metapelite as evidenced by the numerous apatite-like inclusion associated with uraninite in the hydrothermally altered sieve-like monazite grains (Fig. 3.6c, d and e). Interestingly, the host monazite showing the apatite-like replacement is characterized by Ca-depletion (Fig. 3.7). This indicates that the altered monazite may have acted as a Ca-source for the formation of the apatite-like phase.

The age of the hydrothermally altered monazite indicates that the fluid-rock interaction, which is associated with both the hydrothermal alteration of the metapelite and the deposition of Au, Cu and Pb in the veins, actually occurred in the Mesoproterozoic (ca. 1170 Ma) and thus correlates with the age of the Kibaran orogenic belt adjoining the Ubendian Belt to the west. Importantly, dating of monazite and zircons from metapelites of the tectonically adjoining Wakole Block of the Ubendian Belt (Fig. 3.1; Smirnov et al. 1970) yielded a remarkably similar age of 1170 ± 10 Ma of their first amphibolite grade metamorphism during crustal thickening (Boniface 2009). The agreement between the age of the hydrothermal alteration in the Katuma Block with that of the first metamorphism of the Wakole sediments suggests that the release of fluids from the fluid-fertile sediments during this crustal thickening event most likely generated the hydrothermal fluids required for the formation of the Au-Cu-Pb deposits in the tectonically adjoining Katuma Block. Similar ages (ca. 1180 – 1090 Ma) have also been reported for the metamorphic overprinting of the rocks of the Ubende Block (Boniface et al. 2012). The age of the compressional event found in the Wakole and Ubende Blocks is in agreement with the model of Fernandez-Alonso et al. (2012), according to which the closing of intra-cratonic basins and the formation of the Kibaran orogenic belt in east and central Africa during Mesoproterozoic time (ca. 1.0 Ga) was driven by far-field compressional forces related to the amalgamation of the Rodinia supercontinent.

7. Summary and conclusions

In situ U-Th-total Pb dating of monazite grains of hydrothermally altered high-grade metapelites, forming the country rocks of Au-Cu-Pb veins in the Katuma Block of the Ubendian Belt yielded two metamorphic ages of about 1940 Ma and 1830 Ma. As these metamorphic ages are well established for several blocks of the Ubendian Belt, it indicates that the monazite of the hydrothermally altered metapelites preserved the original mineral crystallization ages obtained during prograde Paleoproterozoic metamorphic events. In addition to these unaltered

Paleoproterozoic monazite grains the metapelites contain hydrothermally altered monazites grains that are chemically and texturally distinct and contain relicts of the older metamorphic grains or growth zones. This new hydrothermally crystallized monazite gives Mesoproterozoic ages of about 1170 Ma that correlate with metamorphic ages obtained for the first amphibolite facies metamorphism of metapelites of the Wakole Block. This block is in tectonic contact with the Katuma Block hosting the hydrothermal Au-Cu-Pb deposits. The hydrothermal event coincides with the Mesoproterozoic crustal thickening and shortening that led to the formation of the Kibaran orogenic belt bordering the Ubendian Belt to the west. Our new radiometric age indicates that under-thrusting of metasediments of the adjoining Wakole Block below the rocks of the Katuma Block most likely triggered metamorphism and dehydration of the sediments of the Wakole Block and generated fluids that percolated through the rocks of the Katuma Block and concentrated metals in the veins. The age of the hydrothermal event proposed here is younger than the earlier proposed Pb-Pb sulfides model age of ca. 1660 Ma and older than the Pb-Pb model age of ca. 720 Ma for the mineralization event in the Katuma Block. Moreover, this age is younger than that of the gold mineralization event in the Lupa Block at the southern part of the Ubendian Belt, which was dated at ca. 1950-1940 Ma and at 1880 Ma with the Re-Os method using sulfides (Lawley et al., 2013b). The distinct mineralization ages in the Katuma and Lupa Block indicate that the poly-orogenic Ubendian Belt was at least twice affected by mineralization events.

Acknowledgments

The authors would like to thank the Ministry of Education and Vocational Training of Tanzania (MOEVT), Germany Academic Exchange Programme (DAAD) and the Department of Geology of the University of Dar es Salaam, Tanzania (through the Sida Earth Science Project), for providing funding for this research. We are grateful to Andreas Fehler and Barbara Mader for their service at the laboratories of the Christian-Albrechts-Universität Kiel.

References

Appel P (2010) “AgeFinder”: A Mac OS X computer program to evaluate electron microprobe data of monazite for chemical age dating. Computers & Geosciences 36:559-563. doi:10.1016/j.cageo.2009.09.009

Appel P (2013) CombError. http://www.ifg.uni-kiel.de/339.html. Accessed 18-1-2014

Armstrong JT (1995) CITZAF: A package of correction programs for the quantitative electron microbeam X-ray analysis of thick polished materials, thin films, and particles. Microbeam analysis-Deerfield Beach- 4:177-200

Arne D, Bierlin F, Morgan J, Stein HJ (2001) Re-Os dating of sulfides associated with gold mineralization in central Victoria, Australia. Economic Geology 96:1455-1459

Ayers JC, Loflin M, Miller CF, Barton MD, Coath C (2004) Dating fluid infiltration using monazite. Proceedings of the Eleventh International Symposium on Water-Rock Interaction. A.A. Balkema Publishers,

Ayers JC, Watson EB (1991) Solubility of Apatite, Monazite, Zircon, and Rutile in Supercritical Aqueous Fluids with Implications for Subduction Zone Geochemistry. Philosophical Transactions of the Royal Society A: Mathematical, Physical and Engineering Sciences 335:365-375. doi:10.1098/rsta.1991.0052

Barley M, Groves D (1992) Supercontinent cycles and the distribution of metal deposits through time. Geology 20 (4):291-294

Blümel P, Schreyer W (1977) Phase Relations in Pelitic and Psammitic Gneisses of the Sillimanite-Potash Feldspar and Cordierite- Potash Feldspar Zones in the Moldanubicum of the Lam — Bodenmais Area , Bavaria. Journal of Petrology 18:431-459

Boniface N (2009) Eburnean, Kibaran and Pan-African metamorphic events in the Ubendian belt of Tanzania: Zircon and Monazite geochronology. Unpublished, University of Kiel, Kiel

Boniface N, Schenk V (2012) Neoproterozoic eclogites in the Paleoproterozoic Ubendian Belt of Tanzania : Evidence for a Pan-African suture between the Bangweulu Block and the Tanzania Craton. Precambrian Research 208-211:72-89.

Boniface N, Schenk V, Appel P (2012) Paleoproterozoic eclogites of MORB-type chemistry and three Proterozoic orogenic cycles in the Ubendian Belt (Tanzania): Evidence from monazite and zircon geochronology , and geochemistry. Precambrian Research 192-195:16-33.

Boven A, Theunissen K, Sklyarov E, Klerkx J (1999) Timing of exhumation of a high-pressure mafic granulite terrane of the Paleoproterozoic Ubende belt (West Tanzania). Precambrian Research 93:119-137

Braun I, Appel P (2006) U-Th-total Pb dating of monazite from orthogneisses and their ultra-high temperature metapelitic enclaves implications for the multistage tectonic evolution of the Madurai Block, southern India. European Journal of Mineralogy 18 (4):415-427

Cahen L, Snelling NJ, Delhal J, Vail J (1966) The Geochronology and evolution of Africa. Clarendon Press, Oxford-UK

Daly MC (1988) Crustal Shear Zones in Central Africa: a Kinematic Approach to Proterozoic Tectonics. Episodes 11:5-11

Davis DW, Schandl ES, Wasteneys HA (1994) U-Pb dating of minerals in alteration halos of Superior Province massive sulfide deposits: syngenesis versus metamorphism. Contributions to Mineralogy and Petrology 115:427-437. doi:10.1007/BF00320976

Delvaux D, Kervyn F, Macheyeki A, Temu E (2012) Geodynamic significance of the TRM segment in the East African Rift (W-Tanzania): Active tectonics and paleostress in the Ufipa plateau and Rukwa basin. Journal of Structural Geology 37:161-180.

Donovan JJ, Hanchar JM, Picolli PM, Schrier MD, Boatner LA, Jarosewich E (2003) A re-examination of the Rare-Earth-Element Orthophosphate Standards in Use for Electron-Microprobe Analysis. The Canadian Mineralogist 41:221-232.

Fernandez-Alonso M, Cutten H, De-Waele B, Tack L, Tahon A, Baudet D, Barritt SD (2012) The Mesoproterozoic Karagwe-Ankole Belt (formerly the NE Kibara Belt): The result of prolonged extensional intracratonic basin development punctuated by two short-lived far-field compressional events. Precambrian Research 216-219:63-86. doi:10.1016/j.precamres.2012.06.007

Frei R, Pettke T (1996) Mono-sample Pb-Pb dating of pyrrhotite and tourmaline: Proterozoic vs. Archean intracratonic gold mineralization in Zimbabwe. Geology 24 (9):823-826

Goldfarb RJ, Groves DI, Gardoll S (2001) Orogenic gold and geologic time: A global synthesis. Ore Geology Reviews 18:1 - 75

Gruner JW (1944) The hydrothermal alteration of feldspars in acid solutions between 300 degrees and 400 degrees C. Economic Geology 39:578-589

Holland T, Blundy J (1994) Non-ideal interactions in calcic amphiboles and their bearing on amphibole-plagioclase thermometry. Contributions to Mineralogy and Petrology 116:433-447

Hu F, Fan H, Yang J, Wan Y, Liu D, Mingguo Z, Chengwei J (2004) Mineralizing age of the Rushan lode gold deposit in the Jiaodong Peninsula: SHRIMP U-Pb dating on hydrothermal zircon. Chinese Science Bulletin 49:1629-1636

Jarosewich E, Boatner L (1991) Rare-Earth Element Reference Samples for Electron Microprobe Analysis. Geostandards Newsletter 15 (2):397-399

Jöns N, Schenk V, Appel P, Razakamanana T (2006) Two-stage metamorphic evolution of the Bemarivo Belt of northern Madagascar: constraints from reaction textures and in situ monazite dating. Journal of Metamorphic Geology 24:329-347. doi:10.1111/j.1525-1314.2006.00641.x

Kazimoto EO, Schenk V, Berndt J (in review) Neoarchean and Paleoproterozoic crust formation in the Ubendian Belt of Tanzania: insights from zircon geochronology and geochemistry. Precambrian Research.

Kerrich R, Cassidy KF (1994) Temporal relationships of lode gold mineralization to accretion, magmatism, metamorphism and deformation—Archean to present: A review. Ore Geology Reviews 9 (4):263-310.

Kerrich R, Kyser TK (1994) 100 Ma timing paradox of Archean gold, Abitibi greenstone belt (Canada): New evidence from U-Pb and Pb-Pb evaporation ages of hydrothermal zircons. Geology 22 (12):1131-1134.

Kilembe EA, Rosendahl BR (1992) Structure and stratigraphy of the Rukwa rift. Tectonophysics 209:143-158.

Lawley CJM, Selby D, Condon DJ, Horstwood M, Millar I, Crowley Q, Imber J (2013a) Lithogeochemistry, geochronology and geodynamic setting of the Lupa Terrane, Tanzania: Implications for the extent of the Archean Tanzanian Craton. Precambrian Research 231:174-193. doi:10.1016/j.precamres.2013.02.012

Lawley CJM, Selby D, Condon DJ, Imber J (2013b) Palaeoproterozoic orogenic gold style mineralization at the Southwestern Archaean Tanzanian cratonic margin, Lupa Goldfield, SW Tanzania: Implications from U–Pb titanite geochronology. Gondwana Research.

Lawley CJM, Selby D, Imber J (2013c) Re-Os Molybdenite, Pyrite and Chalcopyrite Geochronology, Lupa Goldfield, Southwestern Tanzania: Tracing Metallogenic Time Scales at Midcrustal Shear Zones Hosting Orogenic Au Deposits. Economic Geology 108:1591-1613

Lenoir JL, Liegeois JP, Theunissen K, Klerkx J (1994) The Palaeoproterozoic Ubendian shear belt in Tanzania: geochronology and structure. Journal of African Earth 19:169-184

Nanyaro J (1989) Proterozoic gold-base metal veins in the Mpanda mineral field, western Tanzania. Annalles Series in-8, Science Geologiques 97. Musée Royale de L'Afrique Centrale Tervuren, Belgium

Paquette JL, Nédélec A, Moine B, Rakotondrazafy M (1994) U-Pb, single zircon Pb-evaporation, and Sm-Nd isotopic study of a granulite domain in SE Madagascar. The Journal of Geology:523-538

Phillips D, Miller JM (2006) 40Ar/39Ar dating of mica-bearing pyrite from thermally overprinted Archean gold deposits. Geology 34:397. doi:10.1130/G22298.1

Poitrasson F, Chenery S, Shepherd TJ (2000) Electron microprobe and LA-ICP-MS study of monazite hydrothermal alteration: Implications for U-Th-Pb geochronology and nuclear ceramics. Geochimica et Cosmochimica Acta 64:3283-3297

Quirion DM, Jenkins DM (1998) Dehydration and partial melting of tremolitic amphibole coexisting with zoisite, quartz, anorthite, diopside, and water in the system H2O-CaO-MgO-Al2O3 -SiO2. Contributions to Mineralogy and Petrology 130:379-389.

Rasmussen B, Sheppard S, Fletcher IR (2006) Testing ore deposit models using in situ U-Pb geochronology of hydrothermal monazite: Paleoproterozoic gold mineralization in northern Australia. Geology 34 (2):77-80

Ring U, Kröner A, Toulkeridis T (1997) Palaeoproterozoic granulite-facies metamorphism and granitoid intrusions in the Ubendian-Usagaran Orogen of northern Malawi, east-central Africa. Precambrian Research 85:27-51

Robinson P, Hollocher K, Tracy R, Dietsch C High grade Acadian regional metamorphism in south-central Massachusetts. In: NEIGC 74th Annual Meeting of the state Geological and Natural History Survey of Connecticut, guidebook for fieldtrips in Connecticut and South-Central Massachusetts (eds Joester, RA & Quarrier, SS), 1982. pp 289-340

Selby D, Creaser RA, Hart CJR, Rombach CS, Thompson JFH, Smith MT, Bakke AA, Goldfarb RJ (2002) Absolute timing of sulfide and gold mineralization: A comparison of Re-Os molybdenite and Ar-Ar mica methods from the Tintina Gold Belt, Alaska. Geology 30 (9):791-794

Semyanov A, Kireev A, Doronkin I, Gavrilov G, Matrenitzky T, Novicov A (1977) Mpanda: Geological Map Quarter Degree Sheet 153. Geological Survey of Tanzania, Dodoma.

Smirnov V, Shulyatin O, Tolochko V, Zhukov S, Mwakisunga M, Matrenitzky T (1970) Katuma: Geological Map Quarter Degree Sheet 152. Ministry of Energy and Minerals.

Spear FS (1995) Metamorphic phase equilibria and pressure-temperature-time paths. Mineralogical Society of America, Washington.

Stein HJ (2001) Re-Os dating of Archean orogenic Au deposits in the Yilgarn, Western Australia. GSA Annual Meeting, November 5-8, 2001:20-21.

Stendal H, Frei R, Muhongo S, Rasmussen TM, Mnali S, Petro F, Brian Temu E (2004a) Gold potential of the Mpanda Mineral Field, SW Tanzania: evaluation based on geological, lead isotopic and aeromagnetic data. Journal of African Earth Sciences 38:437-447.

Stendal H, Frei R, Muhongo S, Rasmussen TM, Mnali SR, Petro F, Brian Temu E (2004b) Gold potential of the Mpanda Mineral Field, SW Tanzania: evaluation based on geological, lead isotopic and aeromagnetic data. Journal of African Earth Sciences 38:437-447.

Theunissen K, Klerkx J, Melnikov A, Mruma AH (1996) Mechanisms of inheritance of rift faulting in the western branch of the East African Rift, Tanzania. Tectonics 15:776-790.

Vielreicher NM, Groves DI, Fletcher IR, McNaughton NJ, Rasmussen B (2003) Hydrothermal monazite and xenotime geochronology: A new direction for precise dating of orogenic gold mineralization. Society of Economic Geologists.

Appendices

Chapter 1

Table 1. Sample locations, protolith/metamorphic age, mineralogy and textural descriptions of the major rock types of the Katuma Block

Lithology	Sample ID	Protolith age (~ Ma)	Location			Mineralogy			Description
			Easting	Northing	Site	Main	Accessory	Late-stage	
Orthogneiss / Meta-granodiorite	T1-17	2710	283664	9296440	Mkwamba (near abandoned Au mine)	Bt + Pl + Kfs + Qz + Hbl ± Opx ± Cpx	Zrn + Ilm	Ser + Chl	Gneissose to migmatitic; sericitized plagioclase and quartz exhibiting undulatory extinction
Orthogneiss / Meta-granite	T6-6	2640	300190	9279922	Singililwa mine	Hbl + Bt + Pl + Kfs + Qz	Zrn		Gneissose to migmatitic; Pl and Kfs alteration vary from weak to strong; retrogressed biotite is surrounded by Ilm exsolution at its rims; Kfs form perthites and microcline twinning
Garnet-amphibolite	T17-3	2650	276706	9317912	North of Mpanda town	Grt + Hbl + Bt + Pl + Qz + Ilm	Zrn		Foliated, occur as enclaves in gabbronorite; both Hbl and Bt are surrounded by Grt rims; Bt is brown surrounded by Hbl rims
Gabbronorite	T17-1	2640				Opx + Cpx + Bt + Hbl + Pl + Ilm + Qz	Zrn		Massive and coarse grained; Hbl form as late rims around ortho- and clinopyroxene
Mafic granulite	T16-1	2650	324240	9283710	South of Mpanda	Opx + Cpx + Hbl + Pl + Qz + Grt + Ilm	Zrn		Fine to medium grained; cut by numerous late fractures/veins; Pl are 2-3 mm in size and zoned; Hbl form rims around Cpx; Garnet form coronas around Opx/Cpx
Granitic gneiss	T19-3	1940	232296	9302368	West of the Katuma village	Hbl + Bt + Pl + Qz + Kfs + Ilm	Ilm + Zrn		Gneissose
Amphibolite	T19-1	2020				Hbl + Bt + Pl + Qz + Ep	Ilm + Zrn		Mainly Hbl and Pl; Ep and Spn occur as inclusions in Hbl; Pl is zoned, with inclusions in the core that are surrounded by clear rims
Granodiorite	T2a-2	1950	286905	9284610	Kapanda (artisanal Au-mines)	Hbl + Bt + Pl + Kfs + Qz	Ilm + Zrn	Ser + Chl	Massive and leucocratic; undulatory extinction of quartz; ; locally cut by Au-Cu-Pb veins; near the veins, Pl and Kfs are sericitized and mild carbonate (Cal?) alteration
Biotite granite	T2c-1	1990	286899	9284454		Bt + Pl + Kfs + Qz	Ilm + Zrn	Ser	Massive; locally cut by Au-Cu-Pb veins; chloritized Amp altered to Chl; sericitized Kfs and Pl
Ikulu metapelite	T4-38	1960 *	288391	9280264	Chemchem (near abandoned Au-Cu mine)	Sil + Kfs + Bt + Pl + Qz + Ilm ± Grt ± pinite	Mg + Py	Ser + Chl	Migmatitic; cordierite is stronly pinitized; silimanite form pseudomorphs after Ky; Pl and Kfs are sericitized; Bt is altered to form Chl, Ilm and Mt exsolutions at its rims
Leucosome of a metapelite	T4-37	1940 *				Bt + Pl + Kfs + Qz		Ser + Chl	with cospicous altered red Kfs
Calc-silicate rock	T4-39	1960 *				Qz + Di + Tr + Zo + Cal + Pl + Spn + Ms	Zrn	Tr + Zo + Cal + Ms + Ab	Foliated; mainly composed of quartz ~ 75 modal vol. %; Di, Qz, Kfs and Pl is replaced Tr, Zo, Cal, Ms and Ab

Eastings and northings as UTM coordinates (WGS84, Zone 36S); Mineral abbreviations are from Whitney and Evans, 2009, * interpreted metamorphic age

Table 2. Description of zircon texture under cathodoluminescence (CL) images, interpretation of zircon growths and their corresponding age and the geologic interpretation

Sample	Rock	Zircon features	Interpretation of Zircon growth	Ages	Geological Interpretation
T1-17-10	Orthogneiss (Hbl-Bt)	*Zircon sizes:* 50 − 200 µm *Shape* : stubby and rounded. (1) CL images show cores with concentric oscillatory zoning and irregular boundaries	Magmatic	$^{207}Pb/^{206}Pb$ age = 2713 ± 11 Ma	Magmatic protolith emplacement
		(2) Rim overgrowths surround the cores	Metamorphic	(1) U-Pb age = 2650 ± 8 Ma (2) Upper intercept 2647 ± 53 Ma and lower intercept -794 ± 2000 Ma	Metamorphism at ~ 2650 Ma and after 2650 Ma
T6-6-10	Orthogneiss (Hbl-Bt)	*Zircon sizes:* 200 − 500 µm *Shape* : prismatic, flat terminations, stubby to equant CL images reveal concentric oscillatory zoning; cores vary from bright luminescent (U = 58-168 ppm) to dark gray non-luminescent (U = 328 − 525 ppm)	Magmatic	U-Pb age = 2638 ± 5 Ma	Magmatic protolith emplacement
T14-3-10	Paleosome of orthogneiss	*Zircon sizes:* <200 − 400 µm Grains are prismatic (1) CL images show cores with concentric oscillatory zoning or recrystallized cores. The cores have spherical, irregular and angular shape	Magmatic	$^{207}Pb/^{206}Pb$ age = 2677 ± 29 Ma	Magmatic protolith emplacement
		(2) Rim overgrowths surround the cores	Metamorphic	(1) U-Pb age = 2025 ± 8 Ma (2) Upper intercept 2643 ± 90 Ma and lower intercept 1758 ± 63 Ma	Metamorphism at ~ 2030 Ma and after 2030 Ma
T14-1-10	Leucosome of orthogneiss	*Zircon sizes:* <200 − 400 µm Grains are prismatic (1) CL images show cores that are unzoned with recrystallized internal textures and few with concentric oscillatory zoning. The cores have also irregular, broken and resorbed margins.	Magmatic	(1) U-Pb age = 2653 ± 10 Ma	Magmatic protolith emplacement
		(2) Rim overgrowths surround the cores	Metamorphic / anatexis	(1) U-Pb age = 2045 ± 12 Ma	Leucosome crystallization / migmatite formation
T17-3-10	Garnet amphibolite	*Zircon sizes:* <300 µm Grains are prismatic to spherical. Some have incomplete crystal faces or concave embayments. CL images of the zircon crystals show oscillatory zoning sometimes with recrystallized zones.	Magmatic	U-Pb age = 2651 ± 5 Ma	Magmatic protolith emplacement
T17-1-10	Gabbronorite	*Zircon sizes:* coarse grained Grains are prismatic CL images with dark inner zones (U < 179 ppm and bright luminescent outer zones (U= 238-524 ppm)	Magmatic	U-Pb age = 2643 ± 4 Ma	Magmatic emplacement
T16-1-10	Mafic granulite	*Zircon sizes:* <200 µm Grains are spherical CL images show concentric magmatic oscillatory zoning	Magmatic	U-Pb age = 2645 ± 34 Ma	Magmatic protolith emplacement
T19-1-10	Amphibolite	Zircon sizes: <200 µm Grains are spherical no visible zoning	Magmatic	$^{207}Pb/^{206}Pb$ age = 2021 ± 11 Ma	Magmatic protolith emplacement

Table 2 continued

Sample	Rock	Zircon texture	Interpretation of Zircon growth	Ages	Geological Interpretation
T2a-2-10	Hbl-Bt granite	*Zircon sizes:* ~250 mm Grains are stubby, equant to spherical CL images show concentric oscillatory zoning	Magmatic	U-Pb age = 1952 ± 7 Ma	Magmatic emplacement
T2c-1-10	Bt-granite	Zircon sizes: <600 mm Grains are short prismatic and ellipsoidal. CL images show concentric magmatic growth zoning	Magmatic	U-Pb age = 1993 ± 6 Ma	Magmatic emplacement
T19-3-10	Hbl-Bt granite	Zircon sizes: <200 mm Grains are long prismatic with rounded terminations (1) CL images show cores with magmatic growth zoning, rounded and irregular boundaries; dark gray luminescence (U = 440 ppm)	Magmatic	$^{207}Pb/^{206}Pb$ age =1936 ± 20 Ma	Magmatic emplacement
		(2) Rim overgrowths surround the cores; gray tones of luminescence (U = 259 ppm)	Metamorphic	U-Pb age = 1879 ± 9 Ma	Metamorphism
T4-39-10	Calc-silicate rock	Zircon sizes: 50 - 300 mm Grains are ellipsoidal, long or short prismatic and broken fragments; grains with irregular or rounded margins (1) CL images show growth oscillatory zoning, cores with rounded and irregular boundaries	Detrital	$^{207}Pb/^{206}Pb$ age = 2640 - 2220 Ma	Sediment source and sedimentation period
		(2) Rim overgrowths surround the cores	Metamorphic	U-Pb age = 1963 ± 14 Ma; upper = 2422 ± 14 Ma and lower intercept ages = 1719 ± 14 Ma	Metamorphism at ~ 1960 Ma and after 1960 Ma
T4-38-10	Metapelite	Zircon sizes: <200 mm Grains are long prismatic with rounded terminations (1) CL images show cores with ellipsoidal to irregular shape; cores show oscillatory growth zoning in part blurred. Convolute zoning and bulbous replacements.	Detrital	$^{207}Pb/^{206}Pb$ age = 2300 - 2060 Ma	Sediment source and sedimentation period
		(2) Rim overgrowths (~ 50 mm in thickness) surrounds the cores; different rim overgrowths with dfferent gray tones of luminescence (e.g. outer U = 334 ppm and inner U = 162 ppm).	Metamorphic	U-Pb age = 1958 ± 8 Ma; upper = 1985 ± 20 Ma and lower intercept ages = 643 ± 440 Ma	Metamorphism
T4-37-10	Leucosome of metapelite	Zircon sizes: <200 mm Grains are long to short prismatic (1) In CL images show cores with oscillatory zoning, surrounded by rim overgrowths	Metamorphic and anatexis	U-Pb age = 1944 ± 9 Ma	Leucosome crystallization / metapelitic migmatite formation

Table 3. LA-ICP-MS analyses for a meta-granodiorite (sample T1-17-10)

	Analysis name	Texture	Spot size	U conc.	Ratios						rho:	Ages (Ma)									Common Pb		Degree of concordance (%)
			(µm)	(ppm)	$^{206}Pb/^{238}U$	± 2σ	$^{207}Pb/^{235}U$	± 2σ	$^{207}Pb/^{206}Pb$	± 2σ		$^{206}Pb/^{238}U$	± 2σ	± 2σ%	$^{207}Pb/^{235}U$	± 2σ	± 2σ%	$^{207}Pb/^{206}Pb$	± 2σ	± 2σ%	$^{206}Pb/^{204}Pb$	ƒ206%	
Orthogneiss	**T1-17-16-1**	**Inh. core**	**25**	**196**	**0.5423**	**0.0110**	**14.7580**	**0.3370**	**0.1974**	**0.0021**	**0.89**	**2793**	**46**	**1.6**	**2800**	**22**	**0.8**	**2805**	**17**	**0.6**		**0.0**	**99.6**
	T1-17-16-4	core	25	167	0.4404	0.0134	11.1243	0.3659	0.1832	0.0023	0.93	2353	60	2.5	2534	31	1.2	2682	21	0.8	9590	0.1	87.7
	T1-17-15-4	core	25	174	0.4776	0.0159	11.8004	0.4278	0.1792	0.0026	0.92	2517	69	2.8	2589	34	1.3	2646	24	0.9	3028	0.6	95.1
	T1-17-8-4	core	25	671	0.5112	0.0074	13.2752	0.2384	0.1884	0.0020	0.81	2662	32	1.2	2699	17	0.6	2728	17	0.6	2510	0.7	97.6
	T1-17-13-4	core	25	571	0.5133	0.0092	13.2413	0.2805	0.1871	0.0021	0.85	2670	39	1.5	2697	20	0.7	2717	19	0.7	11213	0.2	98.3
	T1-17-11-4	core	25	822	0.5131	0.0104	12.9752	0.3188	0.1834	0.0026	0.82	2670	44	1.7	2678	23	0.9	2684	23	0.9	21866	0.1	99.5
	T1-17-7-4	core	25	308	0.5238	0.0077	13.6209	0.2521	0.1886	0.0021	0.80	2715	33	1.2	2724	18	0.6	2730	18	0.7	5701	0.3	99.5
	T1-17-8-5	core	25	724	0.5196	0.0075	13.3359	0.2403	0.1861	0.0020	0.80	2698	32	1.2	2704	17	0.6	2708	18	0.7	4568	0.4	99.6
	T1-17-18-4	core	25	360	0.5216	0.0086	13.3897	0.2624	0.1862	0.0020	0.84	2706	36	1.3	2708	19	0.7	2709	18	0.6	6250	0.3	99.9
	T1-17-17-4	core	25	813	0.5284	0.0142	13.7914	0.4016	0.1893	0.0021	0.92	2735	60	2.2	2735	28	1.0	2736	18	0.7	7198	0.2	99.9
	T1-17-9-4	core	25	349	0.5188	0.0074	13.1172	0.2336	0.1834	0.0020	0.80	2694	31	1.2	2688	17	0.6	2684	18	0.7		0.0	100.4
	T1-17-21-4	core	25	222	0.5315	0.0091	13.7392	0.2887	0.1875	0.0023	0.82	2748	38	1.4	2732	20	0.7	2720	20	0.7	3540	0.5	101.0
	T1-17-19-4	core	25	568	0.5370	0.0069	13.8262	0.2268	0.1868	0.0019	0.79	2771	29	1.0	2738	16	0.6	2714	17	0.6	38103	0.0	102.1
	T1-17-3-4	core	25	404	0.5186	0.0069	13.2112	0.2180	0.1848	0.0018	0.81	2693	29	1.1	2695	16	0.6	2696	16	0.6	15607	0.1	99.9
	T1-17-4-4	core	25	300	0.5260	0.0075	13.6557	0.2469	0.1883	0.0021	0.79	2724	32	1.2	2726	17	0.6	2727	18	0.7	17552	0.1	99.9
	T1-17-1-4	core	25	19	0.3759	0.0081	7.2849	0.2401	0.1406	0.0035	0.66	2057	38	1.9	2147	29	1.4	2234	43	1.9	969	1.3	92.1
	T1-17-12-4	core	25	4594	0.3636	0.0151	6.1753	0.3342	0.1232	0.0043	0.77	1999	72	3.6	2001	47	2.4	2003	61	3.1	895	1.7	99.8
	T1-17-9-7	rim	25	338	0.4601	0.0078	11.2911	0.2180	0.1780	0.0016	0.88	2440	35	1.4	2547	18	0.7	2634	15	0.6	8618	0.2	92.6
	T1-17-4-7	rim	25	329	0.4597	0.0111	11.4429	0.3073	0.1805	0.0021	0.90	2438	49	2.0	2560	25	1.0	2658	19	0.7	2699	0.5	91.7
	T1-17-3-7	rim	25	2452	0.4088	0.0111	10.6723	0.3656	0.1894	0.0040	0.79	2209	51	2.3	2495	32	1.3	2737	35	1.3	2708	0.5	80.7
	T1-17-20-7	rim	25	249	0.5300	0.0070	12.9811	0.2075	0.1776	0.0016	0.83	2741	30	1.1	2678	15	0.6	2631	15	0.6	63976	0.0	104.2
	T1-17-14-7	rim	25	211	0.5022	0.0171	12.6559	0.4625	0.1828	0.0024	0.93	2623	73	2.8	2654	34	1.3	2678	22	0.8	2284	0.8	97.4
	T1-17-5-8	rim	25	118	0.5037	0.0071	12.6255	0.2197	0.1818	0.0019	0.80	2630	30	1.1	2652	16	0.6	2669	17	0.6		0.0	98.5
	T1-17-5-7	rim	25	252	0.5001	0.0072	12.2689	0.2121	0.1779	0.0017	0.83	2614	31	1.2	2625	16	0.6	2634	16	0.6	13031	0.1	99.2
	T1-17-21-7	rim	25	491	0.5034	0.0093	12.4572	0.2557	0.1795	0.0016	0.90	2628	40	1.5	2640	19	0.7	2648	15	0.5	16443	0.1	99.3
	T1-17-19-7	rim	25	148	0.5069	0.0067	12.5402	0.1981	0.1794	0.0016	0.84	2643	29	1.1	2646	15	0.6	2648	14	0.5	13523	0.1	99.8
	T1-17-4-8	rim	25	603	0.5078	0.0099	12.5893	0.2844	0.1798	0.0020	0.86	2647	42	1.6	2649	21	0.8	2651	19	0.7	71069	0.0	99.9
	T1-17-15-7	rim	25	237	0.5108	0.0167	12.7459	0.4418	0.1810	0.0021	0.94	2660	71	2.7	2661	33	1.2	2662	19	0.7	2247	0.8	99.9
	T1-17-5-9	rim	25	189	0.5144	0.0089	12.8040	0.2676	0.1805	0.0021	0.83	2675	38	1.4	2665	20	0.7	2658	19	0.7	19671	0.1	100.7
	T1-17-10-7	rim	25	111	0.5169	0.0099	12.8250	0.3130	0.1799	0.0027	0.79	2686	42	1.6	2667	23	0.9	2652	25	0.9	13832	0.1	101.3
	T1-17-6-7	rim	25	246	0.5173	0.0060	12.7565	0.1819	0.1788	0.0015	0.82	2688	26	1.0	2662	13	0.5	2642	14	0.5	135991	0.0	101.7
	T1-17-2-7		25	21	0.3934	0.0125	7.3670	0.3206	0.1358	0.0040	0.73	2138	58	2.7	2157	39	1.8	2175	52	2.4	556	3.2	98.3
	91500-3		25	89	0.1762	0.0025	1.8072	0.0349	0.0744	0.0010	0.73	1046	14	1.3	1048	13	1.2	1053	27	2.5	2840	0.3	99.4
	91500-4		25	78	0.1822	0.0024	1.8950	0.0361	0.0754	0.0010	0.70	1079	13	1.2	1079	13	1.2	1081	27	2.5	10456	0.1	99.8

Table 4. LA-ICP-MS analyses for a paleosome of an orthogneiss (sample T14-3-10)

	Analysis name	Texture	Spot size	U conc.	Ratios						rho:	Ages (Ma)									Common Pb		Degree of concordance (%)
			(µm)	(ppm)	$^{206}Pb/^{238}U$	± 2σ	$^{207}Pb/^{235}U$	± 2σ	$^{207}Pb/^{206}Pb$	± 2σ		$^{206}Pb/^{238}U$	± 2σ	± 2σ%	$^{207}Pb/^{235}U$	± 2σ	± 2σ%	$^{207}Pb/^{206}Pb$	± 2σ	± 2σ%	$^{206}Pb/^{204}Pb$	ƒ206%	
Melanosome from an orthogneiss	T14-3-12-7	rim	35	813	0.3404	0.0039	5.7286	0.0933	0.1221	0.0014	0.70	1888	19	1.0	1936	14	0.7	1987	21	1.0	687	2.2	95.0
	T14-3-5-7	rim	35	193	0.3926	0.0078	7.8843	0.2068	0.1457	0.0025	0.75	2135	36	1.7	2218	24	1.1	2296	30	1.3	20401	0.1	93.0
	T14-3-4-8	rim	35	1071	0.3431	0.0041	5.9619	0.0942	0.1260	0.0013	0.75	1901	19	1.0	1970	14	0.7	2043	19	0.9	10390	0.2	93.0
	T14-3-19-7	rim	35	1244	0.3299	0.0093	5.4983	0.1949	0.1209	0.0026	0.80	1838	45	2.5	1900	30	1.6	1969	38	1.9	5122	0.3	93.3
	T14-3-8-7	rim	35	368	0.4184	0.0056	8.8944	0.1614	0.1542	0.0019	0.74	2253	26	1.1	2327	17	0.7	2393	21	0.9	17171	0.1	94.2
	T14-3-6-7	rim	35	1286	0.3602	0.0076	6.4678	0.1690	0.1302	0.0020	0.81	1983	36	1.8	2042	23	1.1	2101	27	1.3	5085	0.3	94.4
	T14-3-7-7	rim	35	879	0.3628	0.0059	6.4893	0.1364	0.1297	0.0017	0.77	1995	28	1.4	2044	18	0.9	2094	24	1.1	4281	0.4	95.3
	T14-3-14-7	rim	35	1341	0.4505	0.0073	10.2760	0.2362	0.1654	0.0027	0.70	2397	32	1.3	2460	21	0.9	2512	27	1.1	9233	0.2	95.4
	T14-3-13-7	rim	35	1488	0.3505	0.0044	6.0311	0.0917	0.1248	0.0011	0.82	1937	21	1.1	1980	13	0.7	2026	15	0.8	14842	0.1	95.6
	T14-3-2-7	rim	35	694	0.3770	0.0064	6.6854	0.1483	0.1286	0.0018	0.76	2062	30	1.5	2071	20	0.9	2079	25	1.2	14848	0.1	99.2
	T14-3-16-7	rim	35	633	0.3823	0.0062	6.7692	0.1459	0.1284	0.0018	0.76	2087	29	1.4	2082	19	0.9	2076	25	1.2	19535	0.1	100.5
	T14-3-3-4	rim	35	195	0.4084	0.0087	8.0281	0.2232	0.1426	0.0025	0.77	2208	40	1.8	2234	25	1.1	2259	31	1.4	7776	0.2	97.7
	T14-3-4-7	rim	35	1151	0.3700	0.0109	6.4545	0.2134	0.1265	0.0019	0.89	2030	51	2.5	2040	29	1.4	2050	27	1.3	5291	0.3	99.0
	T14-3-9-7	rim	35	1579	0.3702	0.0049	6.4051	0.1613	0.1255	0.0027	0.53	2030	23	1.1	2033	22	1.1	2036	38	1.9	6030	0.3	99.7
	T14-3-15-7	rim	35	835	0.3658	0.0047	6.2463	0.0993	0.1238	0.0012	0.81	2010	22	1.1	2011	14	0.7	2012	17	0.8	89498	0.0	99.9
	T14-3-3-8	rim	35	833	0.3683	0.0048	6.3241	0.1133	0.1245	0.0015	0.73	2021	23	1.1	2022	16	0.8	2022	22	1.1	32837	0.0	100.0
	T14-3-3-7	rim	35	985	0.3712	0.0056	6.3487	0.1305	0.1240	0.0017	0.73	2035	26	1.3	2025	18	0.9	2015	25	1.2	73800	0.0	101.0
	T14-3-1-7	rim	35	712	0.3748	0.0057	6.3798	0.1241	0.1235	0.0015	0.78	2052	27	1.3	2029	17	0.8	2007	22	1.1	88002	0.0	102.2
	T14-3-10-4	rim	35	258	0.3947	0.0060	6.9512	0.1418	0.1277	0.0018	0.74	2145	28	1.3	2105	18	0.9	2067	24	1.2	6105	0.3	103.8
	T14-3-9-4	rim	35	1482	0.3784	0.0078	6.5510	0.1903	0.1255	0.0026	0.71	2069	36	1.8	2053	26	1.2	2037	36	1.8	217734	0.0	101.6
	T14-3-13-4	core	35	116	0.4295	0.0054	8.7120	0.1527	0.1471	0.0018	0.72	2304	24	1.1	2308	16	0.7	2313	21	0.9	1182	1.5	99.6
	T14-3-2-4	core	35	156	0.5514	0.0070	14.1044	0.2597	0.1855	0.0025	0.69	2831	29	1.0	2757	17	0.6	2703	22	0.8		0.0	104.7
	T14-3-12-4	core	35	126	0.4507	0.0065	10.3873	0.2098	0.1672	0.0023	0.72	2398	29	1.2	2470	19	0.8	2529	24	0.9	681	2.6	94.8
	T14-3-19-4	core	35	1127	0.4385	0.0068	9.4000	0.1728	0.1555	0.0016	0.84	2344	30	1.3	2378	17	0.7	2407	17	0.7	7898	0.2	97.4
	T14-3-16-4	core	35	623	0.4477	0.0075	9.7766	0.1965	0.1584	0.0018	0.83	2385	33	1.4	2414	19	0.8	2439	19	0.8		0.0	97.8
	T14-3-17-4	core	35	143	0.4503	0.0052	9.8989	0.1543	0.1594	0.0017	0.73	2397	23	1.0	2425	14	0.6	2450	18	0.7	1555680	0.0	97.8
	T14-3-7-4	core	35	250	0.4715	0.0058	10.4007	0.1700	0.1600	0.0017	0.75	2490	25	1.0	2471	15	0.6	2456	18	0.7	34743	0.0	101.4
	T14-3-5-4	core	35	673	0.5136	0.0067	12.3241	0.2165	0.1740	0.0021	0.74	2672	28	1.1	2629	16	0.6	2597	20	0.8	13260	0.1	102.9
	T14-3-1-4	core	35	212	0.5177	0.0102	13.4100	0.3141	0.1879	0.0024	0.84	2689	43	1.6	2709	22	0.8	2724	21	0.8		0.0	98.7
	T14-3-11-4	core	35	201	0.5058	0.0077	12.4924	0.2256	0.1791	0.0017	0.84	2639	33	1.3	2642	17	0.6	2645	16	0.6	16239	0.1	99.8
	T14-3-8-4	core	35	2344	0.5144	0.0096	12.9835	0.2915	0.1831	0.0023	0.84	2675	41	1.5	2678	21	0.8	2681	20	0.8	64720	0.0	99.8
	T14-3-15-4	core	35	370	0.5163	0.0124	13.0696	0.3422	0.1836	0.0019	0.92	2683	53	2.0	2685	25	0.9	2686	17	0.6	403283	0.0	99.9
	T14-3-14-4	core	35	467	0.5210	0.0070	13.3335	0.2200	0.1856	0.0018	0.82	2703	30	1.1	2704	16	0.6	2704	16	0.6	11655	0.2	100.0
	T14-3-18-4	core	35	225	0.5099	0.0088	12.6117	0.2639	0.1794	0.0021	0.82	2656	37	1.4	2651	20	0.7	2647	20	0.8	4528	0.4	100.3
	T14-3-6-4	core	35	386	0.5145	0.0131	12.6549	0.3798	0.1784	0.0028	0.85	2676	56	2.1	2654	28	1.1	2638	26	1.0	2072	0.9	101.4
	91500-1		35	76	0.1763	0.0025	1.8056	0.0415	0.0743	0.0013	0.62	1047	14	1.3	1047	15	1.4	1049	36	3.5	2536	0.4	99.8
	91500-2		35	80	0.1823	0.0031	1.8971	0.0505	0.0755	0.0015	0.64	1080	17	1.6	1080	18	1.6	1081	41	3.8	14726	0.1	99.9

Table 5. LA-ICP-MS analyses for a leucosome of an orthogneiss (sample T14-1-10)

	Analysis name	Texture	Spot size	U conc.	Ratios						rho:	Ages (Ma)									Common Pb		Degree of concordance (%)
			(µm)	(ppm)	$^{206}Pb/^{238}U$	± 2σ	$^{207}Pb/^{235}U$	± 2σ	$^{207}Pb/^{206}Pb$	± 2σ		$^{206}Pb/^{238}U$	± 2σ	± 2σ%	$^{207}Pb/^{235}U$	± 2σ	± 2σ%	$^{207}Pb/^{206}Pb$	± 2σ	± 2σ%	$^{206}Pb/^{204}Pb$	ƒ206%	
Leucosome from an orthogneiss	**T14-1-15-1**	**Inh. core**	**35**	**116**	**0.5457**	**0.0086**	**14.9656**	**0.3419**	**0.1989**	**0.0033**	**0.69**	**2807**	**36**	**1.3**	**2813**	**22**	**0.8**	**2817**	**27**	**1.0**		**0.0**	**99.6**
	T14-1-6-1	core	35	1653	0.4116	0.0169	7.8178	0.7716	0.1378	0.0124	0.42	2222	77	3.5	2210	89	4.0	2199	156	7.1	194	7.1	101.0
	T14-1-4-1	core	35	315	0.5004	0.0120	11.8904	0.4042	0.1723	0.0042	0.70	2615	51	2.0	2596	32	1.2	2581	40	1.6	299	4.6	101.4
	T14-1-11-1	core	35	491	0.4610	0.0076	9.3536	0.2564	0.1472	0.0032	0.60	2444	33	1.4	2373	25	1.1	2313	38	1.6	1225	1.1	105.6
	T14-1-13-1	core	35	508	0.3944	0.0089	7.3489	0.2729	0.1352	0.0040	0.61	2143	41	1.9	2155	33	1.5	2166	51	2.4	3517	0.5	98.9
	T14-1-9-1	core	35	189	0.4274	0.0109	8.7521	0.2792	0.1485	0.0028	0.80	2294	49	2.2	2313	29	1.3	2329	33	1.4	7980	0.2	98.5
	T14-1-1-1	core	35	533	0.4278	0.0056	8.7721	0.1907	0.1487	0.0026	0.60	2296	25	1.1	2315	20	0.9	2331	30	1.3	2378	0.6	98.5
	T14-1-12-1	core	35	316	0.4671	0.0086	10.2321	0.2608	0.1589	0.0028	0.72	2471	38	1.5	2456	24	1.0	2444	30	1.2	12160	0.1	101.1
	T14-1-16-1	core	35	559	0.4621	0.0098	10.1673	0.2682	0.1596	0.0025	0.80	2449	43	1.8	2450	24	1.0	2451	27	1.1	2051	0.9	99.9
	T14-1-10-1	core	35	1671	0.4668	0.0109	10.5514	0.3046	0.1639	0.0028	0.81	2470	48	1.9	2484	27	1.1	2497	29	1.2	19016	0.1	98.9
	T14-1-7-1	core	35	831	0.4835	0.0100	11.5290	0.3038	0.1729	0.0028	0.78	2543	43	1.7	2567	25	1.0	2586	27	1.1	13201	0.1	98.3
	T14-1-2-1	core	35	215	0.4886	0.0066	11.8971	0.2336	0.1766	0.0025	0.69	2564	28	1.1	2596	18	0.7	2621	24	0.9	5183	0.3	97.8
	T14-1-14-1	core	35	248	0.5092	0.0102	12.8253	0.3424	0.1827	0.0032	0.75	2653	44	1.6	2667	25	0.9	2677	29	1.1	992	1.8	99.1
	T14-1-5-1	core	35	408	0.5085	0.0070	12.3978	0.2372	0.1768	0.0023	0.72	2650	30	1.1	2635	18	0.7	2624	22	0.8	19651	0.1	101.0
	T14-1-5-4	core	35	996	0.5099	0.0083	12.7026	0.2912	0.1807	0.0029	0.71	2656	35	1.3	2658	22	0.8	2659	27	1.0	52269	0.0	99.9
	T14-1-8-4	rim	35	975	0.5144	0.0104	12.7358	0.3306	0.1796	0.0029	0.78	2675	44	1.7	2660	24	0.9	2649	27	1.0	3545	0.4	101.0
	T14-1-8-1	core	35	174	0.5122	0.0087	12.8191	0.3044	0.1815	0.0030	0.72	2666	37	1.4	2666	22	0.8	2667	27	1.0	11803	0.2	100.0
	T14-1-17-1	core	35	1001	0.5441	0.0079	13.7699	0.2944	0.1836	0.0029	0.68	2800	33	1.2	2734	20	0.7	2685	26	1.0	357334	0.0	104.3
	T14-1-3-4	rim	35	999	0.3774	0.0054	6.5327	0.1279	0.1256	0.0017	0.72	2064	25	1.2	2050	17	0.8	2037	24	1.2	11337	0.2	101.3
	T14-1-9-4	rim	35	659	0.3790	0.0057	6.6953	0.1442	0.1281	0.0020	0.70	2071	27	1.3	2072	19	0.9	2073	27	1.3	3493	0.5	99.9
	T14-1-12-4	rim	35	928	0.3779	0.0069	6.5407	0.1679	0.1255	0.0023	0.71	2067	32	1.6	2051	23	1.1	2036	32	1.6	43780	0.0	101.5
	T14-1-10-4	rim	35	837	0.3660	0.0059	6.2835	0.1420	0.1245	0.0020	0.71	2011	28	1.4	2016	20	1.0	2022	28	1.4	20900	0.1	99.4
	T14-1-15-4	rim	35	1054	0.3724	0.0056	6.4661	0.1399	0.1259	0.0020	0.69	2041	26	1.3	2041	19	0.9	2042	28	1.3	14866	0.1	99.9
	T14-1-16-4	rim	35	1258	0.3718	0.0054	6.4799	0.1364	0.1264	0.0019	0.69	2038	25	1.2	2043	19	0.9	2048	27	1.3	43031	0.0	99.5
	T14-1-12-5	rim	35	480	0.3215	0.0047	6.0453	0.1436	0.1364	0.0026	0.61	1797	23	1.3	1982	21	1.0	2182	33	1.5	4819	0.4	82.4
	T14-1-17-4	rim	35	991	0.3542	0.0045	6.1760	0.1241	0.1265	0.0020	0.64	1954	22	1.1	2001	18	0.9	2050	27	1.3	4557	0.4	95.4
	T14-1-11-4	rim	35	1167	0.3655	0.0045	6.4309	0.1326	0.1276	0.0021	0.60	2008	21	1.1	2037	18	0.9	2065	29	1.4	4113	0.4	97.2
	T14-1-4-2	rim	35	907	0.4005	0.0058	7.1206	0.1436	0.1289	0.0018	0.72	2171	27	1.2	2127	18	0.8	2084	25	1.2	3003	0.6	104.2
	T14-1-6-4	rim	35	1536	0.4813	0.0142	10.6581	0.5194	0.1606	0.0062	0.61	2533	62	2.4	2494	45	1.8	2462	66	2.7	999	1.8	102.9
	T14-1-14-4	rim	35	1508	0.3457	0.0175	5.6425	0.3111	0.1184	0.0026	0.92	1914	84	4.4	1923	48	2.5	1932	39	2.0	915	1.9	99.0
	T14-1-2-4	rim	35	1623	0.4855	0.0085	10.7352	0.5105	0.1604	0.0071	0.37	2551	37	1.5	2500	44	1.8	2460	75	3.0	190	9.3	103.7
	91500-2		35	83	0.1782	0.0031	1.8221	0.0468	0.0742	0.0014	0.68	1057	17	1.6	1053	17	1.6	1046	38	3.6	2550	0.4	101.1
	91500-3		35	73	0.1833	0.0021	1.9082	0.0386	0.0755	0.0013	0.55	1085	11	1.0	1084	13	1.2	1082	34	3.1	3274	0.1	100.3
	91500-4		35	69	0.1851	0.0022	1.9368	0.0423	0.0759	0.0014	0.55	1095	12	1.1	1094	15	1.3	1092	37	3.4			100.3

Table 6. LA-ICP-MS analyses for a granitic gneiss (sample T6-6-10)

	Analysis name	Texture	Spot size	U conc.	Ratios						rho:	Ages (Ma)									Common Pb		Degree of concordance (%)
			(μm)	(ppm)	$^{206}Pb/^{238}U$	± 2σ	$^{207}Pb/^{235}U$	± 2σ	$^{207}Pb/^{206}Pb$	± 2σ		$^{206}Pb/^{238}U$	± 2σ	± 2σ%	$^{207}Pb/^{235}U$	± 2σ	± 2σ%	$^{207}Pb/^{206}Pb$	± 2σ	± 2σ%	$^{206}Pb/^{204}Pb$	ƒ206%	
Granitic gneiss	T6-6-15-1	core	35	2602	0.0265	0.0015	0.4412	0.0375	0.1209	0.0075	0.69	168	10	5.8	371	26	7.1	1970	110	5.6	36	48.9	8.5
	T6-6-1-1	core	35	1097	0.1403	0.0030	2.8430	0.1438	0.1470	0.0067	0.43	846	17	2.0	1367	38	2.8	2311	79	3.4	48	28.5	36.6
	T6-6-21-7	core	35	282	0.2720	0.0167	6.0717	0.4040	0.1619	0.0041	0.92	1551	85	5.5	1986	58	2.9	2476	43	1.7	142	9.7	62.6
	T6-6-7-1	core	35	935	0.4913	0.0112	11.7344	0.3849	0.1732	0.0041	0.70	2576	48	1.9	2583	31	1.2	2589	39	1.5	449	4.0	99.5
	T6-6-2-1	core	35	180	0.4973	0.0073	11.8757	0.2554	0.1732	0.0027	0.68	2602	31	1.2	2595	20	0.8	2589	26	1.0	638	2.8	100.5
	T6-6-6-7	core	35	225	0.3770	0.0061	9.2292	0.2082	0.1775	0.0028	0.72	2062	29	1.4	2361	21	0.9	2630	26	1.0	1119	1.6	78.4
	T6-6-3-7	core	35	184	0.4755	0.0085	11.4831	0.2846	0.1751	0.0030	0.72	2508	37	1.5	2563	23	0.9	2607	29	1.1	12384	0.1	96.2
	T6-6-4-2	core	35	411	0.4870	0.0079	11.9689	0.2588	0.1782	0.0026	0.75	2558	34	1.3	2602	20	0.8	2637	24	0.9		0.0	97.0
	T6-6-5-4	core	35	145	0.5255	0.0070	13.0521	0.2623	0.1801	0.0027	0.66	2722	29	1.1	2683	19	0.7	2654	25	0.9	3326	0.4	102.6
	T6-6-9-4	core	35	253	0.5228	0.0073	12.8797	0.2494	0.1787	0.0024	0.72	2711	31	1.1	2671	18	0.7	2641	22	0.8	99627	0.0	102.7
	T6-6-3-2	core	35	328	0.5221	0.0079	12.8379	0.2688	0.1783	0.0026	0.72	2708	33	1.2	2668	20	0.7	2637	24	0.9		0.0	102.7
	T6-6-7-4	core	35	225	0.5198	0.0087	12.6487	0.2759	0.1765	0.0025	0.77	2698	37	1.4	2654	21	0.8	2620	23	0.9		0.0	103.0
	T6-6-4-1	core	35	463	0.5310	0.0068	13.1332	0.2583	0.1794	0.0027	0.65	2746	29	1.0	2689	19	0.7	2647	25	0.9	28870	0.1	103.7
	T6-6-18-8	core	35	133	0.4851	0.0071	11.6735	0.2034	0.1745	0.0016	0.84	2549	31	1.2	2579	16	0.6	2602	16	0.6	9150	0.2	98.0
	T6-6-17-4	core	35	185	0.4900	0.0093	11.7330	0.2646	0.1736	0.0021	0.84	2571	40	1.6	2583	21	0.8	2593	20	0.8	162638	0.0	99.1
	T6-6-13-1	core	35	58	0.4904	0.0059	12.0045	0.2046	0.1775	0.0021	0.71	2572	26	1.0	2605	16	0.6	2630	20	0.8	20422	0.1	97.8
	T6-6-3-5	core	35	154	0.4919	0.0086	11.6929	0.3056	0.1724	0.0034	0.67	2579	37	1.4	2580	24	0.9	2581	32	1.3		0.0	99.9
	T6-6-3-1	core	35	455	0.4954	0.0082	11.7895	0.2618	0.1726	0.0025	0.75	2594	36	1.4	2588	21	0.8	2583	25	0.9		0.0	100.4
	T6-6-18-7	core	35	111	0.5007	0.0067	11.8769	0.1992	0.1720	0.0017	0.80	2617	29	1.1	2595	16	0.6	2578	17	0.6		0.0	101.5
	T6-6-15-4	core	35	180	0.5075	0.0067	12.5475	0.2033	0.1793	0.0017	0.82	2646	29	1.1	2646	15	0.6	2647	16	0.6	14176	0.1	100.0
	T6-6-16-1	core	35	405	0.5104	0.0090	12.4043	0.2663	0.1763	0.0022	0.82	2658	38	1.4	2636	20	0.8	2618	20	0.8	55013	0.0	101.5
	T6-6-17-7	core	35	113	0.5035	0.0086	12.3302	0.2861	0.1776	0.0028	0.74	2629	37	1.4	2630	22	0.8	2631	26	1.0	27501	0.0	99.9
	T6-6-18-9	core	35	188	0.5104	0.0090	12.4976	0.2652	0.1776	0.0021	0.83	2658	39	1.5	2643	20	0.8	2630	19	0.7	124939	0.0	101.1
	T6-6-19-7	core	35	115	0.5025	0.0083	12.2143	0.2461	0.1763	0.0020	0.82	2624	36	1.4	2621	19	0.7	2618	19	0.7		0.0	100.2
	T6-6-19-8	core	35	140	0.5016	0.0088	12.2395	0.2504	0.1770	0.0018	0.86	2621	38	1.4	2623	19	0.7	2625	17	0.7	319743	0.0	99.8
	T6-6-21-8	core	35	229	0.5088	0.0081	12.6292	0.2422	0.1800	0.0019	0.83	2651	35	1.3	2652	18	0.7	2653	18	0.7	5275	0.3	99.9
	T6-6-1-4	core	35	121	0.4977	0.0056	12.1304	0.1996	0.1768	0.0021	0.69	2604	24	0.9	2615	15	0.6	2623	20	0.8		0.0	99.3
	T6-6-3-4	core	35	135	0.5094	0.0063	12.6347	0.2402	0.1799	0.0026	0.65	2654	27	1.0	2653	18	0.7	2652	24	0.9	3288	0.5	100.1
	T6-6-4-4	core	35	164	0.5088	0.0068	12.4852	0.2497	0.1780	0.0026	0.67	2651	29	1.1	2642	19	0.7	2634	25	0.9		0.0	100.7
	T6-6-8-4	core	35	186	0.5070	0.0063	12.4021	0.2225	0.1774	0.0023	0.69	2644	27	1.0	2635	17	0.6	2629	21	0.8	45127	0.0	100.6
	T6-6-10-4	core	35	144	0.5055	0.0078	12.4071	0.2368	0.1780	0.0020	0.81	2637	34	1.3	2636	18	0.7	2635	18	0.7	60837	0.0	100.1
	T6-6-10-7	core	35	149	0.5084	0.0070	12.5795	0.2240	0.1795	0.0020	0.78	2650	30	1.1	2649	17	0.6	2648	19	0.7	92181	0.0	100.1
	T6-6-11-4	core	35	225	0.5070	0.0084	12.5461	0.2603	0.1795	0.0022	0.80	2644	36	1.4	2646	20	0.7	2648	21	0.8	12309	0.1	99.8
	T6-6-13-4	core	35	165	0.5038	0.0055	12.3353	0.1824	0.1776	0.0018	0.74	2630	23	0.9	2630	14	0.5	2630	17	0.6	16022	0.1	100.0
	T6-6-14-1	core	35	115	0.5078	0.0054	12.7252	0.1811	0.1817	0.0017	0.75	2647	23	0.9	2660	13	0.5	2669	16	0.6	31048	0.0	99.2
	T6-6-14-4	core	35	157	0.5051	0.0069	12.3772	0.2157	0.1777	0.0019	0.78	2635	29	1.1	2633	16	0.6	2632	18	0.7		0.0	100.1
	T6-6-16-4	core	35	197	0.5134	0.0076	12.7543	0.2325	0.1802	0.0019	0.81	2671	32	1.2	2662	17	0.6	2655	18	0.7	8791	0.1	100.6
	T6-6-13-5	core	35	173	0.5134	0.0063	12.8075	0.2045	0.1809	0.0019	0.77	2671	27	1.0	2666	15	0.6	2661	17	0.6	19090	0.1	100.4
	T6-6-2-4	core	35	165	0.5134	0.0064	12.4136	0.2097	0.1754	0.0020	0.73	2671	27	1.0	2636	16	0.6	2609	19	0.7	34351	0.0	102.4
	T6-6-1-5	core	35	159	0.5155	0.0055	12.6054	0.1924	0.1774	0.0019	0.70	2680	24	0.9	2651	14	0.5	2628	18	0.7	41413	0.0	102.0
	T6-6-11-1	core	35	525	0.5155	0.0094	12.8947	0.2954	0.1814	0.0025	0.80	2680	40	1.5	2672	22	0.8	2666	23	0.9	3086	0.6	100.5
	T6-6-10-1	core	35	261	0.5157	0.0088	12.8488	0.2899	0.1807	0.0027	0.75	2681	37	1.4	2669	21	0.8	2659	25	0.9	9337	0.2	100.8
	T6-6-6-4	core	35	75	0.5180	0.0096	13.0244	0.3485	0.1824	0.0035	0.69	2691	41	1.5	2681	25	0.9	2674	32	1.2		0.0	100.6
	T6-6-9-1	core	35	168	0.5223	0.0064	13.3131	0.2391	0.1849	0.0024	0.69	2709	27	1.0	2702	17	0.6	2697	22	0.8	213413	0.0	100.4
	T6-6-8-1	core	35	157	0.5269	0.0093	13.3077	0.3075	0.1832	0.0027	0.76	2728	39	1.4	2702	22	0.8	2682	25	0.9	28138	0.1	101.7
	T6-6-5-7	core	35	310	0.3620	0.0032	6.1297	0.0917	0.1228	0.0015	0.59	1992	15	0.8	1994	13	0.7	1997	21	1.1	7241	0.2	99.7
	T6-6-20-7	core	35	364	0.3747	0.0058	6.4723	0.1207	0.1253	0.0013	0.83	2052	27	1.3	2042	16	0.8	2033	18	0.9	7707	0.2	100.9
	T6-6-20-8	core	35	336	0.3758	0.0063	6.4252	0.1278	0.1240	0.0013	0.85	2056	30	1.4	2036	17	0.9	2015	19	0.9	1833935	0.0	102.1
	91500-4		35	82	0.1814	0.0033	1.8807	0.0519	0.0752	0.0016	0.66	1074	18	1.7	1074	18	1.7	1074	42	3.9		0.0	100.0
	91500-1		35	81	0.1789	0.0023	1.8403	0.0322	0.0746	0.0009	0.73	1061	13	1.2	1060	12	1.1	1059	24	2.3	3652	0.3	100.2
	91500-2		35	81	0.1804	0.0027	1.8660	0.0396	0.0750	0.0011	0.69	1069	15	1.4	1069	14	1.3	1069	31	2.9		0.0	100.1

Table 7. LA-ICP-MS analyses for a garnet amphibolite (sample T17-3-10)

	Analysis name	Texture	Spot size	U conc.	Ratios						rho:	Ages (Ma)									Common Pb		Degree of concordance (%)
			(µm)	(ppm)	$^{206}Pb/^{238}U$	± 2σ	$^{207}Pb/^{235}U$	± 2σ	$^{207}Pb/^{206}Pb$	± 2σ		$^{206}Pb/^{238}U$	± 2σ	± 2σ%	$^{207}Pb/^{235}U$	± 2σ	± 2σ%	$^{207}Pb/^{206}Pb$	± 2σ	± 2σ%	$^{206}Pb/^{204}Pb$	ƒ206%	
Garnet amphibolite	T17-3-23-1	core	35	150	0.7081	0.0179	22.0248	1.3436	0.2256	0.0125	0.41	3451	68	2.0	3185	59	1.9	3021	89	3.0	349	3.9	114.2
	T17-3-20-4	core	35	220	0.4850	0.0113	12.1520	0.3533	0.1817	0.0031	0.80	2549	49	1.9	2616	27	1.0	2669	29	1.1	19826	0.1	95.5
	T17-3-3-1	core	25	312	0.4906	0.0095	12.2402	0.3552	0.1810	0.0039	0.67	2573	41	1.6	2623	27	1.0	2662	36	1.3	296115	0.0	96.7
	T17-3-10-1	core	35	94	0.5329	0.0117	13.3904	0.3783	0.1823	0.0032	0.78	2753	49	1.8	2708	27	1.0	2674	29	1.1		0.0	103.0
	T17-3-18-5	core	35	53	0.5294	0.0157	12.9640	0.4829	0.1776	0.0040	0.80	2739	66	2.4	2677	35	1.3	2631	37	1.4	2247	0.7	104.1
	T17-3-23-4	core	35	346	0.5800	0.0172	14.0004	0.4900	0.1751	0.0033	0.85	2949	70	2.4	2750	33	1.2	2607	31	1.2	3675	0.5	113.1
	T17-3-6-7	core	35	175	0.5034	0.0152	12.7204	0.4546	0.1833	0.0035	0.84	2628	65	2.5	2659	34	1.3	2683	32	1.2	16775	0.1	98.0
	T17-3-14-1	core	35	248	0.5104	0.0118	12.3112	0.3422	0.1749	0.0027	0.83	2658	50	1.9	2628	26	1.0	2606	26	1.0		0.0	102.0
	T17-3-22-7	core	35	135	0.5294	0.0117	13.3167	0.3446	0.1824	0.0025	0.85	2739	49	1.8	2702	24	0.9	2675	22	0.8	9739	0.2	102.4
	T17-3-24-4	core	35	77	0.4992	0.0208	12.2714	0.5860	0.1783	0.0042	0.87	2610	89	3.4	2625	45	1.7	2637	39	1.5		0.0	99.0
	T17-3-10-4	core	35	394	0.5003	0.0155	12.3016	0.4313	0.1783	0.0029	0.89	2615	67	2.6	2628	33	1.3	2637	27	1.0	16625	0.1	99.1
	T17-3-6-4	core	35	50	0.5051	0.0144	12.5638	0.4291	0.1804	0.0034	0.83	2636	61	2.3	2648	32	1.2	2657	31	1.2	25780	0.0	99.2
	T17-3-6-1	core	35	82	0.5078	0.0165	12.6478	0.4834	0.1806	0.0036	0.85	2647	70	2.7	2654	36	1.4	2659	33	1.3	23831	0.1	99.6
	T17-3-18-4	core	35	52	0.5108	0.0147	12.8193	0.4545	0.1820	0.0038	0.81	2660	63	2.4	2666	33	1.3	2671	34	1.3		0.0	99.6
	T17-3-5-1	core	35	99	0.5104	0.0150	12.7877	0.4477	0.1817	0.0035	0.84	2658	64	2.4	2664	33	1.2	2669	32	1.2		0.0	99.6
	T17-3-12-4	core	35	83	0.5178	0.0137	13.2037	0.3996	0.1849	0.0027	0.87	2690	58	2.2	2694	29	1.1	2698	24	0.9	5155	0.2	99.7
	T17-3-13-4	core	35	178	0.5084	0.0095	12.6432	0.3245	0.1804	0.0032	0.73	2650	41	1.5	2653	24	0.9	2656	29	1.1	13009	0.1	99.7
	T17-3-1-1	core	25	253	0.5057	0.0136	12.4871	0.4252	0.1791	0.0038	0.79	2638	58	2.2	2642	32	1.2	2644	35	1.3	19497	0.1	99.8
	T17-3-21-4	core	35	90	0.5098	0.0169	12.7116	0.4909	0.1808	0.0036	0.86	2656	72	2.7	2659	36	1.4	2661	33	1.2	12995	0.1	99.8
	T17-3-12-1	core	35	130	0.5095	0.0106	12.6848	0.3368	0.1806	0.0030	0.79	2654	45	1.7	2657	25	0.9	2658	27	1.0	13508	0.1	99.8
	T17-3-18-7	core	35	148	0.4986	0.0120	12.0685	0.3541	0.1755	0.0029	0.82	2608	52	2.0	2610	28	1.1	2611	28	1.1	9126	0.1	99.9
	T17-3-17-4	core	35	65	0.5062	0.0136	12.4761	0.4127	0.1787	0.0035	0.81	2640	58	2.2	2641	31	1.2	2641	32	1.2		0.0	100.0
	T17-3-20-1	core	35	163	0.5091	0.0149	12.6356	0.4254	0.1800	0.0030	0.87	2653	64	2.4	2653	32	1.2	2653	27	1.0		0.0	100.0
	T17-3-2-7	core	35	222	0.5075	0.0122	12.5457	0.3545	0.1793	0.0027	0.85	2646	52	2.0	2646	27	1.0	2646	25	0.9		0.0	100.0
	T17-3-19-4	core	35	41	0.5084	0.0173	12.5938	0.5435	0.1797	0.0048	0.79	2650	74	2.8	2650	41	1.5	2650	44	1.7		0.0	100.0
	T17-3-17-1	core	35	100	0.5042	0.0137	12.3563	0.3848	0.1777	0.0027	0.87	2632	59	2.2	2632	29	1.1	2632	25	1.0		0.0	100.0
	T17-3-22-1	core	35	126	0.5064	0.0160	12.4752	0.4508	0.1787	0.0031	0.87	2641	68	2.6	2641	34	1.3	2641	29	1.1	5148	0.2	100.0
	T17-3-17-2	core	35	122	0.5145	0.0126	12.9413	0.3924	0.1824	0.0033	0.81	2676	54	2.0	2675	29	1.1	2675	30	1.1	14274	0.1	100.0
	T17-3-1-4	core	25	621	0.5091	0.0124	12.6232	0.4190	0.1798	0.0040	0.74	2653	53	2.0	2652	31	1.2	2651	37	1.4	12035663	0.0	100.0
	T17-3-13-1	core	35	88	0.5172	0.0141	13.0934	0.4289	0.1836	0.0033	0.83	2687	60	2.2	2686	31	1.2	2686	30	1.1		0.0	100.0
	T17-3-21-1	core	35	107	0.5045	0.0162	12.3606	0.4753	0.1777	0.0038	0.83	2633	69	2.6	2632	36	1.4	2632	35	1.3		0.0	100.1
	T17-3-2-4	core	35	47	0.5130	0.0130	12.6602	0.3748	0.1790	0.0028	0.85	2669	55	2.1	2655	28	1.0	2644	26	1.0	2566	0.3	101.0
	T17-3-5-4	core	35	283	0.5135	0.0168	12.6630	0.4787	0.1788	0.0034	0.87	2672	72	2.7	2655	36	1.3	2642	31	1.2		0.0	101.1
	T17-3-4-4	core	35	47	0.5135	0.0153	12.6322	0.4507	0.1784	0.0035	0.84	2671	65	2.4	2653	34	1.3	2638	32	1.2	10083	0.1	101.3
	T17-3-24-1	core	35	111	0.5175	0.0180	12.8209	0.5261	0.1797	0.0039	0.85	2688	77	2.8	2667	39	1.5	2650	36	1.4	6665	0.2	101.4
	91500-4		35	72	0.1727	0.0053	1.7346	0.0720	0.0728	0.0021	0.73	1027	29	2.8	1021	27	2.6	1009	57	5.7	2836	0.3	101.8
	91500-6		35	104	0.1796	0.0071	1.8588	0.0959	0.0751	0.0025	0.77	1065	39	3.6	1067	34	3.2	1070	67	6.2		0.0	99.5
	91500-1		25	150	0.1808	0.0025	1.8677	0.0457	0.0749	0.0015	0.56	1071	13	1.3	1070	16	1.5	1067	41	3.8	6445	0.1	100.4

Table 8. LA-ICP-MS analyses for a gabbronorite (sample T17-1-10)

	Analysis name	Texture	Spot size	U conc.	Ratios						rho:	Ages (Ma)									Common Pb		Degree of concordance (%)
			(μm)	(ppm)	$^{206}Pb/^{238}U$	± 2σ	$^{207}Pb/^{235}U$	± 2σ	$^{207}Pb/^{206}Pb$	± 2σ		$^{206}Pb/^{238}U$	± 2σ	± 2σ%	$^{207}Pb/^{235}U$	± 2σ	± 2σ%	$^{207}Pb/^{206}Pb$	± 2σ	± 2σ%	$^{206}Pb/^{204}Pb$	ƒ206%	
Gabbronorite	T17-1-12-4	core	35	135	0.4210	0.0082	10.1467	0.2933	0.1748	0.0037	0.68	2265	37	1.6	2448	27	1.1	2604	36	1.4	8667	0.2	87.0
	T17-1-6-4	core	35	90	0.4672	0.0080	11.6434	0.2436	0.1807	0.0022	0.81	2471	35	1.4	2576	20	0.8	2660	20	0.8		0.0	92.9
	T17-1-7-4	core	35	153	0.4738	0.0077	11.7160	0.2331	0.1793	0.0021	0.82	2500	34	1.3	2582	19	0.7	2647	19	0.7	12860	0.1	94.5
	T17-1-5-5	core	35	428	0.4796	0.0082	11.9721	0.2428	0.1810	0.0020	0.84	2525	36	1.4	2602	19	0.7	2663	18	0.7		0.0	94.9
	T17-1-14-4	core	35	323	0.4808	0.0059	11.9493	0.1861	0.1803	0.0017	0.79	2531	26	1.0	2600	15	0.6	2655	16	0.6	82350	0.0	95.3
	T17-1-3-4	core	35	82	0.4890	0.0068	11.9874	0.2160	0.1778	0.0020	0.78	2566	30	1.2	2603	17	0.6	2632	19	0.7		0.0	97.5
	T17-1-9-4	core	35	233	0.4893	0.0075	11.9639	0.2231	0.1773	0.0019	0.83	2568	33	1.3	2602	17	0.7	2628	17	0.7		0.0	97.7
	T17-1-10-5	core	35	474	0.4913	0.0072	12.0746	0.2184	0.1782	0.0019	0.81	2576	31	1.2	2610	17	0.6	2637	18	0.7	105204	0.0	97.7
	T17-1-4-4	core	35	365	0.4992	0.0084	12.3364	0.2455	0.1792	0.0019	0.85	2610	36	1.4	2630	19	0.7	2646	18	0.7		0.0	98.7
	T17-1-2-4	core	35	435	0.5021	0.0063	12.4509	0.2046	0.1798	0.0019	0.77	2623	27	1.0	2639	15	0.6	2652	17	0.7	175965	0.0	98.9
	T17-1-8-4	core	35	423	0.5007	0.0086	12.3367	0.2578	0.1787	0.0021	0.83	2617	37	1.4	2630	20	0.7	2641	20	0.7	39897	0.0	99.1
	T17-1-11-4	core	35	52	0.5053	0.0089	12.5479	0.2621	0.1801	0.0020	0.84	2636	38	1.4	2646	20	0.7	2654	19	0.7	6803	0.1	99.3
	T17-1-10-4	core	35	110	0.5030	0.0094	12.4036	0.2670	0.1789	0.0019	0.87	2626	40	1.5	2635	20	0.8	2642	18	0.7		0.0	99.4
	T17-1-9-5	core	35	184	0.5010	0.0074	12.2921	0.2170	0.1779	0.0017	0.83	2618	32	1.2	2627	17	0.6	2634	16	0.6	8434	0.2	99.4
	T17-1-1-4	core	35	232	0.5062	0.0070	12.5810	0.2192	0.1803	0.0019	0.80	2640	30	1.1	2649	16	0.6	2655	18	0.7		0.0	99.4
	T17-1-5-4	core	35	107	0.5046	0.0090	12.4896	0.2659	0.1795	0.0021	0.83	2634	38	1.5	2642	20	0.8	2648	19	0.7	43126	0.0	99.4
	T17-1-6-5	core	35	427	0.5095	0.0079	12.7074	0.2356	0.1809	0.0019	0.83	2654	34	1.3	2658	17	0.7	2661	17	0.6	373132	0.0	99.8
	T17-1-13-5	core	35	148	0.5064	0.0080	12.5081	0.2436	0.1791	0.0021	0.81	2641	34	1.3	2643	18	0.7	2645	19	0.7	34074	0.0	99.9
	T17-1-14-5	core	35	85	0.5037	0.0103	12.3535	0.2880	0.1779	0.0020	0.88	2630	44	1.7	2632	22	0.8	2633	19	0.7	25677	0.0	99.9
	T17-1-13-4	core	35	179	0.4995	0.0086	12.1169	0.2505	0.1759	0.0020	0.83	2612	37	1.4	2613	19	0.7	2615	19	0.7	24018	0.1	99.9
	T17-1-3-6	core	35	492	0.5091	0.0083	12.6467	0.2488	0.1802	0.0020	0.83	2653	36	1.3	2654	19	0.7	2655	18	0.7		0.0	99.9
	T17-1-5-6	core	35	456	0.5069	0.0077	12.5146	0.2320	0.1791	0.0019	0.82	2643	33	1.2	2644	17	0.7	2644	18	0.7		0.0	100.0
	T17-1-3-5	core	35	296	0.5086	0.0054	12.6049	0.1735	0.1797	0.0016	0.78	2651	23	0.9	2651	13	0.5	2651	14	0.5	329122	0.0	100.0
	T17-1-7-5	core	35	504	0.5087	0.0080	12.5981	0.2378	0.1796	0.0019	0.83	2651	34	1.3	2650	18	0.7	2649	17	0.7	48526	0.0	100.1
	T17-1-11-5	core	35	354	0.5067	0.0088	12.4643	0.2465	0.1784	0.0017	0.88	2642	38	1.4	2640	19	0.7	2638	16	0.6		0.0	100.2
	91500-3		35	75	0.1780	0.0023	1.8309	0.0366	0.0746	0.0011	0.65	1056	13	1.2	1057	13	1.2	1057	31	2.9	6333	0.2	99.9
	91500-4		25	1383	0.3529	0.0212	9.1054	0.5981	0.1871	0.0050	0.91	1949	101	5.2	2349	60	2.6	2717	44	1.6	615	2.9	71.7
	91500-1		25	82	0.1808	0.0026	1.8722	0.0398	0.0751	0.0012	0.68	1071	14	1.3	1071	14	1.3	1071	31	2.9	64446	0.0	100.0
	91500-2		25	78	0.1779	0.0022	1.8290	0.0358	0.0745	0.0011	0.63	1056	12	1.1	1056	13	1.2	1056	31	2.9	6344	0.2	99.9

Table 9. LA-ICP-MS analyses for a mafic granulite (sample T16-1-10)

	Analysis name	Texture	Spot size	U conc.	Ratios						rho:	Ages (Ma)									Common Pb		Degree of concordance (%)
			(μm)	(ppm)	$^{206}Pb/^{238}U$	± 2σ	$^{207}Pb/^{235}U$	± 2σ	$^{207}Pb/^{206}Pb$	± 2σ		$^{206}Pb/^{238}U$	± 2σ	± 2σ%	$^{207}Pb/^{235}U$	± 2σ	± 2σ%	$^{207}Pb/^{206}Pb$	± 2σ	± 2σ%	$^{206}Pb/^{204}Pb$	ƒ206%	
	91500-1		25	55	0.1800	0.0045	1.8585	0.0788	0.0749	0.0026	0.59	1067	24	2.3	1066	28	2.6	1065	69	6.5		0.0	100.1
	91500-2		25	69	0.1818	0.0044	1.8927	0.0743	0.0755	0.0023	0.61	1077	24	2.2	1079	26	2.4	1082	62	5.8	18282	0.1	99.5
Mafic granulite	T16-1-2-4	core	25	597	0.4284	0.0219	10.8102	1.1748	0.1830	0.0175	0.47	2299	99	4.3	2507	101	4.0	2680	159	5.9	13450	0.1	85.8
	T16-1-3-1	core	25	148	0.4168	0.0128	9.7355	0.3957	0.1694	0.0045	0.76	2246	58	2.6	2410	37	1.6	2552	44	1.7	2235	0.8	88.0
	T16-1-3-5	core	25	165	0.4345	0.0220	10.3666	0.5809	0.1730	0.0041	0.90	2326	99	4.3	2468	52	2.1	2587	40	1.5	2108	0.8	89.9
	T16-1-1-3	core	25	173	0.4949	0.0097	11.1258	0.5817	0.1630	0.0079	0.38	2592	42	1.6	2534	49	1.9	2488	82	3.3	1638	0.9	104.2
	T16-1-4-1	core	25	310	0.4934	0.0129	11.8247	0.4791	0.1738	0.0054	0.64	2585	56	2.1	2591	38	1.5	2595	52	2.0	9877	0.2	99.6
	T16-1-1-1	core	25	127	0.5124	0.0257	12.9178	1.3074	0.1828	0.0161	0.50	2667	109	4.1	2674	96	3.6	2679	146	5.4	11692	0.2	99.6
	T16-1-2-1	core	25	307	0.5419	0.0307	14.6992	1.3431	0.1967	0.0141	0.62	2791	128	4.6	2796	87	3.1	2799	118	4.2	11458	0.2	99.7
	T16-1-1-2	core	25	170	0.5187	0.0197	13.2137	1.1668	0.1847	0.0147	0.43	2694	84	3.1	2695	84	3.1	2696	132	4.9	39746	0.0	99.9
	T16-1-2-2	core	25	236	0.5324	0.0240	14.0341	1.1478	0.1912	0.0131	0.55	2751	101	3.7	2752	78	2.8	2753	112	4.1	5799	0.3	100.0
	T16-1-3-4	core	25	254	0.5022	0.0153	12.2063	0.5328	0.1763	0.0055	0.70	2623	65	2.5	2620	41	1.6	2618	52	2.0	1404	1.3	100.2
	T16-1-4-2	core	25	307	0.5141	0.0253	12.8592	0.7533	0.1814	0.0057	0.84	2674	108	4.0	2669	55	2.1	2666	52	2.0	27686	0.1	100.3
	91500-3		25	78	0.1816	0.0044	1.8929	0.0666	0.0756	0.0019	0.69	1076	24	2.2	1079	23	2.2	1085	51	4.7		0.0	99.2
	91500-4		25	67	0.1788	0.0048	1.8407	0.0712	0.0747	0.0021	0.69	1060	26	2.5	1060	25	2.4	1060	56	5.3	3028	0.6	100.0

Table 10. LA-ICP-MS analyses for an amphibolite (sample T19-1-10)

	Analysis name	Texture	Spot size	U conc.	Ratios						rho:	Ages (Ma)									Common Pb		Degree of concordance (%)
			(μm)	(ppm)	$^{206}Pb/^{238}U$	± 2σ	$^{207}Pb/^{235}U$	± 2σ	$^{207}Pb/^{206}Pb$	± 2σ		$^{206}Pb/^{238}U$	± 2σ	± 2σ%	$^{207}Pb/^{235}U$	± 2σ	± 2σ%	$^{207}Pb/^{206}Pb$	± 2σ	± 2σ%	$^{206}Pb/^{204}Pb$	ƒ206%	
Amphibolite	T19-1-3-7	core	25	119	0.3067	0.0070	5.1190	0.1420	0.1210	0.0019	0.82	1725	35	2.0	1839	24	1.3	1972	28	1.4	1541	1.2	87.5
	T19-1-3-4	core	25	150	0.2768	0.0043	4.4718	0.0855	0.1172	0.0013	0.81	1575	22	1.4	1726	16	0.9	1914	20	1.1	2782	0.6	82.3
	T19-1-1-5	core	25	18	0.3772	0.0068	6.2764	0.1440	0.1207	0.0017	0.79	2063	32	1.5	2015	20	1.0	1966	25	1.3		0.0	104.9
	T19-1-1-4	core	25	9	0.3628	0.0276	6.1961	0.7159	0.1239	0.0108	0.66	1996	131	6.6	2004	101	5.1	2013	155	7.7	5434	0.2	99.2
	T19-1-1-6	core	25	20	0.3656	0.0079	6.2458	0.1629	0.1239	0.0018	0.83	2008	37	1.9	2011	23	1.1	2013	26	1.3		0.0	99.8
	T19-1-2-6	core	25	13	0.3648	0.0114	6.2209	0.2348	0.1237	0.0026	0.83	2005	54	2.7	2007	33	1.6	2010	37	1.9	1851	0.7	99.8
	T19-1-1-10	core	25	15	0.3756	0.0076	6.5884	0.2002	0.1272	0.0029	0.67	2056	36	1.7	2058	27	1.3	2060	40	1.9	9812	0.2	99.8
	T19-1-2-5	core	25	10	0.3707	0.0113	6.4192	0.2603	0.1256	0.0034	0.75	2033	53	2.6	2035	36	1.8	2037	48	2.3		0.0	99.8
	T19-1-1-7	core	25	18	0.3734	0.0067	6.5043	0.1493	0.1263	0.0018	0.79	2045	32	1.5	2046	20	1.0	2048	25	1.2	1825	0.7	99.9
	T19-1-1-8	core	25	21	0.3642	0.0088	6.1896	0.1779	0.1233	0.0019	0.84	2002	41	2.1	2003	25	1.3	2004	28	1.4		0.0	99.9
	T19-1-1-9	core	25	16	0.3693	0.0077	6.3575	0.1649	0.1248	0.0019	0.81	2026	36	1.8	2026	23	1.1	2027	27	1.3		0.0	100.0
	T19-1-2-4	core	25	11	0.3628	0.0080	6.1220	0.1719	0.1224	0.0021	0.78	1995	38	1.9	1993	25	1.2	1991	31	1.6	10463	0.1	100.2
	T19-1-1-11	core	25	14	0.3726	0.0073	6.2977	0.1550	0.1226	0.0018	0.80	2042	35	1.7	2018	22	1.1	1994	26	1.3	2075	0.4	102.4
	91500-1		25	158	0.1828	0.0023	1.9135	0.0368	0.0759	0.0011	0.65	1082	13	1.2	1086	13	1.2	1092	29	2.7	6665	0.2	99.1
	91500-2		35	81	0.1695	0.0026	1.7528	0.0378	0.0750	0.0011	0.71	1009	14	1.4	1028	14	1.4	1069	30	2.8		0.0	94.4

Table 11. LA-ICP-MS analyses for a granodiorite (sample T2a-2-10)

	Analysis name	Texture	Spot size	U conc.	Ratios						rho:	Ages (Ma)									Common Pb		Degree of concordance (%)
			(μm)	(ppm)	$^{206}Pb/^{238}U$	± 2σ	$^{207}Pb/^{235}U$	± 2σ	$^{207}Pb/^{206}Pb$	± 2σ		$^{206}Pb/^{238}U$	± 2σ	± 2σ%	$^{207}Pb/^{235}U$	± 2σ	± 2σ%	$^{207}Pb/^{206}Pb$	± 2σ	± 2σ%	$^{206}Pb/^{204}Pb$	ƒ206%	
Granodiorite	T2a-2-4-1	core	35	4043	0.0463	0.0017	0.6745	0.0473	0.1057	0.0063	0.52	292	10	3.6	523	29	5.5	1726	110	6.4	254	6.0	16.9
	T2a-2-3-1	core	35	709	0.0465	0.0021	0.5371	0.0886	0.0837	0.0133	0.28	293	13	4.5	437	59	13.4	1286	313	24.3	34	52.2	22.8
	T2a-2-10-2	core	35	1755	0.0756	0.0017	1.1421	0.0701	0.1095	0.0062	0.37	470	10	2.2	774	33	4.3	1791	104	5.8	168	10.6	26.2
	T2a-2-13-1	core	35	1967	0.0848	0.0016	1.3632	0.1105	0.1166	0.0092	0.23	525	10	1.8	873	48	5.4	1904	142	7.5	47	37.6	27.6
	T2a-2-15-1	core	35	5417	0.0990	0.0030	1.3370	0.1863	0.0979	0.0133	0.22	609	18	2.9	862	81	9.4	1585	257	16.2	258	6.9	38.4
	T2a-2-10-1	core	35	2757	0.0695	0.0059	0.6467	0.5832	0.0675	0.0606	0.09	433	35	8.2	506	376	74.2	854	1037	121.3	329	5.4	50.7
	T2a-2-6-1	core	35	1354	0.1166	0.0057	1.4055	0.6101	0.0874	0.0377	0.11	711	33	4.6	891	263	29.5	1370	924	67.5	40	34.7	51.9
	T2a-2-12-1	core	35	2730	0.1953	0.0047	2.7595	0.1670	0.1025	0.0057	0.40	1150	25	2.2	1345	45	3.4	1670	103	6.2	127	13.9	68.9
	T2a-2-3-4	core	35	366	0.3555	0.0055	5.9160	0.1244	0.1207	0.0017	0.74	1961	26	1.3	1964	18	0.9	1966	25	1.3	6290	0.2	99.7
	T2a-2-5-4	core	35	439	0.3572	0.0052	5.8601	0.1234	0.1190	0.0018	0.70	1969	25	1.3	1955	18	0.9	1941	27	1.4		0.0	101.4
	T2a-2-7-4	core	35	425	0.3561	0.0058	5.8552	0.1253	0.1193	0.0016	0.77	1964	28	1.4	1955	19	0.9	1945	25	1.3	150246	0.0	100.9
	T2a-2-8-4	core	35	639	0.3507	0.0048	5.7807	0.1037	0.1196	0.0014	0.77	1938	23	1.2	1944	16	0.8	1950	20	1.0	87292	0.0	99.4
	T2a-2-9-4	core	35	537	0.3498	0.0096	5.8396	0.1830	0.1211	0.0018	0.88	1933	46	2.4	1952	27	1.4	1972	27	1.4	8105	0.2	98.0
	T2a-2-9-5	core	35	571	0.3571	0.0056	5.9531	0.1229	0.1209	0.0016	0.76	1968	27	1.4	1969	18	0.9	1970	24	1.2		0.0	99.9
	T2a-2-11-2	core	35	584	0.3470	0.0110	5.6422	0.1987	0.1179	0.0018	0.90	1920	53	2.7	1923	30	1.6	1925	27	1.4	375	4.7	99.8
	T2a-2-12-4	core	35	302	0.3551	0.0060	5.8360	0.1166	0.1192	0.0013	0.85	1959	29	1.5	1952	17	0.9	1944	19	1.0	761	2.0	100.8
	T2a-2-13-4	core	35	505	0.3507	0.0056	5.6471	0.1200	0.1168	0.0016	0.75	1938	27	1.4	1923	18	1.0	1908	25	1.3	4234	0.4	101.6
	T2a-2-14-7	core	35	441	0.3528	0.0064	5.8113	0.1323	0.1195	0.0016	0.80	1948	31	1.6	1948	20	1.0	1948	24	1.3	8929	0.2	100.0
	T2a-2-2-4	core	35	482	0.3577	0.0059	5.9511	0.1337	0.1206	0.0018	0.73	1971	28	1.4	1969	20	1.0	1966	27	1.4	95096	0.0	100.3
	T2a-2-2-5	core	35	455	0.3575	0.0049	5.9602	0.1255	0.1209	0.0019	0.65	1970	23	1.2	1970	18	0.9	1970	28	1.4		0.0	100.0
	T2a-2-5-5	core	35	518	0.3621	0.0045	6.0019	0.1123	0.1202	0.0017	0.67	1992	21	1.1	1976	16	0.8	1959	25	1.3		0.0	101.7
	T2a-2-6-4	core	35	404	0.3700	0.0051	6.3339	0.1194	0.1242	0.0016	0.73	2029	24	1.2	2023	17	0.8	2017	23	1.1	2869	0.6	100.6
	T2a-2-11-1	core	35	665	0.3646	0.0050	6.1853	0.1089	0.1230	0.0013	0.79	2004	24	1.2	2002	15	0.8	2001	19	1.0	2988	0.6	100.2
	T2a-2-14-4	core	35	365	0.3620	0.0050	5.9888	0.1062	0.1200	0.0013	0.78	1992	24	1.2	1974	15	0.8	1956	20	1.0	11239	0.1	101.8
	T2a-2-15-4	core	35	460	0.3659	0.0065	6.1844	0.1714	0.1226	0.0026	0.64	2010	31	1.5	2002	24	1.2	1994	38	1.9	62309	0.0	100.8
	T2a-2-1-4	core	35	236	0.3366	0.0052	5.5893	0.1218	0.1204	0.0018	0.71	1870	25	1.4	1914	19	1.0	1963	27	1.4	69080	0.0	95.3
	T2a-2-14-5	core	35	602	0.2796	0.0046	4.7019	0.0952	0.1220	0.0015	0.81	1589	23	1.4	1768	17	1.0	1985	21	1.1	6781	0.3	80.1
	91500-1		35	87	0.1715	0.0024	1.7397	0.0371	0.0736	0.0012	0.65	1020	13	1.3	1023	14	1.3	1030	33	3.2		0.0	99.0
	91500-2		35	90	0.1771	0.0028	1.8216	0.0464	0.0746	0.0015	0.62	1051	15	1.4	1053	17	1.6	1057	40	3.8	5096	0.2	99.4
	91500-3		35	85	0.1756	0.0027	1.7944	0.0398	0.0741	0.0012	0.69	1043	15	1.4	1043	14	1.4	1045	32	3.1	32434	0.0	99.8

Table 12. LA-ICP-MS analyses for a Bt-granite (sample T2c-1-10)

	Analysis name	Texture	Spot size	U conc.	Ratios						rho:	Ages (Ma)									Common Pb		Degree of concordance (%)
			(µm)	(ppm)	$^{206}Pb/^{238}U$	± 2σ	$^{207}Pb/^{235}U$	± 2σ	$^{207}Pb/^{206}Pb$	± 2σ		$^{206}Pb/^{238}U$	± 2σ	± 2σ%	$^{207}Pb/^{235}U$	± 2σ	± 2σ%	$^{207}Pb/^{206}Pb$	± 2σ	± 2σ%	$^{206}Pb/^{204}Pb$	ƒ206%	
Biotite granite	T2c-1-6-4	core	35	827	0.3392	0.0065	5.6460	0.1308	0.1207	0.0016	0.83	1883	31	1.7	1923	20	1.0	1967	23	1.2	18229	0.1	95.7
	T2c-1-9-4	core	35	385	0.3642	0.0050	5.8059	0.0979	0.1156	0.0011	0.82	2002	24	1.2	1947	15	0.8	1890	18	0.9	33556	0.0	105.9
	T2c-1-12-4	core	35	1133	0.3497	0.0071	5.8879	0.1402	0.1221	0.0015	0.85	1933	34	1.7	1959	21	1.1	1987	22	1.1	1876	0.9	97.3
	T2c-1-19-4	core	35	274	0.3702	0.0041	6.1685	0.0958	0.1208	0.0013	0.71	2030	19	0.9	2000	14	0.7	1969	19	1.0	50756	0.0	103.1
	T2c-1-20-4	core	35	248	0.3356	0.0043	5.5324	0.1042	0.1195	0.0016	0.69	1866	21	1.1	1906	16	0.9	1950	24	1.3	5433	0.2	95.7
	T2c-1-10-4	core	35	628	0.3718	0.0057	6.3200	0.1236	0.1233	0.0015	0.79	2038	27	1.3	2021	17	0.8	2005	21	1.1	8388	0.2	101.7
	T2c-1-15-4	core	35	718	0.3519	0.0034	5.9260	0.0875	0.1221	0.0014	0.66	1944	16	0.8	1965	13	0.7	1988	20	1.0	108761	0.0	97.8
	T2c-1-15-5	core	35	249	0.3434	0.0057	5.5434	0.1185	0.1171	0.0016	0.78	1903	27	1.4	1907	18	1.0	1912	24	1.3	14167	0.1	99.5
	T2c-1-1-4	core	35	656	0.3599	0.0052	6.0519	0.1012	0.1220	0.0011	0.86	1981	24	1.2	1983	15	0.7	1985	15	0.8	19218	0.1	99.8
	T2c-1-2-4	core	35	500	0.3611	0.0091	6.0895	0.1648	0.1223	0.0012	0.93	1987	43	2.2	1989	24	1.2	1990	18	0.9	16670	0.1	99.9
	T2c-1-3-4	core	35	861	0.3623	0.0066	6.1405	0.1252	0.1229	0.0011	0.89	1993	31	1.6	1996	18	0.9	1999	16	0.8	14379	0.1	99.7
	T2c-1-4-4	core	35	343	0.3659	0.0054	6.1231	0.1047	0.1214	0.0011	0.86	2010	25	1.3	1994	15	0.7	1976	15	0.8	11474	0.2	101.7
	T2c-1-5-4	core	35	836	0.3689	0.0056	6.2420	0.1136	0.1227	0.0012	0.83	2024	26	1.3	2010	16	0.8	1996	18	0.9	61603	0.0	101.4
	T2c-1-7-4	core	35	953	0.3618	0.0056	6.1008	0.1118	0.1223	0.0012	0.84	1990	26	1.3	1990	16	0.8	1990	18	0.9	53488	0.0	100.0
	T2c-1-8-4	core	35	558	0.3594	0.0068	6.0356	0.1335	0.1218	0.0014	0.86	1979	32	1.6	1981	19	1.0	1983	20	1.0	96141	0.0	99.8
	T2c-1-11-4	core	35	906	0.3544	0.0056	5.9957	0.1134	0.1227	0.0013	0.84	1956	27	1.4	1975	16	0.8	1996	18	0.9	24443	0.1	98.0
	T2c-1-13-4	core	35	981	0.3584	0.0059	6.0437	0.1241	0.1223	0.0015	0.80	1974	28	1.4	1982	18	0.9	1990	22	1.1	10812	0.1	99.2
	T2c-1-14-4	core	35	950	0.3657	0.0051	6.1391	0.1106	0.1217	0.0014	0.78	2009	24	1.2	1996	16	0.8	1982	20	1.0	131284	0.0	101.4
	T2c-1-16-4	core	35	1367	0.3665	0.0081	6.2942	0.1628	0.1245	0.0017	0.86	2013	38	1.9	2018	23	1.1	2022	23	1.2	4655	0.4	99.5
	T2c-1-17-4	core	35	904	0.3664	0.0051	6.1510	0.1107	0.1217	0.0014	0.77	2012	24	1.2	1998	16	0.8	1982	20	1.0	30519	0.1	101.5
	T2c-1-18-4	core	35	388	0.3655	0.0041	6.2621	0.1017	0.1243	0.0014	0.70	2008	20	1.0	2013	14	0.7	2019	21	1.0	3701	0.5	99.5
	91500-3		35	92	0.1838	0.0024	1.9185	0.0412	0.0757	0.0013	0.62	1088	13	1.2	1088	14	1.3	1087	34	3.1	3995	0.1	100.0
	91500-4		35	88	0.1798	0.0025	1.8570	0.0377	0.0749	0.0011	0.68	1066	14	1.3	1066	13	1.3	1066	30	2.8	5526	0.1	100.0

Table 13. LA-ICP-MS analyses for a granitic gneiss (sample T19-3-10)

	Analysis name	Texture	Spot size	U conc.	Ratios						rho:	Ages (Ma)									Common Pb		Degree of concordance (%)
			(μm)	(ppm)	$^{206}Pb/^{238}U$	± 2σ	$^{207}Pb/^{235}U$	± 2σ	$^{207}Pb/^{206}Pb$	± 2σ		$^{206}Pb/^{238}U$	± 2σ	± 2σ%	$^{207}Pb/^{235}U$	± 2σ	± 2σ%	$^{207}Pb/^{206}Pb$	± 2σ	± 2σ%	$^{206}Pb/^{204}Pb$	ƒ206%	
Granitic gneiss (Ms Bt)	T19-3-18-4	core	25	1059	0.2470	0.0056	3.8124	0.1292	0.1119	0.0028	0.67	1423	29	2.0	1595	27	1.7	1831	46	2.5	481	3.2	77.7
	T19-3-11-4	core	25	1443	0.3246	0.0062	4.9531	0.1076	0.1107	0.0011	0.88	1812	30	1.7	1811	18	1.0	1810	19	1.0	1430	1.1	100.1
	T19-3-13-4	core	25	265	0.3942	0.0068	9.2622	0.2023	0.1704	0.0023	0.79	2142	32	1.5	2364	20	0.8	2562	22	0.9	12152	0.1	83.6
	T19-3-20-4	core	25	697	0.3201	0.0052	5.1071	0.0962	0.1157	0.0011	0.86	1790	25	1.4	1837	16	0.9	1891	17	0.9	5273	0.3	94.6
	T19-3-6-4	core	25	155	0.3341	0.0097	5.5001	0.2005	0.1194	0.0026	0.79	1858	47	2.5	1901	31	1.6	1947	40	2.0	1815	1.0	95.4
	T19-3-17-4	core	25	195	0.3781	0.0093	6.0473	0.1652	0.1160	0.0014	0.90	2067	43	2.1	1983	24	1.2	1895	21	1.1	2091	0.8	109.1
	T19-3-14-4	core	25	589	0.3448	0.0053	5.5601	0.1076	0.1169	0.0014	0.79	1910	25	1.3	1910	17	0.9	1910	21	1.1	4089	0.4	100.0
	T19-3-16-4	core	25	753	0.3516	0.0092	5.7710	0.1969	0.1191	0.0026	0.77	1942	44	2.3	1942	30	1.5	1942	39	2.0	2119	0.8	100.0
	T19-3-19-4	core	25	859	0.3504	0.0064	5.7402	0.1252	0.1188	0.0014	0.84	1936	31	1.6	1937	19	1.0	1939	21	1.1	2153	0.8	99.9
	T19-3-1-4	core	25	106	0.3368	0.0083	5.4427	0.1651	0.1172	0.0021	0.81	1871	40	2.1	1892	26	1.4	1914	32	1.7		0.0	97.8
	T19-3-2-1	core	25	471	0.3487	0.0069	5.7862	0.1394	0.1203	0.0017	0.82	1928	33	1.7	1944	21	1.1	1961	25	1.3	2159	0.8	98.3
	T19-3-2-9	core	25	148	0.3625	0.0138	6.1384	0.3062	0.1228	0.0040	0.76	1994	65	3.3	1996	44	2.2	1998	57	2.9	1937	0.9	99.8
	T19-3-3-4	core	25	458	0.3581	0.0062	5.9970	0.1365	0.1215	0.0018	0.77	1973	30	1.5	1975	20	1.0	1978	26	1.3	1995	0.9	99.7
	T19-3-7-4	core	25	415	0.3566	0.0078	5.9596	0.1596	0.1212	0.0019	0.82	1966	37	1.9	1970	23	1.2	1974	27	1.4	2066	0.9	99.6
	T19-3-9-4	core	25	252	0.3436	0.0057	5.5426	0.1131	0.1170	0.0014	0.81	1904	27	1.4	1907	18	0.9	1911	21	1.1	3964	0.4	99.7
	T19-3-12-4	core	25	351	0.3420	0.0110	5.4743	0.1909	0.1161	0.0016	0.92	1896	53	2.8	1897	30	1.6	1897	24	1.3	5186	0.3	100.0
	T19-3-21-4	rim	25	681	0.3426	0.0039	5.4662	0.0753	0.1157	0.0009	0.82	1899	19	1.0	1895	12	0.6	1891	14	0.8	12291	0.1	100.4
	T19-3-21-7	rim	25	141	0.3365	0.0077	5.2889	0.1754	0.1140	0.0027	0.69	1870	37	2.0	1867	28	1.5	1864	43	2.3	87490	0.0	100.3
	T19-3-1-7	rim	25	283	0.3380	0.0100	5.3803	0.1788	0.1154	0.0018	0.89	1877	48	2.6	1882	28	1.5	1887	28	1.5	1609	1.1	99.5
	T19-3-2-8	rim	25	134	0.3374	0.0066	5.3413	0.1232	0.1148	0.0014	0.85	1874	32	1.7	1875	20	1.1	1877	22	1.2	4326	0.4	99.9
	T19-3-3-7	rim	25	172	0.3411	0.0065	5.4497	0.1228	0.1159	0.0014	0.85	1892	31	1.7	1893	19	1.0	1894	21	1.1	3862	0.5	99.9
	T19-3-4-7	rim	25	104	0.3335	0.0036	5.2170	0.0728	0.1135	0.0010	0.77	1855	17	0.9	1855	12	0.6	1856	16	0.9	13407	0.1	100.0
	T19-3-5-7	rim	25	285	0.3440	0.0044	5.5619	0.0928	0.1173	0.0013	0.76	1906	21	1.1	1910	14	0.8	1915	19	1.0	4890	0.4	99.5
	T19-3-10-7	rim	25	266	0.3364	0.0072	5.3265	0.1312	0.1148	0.0014	0.87	1869	35	1.9	1873	21	1.1	1877	22	1.2	11441	0.2	99.6
	T19-3-2-7	rim	25	83	0.3076	0.0048	4.5770	0.0813	0.1079	0.0009	0.87	1729	23	1.4	1745	15	0.8	1765	16	0.9	95284	0.0	98.0
	T19-3-8-7	rim	25	282	0.3278	0.0036	5.1931	0.0692	0.1149	0.0009	0.83	1828	18	1.0	1851	11	0.6	1878	13	0.7	6227	0.3	97.3
	T19-3-14-7	rim	25	172	0.3239	0.0050	4.9696	0.0951	0.1113	0.0012	0.81	1809	25	1.4	1814	16	0.9	1820	20	1.1	7857	0.1	99.4
	T19-3-15-4	rim	25	504	0.3341	0.0061	5.1543	0.1106	0.1119	0.0013	0.84	1858	29	1.6	1845	18	1.0	1830	21	1.1	1665	0.9	101.5
	91500-3		35	733	0.1771	0.0030	1.8135	0.0443	0.0743	0.0013	0.70	1051	17	1.6	1050	16	1.5	1049	35	3.3		0.0	100.2
	91500-4		35	628	0.1823	0.0027	1.9038	0.0439	0.0757	0.0013	0.65	1079	15	1.4	1082	15	1.4	1089	35	3.2		0.0	99.2

Table 14. LA-ICP-MS analyses for a calc-silicate rock (sample T4-39-10)

	Analysis name	Texture	Spot size	U conc.	Ratios						rho:	Ages (Ma)									Common Pb		Degree of concordance (%)
			(µm)	(ppm)	$^{206}Pb/^{238}U$	± 2σ	$^{207}Pb/^{235}U$	± 2σ	$^{207}Pb/^{206}Pb$	± 2σ		$^{206}Pb/^{238}U$	± 2σ	± 2σ%	$^{207}Pb/^{235}U$	± 2σ	± 2σ%	$^{207}Pb/^{206}Pb$	± 2σ	± 2σ%	$^{206}Pb/^{204}Pb$	ƒ206%	
Calc-silicate rock	T4-39-3-3	Det. Core	25	343	0.4614	0.0135	10.9769	0.5573	0.1725	0.0072	0.58	2446	59	2.4	2521	47	1.9	2583	69	2.7	8789	0.2	94.7
	T4-39-16-1	Det. Core	25	466	0.4775	0.0111	11.4830	0.5446	0.1744	0.0072	0.49	2516	49	1.9	2563	44	1.7	2600	69	2.6	56240	0.0	96.8
	T4-39-20-1	Det. Core	25	330	0.4890	0.0128	11.8683	0.5794	0.1760	0.0073	0.54	2566	55	2.2	2594	46	1.8	2616	69	2.6		0.0	98.1
	T4-39-21-3	Det. Core	25	456	0.4786	0.0153	11.1668	0.6441	0.1692	0.0081	0.56	2521	67	2.7	2537	54	2.1	2550	80	3.2	16461	0.1	98.9
	T4-39-17-3	Det. Core	25	626	0.4364	0.0240	9.0281	0.6355	0.1501	0.0066	0.78	2334	108	4.6	2341	64	2.8	2347	75	3.2	4999	0.4	99.5
	T4-39-12-3	Det. Core	25	404	0.4843	0.0127	11.3251	0.5884	0.1696	0.0076	0.50	2546	55	2.2	2550	49	1.9	2554	75	2.9	19394	0.1	99.7
	T4-39-2-3	Det. Core	25	163	0.5047	0.0121	12.4184	0.5316	0.1785	0.0063	0.56	2634	52	2.0	2637	40	1.5	2639	59	2.2	98821	0.0	99.8
	T4-39-5-1	Det. Core	25	337	0.4703	0.0097	10.5717	0.3470	0.1630	0.0042	0.63	2485	43	1.7	2486	30	1.2	2487	43	1.7	12433	0.1	99.9
	T4-39-15-1	Det. Core	25	283	0.4998	0.0160	12.1189	0.6124	0.1758	0.0069	0.63	2613	69	2.6	2614	47	1.8	2614	65	2.5	58407	0.0	100.0
	T4-39-1-3	Det. Core	25	696	0.4118	0.0178	7.9271	0.5048	0.1396	0.0065	0.68	2223	81	3.7	2223	57	2.6	2222	81	3.6	21439	0.1	100.0
	T4-39-11-3	Det. Core	25	263	0.5005	0.0140	12.1389	0.6389	0.1759	0.0078	0.53	2616	60	2.3	2615	49	1.9	2615	74	2.8		0.0	100.1
	T4-39-19-1	Det. Core	25	457	0.4973	0.0175	11.9054	0.6162	0.1736	0.0066	0.68	2602	75	2.9	2597	49	1.9	2593	63	2.4	47960	0.0	100.4
	T4-39-6-3	Det. Core	25	253	0.4958	0.0116	11.7530	0.4117	0.1719	0.0045	0.67	2596	50	1.9	2585	33	1.3	2577	43	1.7	127294	0.0	100.7
	T4-39-3-6	rim	25	825	0.3630	0.0106	6.5186	0.4314	0.1302	0.0077	0.44	1996	50	2.5	2048	58	2.8	2101	104	5.0	7582	0.2	95.0
	T4-39-4-6	rim	25	1089	0.3890	0.0135	7.5084	0.4257	0.1400	0.0063	0.61	2118	63	3.0	2174	51	2.3	2227	78	3.5	39313	0.0	95.1
	T4-39-12-7	rim	25	732	0.3407	0.0129	5.7222	0.3723	0.1218	0.0064	0.58	1890	62	3.3	1935	56	2.9	1983	94	4.8		0.0	95.3
	T4-39-11-6	rim	25	1002	0.3471	0.0087	5.9190	0.2153	0.1237	0.0033	0.69	1921	42	2.2	1964	32	1.6	2010	47	2.3	8119	0.2	95.6
	T4-39-16-6	rim	25	816	0.3333	0.0079	5.4541	0.3371	0.1187	0.0068	0.39	1854	38	2.1	1893	53	2.8	1937	102	5.3	26757	0.1	95.7
	T4-39-2-6	rim	25	869	0.3376	0.0095	5.5759	0.2687	0.1198	0.0047	0.59	1875	46	2.5	1912	42	2.2	1953	70	3.6		0.0	96.0
	T4-39-21-6	rim	25	577	0.4011	0.0085	7.8475	0.3354	0.1419	0.0053	0.49	2174	39	1.8	2214	39	1.7	2251	64	2.9	12180	0.1	96.6
	T4-39-13-3	rim	25	930	0.3608	0.0109	6.0969	0.2695	0.1226	0.0040	0.68	1986	52	2.6	1990	39	1.9	1994	57	2.9	73115	0.0	99.6
	T4-39-13-4	rim	25	961	0.3647	0.0088	6.1920	0.2552	0.1231	0.0041	0.59	2004	42	2.1	2003	36	1.8	2002	59	3.0	344985	0.0	100.1
	T4-39-14-3	rim	25	1097	0.3528	0.0098	5.7018	0.2443	0.1172	0.0038	0.65	1948	47	2.4	1932	37	1.9	1914	59	3.1	15470	0.1	101.7
	T4-39-2-7	rim	25	1033	0.3451	0.0153	5.7521	0.4752	0.1209	0.0084	0.54	1911	73	3.8	1939	72	3.7	1969	125	6.3	20309	0.1	97.0
	T4-39-7-6	rim	25	705	0.3436	0.0092	5.5945	0.2453	0.1181	0.0041	0.61	1904	44	2.3	1915	38	2.0	1928	62	3.2	18381	0.1	98.7
	T4-39-20-6	rim	25	1071	0.3610	0.0076	6.1479	0.3027	0.1235	0.0055	0.43	1987	36	1.8	1997	43	2.2	2008	79	3.9		0.0	99.0
	T4-39-12-6	rim	25	824	0.3512	0.0184	5.7809	0.5714	0.1194	0.0100	0.53	1940	88	4.5	1944	86	4.4	1947	150	7.7	26237	0.1	99.7
	T4-39-5-6	rim	25	948	0.3576	0.0106	5.9497	0.3692	0.1207	0.0066	0.48	1971	50	2.5	1969	54	2.7	1966	97	5.0	21001	0.1	100.2
	T4-39-6-6	rim	25	923	0.3388	0.0104	5.4081	0.2327	0.1158	0.0035	0.71	1881	50	2.7	1886	37	2.0	1892	54	2.9	76135	0.0	99.4
	91500-5		25	78	0.1787	0.0050	1.8400	0.0814	0.0747	0.0026	0.63	1060	27	2.6	1060	29	2.7	1060	69	6.5		0.0	100.0
	91500-6		25	74	0.1828	0.0039	1.9030	0.0693	0.0755	0.0022	0.59	1082	21	2.0	1082	24	2.2	1082	59	5.4		0.0	100.0
	91500-2		35	74	0.1755	0.0051	1.7845	0.0678	0.0738	0.0018	0.77	1042	28	2.7	1040	25	2.4	1035	49	4.7		0.0	100.7

Table 15. LA-ICP-MS analyses for a metapelite (sample T4-38-10)

	Analysis name	Texture	Spot size	U conc.	Ratios						rho:	Ages (Ma)									Common Pb		Degree of concordance (%)
			(μm)	(ppm)	$^{206}Pb/^{238}U$	± 2σ	$^{207}Pb/^{235}U$	± 2σ	$^{207}Pb/^{206}Pb$	± 2σ		$^{206}Pb/^{238}U$	± 2σ	± 2σ%	$^{207}Pb/^{235}U$	± 2σ	± 2σ%	$^{207}Pb/^{206}Pb$	± 2σ	± 2σ%	$^{206}Pb/^{204}Pb$	ƒ206%	
Metapelite	T4-38-6-1	Det. Core	25	1161	0.1220	0.0051	1.8993	0.1127	0.1129	0.0047	0.71	742	29	4.0	1081	39	3.7	1847	76	4.1	102	14.9	40.2
	T4-38-3-1	Det. Core	25	839	0.2594	0.0035	5.0267	0.2036	0.1406	0.0054	0.33	1486	18	1.2	1824	34	1.9	2234	66	3.0	141	10.8	66.5
	T4-38-28-1	Det. Core	25	869	0.2088	0.0068	3.5859	0.2541	0.1246	0.0078	0.46	1222	36	3.0	1546	56	3.6	2023	112	5.5	251	6.0	60.4
	T4-38-19-3	Det. Core	25	758	0.2922	0.0083	4.8450	0.1840	0.1202	0.0030	0.75	1653	42	2.5	1793	32	1.8	1960	45	2.3	640	2.8	84.3
	T4-38-23-3	Det. Core	25	534	0.3695	0.0087	6.3421	0.2303	0.1245	0.0034	0.65	2027	41	2.0	2024	32	1.6	2022	49	2.4	747	2.4	100.3
	T4-38-12-1	Det. Core	25	584	0.4155	0.0110	8.5939	0.3293	0.1500	0.0042	0.69	2240	50	2.2	2296	35	1.5	2346	47	2.0	818	2.2	95.5
	T4-38-5-1	Det. Core	25	79	0.3435	0.0284	5.5618	0.5380	0.1174	0.0059	0.85	1903	136	7.2	1910	83	4.4	1918	90	4.7	1004	1.5	99.2
	T4-38-13-4	Det. Core	25	1119	0.3524	0.0112	5.8122	0.2405	0.1196	0.0032	0.77	1946	53	2.7	1948	36	1.8	1951	47	2.4	1222	1.5	99.7
	T4-38-3-2	Det. Core	25	508	0.3834	0.0122	6.4680	0.2727	0.1223	0.0034	0.76	2092	57	2.7	2042	37	1.8	1991	49	2.5	1308	1.4	105.1
	T4-38-40-4	Det. Core	35	355	0.3579	0.0046	5.9966	0.1029	0.1215	0.0014	0.75	1972	22	1.1	1975	15	0.8	1978	20	1.0	1518	1.0	99.7
	T4-38-32-3	Det. Core	25	137	0.3689	0.0140	6.7658	0.3216	0.1330	0.0038	0.80	2024	66	3.2	2081	42	2.0	2138	50	2.4	11347	0.2	94.7
	T4-38-38-1	Det. Core	35	274	0.3331	0.0064	5.6763	0.1295	0.1236	0.0015	0.84	1853	31	1.7	1928	20	1.0	2009	22	1.1	3697	0.5	92.3
	T4-38-17-1	Det. Core	25	395	0.4270	0.0121	10.7575	0.4272	0.1827	0.0051	0.72	2292	55	2.4	2502	37	1.5	2678	46	1.7	3922	0.5	85.6
	T4-38-49-1	Det. Core	35		0.2511	0.0063	4.2401	0.1602	0.1225	0.0034	0.67	1444	33	2.3	1682	31	1.8	1993	50	2.5	5800	0.3	72.5
	T4-38-29-1	Det. Core	25	415	0.4123	0.0114	7.3158	0.3096	0.1287	0.0041	0.66	2225	52	2.3	2151	38	1.8	2080	56	2.7	27205	0.1	107.0
	T4-38-47-4	Det. Core	25		0.3813	0.0088	6.7723	0.2051	0.1288	0.0025	0.76	2082	41	2.0	2082	27	1.3	2082	35	1.7	32944	0.1	100.0
	T4-38-20-3	Det. Core	25	368	0.3859	0.0128	6.9394	0.3067	0.1304	0.0038	0.75	2104	60	2.8	2104	39	1.9	2104	51	2.4	7206	0.2	100.0
	T4-38-1-2	Det. Core	25	217	0.3778	0.0159	6.6518	0.3432	0.1277	0.0038	0.81	2066	74	3.6	2066	46	2.2	2067	53	2.6	42510	0.0	100.0
	T4-38-33-1	Det. Core	35	282	0.3917	0.0046	7.1557	0.1065	0.1325	0.0012	0.78	2130	21	1.0	2131	13	0.6	2132	16	0.8		0.0	99.9
	T4-38-35-1	Det. Core	25	222	0.4295	0.0074	8.6719	0.1842	0.1464	0.0018	0.81	2303	33	1.4	2304	19	0.8	2305	22	0.9	1947	0.9	99.9
	T4-38-27-3	Det. Core	25	812	0.3840	0.0119	6.8860	0.3160	0.1301	0.0044	0.67	2095	55	2.6	2097	41	1.9	2099	60	2.8	17066	0.1	99.8
	T4-38-25-1	Det. Core	25	322	0.3925	0.0129	7.2033	0.3409	0.1331	0.0045	0.70	2135	60	2.8	2137	42	2.0	2139	59	2.8	63337	0.0	99.8
	T4-38-7-3	Det. Core	25	96	0.3872	0.0113	7.0059	0.2751	0.1312	0.0034	0.74	2110	53	2.5	2112	35	1.7	2115	46	2.2	4612	0.4	99.8
	T4-38-36-1	Det. Core	25	439	0.3769	0.0082	6.7127	0.1786	0.1292	0.0020	0.81	2062	38	1.9	2074	24	1.1	2087	27	1.3	22915	0.1	98.8

Table 5 continued

	Analysis name	Texture	Spot size	U conc.	Ratios						rho:	Ages (Ma)									Common Pb		Degree of concordance (%)
			(μm)	(ppm)	$^{206}Pb/^{238}U$	± 2σ	$^{207}Pb/^{235}U$	± 2σ	$^{207}Pb/^{206}Pb$	± 2σ		$^{206}Pb/^{238}U$	± 2σ	± 2σ%	$^{207}Pb/^{235}U$	± 2σ	± 2σ%	$^{207}Pb/^{206}Pb$	± 2σ	± 2σ%	$^{206}Pb/^{204}Pb$	ƒ206%	
Metapelite	T4-38-31-6	rim	25	577	0.0949	0.0060	1.5716	0.1156	0.1201	0.0045	0.86	584	35	6.1	959	46	4.8	1958	67	3.4	421	3.6	29.9
	T4-38-20-9	rim	25	741	0.2318	0.0086	3.8603	0.1738	0.1208	0.0031	0.82	1344	45	3.3	1605	36	2.3	1968	46	2.3	433	3.5	68.3
	T4-38-42-7	rim	35	1482	0.2533	0.0171	4.9503	0.3986	0.1417	0.0062	0.84	1456	88	6.0	1811	68	3.8	2248	76	3.4	551	3.2	64.7
	T4-38-13-5	rim	25	515	0.3126	0.0076	4.9149	0.2185	0.1140	0.0043	0.55	1754	37	2.1	1805	38	2.1	1865	67	3.6	247	6.2	94.0
	T4-38-7-6	rim	25	516	0.3578	0.0070	5.9843	0.2153	0.1213	0.0037	0.55	1972	33	1.7	1974	31	1.6	1975	54	2.7	327	5.4	99.8
	T4-38-45-7	rim	35	525	0.3254	0.0048	5.2405	0.1041	0.1168	0.0015	0.74	1816	23	1.3	1859	17	0.9	1908	24	1.2	540	2.8	95.2
	T4-38-9-5	rim	25	610	0.2572	0.0096	4.2405	0.2194	0.1196	0.0043	0.73	1476	49	3.4	1682	43	2.5	1950	64	3.3	596	2.6	75.7
	T4-38-44-7	rim	35	818	0.3353	0.0112	5.5398	0.2526	0.1198	0.0037	0.73	1864	54	2.9	1907	39	2.1	1954	55	2.8	733	2.1	95.4
	T4-38-16-8	rim	25	492	0.3404	0.0065	5.4603	0.1487	0.1163	0.0022	0.70	1889	31	1.7	1894	23	1.2	1901	35	1.8	874	2.0	99.4
	T4-38-46-7	rim	25	452	0.3437	0.0072	5.6359	0.1485	0.1189	0.0019	0.80	1904	35	1.8	1922	23	1.2	1940	29	1.5	1100	1.6	98.1
	T4-38-23-6	rim	25	372	0.3547	0.0084	5.8934	0.2419	0.1205	0.0040	0.58	1957	40	2.0	1960	36	1.8	1964	60	3.0	1102	1.6	99.7
	T4-38-17-3	rim	25	334	0.3471	0.0091	5.9269	0.2236	0.1238	0.0034	0.69	1921	43	2.3	1965	33	1.7	2012	48	2.4		0.0	95.5
	T4-38-5-6	rim	25	145	0.3154	0.0069	5.3050	0.1975	0.1220	0.0037	0.59	1767	34	1.9	1870	32	1.7	1985	53	2.7	8931	0.2	89.0
	T4-38-31-7	rim	25	237	0.3147	0.0040	5.1050	0.1381	0.1176	0.0028	0.47	1764	19	1.1	1837	23	1.3	1921	43	2.2	4123	0.4	91.8
	T4-38-29-3	rim	25	322	0.3292	0.0085	5.5228	0.2259	0.1217	0.0039	0.63	1835	41	2.3	1904	35	1.8	1981	56	2.8	11284	0.1	92.6
	T4-38-14-4	rim	25	432	0.3147	0.0044	5.0556	0.1194	0.1165	0.0022	0.59	1764	21	1.2	1829	20	1.1	1903	34	1.8	8440	0.2	92.7
	T4-38-38-7	rim	35	362	0.3280	0.0062	5.3878	0.1161	0.1191	0.0012	0.88	1828	30	1.7	1883	18	1.0	1944	18	0.9	2715	0.7	94.1
	T4-38-17-6	rim	25	162	0.3322	0.0051	5.5130	0.1613	0.1203	0.0030	0.53	1849	25	1.3	1903	25	1.3	1961	44	2.3	7573	0.2	94.3
	T4-38-41-7	rim	25	401	0.3319	0.0062	5.4867	0.1384	0.1199	0.0020	0.74	1847	30	1.6	1899	22	1.1	1955	31	1.6	4599	0.4	94.5
	T4-38-24-4	rim	25	296	0.3425	0.0057	5.8044	0.1702	0.1229	0.0030	0.57	1898	27	1.4	1947	25	1.3	1999	43	2.1	10584	0.2	95.0
	T4-38-32-7	rim	25	221	0.3433	0.0148	5.8289	0.3042	0.1231	0.0036	0.83	1902	71	3.7	1951	45	2.3	2002	52	2.6	7110	0.2	95.0
	T4-38-10-5	rim	25	318	0.3363	0.0066	5.5471	0.1880	0.1196	0.0033	0.58	1869	32	1.7	1908	29	1.5	1951	49	2.5	4232	0.4	95.8
	T4-38-9-6	rim	25	194	0.3589	0.0073	6.2695	0.1822	0.1267	0.0026	0.70	1977	35	1.8	2014	25	1.3	2053	37	1.8	2506	0.7	96.3
	T4-38-43-7	rim	25	613	0.3673	0.0063	6.0972	0.1329	0.1204	0.0016	0.79	2017	30	1.5	1990	19	1.0	1962	24	1.2	5744	0.3	102.8
	T4-38-25-6	rim	25	493	0.3746	0.0145	6.3188	0.2946	0.1223	0.0032	0.83	2051	68	3.3	2021	41	2.0	1991	46	2.3	34065	0.1	103.0
	T4-38-11-7	rim	25	36	0.3540	0.0109	5.9292	0.3389	0.1215	0.0058	0.54	1953	52	2.7	1966	50	2.5	1978	86	4.3	143808	0.0	98.7
	T4-38-30-4	rim	25	478	0.3491	0.0078	5.7429	0.1847	0.1193	0.0028	0.70	1930	37	1.9	1938	28	1.4	1946	41	2.1	61438	0.0	99.2
	T4-38-32-6	rim	25	220	0.3588	0.0116	6.0494	0.2562	0.1223	0.0033	0.77	1976	55	2.8	1983	37	1.9	1990	49	2.4	12996	0.1	99.3
	T4-38-36-7	rim	25	380	0.3525	0.0062	5.8222	0.1186	0.1198	0.0012	0.86	1947	29	1.5	1950	18	0.9	1953	19	1.0	8298	0.2	99.7
	T4-38-22-6	rim	25	183	0.3564	0.0131	5.9378	0.3120	0.1208	0.0045	0.70	1965	62	3.2	1967	46	2.3	1968	67	3.4	2212	0.8	99.8
	T4-38-19-6	rim	25	401	0.3645	0.0104	6.2044	0.2733	0.1234	0.0041	0.65	2004	49	2.5	2005	39	1.9	2007	59	3.0	3077	0.6	99.8
	T4-38-11-6	rim	25	170	0.3547	0.0121	5.8783	0.2399	0.1202	0.0027	0.84	1957	58	3.0	1958	35	1.8	1959	40	2.0	8342	0.2	99.9
	T4-38-24-3	rim	25	453	0.3608	0.0123	6.0679	0.3228	0.1220	0.0050	0.64	1986	58	2.9	1986	46	2.3	1986	73	3.7	8180	0.2	100.0
	T4-38-37-7	rim	25	259	0.3579	0.0090	5.9673	0.1767	0.1209	0.0019	0.85	1972	43	2.2	1971	26	1.3	1970	28	1.4	4273	0.4	100.1
	T4-38-39-7	rim	25	426	0.3568	0.0072	5.8681	0.1390	0.1193	0.0015	0.86	1967	34	1.7	1957	21	1.1	1945	22	1.1	50976	0.0	101.1
	T4-38-14-3	rim	25	572	0.3544	0.0117	5.7756	0.2446	0.1182	0.0031	0.78	1955	56	2.8	1943	37	1.9	1929	48	2.5	10681	0.2	101.3
	91500-5		25	72	0.1800	0.0040	1.8681	0.0586	0.0753	0.0017	0.70	1067	22	2.0	1070	21	1.9	1076	45	4.2		0.0	99.2
	91500-6		25	69	0.1748	0.0041	1.7806	0.0655	0.0739	0.0021	0.63	1038	22	2.1	1038	24	2.3	1038	58	5.5		0.0	100.0
	91500-1		25	68	0.1806	0.0046	1.8182	0.0692	0.0730	0.0021	0.67	1070	25	2.3	1052	25	2.4	1015	57	5.7	1145	1.4	105.5
	91500-2		25	75	0.1810	0.0044	1.8752	0.0665	0.0752	0.0020	0.68	1072	24	2.2	1072	23	2.2	1073	52	4.9		0.0	100.0

Table 16. LA-ICP-MS analyses for a leucosome of a metapelite (sample T4-37-10)

	Analysis name	Texture	Spot size	U conc.	Ratios						rho:	Ages (Ma)									Common Pb		Degree of concordance (%)
			(µm)	(ppm)	$^{206}Pb/^{238}U$	± 2σ	$^{207}Pb/^{235}U$	± 2σ	$^{207}Pb/^{206}Pb$	± 2σ		$^{206}Pb/^{238}U$	± 2σ	± 2σ%	$^{207}Pb/^{235}U$	± 2σ	± 2σ%	$^{207}Pb/^{206}Pb$	± 2σ	± 2σ%	$^{206}Pb/^{204}Pb$	ƒ206%	
Leucosome from a metapelite	T4-37-2-5	core	25	259	0.3355	0.0078	5.5205	0.1710	0.1193	0.0024	0.75	1865	38	2.0	1904	27	1.4	1946	36	1.9	3635	0.5	95.8
	T4-37-12-5	core	25	344	0.3336	0.0077	5.3452	0.1531	0.1162	0.0020	0.81	1856	37	2.0	1876	25	1.3	1899	30	1.6	105582	0.0	97.7
	T4-37-3-6	core	25	265	0.3251	0.0093	4.9889	0.1983	0.1113	0.0031	0.72	1815	45	2.5	1817	34	1.9	1821	50	2.8	2859	0.5	99.7
	T4-37-1-5	core	25	376	0.3495	0.0096	5.7234	0.2019	0.1188	0.0026	0.78	1932	46	2.4	1935	30	1.6	1938	40	2.0	86867	0.0	99.7
	T4-37-9-2	core	25	401	0.3553	0.0121	5.9073	0.2367	0.1206	0.0025	0.85	1960	58	2.9	1962	35	1.8	1965	37	1.9	4529	0.4	99.8
	T4-37-14-6	core	25	337	0.3532	0.0075	5.8375	0.1644	0.1199	0.0022	0.76	1950	36	1.8	1952	24	1.3	1954	33	1.7	7900	0.2	99.8
	T4-37-14-2	core	25	331	0.3517	0.0093	5.7827	0.1903	0.1192	0.0023	0.80	1943	44	2.3	1944	28	1.5	1945	35	1.8	23082	0.1	99.9
	T4-37-10-1	core	25	450	0.3518	0.0106	5.7811	0.2296	0.1192	0.0031	0.76	1943	51	2.6	1944	34	1.8	1944	46	2.4	19599	0.1	99.9
	T4-37-1-6	core	25	379	0.3547	0.0101	5.8711	0.2112	0.1201	0.0026	0.79	1957	48	2.5	1957	31	1.6	1957	39	2.0	6340	0.2	100.0
	T4-37-13-5	core	25	268	0.3443	0.0092	5.5393	0.1826	0.1167	0.0022	0.81	1907	44	2.3	1907	28	1.5	1906	34	1.8	1931	0.9	100.0
	T4-37-11-3	core	25	397	0.3503	0.0077	5.7103	0.1719	0.1182	0.0024	0.73	1936	37	1.9	1933	26	1.3	1930	37	1.9	93361	0.0	100.3
	T4-37-3-1	core	25	305	0.3558	0.0165	5.8855	0.3453	0.1200	0.0043	0.79	1962	78	4.0	1959	51	2.6	1956	64	3.3	1803	0.8	100.3
	T4-37-11-2	core	25	281	0.3630	0.0110	6.0088	0.2159	0.1201	0.0023	0.84	1996	52	2.6	1977	31	1.6	1957	34	1.8	12235	0.1	102.0
	T4-37-9-3	core	25	564	0.3445	0.0152	5.5707	0.2942	0.1173	0.0034	0.83	1908	73	3.8	1912	45	2.4	1915	52	2.7	1668	1.1	99.7
	T4-37-1-1	core	25	634	0.3413	0.0196	5.5676	0.3657	0.1183	0.0038	0.88	1893	94	5.0	1911	57	3.0	1931	57	2.9	1095	1.6	98.0
	T4-37-7-3	core	25	1034	0.3449	0.0186	5.5725	0.3392	0.1172	0.0033	0.88	1910	89	4.7	1912	52	2.7	1914	51	2.7	684	2.2	99.8
	T4-37-4-2	core	25	816	0.3616	0.0194	6.1732	0.4034	0.1238	0.0046	0.82	1990	92	4.6	2001	57	2.9	2012	66	3.3	598	2.5	98.9
	T4-37-5-2	core	25	1502	0.3510	0.0186	5.7668	0.3613	0.1192	0.0040	0.85	1939	89	4.6	1941	54	2.8	1944	60	3.1	499	3.1	99.8
	T4-37-4-3	core	25	625	0.3485	0.0096	5.6603	0.2298	0.1178	0.0035	0.68	1927	46	2.4	1925	35	1.8	1923	53	2.8	357	4.2	100.2
	T4-37-7-2	core	25	979	0.2265	0.0189	3.6951	0.3496	0.1183	0.0053	0.88	1316	99	7.5	1570	76	4.8	1931	80	4.2	306	5.8	68.1
	T4-37-12-3	core	25	1063	0.2635	0.0079	4.3406	0.1793	0.1195	0.0034	0.72	1508	40	2.7	1701	34	2.0	1948	51	2.6	209	7.3	77.4
	T4-37-3-5	core	25	297	0.3303	0.0138	5.0437	0.9973	0.1108	0.0214	0.21	1840	67	3.6	1827	169	9.3	1812	358	19.7	45	33.9	101.5
	91500-3		25	71	0.1829	0.0029	1.9090	0.0525	0.0757	0.0017	0.57	1083	16	1.5	1084	18	1.7	1087	45	4.2	4215	0.4	99.7
	91500-4		25	80	0.1769	0.0051	1.8136	0.0850	0.0743	0.0027	0.62	1050	28	2.7	1050	31	2.9	1051	74	7.1		0.0	99.9

Table 17. Geochemical composition of the Katuma metabasites and gabbronorites; major elements in wt. % and trace elements in ppm.

	Metabasite																		Gabbronorite				
Sample ID	T1-12	T1-13	T1-16	T2-9	T3-8	T4-5	T6-5	T7-3	T9-1	T10-1	T11-1	T14-2	T16-1	T17-3	T19-1	T21-1	T22-3	T26-3	T1-18	T1-19	T5-2	T13-1	T17-1
SiO_2	49.33	48.98	49.97	54.53	49.25	49.69	55.96	58.87	49.20	49.40	48.80	48.35	50.14	53.96	48.36	50.49	43.46	50.60	51.01	51.04	51.73	51.97	53.56
TiO_2	1.06	2.26	2.03	0.76	1.04	1.36	1.02	0.77	1.57	0.82	1.74	1.94	0.72	0.55	1.28	2.37	3.08	0.87	0.35	0.45	0.32	0.33	11.48
Al_2O_3	13.80	12.00	11.83	16.14	13.64	14.08	17.42	17.29	12.94	15.19	12.45	12.32	14.39	11.62	13.61	11.67	14.67	14.17	8.41	8.11	8.36	10.16	0.56
Fe_2O_3	14.72	18.01	18.53	8.43	13.74	13.96	7.37	6.25	16.22	11.82	16.94	16.84	11.21	8.91	13.89	18.89	16.24	12.90	10.06	10.38	10.07	9.42	13.21
MnO	0.21	0.25	0.26	0.13	0.22	0.24	0.10	0.07	0.24	0.20	0.24	0.24	0.20	0.14	0.22	0.24	0.22	0.20	0.15	0.17	0.17	0.16	8.69
MgO	6.61	4.89	4.41	5.34	6.76	6.25	3.19	3.45	6.10	6.91	4.78	5.44	8.46	13.44	7.14	3.87	5.76	7.37	19.05	19.40	19.11	17.26	6.97
CaO	10.58	9.30	9.09	6.81	9.91	10.21	6.06	5.29	10.27	11.84	9.40	9.51	12.64	6.93	10.77	8.42	7.54	11.25	5.27	4.61	6.28	7.26	0.04
Na_2O	2.06	2.21	2.40	3.57	2.37	1.04	4.67	3.98	2.09	1.83	2.76	1.98	1.61	2.12	2.50	2.24	3.06	1.94	1.00	0.75	1.18	1.42	2.11
K_2O	0.24	0.72	0.57	1.67	1.07	1.03	1.76	2.08	0.37	0.17	0.72	1.34	0.14	0.50	0.98	0.74	0.26	0.20	0.69	0.88	0.41	0.37	0.51
P_2O_5	0.12	0.25	0.20	0.26	0.10	0.11	0.36	0.23	0.13	0.06	0.16	0.17	0.05	0.04	0.10	0.15	0.85	0.07	0.06	0.06	0.04	0.05	0.14
LOI	0.50	-0.31	-0.75	1.81	0.89	1.90	1.20	0.64	-0.16	-0.10	0.23	0.94	-0.25	0.60	0.75	0.27	2.90	-0.39	2.94	3.96		0.31	0.60
Total	99.2	98.9	99.3	99.5	99.0	99.9	99.1	98.9	99.1	98.2	98.2	99.1	99.3	98.81	99.6	99.4	98.0	99.6	99.0	99.8	97.7	98.7	97.4
Cr	100	82	58	202	257	172	23	96	149	335	80	85	570		126	25	43	211	2542	2526	2484	2093	916.00
Ni	25.4	28.5	19.7	44.1	27.2	47.4	3.4	30.5	22.3	14.5	15.8	26.9	15.6	3.3	29.0	9.1	82.5	53.8	149.7	194.5	151.2	168.2	242.7
V	350	419	425	205	282	341	189	150	373	267	375	442	281	269	342	750	260	285	160	158	165	168	121
Zr	72.5	223.3	163.3	82.0	83.2	91.3	253.8	120.9	105.4	49.0	133.7	135.5	42.0	52.0	71.6	137.0	197.9	54.5	42.0	38.0	30.6	34.3	32.1
Hf	2.0	6.1	4.2	2.1	2.5	2.6	6.6	2.9	2.9	1.4	3.9	3.9	1.3	1.7	2.0	3.8	4.4	1.7	1.1	1.1	0.8	0.9	1.0
Nb	5.7	14.3	12.5	9.3	5.4	4.0	10.3	8.7	6.9	3.2	10.6	8.5	2.7	3.7	5.7	7.4	11.3	3.1	1.3	1.8	1.2	1.2	1.7
Ta	0.4	1.1	0.7	0.5	0.2	0.3	0.5	0.4	0.4	0.2	0.6	0.6	0.1	0.2	0.3	0.4	0.6	0.1	b.d	0.1	b.d	b.d	b.d
Cs	0.4	1.3	0.8	0.3	0.3	0.3	0.3	0.9	0.5	0.2	b.d	b.d	0.2	0.4	0.1	2.3	b.d	0.4	3.2	4.4	0.9	0.7	0.3
Rb	8.5	33.7	19.6	55.9	26.9	38.8	32.3	90.9	15.0	6.1	9.8	20.7	4.5	9.0	15.7	34.8	5.9	4.7	33.2	45.5	13.3	11.8	15.8
Sr	115.8	141.5	165.8	504.4	192.7	217.0	998.9	598.8	141.5	139.3	190.5	130.1	121.2	511.4	229.8	163.9	551.1	127.3	126.8	126.7	142.0	175.7	262.0
Y	24.3	55.8	44.5	22.9	23.5	28.9	28.3	12.9	32.5	17.3	42.1	39.0	16.6	23.9	25.0	40.0	34.6	18.8	8.7	8.2	7.1	7.8	5.9
Ba	35	167	206	680	184	385	1199	697	83	51	772	163	122	221	358	187	170	78	154	196	128	133	84
La	6.6	21.7	18.5	30.9	9.9	10.1	54.4	25.1	9.6	4.9	25.0	12.7	5.8	12.3	9.0	14.6	31.0	4.7	7.7	7.5	5.9	6.7	5.3
Ce	16.4	50.5	41.8	73.0	22.1	19.2	117.0	54.4	22.4	11.0	28.1	30.4	9.3	31.6	16.0	30.7	69.2	11.1	16.1	15.5	13.8	13.3	11.8
Pr	2.19	6.50	5.18	8.60	2.66	2.93	13.59	6.32	3.11	1.51	5.34	4.03	1.65	4.41	2.49	4.01	8.88	1.54	1.92	1.82	1.57	1.59	1.34
Nd	10.4	26.6	23.1	33.1	10.1	13.2	52.6	22.9	14.7	6.5	21.4	17.3	7.2	22.3	11.6	19.2	36.4	6.4	8.0	7.1	6.6	7.3	5.2
Sm	2.88	7.23	5.94	6.41	2.97	3.77	10.04	4.34	3.86	2.04	5.41	4.98	1.84	4.71	3.19	5.20	8.02	2.27	1.63	1.57	1.28	1.49	1.38
Eu	0.86	1.84	1.73	1.76	0.93	1.25	2.26	1.34	1.29	0.74	1.52	1.45	0.76	1.5	1.13	1.71	2.53	0.80	0.46	0.45	0.40	0.41	0.51
Gd	3.57	8.99	6.62	4.95	3.47	4.81	7.40	3.38	4.96	2.47	6.71	6.15	2.45	4.86	3.97	6.40	7.86	2.78	1.68	1.52	1.33	1.38	1.29
Tb	0.65	1.61	1.22	0.74	0.62	0.85	1.02	0.47	0.90	0.47	1.16	1.10	0.45	0.79	0.73	1.13	1.22	0.54	0.25	0.25	0.23	0.23	0.22
Dy	3.69	9.44	7.28	3.78	3.89	5.20	5.22	2.45	5.50	2.73	6.85	6.76	2.66	4.66	4.40	6.52	6.34	2.99	1.57	1.30	1.29	1.34	1.08
Ho	0.96	2.17	1.69	0.77	0.90	1.09	0.97	0.45	1.24	0.66	1.53	1.57	0.59	0.93	0.89	1.58	1.30	0.80	0.31	0.33	0.31	0.27	0.20
Er	2.82	6.46	4.64	2.20	2.52	3.19	2.56	1.16	3.62	1.84	4.86	4.37	1.82	2.58	2.37	4.44	3.87	2.21	0.96	0.92	0.85	0.78	0.56
Tm	0.43	0.92	0.69	0.31	0.35	0.45	0.37	0.17	0.56	0.28	0.65	0.66	0.26	0.39	0.38	0.61	0.51	0.31	0.13	0.13	0.12	0.13	0.09
Yb	2.69	5.47	4.23	1.96	2.41	2.91	2.26	1.11	3.34	1.77	4.14	4.08	1.43	2.58	2.17	3.66	2.97	2.00	0.83	0.80	0.76	0.74	0.46
Lu	0.45	0.95	0.70	0.32	0.40	0.46	0.36	0.19	0.53	0.27	0.68	0.65	0.25	0.34	0.33	0.60	0.48	0.30	0.13	0.13	0.12	0.13	0.08
Th	1	5	2	4	2	1	7	1	1	1	1	2	0	1	1	3	1	1	2	1	1	1	2

Table 17 continued

	Metabasite																		Gabbronorite				
Sample ID	T1-12	T1-13	T1-16	T2-9	T3-8	T4-5	T6-5	T7-3	T9-1	T10-1	T11-1	T14-2	T16-1	T17-3	T19-1	T21-1	T22-3	T26-3	T1-18	T1-19	T5-2	T13-1	T17-1
U	0.3	1.4	0.7	0.5	0.5	0.4	0.4	0.2	0.4	b.d	0.5	0.6	b.d	0.2	0.3	0.8	0.2	b.d	0.3	0.4	0.3	0.3	0.7
Pb	1.4	2.1	2.8	9.1	7.7	3.6	47.1	4.5	0.6	0.7	4.8	2.6	0.7	1.1	2.2	2.0	2.0	1.9	2.9	3.7	2.8	3.1	0.9
Au	6.3	2.6	7.6	0.5	5.8	2.4	0.5	2.7	6.6	3.2	8.8	1.6	3.4	b.d	b.d	0.8	b.d	3.1	b.d	0.7	1.7	4.6	1.0
Co	55.5	53.0	56.6	30.7	56.0	51.2	19.1	19.3	55.5	48.6	52.2	52.3	50.0	26.4	55.8	54.7	47.4	52.8	73.8	74.1	77.4	71.5	54.8
Cu	161.6	365.5	342.8	135.9	116.6	38.7	17.8	37.7	268.8	152.5	315.3	118.8	110.7	16.5	51.4	21.4	47.4	166.3	42.9	39.9	59.9	51.9	83.1
Zn	15	43	44	48	34	37	53	62	21	10	35	46	7	46	34	68	91	19	14	17	5	5	12
Th/Yb	0.37	0.88	0.52	1.89	0.66	0.38	2.96	0.90	0.36	0.34	0.31	0.51	0.28	0.23	0.37	0.79	0.47	0.30	1.81	1.50	1.32	1.62	3.91
Th/Nb	0.18	0.34	0.18	0.40	0.30	0.28	0.65	0.11	0.17	0.19	0.12	0.25	0.15	0.16	0.14	0.39	0.12	0.19	1.15	0.67	0.83	1.00	1.06
Nb/La	0.86	0.66	0.68	0.30	0.55	0.40	0.19	0.35	0.72	0.65	0.42	0.67	0.47	0.30	0.63	0.51	0.36	0.66	0.17	0.24	0.20	0.18	0.32
Hf/Th	2.00	1.27	1.91	0.57	1.56	2.36	0.99	2.90	2.42	2.33	3.00	1.86	3.25	2.83	2.50	1.31	3.14	2.83	0.73	0.92	0.80	0.75	0.56
Zr/Y	2.98	4.00	3.67	3.58	3.54	3.16	8.97	9.37	3.24	2.83	3.18	3.47	2.53	2.18	2.86	3.43	5.72	2.90	4.83	4.63	4.31	4.40	5.44
Ta/Yb	0.15	0.20	0.17	0.26	0.08	0.10	0.22	0.36	0.12	0.11	0.14	0.15	0.07	0.08	0.14	0.11	0.20	0.05		0.13			
Ti/Zr	87.63	60.66	74.50	55.55	74.92	89.28	24.09	38.17	89.28	100.30	78.00	85.81	102.74	0.01	107.15	103.68	93.28	95.67	49.95	70.97	62.68	57.66	102.69
La/Ta	16.50	19.73	26.43	61.80	49.50	33.67	108.80	62.75	24.00	24.50	41.67	21.17	58.00	61.50	30.00	36.50	51.67	47.00		75.00			
Nb/Zr	0.08	0.06	0.08	0.11	0.06	0.04	0.04	0.07	0.07	0.07	0.08	0.06	0.06	0.07	0.08	0.05	0.06	0.06	0.03	0.05	0.04	0.03	0.05
Ti/Y	261.44	242.74	273.41	198.91	265.24	282.04	216.02	357.75	289.53	284.08	247.71	298.13	259.96	0.01	306.86	355.11	533.52	277.36	241.11	328.91	270.13	253.57	558.71
Ta/Hf	0.20	0.18	0.17	0.24	0.08	0.12	0.08	0.14	0.14	0.14	0.15	0.15	0.08	0.12	0.15	0.11	0.14	0.06		0.09			
Eu/Eu*	0.82	0.70	0.84	0.96	0.89	0.90	0.80	1.07	0.90	1.01	0.77	0.80	1.09	0.96	0.97	0.91	0.97	0.97	0.85	0.89	0.94	0.87	1.17
$(La/Yb)_{CN}$	1.65	2.67	2.95	10.63	2.77	2.34	16.23	15.25	1.94	1.87	4.07	2.10	2.73	3.76	2.80	2.69	7.04	1.58	6.25	6.32	5.23	6.10	7.77

Table 18. Geochemical composition of the Katuma orthogneisses and granitoids; major elements are presented in wt. % and trace elements in ppm.

	Neoarchean								Paleoroterozoic				
Sample ID	T1-17	T2-10	T6-6	T7-2	T17-2	T20-2	T14-3	T26-2	T2a-1	T2a-2	T2c-1	T19-3	T20-1
SiO_2	67.58	67.51	71.79	67.09	68.97	73.89	65.90	69.43	55.32	73.05	64.07	66.34	63.04
TiO_2	15.90	14.03	15.88	15.35	16.12	12.95	15.66	15.17	15.09	12.68	19.65	14.90	15.53
Al_2O_3	0.44	0.39	0.14	0.54	0.44	0.09	0.55	0.47	0.67	0.20	0.15	0.69	0.58
Fe_2O_3	1.28	2.92	0.26	1.22	0.90	0.32	2.56	1.61	7.84	0.37	0.53	2.48	2.46
MnO	2.81	4.47	1.44	3.44	1.92	0.77	4.24	3.29	7.29	3.31	1.29	4.14	4.93
MgO	2.55	3.58	0.62	2.45	2.13	1.04	3.09	2.04	4.28	0.12	3.57	1.80	4.05
CaO	0.08	0.10	0.28	0.28	0.09	0.02	0.16	0.08	0.08	0.05	0.09	0.23	0.20
Na_2O	4.36	3.73	4.43	3.53	3.94	2.61	4.06	4.09	2.67	2.92	5.15	4.20	3.55
K_2O	2.83	1.67	3.21	4.49	4.25	5.45	2.33	2.52	3.93	3.32	3.38	3.33	3.46
P_2O_5	0.03	0.06	bd.	0.03	0.02	0.01	0.04	0.04	0.15	0.43	0.02	0.05	0.09
LOI	0.72	1.28	1.32	0.27	0.52	0.54	0.70	0.53	1.60	2.56	0.77	0.63	1.40
Total	98.6	99.7	99.4	98.7	99.3	97.7	99.3	99.3	98.9	99.0	98.7	98.8	99.3
Cr	23	137	bd.	bd.	bd.	bd.	108	104	64	bd.	bd.	37	25
Ni	17.5	34.8	2.8	5.3	3.2	4.0	83.0	16.5	72.9	17.6	10.5	22.9	13.5
V	50	69	15	52	37	b.d	79	65	107	23	16	74	91
Zr	132.6	77.2	279.3	398.5	161.1	198.9	136.2	142.1	90.7	137.4	104.6	376.0	180.0
Hf	3.4	2.6	7.4	10.3	3.9	5.3	3.8	3.8	2.4	3.5	2.8	8.7	4.7
Nb	5.3	5.0	1.0	4.0	3.9	1.7	4.3	7.5	9.6	6.2	3.8	8.5	8.6
Ta	0.2	0.3	b.d	0.2	0.1	b.d	0.2	0.6	0.8	0.5	0.4	0.4	0.6
Cs	1.9	0.2	0.5	0.7	0.6	0.2	2.2	3.7	3.5	1.0	0.4	0.3	1.0
Rb	89.8	48.1	84.5	127.9	113.3	137.4	88.7	99.8	234.2	143.9	94.9	69.2	118.7
Sr	370.3	345.7	171.3	522.8	287.9	336.9	451.1	357.0	195.2	72.4	488.5	229.4	452.3
Y	4.2	10.2	7.4	4.7	4.7	1.6	7.3	7.4	15.3	8.7	4.3	9.9	21.6
Ba	541	843	928	1373	537	1592	421	375	558	597	870	1351	1026
La	46.1	13.1	68.4	76.2	61.3	36.2	28.7	25.9	30.7	270.8	15.5	69.7	53.3
Ce	93.7	29.5	119.9	135.6	138.5	64.4	59.9	52.0	60.1	436.6	22.6	131.2	94.2
Pr	10.73	4.08	11.47	13.71	16.76	5.24	6.61	5.85	6.77	40.10	2.33	13.08	9.88
Nd	40.3	18.2	37.5	43.0	62.4	14.4	24.3	21.0	24.6	109.8	8.1	42.9	35.9
Sm	6.17	2.85	3.86	5.17	10.30	1.30	4.00	3.58	4.48	10.26	1.07	5.06	5.50
Eu	0.75	0.94	1.12	1.09	0.78	0.63	0.80	0.84	1.01	1.06	0.77	0.93	1.28
Gd	3.31	2.47	2.53	2.53	5.55	0.68	2.86	2.57	3.58	4.52	0.90	3.09	4.49
Tb	0.32	0.34	0.29	0.23	0.50	0.07	0.36	0.33	0.53	0.46	0.13	0.37	0.68
Dy	1.12	1.72	1.47	0.86	1.58	0.29	1.55	1.49	2.45	1.90	0.77	1.77	3.65
Ho	0.10	0.38	0.23	0.14	0.15	0.05	0.29	0.26	0.56	0.27	0.13	0.33	0.71
Er	0.31	1.07	0.69	0.40	0.29	0.17	0.75	0.78	1.68	0.67	0.46	0.99	2.29
Tm	0.02	0.14	0.09	0.06	0.03	0.02	0.08	0.07	0.23	0.08	0.06	0.14	0.32
Yb	0.20	0.95	0.62	0.46	0.22	0.23	0.59	0.47	1.50	0.81	0.46	0.91	2.25
Lu	0.03	0.14	0.10	0.07	0.03	0.03	0.08	0.08	0.23	0.09	0.07	0.12	0.36
Th	23.9	2.8	6.0	40.8	44.2	13.5	9.1	8.3	9.4	80.3	4.3	40.9	23.2
U	1.4	0.2	0.9	0.9	1.4	0.4	1.2	2.9	1.4	1.3	1.0	0.9	1.7
Pb	7.6	7.6	4.3	7.0	9.6	20.5	4.8	3.8	4.9	12.0	13.1	7.8	21.3
Au	b.d	b.d	1.2	b.d	b.d	b.d	b.d	b.d	b.d	3.9	b.d	b.d	b.d
Co	7.3	11.0	5.9	6.6	4.0	3.1	17.3	7.0	23.3	20.0	2.9	7.6	13.9
Cu	11.1	114.7	449.8	9.8	1.4	35.0	35.2	10.2	1.0	160.9	11.2	6.5	26.9
Zn	63	29	3	48	56	16	54	77	108	23	10	48	30
K_2O/Na_2O	0.6	0.4	0.7	1.3	1.1	2.1	0.6	0.6	1.5	1.1	0.7	0.8	1.0
Fe#	0.7	0.6	0.8	0.6	0.7	0.7	0.6	0.7	0.5	0.9	0.7	0.6	0.6
Th/Hf	7.03	1.08	0.81	3.96	11.33	2.55	2.39	2.18	3.92	22.94	1.54	4.70	4.94
Th/Ta	119.50	9.33		204.00	442.00		45.50	13.83	11.75	160.60	10.75	102.25	38.67
Ta/Hf	0.06	0.12		0.02	0.03		0.05	0.16	0.33	0.14	0.14	0.05	0.13
Eu/Eu*	0.51	1.08	1.10	0.92	0.32	2.05	0.72	0.85	0.77	0.48	2.40	0.72	0.79
$(La/Yb)_{CN}$	165.34	9.89	79.13	118.82	199.87	112.90	34.89	39.53	14.68	239.81	24.17	54.94	16.99

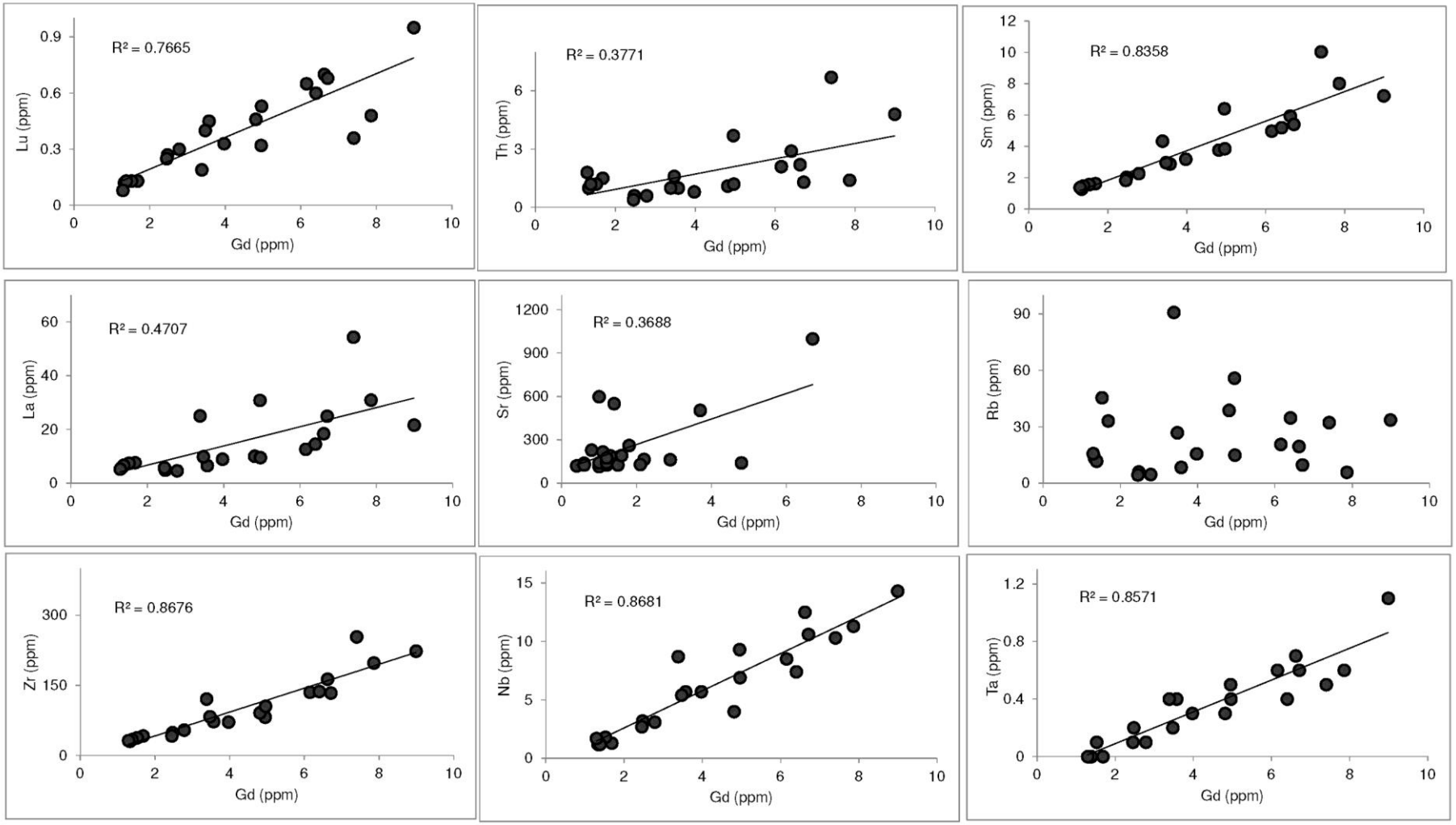

Fig. 1.16 Trace elements (ppm) versus Gd (ppm) diagrams for the Katuma metabasites and gabbros.

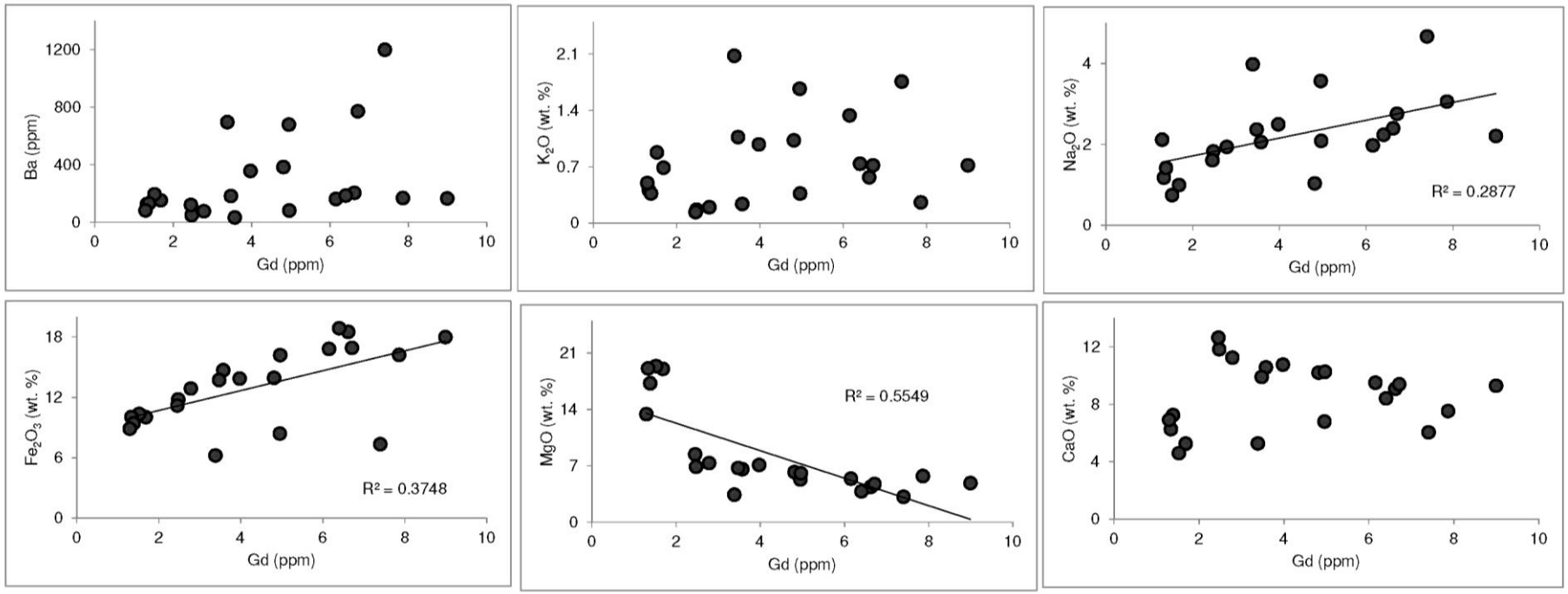

Fig. 1.16 Continued

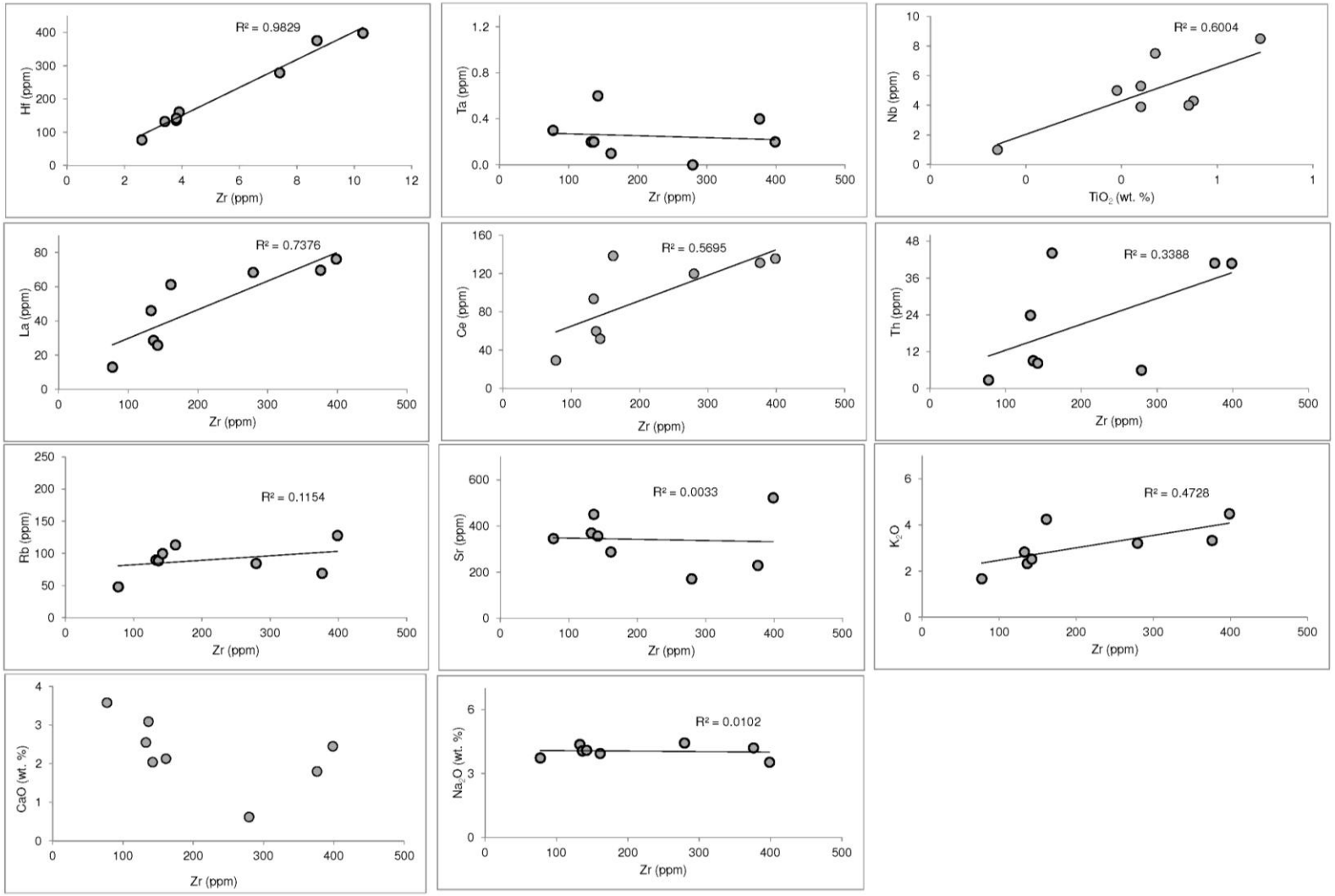

Fig. 1.17 Diagrams showing trace elements (ppm) versus Zr (ppm) or TiO_2 (wt. %) for the Katuma orthogneisses and granitoids

Chapter 2

Table 2 Representative mineral chemical data for metabasites

	Plagioclase						Clinopyroxene					Orthopyroxene	
	T1-16	T16-1	T9-1	T10-1	T13-3	T17-3	T1-16	T16-1	T9-1	T10-1	T13-3	T1-16	T16-1
No.	382	472	165	160	524	371	426	592	259	264	653	448	497
SiO_2	62.55	55.74	60.01	56.98	59.73	56.61	51.82	53.07	52.08	53.03	52.72	49.92	52.60
TiO_2	0.00	0.00	0.00	0.00	0.00	0.00	0.03	0.11	0.09	0.11	0.15	0.01	0.00
Al_2O_3	23.66	27.75	26.12	26.75	24.94	27.27	1.10	1.37	0.90	1.30	1.03	0.64	1.09
Cr_2O_3	0.00	0.00	0.00	0.00	0.00	0.00	0.06	0.26	0.10	0.15	0.02	0.00	0.03
Fe_2O_3	n.d	n.d	0.14	n.d	0.23	0.16	nc	nc	nc	nc	nc	nc	nc
FeO	0.19	0.28	nc	0.08	nc	nc	14.17	7.47	12.74	8.52	11.07	35.89	25.71
MgO	0.00	0.00	0.00	0.00	0.00	0.00	10.24	13.90	11.42	13.72	12.54	12.37	20.31
MnO	0.00	0.00	0.00	0.00	0.00	0.00	0.13	0.08	0.24	0.12	0.12	0.41	0.43
CaO	4.50	9.86	6.78	9.09	6.28	9.00	21.60	23.20	22.16	22.84	22.79	0.58	0.34
Na_2O	8.97	6.03	8.00	6.36	5.62	6.72	0.40	0.32	0.23	0.30	0.27	0.00	0.02
K_2O	0.22	0.15	0.05	0.13	4.01	0.04	0.02	0.00	0.00	0.00	0.00	0.00	0.01
Total	100.15	99.84	101.10	99.41	100.81	99.80	99.55	99.78	99.96	100.08	100.71	99.82	100.54
Structural formulae													
Si	2.77	2.51	2.65	2.57	2.68	2.55	1.99	1.98	1.98	1.98	1.97	1.99	1.98
Ti	0.00	0.00	0.00	0.00	0.00	0.00	0.00	0.00	0.00	0.00	0.00	0.00	0.00
Al	1.23	1.48	1.36	1.42	1.32	1.45	0.05	0.06	0.04	0.06	0.05	0.03	0.05
Fe^{2+}	0.01	0.01	nc	0.00	nc	nc	0.45	0.23	0.41	0.27	0.32	1.20	0.81
Mg	0.00	0.00	0.00	0.00	0.00	0.00	0.59	0.77	0.65	0.76	0.70	0.74	1.14
Mn^{2+}	0.00	0.00	0.00	0.00	0.00	0.00	0.00	0.00	0.01	0.00	0.00	0.01	0.01
Ca	0.21	0.48	0.32	0.44	0.30	0.43	0.89	0.93	0.90	0.91	0.91	0.02	0.01
Na	0.77	0.53	0.68	0.56	0.49	0.59	0.03	0.02	0.02	0.02	0.00	0.00	0.00
K	0.01	0.01	0.00	0.01	0.23	0.00	0.00	0.00	0.00	0.00	0.02	0.00	0.00
Total	5.00	5.01	5.02	5.00	5.02	5.02	4.00	4.00	4.00	4.00	4.00	3.99	4.00
An	21.43	47.07	31.81	43.79	29.59	42.43							
Ab	77.31	52.09	67.91	55.45	47.92	57.33							
Or	1.25	0.85	0.28	0.76	22.50	0.24							

n.c - not calculated, n.d - not determined

Table 2 continued

	Garnet								Biotite	Hornblende		
	T1-16	T16-1	T9-1	T10-1	T13-3	T17-3	T17-3	T17-3	T17-3	T17-3	T17-3	T17-3
No.	367	541	312	43	622	211	225	333	311	297	325	356
SiO_2	38.15	39.03	38.45	38.99	38.15	38.79	38.77	38.42	36.29	42.81	41.42	42.68
TiO_2	0.00	0.00	0.02	0.00	0.08	0.27	0.24	0.14	3.33	1.68	1.74	1.86
Al_2O_3	21.32	22.32	22.35	22.11	21.87	21.71	21.75	21.85	14.69	12.69	13.59	12.28
Cr_2O_3	0.00	0.00	nd	0.00	nd	nd	nd	nd	0.00	0.02	0.04	0.00
Fe_2O_3	nc	nc	nc	nc	nc	nc	nc	nc	nc	nc	nc	nc
FeO	30.37	24.72	27.29	24.38	26.84	25.20	24.09	25.98	16.74	15.06	16.12	14.23
MgO	2.71	6.20	3.89	5.27	4.03	5.52	6.21	5.14	13.83	10.73	10.24	11.41
MnO	0.89	0.70	0.61	0.87	0.64	0.92	0.79	1.10	0.03	0.11	0.10	0.12
CaO	7.06	7.82	9.28	8.70	9.18	8.66	8.95	8.24	0.05	11.35	11.36	11.40
Na_2O									0.17	1.15	1.32	1.30
K_2O									9.58	1.13	1.45	1.31
Total	100.50	100.79	101.89	100.32	100.80	101.06	100.80	100.87	94.71	96.73	97.38	96.59
Structural formulae												
Si	3.02	3.00	2.97	3.01	2.97	2.99	2.98	2.98	5.52	6.42	6.24	6.41
Ti	0.00	0.00	0.00	0.00	0.00	0.02	0.01	0.01	0.38	0.19	0.20	0.21
Al	1.99	2.02	2.03	2.01	2.01	1.97	1.97	2.00	2.64	2.24	2.41	2.17
Fe^{2+}	2.01	1.59	1.76	1.58	1.75	1.62	1.55	1.68	2.13	1.89	2.03	1.79
Mg	0.32	0.71	0.45	0.61	0.47	0.64	0.71	0.59	3.14	2.40	2.30	2.55
Mn^{2+}	0.06	0.05	0.04	0.06	0.04	0.06	0.05	0.07	0.00	0.01	0.01	0.02
Ca	0.60	0.64	0.77	0.72	0.77	0.72	0.74	0.68	0.01	1.82	1.83	1.83
Na									0.05	0.33	0.38	0.38
K									1.86	0.22	0.28	0.25
Total	7.99	8.00	8.02	7.98	8.02	8.01	8.02	8.02	15.73	15.54	15.69	15.61
X_{Mg}	0.14	0.31	0.20	0.28	0.21	0.28	0.31	0.26	0.60	0.60	0.58	0.63
X_{Alm}	67.22	53.33	57.71	53.61	57.04	52.86	49.66	54.66				
X_{Prp}	10.72	23.68	15.08	20.34	15.75	21.21	23.88	19.94				
X_{Grs}	20.07	21.47	25.86	24.14	25.21	22.74	23.11	22.07				
X_{Sps}	2.00	1.52	1.35	1.90	1.43	2.00	1.73	2.42				

n.c - not calculated, n.d - not determined

Table 3 Representative mineral chemical data for metapelites

	Biotite						Biotite Incl. In Grt		Muscovite	
	T18-2	T18-2	T18-2	T4-11	T4-11	T4-11	T18-2	T18-2	T18-2	T18-2
No.	29	68	127	31	134	151	78	87	99	578
SiO_2	34.60	33.75	34.37	34.37	36.25	36.29	33.73	34.10	52.51	45.42
TiO_2	2.49	1.39	2.10	1.14	2.38	2.01	0.10	0.00	0.06	0.81
Al_2O_3	18.15	18.23	17.99	17.90	18.03	18.62	18.68	20.16	29.74	34.44
Cr_2O_3	0.08	0.05	0.08	0.05	0.02	0.04	0.00	0.02	0.06	0.06
Fe_2O_3	nc	nc	nc	nc	nc	nc	nc	nc	nc	nc
FeO	23.77	23.22	23.61	19.95	16.51	16.15	22.78	20.59	2.21	2.25
MgO	7.48	7.75	7.86	12.16	12.38	12.72	8.77	10.61	0.54	0.56
MnO	0.26	0.09	0.26	0.41	0.25	0.24	0.30	0.18	0.04	0.00
CaO	0.00	0.00	0.00	0.03	0.00	0.01	0.04	0.00	0.01	0.00
Na_2O	0.12	0.12	0.10	0.12	0.28	0.26	0.03	0.07	0.34	0.58
K_2O	10.07	10.07	10.24	8.35	9.91	9.67	9.59	9.74	9.54	10.77
Total	97.03	94.67	96.61	94.48	96.01	96.02	94.03	95.46	95.05	94.90
Structural formulae										
Si	5.30	5.32	5.29	5.30	5.42	5.41	5.33	5.23	6.92	6.12
Ti	0.29	3.39	0.24	3.25	3.18	3.27	3.48	3.65	0.01	0.08
Al	3.28	0.16	3.27	0.13	0.27	0.23	0.01	0.00	4.62	5.47
Cr	0.01	0.01	0.01	0.01	0.00	0.00	0.00	0.00	0.01	0.01
Fe^{3+}	nc	nc	nc	nc	nc	nc	nc	nc	nc	nc
Fe^{2+}	3.04	3.06	3.07	2.57	2.07	2.01	3.01	2.64	0.24	0.25
Mg	1.71	1.82	1.87	2.79	2.76	2.82	2.07	2.43	0.11	0.11
Mn^{2+}	0.03	0.01	0.03	0.05	0.03	0.03	0.04	0.02	0.00	0.00
Ca	0.00	0.00	0.00	0.01	0.00	0.00	0.01	0.00	0.00	0.00
Na	0.04	0.04	0.03	0.04	0.08	0.08	0.01	0.02	0.09	0.15
K	1.97	2.03	1.95	1.64	1.89	1.84	1.93	1.91	1.60	1.85
Total	15.66	15.85	15.77	15.78	15.70	15.69	15.89	15.90	13.60	14.06
X_{Mg}	0.36	0.33	0.34	0.52	0.57	0.58	0.41	0.48		

n.c - not calculated, n.d - not determined, Incl. - inclusion

Table 3 continued

	Garnet				K-feldspar			Plagioclase				Albite		Ab exs. in Kfs	
	T18-2	T18-2	T18-2		T18-2	T18-2	T18-2	T18-2	T18-2	T18-2	T18-2	T18-2	T18-2	T18-2	T18-2
No.	40	42	45		467	495	510	174	181	527	561	65	538	480	486
SiO_2	37.06	37.41	37.38		63.62	63.99	63.88	61.90	62.14	61.83	62.13	66.44	65.97	66.21	66.47
TiO_2	0.02	0.00	0.02		nd	nd	nd	nd	nd	nd	nd	nd	nd	nd	nd
Al_2O_3	21.59	21.76	21.75		19.06	18.85	19.03	23.97	23.89	23.89	23.88	20.78	20.19	20.99	20.83
Cr_2O_3	nd	nd	nd		nd	nd	nd	nd	nd	nd	nd	nd	nd	nd	nd
Fe_2O_3	nc	nc	nc		0.04	0.00	0.11	0.26	0.20	0.16	0.04	0.01	0.07	0.05	0.00
FeO	31.85	32.92	32.38		nd	nd	nd	nd	nd	nd	nd	nd	nd	nd	nd
MgO	4.48	4.41	4.40		nd	nd	nd	nd	nd	nd	nd	nd	nd	nd	nd
MnO	5.12	5.25	5.00		nd	nd	nd	nd	nd	nd	nd	nd	nd	nd	nd
CaO	0.72	0.68	0.69		0.11	0.05	0.09	4.66	4.55	4.60	4.68	1.22	0.48	1.38	1.31
Na_2O	nd	nd	nd		1.10	1.29	1.37	9.20	9.04	9.51	9.10	11.43	11.51	11.35	10.97
K_2O	nd	nd	nd		16.07	15.14	15.53	0.08	0.17	0.07	0.21	0.08	0.03	0.08	0.18
Total	100.83	102.43	101.62		100.00	99.89	100.01	100.07	99.99	100.05	100.04	100.06	100.00	100.06	99.76
Structural formulae															
Si	2.95	2.94	2.95		2.95	2.97	2.96	2.75	2.75	2.74	2.75	2.92	2.94	2.91	2.92
Ti	0.00	0.00	0.00		nd	nd	nd	nd	nd	nd	nd	nd	nd	nd	nd
Al	2.03	2.02	2.03		1.04	1.03	1.04	1.25	1.25	1.25	1.25	1.08	1.06	1.09	1.08
Cr	nd	nd	nd		nd	nd	nd	nd	nd	nd	nd	nd	nd	nd	nd
Fe^{3+}	nc	nc	nc		0.00	0.00	0.00	0.01	0.01	0.01	0.00	0.00	0.00	0.00	0.00
Fe^{2+}	2.12	2.17	2.14		nd	nd	nd	nd	nd	nd	nd	nd	nd	nd	nd
Mg	0.53	0.52	0.52		nd	nd	nd	nd	nd	nd	nd	nd	nd	nd	nd
Mn^{2+}	0.35	0.35	0.34		nd	nd	nd	nd	nd	nd	nd	nd	nd	nd	nd
Ca	0.06	0.06	0.06		0.01	0.00	0.00	0.22	0.22	0.22	0.22	0.06	0.02	0.06	0.06
Na	nd	nd	nd		0.10	0.12	0.12	0.79	0.78	0.82	0.78	0.97	1.00	0.97	0.94
K	nd	nd	nd		0.95	0.90	0.92	0.00	0.01	0.00	0.01	0.00	0.00	0.00	0.01
Total	8.03	8.05	8.03		5.05	5.02	5.04	5.02	5.01	5.04	5.02	4.97	5.03	5.03	5.01
X_{Mg}	0.20	0.19	0.19	An	0.54	0.22	0.41	21.78	21.56	21.02	21.88	5.55	2.26	6.26	6.11
X_{Alm}	68.21	68.59	69.14	Ab	9.34	11.45	11.77	77.80	77.51	78.63	76.98	94.00	97.56	93.30	92.89
X_{Prp}	18.02	17.57	17.55	Or	90.12	88.33	87.81	0.42	0.94	0.36	1.15	0.45	0.18	0.43	1.00
X_{Grs}	0.91	0.00	1.00												
X_{Sps}	11.70	11.89	11.33												

n.c - not calculated, n.d - not determined, exs - exsolution

Table 4 Geothermobarometric results of metabasites and metapelites of Katuma Block

Sample	Analyses	T ℃		P (Kbar)	
		Cpx-Grt		**Grt-Pl-Opx-Qz**	
T1-16-10	Pl_{382}-Cpx_{426}-Opx_{358}-Grt_{367}	660	EG	8.0	NP
		660	EG	7.4	ENK
		640	P	7.9	NP
		640	P	7.3	ENK
T16-01-10	Pl_{472}-Cpx_{592}-Opx_{497}-Grt_{541}	670	EG	7.9	NP
		670	EG	7.4	ENK
		650	P	7.9	NP
		Cpx-Grt		**Grt-Pl-Cpx-Qz**	
T9-1-10	Pl_{165}-Cpx_{259}-Grt_{312}	750	EG	8.7	NP
		750	EG	8.9	ENK
		730	P	8.6	NP
		730	P	8.8	ENK
T10-1-10	Pl_{160}-Cpx_{264}-Grt_{43}	700	EG	8.2	NP
		700	EG	8.5	ENK
		680	P	8.1	NP
		680	P	8.3	ENK
T13-3-10	Pl_{524}-Cpx_{653}-Grt_{622}	700	EG	10.7	NP
		700	EG	8.6	ENK
		680	P	10.5	NP
		680	P	8.4	ENK
		Hbl-Grt		**Grt-Pl-Hbl-Qz**	
T17-3-10	Pl_{286}-Hbl_{356}-Grt_{311} Pl_{325}-Hbl_{297}-Grt_{225}	680 - 790	GP Pet	6.6 - 8.7	KS
				Grt-Pl-Sil-Qz	
T18-2-10	Grt_{32}-Pl_{176b}	770		6.8	
	Grt_{53}-Pl_{186b}	770		7.1	NH
	Grt_{298}-Pl_{375}	770		6.7	
	Grt_{312}-Pl_{379}	770		6.8	
	Grt_{32}-Pl_{176b}	770		6.2	
	Grt_{53}-Pl_{186b}	770		6.4	HC
	Grt_{298}-Pl_{375}	770		6.1	
	Grt_{312}-Pl_{379}	770		6.3	
	Grt_{32}-Pl_{176b}	770		6.9	
	Grt_{53}-Pl_{186b}	770		7.1	KN
	Grt_{298}-Pl_{375}	770		6.8	
	Grt_{312}-Pl_{379}	770		6.9	

Geothermometers: EG, Ellis and Green (1979); P, Powell (1985); GP, Graham and Powell (1984); Pet, Perchuk et al. (1985). **Geobarometers**; NP, Newton and Perkins (1982); ENK, Eckert et. al. (1991); KS, Kohn and Spear (1990); NH, Newton and Haselton (1981); HC, Hodges and Crowley (1985); and KC, Koziol and Newton (1988).

Table 5 Major elements composition of metabasites and one metapelite sample (T18-2-10)

	T9-1-10	T10-1-10	T26-3-10	T18-2-10
Wt. %				
SiO_2	49.20	49.40	50.60	49.48
TiO_2	1.57	0.82	0.87	0.94
Al_2O_3	12.94	15.19	14.17	21.89
Fe_2O_3	16.22	11.82	12.90	10.51
MgO	6.10	6.91	7.37	2.94
CaO	10.27	11.84	11.25	0.66
Na_2O	2.09	1.83	1.94	1.89
K_2O	0.37	0.17	0.20	8.43
P_2O_5	0.13	0.06	0.07	0.05
MnO	0.24	0.20	0.20	0.23
LOI	0.31	0.60	0.50	1.46
Sum	99.44	98.74	100.07	98.48
Mole %				
Si	47.08	45.92	46.83	43.73
Ti	1.13	0.57	0.61	0.62
Al	14.59	16.64	15.46	22.80
Fe	11.68	8.27	8.98	6.99
Mg	8.70	9.58	10.17	3.87
Ca	10.53	11.79	11.16	0.62
Na	3.88	3.30	3.48	3.24
K	0.45	0.20	0.24	9.50
P	0.11	0.05	0.05	0.04
Mn	0.19	0.16	0.16	0.17
H	1.95	3.73	3.08	8.61

Table 6 Monazite core compositions and calculated U-Th-total Pb ages of a cordierite bearing metapelite (T4-11-10)

No.	265	273	274	275	276	277	280	281	284	287	288	289	294	297	299	300	304	307	312	313	319	320	321	326	327
Monazite	m7	m12	m12	m12	m12	m12	m15	m15	m15	m17	m17	m17	m19	m19	m21	m21	m22	m22	m24	m24	m27	m27	m27	m27	m27
SiO_2	0.17	0.71	0.16	1.01	0.32	0.39	0.63	0.58	0.83	0.82	0.67	1.07	0.34	0.59	1.81	1.68	0.55	0.69	0.83	0.81	0.36	0.37	0.17	0.24	0.30
P_2O_5	31.25	28.35	29.66	27.47	28.98	28.56	29.12	29.03	29.03	28.69	28.66	28.27	29.88	29.28	27.32	27.45	29.50	28.93	29.20	29.03	30.00	29.43	29.81	29.69	29.73
Al_2O_3	0.00	0.00	0.00	0.00	0.00	0.00	0.00	0.00	0.00	0.00	0.00	0.00	0.00	0.00	0.00	0.00	0.00	0.00	0.00	0.00	0.00	0.00	0.00	0.00	0.00
CaO	1.83	1.33	1.60	1.22	1.51	1.20	1.32	1.31	1.51	1.16	1.19	1.31	1.34	1.53	1.22	1.12	1.74	1.42	1.20	1.22	1.57	1.84	1.72	1.20	1.57
ThO_2	5.51	3.97	4.32	5.68	4.40	2.89	4.12	3.96	5.17	4.44	3.77	5.64	3.88	4.12	8.51	7.95	4.08	4.76	4.57	4.40	6.40	5.60	5.68	4.80	6.10
UO_2	0.50	0.03	0.09	0.01	0.16	0.05	0.04	0.03	0.08	0.04	0.02	0.03	0.17	0.10	0.04	0.01	0.04	0.01	0.05	0.03	0.66	0.40	0.34	0.56	0.64
PbO	0.65	0.35	0.41	0.50	0.43	0.27	0.37	0.36	0.47	0.39	0.34	0.52	0.40	0.38	0.74	0.68	0.37	0.41	0.40	0.39	0.82	0.61	0.59	0.59	0.74
La_2O_3	12.83	12.18	11.85	12.05	12.78	13.66	12.85	13.10	12.49	12.55	12.93	12.27	13.92	12.61	11.82	12.41	13.27	13.20	13.03	13.08	13.05	13.32	13.31	13.46	13.18
Ce_2O_3	25.81	27.09	25.46	26.79	26.11	27.91	27.28	26.97	26.11	26.86	27.76	26.23	26.95	26.84	25.52	25.69	26.45	26.88	27.10	27.44	25.62	26.07	25.79	26.53	25.53
Pr_2O_3	2.75	2.98	2.87	2.92	2.89	3.01	3.04	3.08	2.93	3.00	3.01	2.91	2.81	2.94	2.85	2.95	2.82	2.92	2.91	2.97	2.73	2.78	2.94	2.91	2.80
Nd_2O_3	11.34	12.24	11.13	12.20	11.08	11.49	11.72	11.68	11.29	12.22	11.98	11.63	10.99	11.15	11.54	11.56	10.94	11.55	11.98	11.94	10.90	10.80	10.89	11.22	10.87
Sm_2O_3	1.98	2.03	1.94	1.95	1.80	1.87	1.88	2.04	1.83	2.00	1.84	1.96	1.90	1.87	1.95	1.78	1.87	1.89	1.89	1.88	2.00	1.82	1.79	1.95	1.94
Eu_2O_3	0.33	0.22	0.45	0.15	0.26	0.09	0.19	0.15	0.15	0.25	0.17	0.17	0.33	0.23	0.20	0.20	0.23	0.17	0.05	0.00	0.00	0.00	0.00	0.00	0.00
Gd_2O_3	1.63	1.63	1.77	1.56	1.50	1.42	1.67	1.71	1.79	1.77	1.70	1.69	1.68	1.79	1.58	1.55	1.73	1.56	1.64	1.66	1.73	1.55	1.59	1.68	1.74
Dy_2O_3	0.72	0.69	0.96	0.60	0.69	0.56	0.75	0.78	0.80	0.68	0.69	0.73	0.72	0.80	0.65	0.62	0.77	0.65	0.65	0.63	0.80	0.67	0.70	0.75	0.81
Y_2O_3	3.12	2.94	4.54	2.52	3.20	2.80	3.43	3.46	3.54	2.91	2.87	3.25	3.10	3.74	2.69	2.58	3.50	2.73	3.03	2.90	2.59	2.75	2.73	2.46	2.66
Er_2O_3	0.21	0.20	0.31	0.18	0.25	0.22	0.20	0.22	0.26	0.21	0.22	0.24	0.24	0.25	0.18	0.18	0.28	0.20	0.19	0.22	0.11	0.19	0.19	0.13	0.15
Total	100.62	96.95	97.52	96.79	96.35	96.38	98.62	98.47	98.26	97.98	97.82	97.90	98.63	98.23	98.62	98.42	98.15	97.97	98.71	98.59	99.31	98.20	98.24	98.18	98.76
Si	0.006	0.029	0.006	0.041	0.013	0.016	0.025	0.023	0.033	0.033	0.027	0.043	0.013	0.023	0.073	0.068	0.022	0.027	0.033	0.032	0.014	0.014	0.007	0.010	0.012
P	1.007	0.967	0.991	0.950	0.986	0.978	0.972	0.972	0.970	0.968	0.969	0.957	0.991	0.976	0.929	0.934	0.980	0.973	0.973	0.970	0.993	0.985	0.995	0.995	0.991
Al	0.000	0.000	0.000	0.000	0.000	0.000	0.000	0.000	0.000	0.000	0.000	0.000	0.000	0.000	0.000	0.000	0.000	0.000	0.000	0.000	0.000	0.000	0.000	0.000	0.000
Ca	0.075	0.058	0.068	0.053	0.065	0.052	0.056	0.056	0.064	0.050	0.051	0.056	0.056	0.065	0.053	0.048	0.073	0.060	0.050	0.052	0.066	0.078	0.073	0.051	0.066
Th	0.048	0.036	0.039	0.053	0.040	0.027	0.037	0.036	0.046	0.040	0.034	0.051	0.035	0.037	0.078	0.073	0.037	0.043	0.041	0.040	0.057	0.050	0.051	0.043	0.055
U	0.004	0.000	0.001	0.000	0.001	0.000	0.000	0.000	0.001	0.000	0.000	0.000	0.002	0.001	0.000	0.000	0.000	0.000	0.000	0.000	0.006	0.004	0.003	0.005	0.006
Pb	0.007	0.004	0.004	0.006	0.005	0.003	0.004	0.004	0.005	0.004	0.004	0.006	0.004	0.004	0.008	0.007	0.004	0.004	0.004	0.004	0.009	0.007	0.006	0.006	0.008
La	0.180	0.181	0.173	0.182	0.190	0.204	0.187	0.191	0.182	0.184	0.191	0.181	0.201	0.183	0.175	0.184	0.192	0.193	0.189	0.190	0.188	0.194	0.194	0.197	0.191
Ce	0.360	0.400	0.368	0.401	0.384	0.413	0.394	0.391	0.377	0.392	0.406	0.384	0.386	0.387	0.375	0.378	0.380	0.391	0.390	0.397	0.367	0.377	0.372	0.385	0.368
Pr	0.038	0.044	0.041	0.044	0.042	0.044	0.044	0.044	0.042	0.044	0.044	0.042	0.040	0.042	0.042	0.043	0.040	0.042	0.042	0.043	0.039	0.040	0.042	0.042	0.040
Nd	0.154	0.176	0.157	0.178	0.159	0.166	0.165	0.165	0.159	0.174	0.171	0.166	0.154	0.157	0.166	0.166	0.153	0.164	0.168	0.168	0.152	0.152	0.153	0.159	0.153
Sm	0.026	0.028	0.026	0.027	0.025	0.026	0.026	0.028	0.025	0.028	0.025	0.027	0.026	0.025	0.027	0.025	0.025	0.026	0.026	0.026	0.027	0.025	0.024	0.027	0.026
Eu	0.004	0.003	0.006	0.002	0.004	0.001	0.003	0.002	0.002	0.003	0.002	0.002	0.004	0.003	0.003	0.003	0.003	0.002	0.001	0.000	0.000	0.000	0.000	0.000	0.000
Gd	0.021	0.022	0.023	0.021	0.020	0.019	0.022	0.023	0.023	0.023	0.023	0.022	0.022	0.023	0.021	0.021	0.023	0.021	0.021	0.022	0.022	0.020	0.021	0.022	0.023
Dy	0.009	0.009	0.012	0.008	0.009	0.007	0.010	0.010	0.010	0.009	0.009	0.009	0.009	0.010	0.008	0.008	0.010	0.008	0.008	0.008	0.010	0.009	0.009	0.010	0.010
Y	0.063	0.063	0.095	0.055	0.069	0.060	0.072	0.073	0.074	0.062	0.061	0.069	0.065	0.078	0.058	0.055	0.073	0.058	0.064	0.061	0.054	0.058	0.057	0.052	0.056
Er	0.003	0.003	0.004	0.002	0.003	0.003	0.003	0.003	0.003	0.003	0.003	0.003	0.003	0.003	0.002	0.002	0.003	0.003	0.002	0.003	0.001	0.002	0.002	0.002	0.002
Total	2.003	2.021	2.015	2.022	2.014	2.019	2.018	2.019	2.016	2.015	2.018	2.018	2.010	2.019	2.018	2.015	2.020	2.016	2.012	2.015	2.004	2.016	2.009	2.003	2.007
X_{LREE}	0.901	0.853	0.862	0.859	0.862	0.821	0.848	0.842	0.867	0.869	0.857	0.852	0.826	0.847	0.809	0.859	0.841	0.824	0.811	0.815	0.843	0.807	0.857	0.839	0.862
X_{HREE}	0.021	0.030	0.019	0.018	0.018	0.029	0.026	0.027	0.013	0.016	0.016	0.029	0.029	0.031	0.030	0.024	0.015	0.031	0.033	0.028	0.025	0.032	0.017	0.026	0.031
X_{Hut}	-0.001	0.007	0.046	0.059	0.048	0.026	0.018	0.020	0.061	0.049	0.059	0.004	0.019	0.019	0.037	0.005	0.079	0.016	0.025	0.010	0.037	0.026	0.060	0.050	0.010
X_{Brb}	0.059	0.064	0.068	0.059	0.066	0.070	0.057	0.060	0.056	0.060	0.061	0.072	0.069	0.051	0.076	0.074	0.061	0.082	0.078	0.102	0.068	0.079	0.061	0.058	0.048
X_{YPO4}	0.020	0.046	0.006	0.005	0.005	0.055	0.051	0.051	0.004	0.006	0.008	0.042	0.056	0.052	0.048	0.038	0.004	0.047	0.054	0.044	0.027	0.056	0.005	0.027	0.049
App. age (Ma)	1984.9	1985.8	1964.0	1972.9	1974.1	1990.5	1950.9	2004.5	1934.7	1922.7	2010.3	2054.5	1984.7	1937.9	1933.8	1934.7	1990.9	1925.3	1923.1	1958.5	2078.3	1933.0	1914.4	1944.4	1976.0
2σ err. age (± , Ma)	72.5	93.0	88.6	102.0	78.3	130.2	98.3	102.6	81.5	93.1	107.0	78.3	94.3	93.5	57.9	61.3	100.2	89.2	90.5	95.1	59.6	67.1	67.5	69.1	59.7

Table 7 Monazite rim compositions and calculated U-Th-total Pb ages of a cordierite bearing metapelite (T4-11-10)

No.	264	268	272	283	285	286	291	293	298	301	303	305	314	315	316	317	318
Monazite	m7	m7	m12	m15	m17	m17	m19	m19	m19	m21	m21	m22	m24	m24	m24	m27	m27
SiO_2	1.43	2.52	1.08	1.07	1.31	1.46	1.01	1.03	1.08	0.88	1.44	0.86	1.12	1.00	0.70	2.10	0.37
P_2O_5	28.11	26.72	28.09	28.41	27.67	27.65	28.85	29.11	29.02	29.08	28.19	29.08	28.46	29.51	29.73	27.08	29.94
Al_2O_3	0.00	0.10	0.00	0.00	0.00	0.00	0.00	0.00	0.00	0.00	0.00	0.00	0.00	0.00	0.00	0.00	0.00
CaO	1.27	1.09	1.16	1.14	1.02	1.07	1.17	1.07	1.05	1.46	1.16	1.18	1.22	1.19	1.49	1.16	1.43
ThO_2	7.93	9.81	6.09	5.66	6.56	7.27	5.45	5.38	5.58	6.60	7.40	4.80	5.76	5.87	6.04	9.82	6.12
UO_2	0.05	0.04	0.03	0.02	0.06	0.00	0.03	0.02	0.02	0.04	0.05	0.04	0.04	0.04	0.11	0.03	0.60
PbO	0.66	0.80	0.50	0.46	0.56	0.58	0.46	0.45	0.46	0.55	0.60	0.40	0.49	0.49	0.52	0.80	0.69
La_2O_3	13.27	11.56	12.29	12.48	12.91	12.35	12.76	12.81	12.81	13.31	12.55	12.90	13.45	13.70	13.81	12.02	13.18
Ce_2O_3	26.32	25.17	26.63	26.89	26.46	25.76	27.30	27.47	27.54	26.21	26.61	27.41	27.11	27.19	26.22	25.41	26.44
Pr_2O_3	2.96	2.77	2.94	3.09	2.90	2.86	2.97	3.07	3.12	2.85	2.97	3.07	2.91	2.97	2.77	2.89	3.01
Nd_2O_3	11.52	11.68	11.99	12.15	11.70	12.23	12.27	12.21	12.31	11.33	11.83	12.09	11.45	11.39	10.91	11.91	11.21
Sm_2O_3	1.73	1.81	1.93	1.93	1.75	1.96	1.88	1.98	1.91	1.73	1.79	1.85	1.70	1.66	1.62	1.71	1.93
Eu_2O_3	0.05	0.00	0.22	0.04	0.00	0.11	0.22	0.14	0.13	0.19	0.10	0.14	0.02	0.00	0.07	0.00	0.00
Gd_2O_3	1.26	1.36	1.42	1.51	1.50	1.55	1.60	1.61	1.50	1.47	1.58	1.62	1.46	1.46	1.37	1.35	1.68
Dy_2O_3	0.48	0.54	0.54	0.56	0.54	0.54	0.58	0.54	0.56	0.58	0.56	0.54	0.53	0.54	0.57	0.51	0.71
Y_2O_3	1.96	2.19	2.43	2.39	2.34	2.28	2.59	2.49	2.34	2.45	2.57	2.52	2.38	2.38	2.69	2.13	2.37
Er_2O_3	0.13	0.15	0.19	0.17	0.16	0.15	0.16	0.18	0.12	0.15	0.18	0.15	0.18	0.14	0.21	0.14	0.16
Total	99.14	98.31	97.51	97.95	97.44	97.82	99.29	99.57	99.56	98.89	99.58	98.63	98.26	99.53	98.82	99.06	99.85
Si	0.057	0.101	0.043	0.043	0.053	0.059	0.040	0.040	0.042	0.035	0.057	0.034	0.045	0.039	0.027	0.084	0.014
P	0.947	0.911	0.958	0.961	0.948	0.944	0.963	0.966	0.965	0.971	0.945	0.972	0.959	0.974	0.984	0.921	0.989
Al	0.000	0.005	0.000	0.000	0.000	0.000	0.000	0.000	0.000	0.000	0.000	0.000	0.000	0.000	0.000	0.000	0.000
Ca	0.054	0.047	0.050	0.049	0.044	0.046	0.049	0.045	0.044	0.061	0.049	0.050	0.052	0.050	0.062	0.050	0.060
Th	0.072	0.090	0.056	0.051	0.060	0.067	0.049	0.048	0.050	0.059	0.067	0.043	0.052	0.052	0.054	0.090	0.054
U	0.001	0.000	0.000	0.000	0.001	0.000	0.000	0.000	0.000	0.000	0.000	0.000	0.000	0.000	0.001	0.000	0.005
Pb	0.007	0.009	0.005	0.005	0.006	0.006	0.005	0.005	0.005	0.006	0.006	0.004	0.005	0.005	0.006	0.009	0.007
La	0.195	0.172	0.183	0.184	0.193	0.184	0.186	0.185	0.186	0.194	0.183	0.188	0.198	0.197	0.199	0.178	0.190
Ce	0.383	0.371	0.393	0.394	0.392	0.381	0.394	0.394	0.396	0.378	0.386	0.396	0.395	0.388	0.375	0.374	0.378
Pr	0.043	0.041	0.043	0.045	0.043	0.042	0.043	0.044	0.045	0.041	0.043	0.044	0.042	0.042	0.039	0.042	0.043
Nd	0.164	0.168	0.172	0.173	0.169	0.176	0.173	0.171	0.173	0.160	0.167	0.170	0.163	0.159	0.152	0.171	0.156
Sm	0.024	0.025	0.027	0.027	0.024	0.027	0.026	0.027	0.026	0.024	0.024	0.025	0.023	0.022	0.022	0.024	0.026
Eu	0.001	0.000	0.003	0.001	0.000	0.002	0.003	0.002	0.002	0.003	0.001	0.002	0.000	0.000	0.001	0.000	0.000
Gd	0.017	0.018	0.019	0.020	0.020	0.021	0.021	0.021	0.020	0.019	0.021	0.021	0.019	0.019	0.018	0.018	0.022
Dy	0.006	0.007	0.007	0.007	0.007	0.007	0.007	0.007	0.007	0.007	0.007	0.007	0.007	0.007	0.007	0.007	0.009
Y	0.042	0.047	0.052	0.051	0.050	0.049	0.054	0.052	0.049	0.052	0.054	0.053	0.050	0.049	0.056	0.046	0.049
Er	0.002	0.002	0.002	0.002	0.002	0.002	0.002	0.002	0.002	0.002	0.002	0.002	0.002	0.002	0.003	0.002	0.002
Total	2.013	2.014	2.014	2.013	2.014	2.013	2.013	2.010	2.009	2.011	2.014	2.011	2.014	2.005	2.006	2.014	2.005
X_{LREE}	0.802	0.779	0.810	0.816	0.811	0.804	0.814	0.820	0.824	0.794	0.795	0.820	0.813	0.815	0.793	0.781	0.792
X_{HREE}	0.024	0.027	0.028	0.029	0.029	0.029	0.030	0.030	0.028	0.028	0.030	0.030	0.028	0.028	0.028	0.026	0.033
X_{Hut}	0.025	0.052	0.011	0.008	0.022	0.026	0.005	0.008	0.011	0.004	0.024	-0.002	0.006	0.008	-0.002	0.048	0.007
X_{Brb}	0.108	0.094	0.099	0.097	0.088	0.092	0.098	0.090	0.088	0.122	0.097	0.099	0.103	0.100	0.125	0.099	0.119
X_{YPO4}	0.041	0.047	0.052	0.050	0.050	0.049	0.054	0.052	0.049	0.051	0.054	0.053	0.050	0.050	0.056	0.045	0.049
App. age (Ma)	1855.5	1824.2	1829.5	1839.8	1863.7	1806.4	1891.0	1870.4	1838.9	1864.2	1813.2	1851.6	1892.6	1863.4	1837.8	1842.4	1883.7
2σ err. age (± , Ma)	69.5	51.3	72.8	77.1	68.5	64.2	78.1	78.2	76.6	68.6	62.5	87.1	76.7	75.1	71.2	52.3	60.8

Table 8 Monazite core compositions and calculated U-Th-total Pb ages of a garnet bearing metapelite (T18-2-10)

Analysis No	25	26	27	28	29	30	31	32	33	43	46	46	47	48	49	50	53
Monazite	M2-1	M2-2	M2-3	M2-4	M2-5	M2 -6	M2-7	M2 -8	M2-9	m2	m2	m11-1	m11-2	m11-3	m11-4	m11-5	m2
SiO_2	0.20	0.27	0.21	0.24	0.19	0.17	0.18	0.19	0.19	0.24	0.17	0.35	0.40	0.36	0.36	0.38	0.35
P_2O_5	29.80	29.69	29.98	29.77	29.81	29.51	29.47	29.47	29.51	30.12	29.98	29.55	29.55	29.75	29.64	29.13	30.50
Al_2O_3	0.02	0.01	0.00	0.00	0.00	0.00	0.00	0.00	0.01	0.00	0.00	0.00	0.00	0.00	0.00	0.00	0.00
CaO	1.52	1.55	1.45	1.49	1.74	1.83	1.67	1.82	1.69	1.61	1.67	1.78	1.79	1.74	1.78	1.52	1.62
ThO_2	3.92	4.92	4.15	4.51	3.99	3.98	3.88	4.49	4.17	4.95	3.92	6.33	6.49	6.36	6.36	5.69	5.90
UO_2	0.41	0.62	0.47	0.52	0.36	0.43	0.44	1.34	0.48	0.62	0.45	0.60	0.57	0.60	0.60	0.50	0.10
PbO	0.46	0.63	0.53	0.57	0.47	0.50	0.49	0.83	0.51	0.63	0.49	0.75	0.76	0.74	0.76	0.64	0.54
La_2O_3	15.34	13.52	15.08	14.77	16.72	16.33	15.89	13.97	15.34	13.56	15.24	13.19	13.55	13.31	13.38	13.58	13.52
Ce_2O_3	28.59	27.20	27.69	27.52	28.45	27.25	27.75	27.17	27.51	27.52	28.18	26.53	26.37	26.50	26.35	26.49	27.24
Pr_2O_3	3.02	3.07	2.91	2.95	2.87	2.83	2.88	2.83	2.97	2.95	2.90	2.92	2.94	2.96	2.92	2.93	2.85
Nd_2O_3	11.06	11.85	11.43	11.44	10.84	10.64	10.82	10.89	10.96	11.59	10.89	11.47	11.19	11.36	11.33	11.34	11.45
Sm_2O_3	1.80	2.07	1.96	1.92	1.58	1.78	1.72	1.85	1.89	1.87	1.72	2.10	1.99	2.11	2.01	2.13	1.80
Eu_2O_3	0.00	0.02	0.24	0.26	0.00	0.00	0.00	0.00	0.14	0.12	0.09	0.15	0.16	0.25	0.27	0.23	0.23
Gd_2O_3	1.27	1.57	1.46	1.46	1.16	1.24	1.34	1.44	1.43	1.67	1.36	1.60	1.54	1.60	1.60	1.70	1.52
Dy_2O_3	0.42	0.67	0.49	0.49	0.34	0.39	0.44	0.54	0.47	0.59	0.47	0.62	0.54	0.58	0.58	0.64	0.63
Y_2O_3	1.69	2.20	1.93	1.96	1.44	1.73	1.82	2.12	1.92	2.24	1.90	2.02	1.95	2.02	2.03	2.12	2.58
Er_2O_3	0.08	0.11	0.11	0.11	0.08	0.09	0.10	0.14	0.11	0.12	0.10	0.12	0.12	0.12	0.12	0.11	0.21
Total	99.61	99.96	100.08	99.97	100.02	98.69	98.88	99.08	99.29	100.39	99.52	100.09	99.89	100.34	100.08	99.13	101.04
Si	0.01	0.01	0.01	0.01	0.01	0.01	0.01	0.01	0.01	0.01	0.01	0.01	0.02	0.01	0.01	0.01	0.01
P	0.99	0.98	0.99	0.99	0.99	0.99	0.99	0.99	0.98	0.99	0.99	0.98	0.98	0.98	0.98	0.98	0.99
Al	0.00	0.00	0.00	0.00	0.00	0.00	0.00	0.00	0.00	0.00	0.00	0.00	0.00	0.00	0.00	0.00	0.00
Ca	0.06	0.07	0.06	0.06	0.07	0.08	0.07	0.08	0.07	0.07	0.07	0.07	0.08	0.07	0.07	0.06	0.07
Th	0.04	0.04	0.04	0.04	0.04	0.04	0.03	0.04	0.04	0.04	0.03	0.06	0.06	0.06	0.06	0.05	0.05
U	0.00	0.01	0.00	0.00	0.00	0.00	0.00	0.01	0.00	0.01	0.00	0.01	0.00	0.01	0.01	0.00	0.00
Pb	0.00	0.01	0.01	0.01	0.00	0.01	0.01	0.01	0.01	0.01	0.01	0.01	0.01	0.01	0.01	0.01	0.01
La	0.22	0.20	0.22	0.21	0.24	0.24	0.23	0.20	0.22	0.19	0.22	0.19	0.20	0.19	0.19	0.20	0.19
Ce	0.41	0.39	0.40	0.39	0.41	0.39	0.40	0.39	0.40	0.39	0.40	0.38	0.38	0.38	0.38	0.38	0.38
Pr	0.04	0.04	0.04	0.04	0.04	0.04	0.04	0.04	0.04	0.04	0.04	0.04	0.04	0.04	0.04	0.04	0.04
Nd	0.15	0.17	0.16	0.16	0.15	0.15	0.15	0.15	0.15	0.16	0.15	0.16	0.16	0.16	0.16	0.16	0.16
Sm	0.02	0.03	0.03	0.03	0.02	0.02	0.02	0.03	0.03	0.03	0.02	0.03	0.03	0.03	0.03	0.03	0.02
Eu	0.00	0.00	0.00	0.00	0.00	0.00	0.00	0.00	0.00	0.00	0.00	0.00	0.00	0.00	0.00	0.00	0.00
Gd	0.02	0.02	0.02	0.02	0.02	0.02	0.02	0.02	0.02	0.02	0.02	0.02	0.02	0.02	0.02	0.02	0.02
Dy	0.01	0.01	0.01	0.01	0.00	0.00	0.01	0.01	0.01	0.01	0.01	0.01	0.01	0.01	0.01	0.01	0.01
Y	0.04	0.05	0.04	0.04	0.03	0.04	0.04	0.04	0.04	0.05	0.04	0.04	0.04	0.04	0.04	0.04	0.05
Er	0.00	0.00	0.00	0.00	0.00	0.00	0.00	0.00	0.00	0.00	0.00	0.00	0.00	0.00	0.00	0.00	0.00
Total	2.02	2.01	2.01	2.01	2.02	2.02	2.02	2.02	2.02	2.01	2.02	2.02	2.01	2.01	2.01	2.02	2.01
X_{LREE}	0.84	0.81	0.83	0.82	0.84	0.82	0.83	0.80	0.82	0.80	0.82	0.79	0.79	0.79	0.79	0.80	0.79
X_{HREE}	0.02	0.03	0.03	0.03	0.02	0.02	0.02	0.03	0.03	0.03	0.02	0.03	0.03	0.03	0.03	0.03	0.03
X_{Hut}	-0.02	-0.01	-0.01	-0.01	-0.03	-0.03	-0.03	-0.02	-0.02	-0.01	-0.03	-0.01	0.00	0.00	0.00	0.00	-0.01
X_{Brb}	0.13	0.13	0.12	0.12	0.14	0.15	0.14	0.15	0.14	0.13	0.14	0.15	0.15	0.14	0.15	0.13	0.13
X_{YPO4}	0.03	0.04	0.04	0.04	0.03	0.04	0.04	0.04	0.04	0.05	0.04	0.04	0.04	0.04	0.04	0.04	0.05
App. age (Ma)	1923.58	1966.96	2027.94	2004.76	1992.48	2023.66	1998.69	1962.10	1931.32	1955.89	1984.47	1962.51	1995.67	1939.11	1983.97	1929.16	1952.43
2σ err. age (± , Ma)	76.42	59.68	69.55	64.32	73.83	71.61	72.38	49.75	67.93	61.02	63.46	51.94	52.22	51.92	52.31	56.93	53.66

Table 8 continued

Analysis No	56	61	63	64	68	77	78	82	83	84	85	86	87	87	88	144	159
Monazite	m2	m5	m5	m5	m5	m11	m17	m17	Grt-m1-1	Grt-m1-2	Grt-m1-3	Grt-m1-4	m14	Grt-m1-5	m12		m5
SiO_2	0.47	0.13	0.64	0.68	0.11	0.37	0.14	0.22	0.20	0.59	0.15	0.21	0.34	0.22	0.80	0.70	0.10
P_2O_5	30.69	29.66	29.45	29.62	30.77	29.64	30.53	29.58	29.64	29.47	29.70	29.49	33.59	29.24	29.28	29.10	30.16
Al_2O_3	0.00	0.00	0.00	0.00	0.00	0.00	0.00	0.00	0.00	0.00	0.00	0.00	0.00	0.00	0.01	0.00	0.00
CaO	0.63	2.17	0.93	0.89	2.15	1.70	1.33	1.61	1.50	0.73	1.23	1.27	0.02	1.52	1.00	0.99	2.15
ThO_2	3.92	5.77	5.72	5.80	5.18	6.15	2.84	4.10	4.56	4.93	3.59	4.44	0.57	4.90	6.42	6.00	5.54
UO_2	0.14	0.40	0.20	0.16	0.32	0.59	0.36	0.41	0.66	0.11	0.56	0.55	0.55	0.60	0.37	0.38	0.32
PbO	0.37	0.64	0.54	0.54	0.56	0.73	0.38	0.48	0.61	0.45	0.48	0.56	0.22	0.63	0.66	0.63	0.58
La_2O_3	15.05	12.92	14.32	14.82	14.02	13.33	13.45	14.85	13.56	14.68	15.21	13.73	0.03	13.66	11.55	12.93	13.85
Ce_2O_3	29.76	25.70	28.73	28.68	26.68	27.05	27.87	28.61	27.00	28.51	28.25	27.61	0.09	27.01	28.05	27.92	25.81
Pr_2O_3	2.94	2.70	3.00	2.90	2.69	2.84	2.91	2.82	3.11	3.00	2.95	3.01	0.06	2.99	3.18	3.15	2.82
Nd_2O_3	11.12	10.85	11.87	11.83	10.47	10.91	11.61	10.65	11.97	11.24	11.43	12.08	0.31	11.51	12.11	11.76	10.62
Sm_2O_3	1.58	1.90	1.90	1.92	1.66	1.80	2.03	1.59	2.21	1.62	2.00	2.19	0.17	2.12	1.73	2.13	1.68
Eu_2O_3	0.01	0.00	0.14	0.05	0.00	0.20	0.08	0.00	0.10	0.00	0.11	0.32	0.32	0.26	0.00	0.00	0.00
Gd_2O_3	1.20	1.64	1.41	1.46	1.48	1.63	1.87	1.34	1.65	1.32	1.43	1.57	3.05	1.60	2.27	1.69	1.49
Dy_2O_3	0.62	0.74	0.35	0.34	0.64	0.59	0.85	0.48	0.59	0.68	0.46	0.60	5.66	0.55	0.70	0.48	0.66
Y_2O_3	2.54	3.13	1.10	1.16	2.73	1.99	3.53	1.73	2.16	2.56	1.83	2.01	40.73	2.07	1.93	1.54	2.75
Er_2O_3	0.19	0.26	0.06	0.05	0.21	0.14	0.24	0.11	0.12	0.19	0.10	0.12	4.74	0.12	0.07	0.07	0.23
Total	101.25	98.60	100.35	100.89	99.66	99.65	100.01	98.56	99.62	100.07	99.49	99.74	90.47	99.01	100.12	99.46	98.76
Si	0.02	0.01	0.02	0.03	0.00	0.01	0.01	0.01	0.01	0.02	0.01	0.01	0.01	0.01	0.03	0.03	0.00
P	0.99	0.99	0.98	0.98	1.00	0.98	1.00	0.99	0.99	0.98	0.99	0.98	1.02	0.98	0.97	0.98	1.00
Al	0.00	0.00	0.00	0.00	0.00	0.00	0.00	0.00	0.00	0.00	0.00	0.00	0.00	0.00	0.00	0.00	0.00
Ca	0.03	0.09	0.04	0.04	0.09	0.07	0.06	0.07	0.06	0.03	0.05	0.05	0.00	0.06	0.04	0.04	0.09
Th	0.03	0.05	0.05	0.05	0.05	0.05	0.02	0.04	0.04	0.04	0.03	0.04	0.00	0.04	0.06	0.05	0.05
U	0.00	0.00	0.00	0.00	0.00	0.01	0.00	0.00	0.01	0.00	0.00	0.00	0.00	0.01	0.00	0.00	0.00
Pb	0.00	0.01	0.01	0.01	0.01	0.01	0.00	0.01	0.01	0.00	0.01	0.01	0.00	0.01	0.01	0.01	0.01
La	0.21	0.19	0.21	0.21	0.20	0.19	0.19	0.22	0.20	0.21	0.22	0.20	0.00	0.20	0.17	0.19	0.20
Ce	0.42	0.37	0.41	0.41	0.38	0.39	0.39	0.41	0.39	0.41	0.41	0.40	0.00	0.39	0.40	0.40	0.37
Pr	0.04	0.04	0.04	0.04	0.04	0.04	0.04	0.04	0.04	0.04	0.04	0.04	0.00	0.04	0.05	0.05	0.04
Nd	0.15	0.15	0.17	0.16	0.14	0.15	0.16	0.15	0.17	0.16	0.16	0.17	0.00	0.16	0.17	0.17	0.15
Sm	0.02	0.03	0.03	0.03	0.02	0.02	0.03	0.02	0.03	0.02	0.03	0.03	0.00	0.03	0.02	0.03	0.02
Eu	0.00	0.00	0.00	0.00	0.00	0.00	0.00	0.00	0.00	0.00	0.00	0.00	0.00	0.00	0.00	0.00	0.00
Gd	0.02	0.02	0.02	0.02	0.02	0.02	0.02	0.02	0.02	0.02	0.02	0.02	0.04	0.02	0.03	0.02	0.02
Dy	0.01	0.01	0.00	0.00	0.01	0.01	0.01	0.01	0.01	0.01	0.01	0.01	0.07	0.01	0.01	0.01	0.01
Y	0.05	0.07	0.02	0.02	0.06	0.04	0.07	0.04	0.05	0.05	0.04	0.04	0.77	0.04	0.04	0.03	0.06
Er	0.00	0.00	0.00	0.00	0.00	0.00	0.00	0.00	0.00	0.00	0.00	0.00	0.05	0.00	0.00	0.00	0.00
Total	2.00	2.02	2.00	2.00	2.01	2.01	2.01	2.02	2.01	2.00	2.01	2.01	1.98	2.02	2.00	2.00	2.02
X_{LREE}	0.86	0.75	0.86	0.86	0.77	0.79	0.80	0.83	0.81	0.84	0.84	0.83	0.01	0.81	0.81	0.83	0.77
X_{HREE}	0.03	0.03	0.02	0.02	0.03	0.03	0.04	0.02	0.03	0.03	0.03	0.03	0.16	0.03	0.04	0.03	0.03
X_{Hut}	0.01	-0.03	0.02	0.02	-0.03	0.00	-0.02	-0.02	-0.01	0.02	-0.01	0.00	0.01	-0.01	0.03	0.02	-0.03
X_{Brb}	0.05	0.18	0.08	0.07	0.18	0.14	0.11	0.13	0.12	0.06	0.10	0.11	0.00	0.13	0.08	0.08	0.18
X_{YPO4}	0.05	0.06	0.02	0.02	0.06	0.04	0.07	0.04	0.04	0.05	0.04	0.04	0.82	0.04	0.04	0.03	0.06
App. age (Ma)	1913.91	1992.34	1906.98	1907.83	1966.02	1974.97	2034.91	1937.31	1958.41	1925.70	1912.69	1947.61	1919.49	1984.24	1914.63	1915.39	1947.66
2σ err. age (± , Ma)	69.98	50.57	53.14	53.02	54.95	45.93	77.66	60.26	61.03	71.94	70.07	63.81	120.46	59.63	47.03	48.88	59.19

Table 9 Monazite rim compositions and calculated U-Th-total Pb ages of a garnet bearing metapelite (T18-2-10)

Analysis No	34	35	36	39	40	41	42	43	44	44	45	45	47	48	49	50	51	51
Monazite	m2 -10	m2 -11	m2 -12	m2 -15	m2 -16	m2 -17	m2 -18	m2 -19	m2 -20	m2	m2 -21	m2	m2	m2	m2	m2	m2	m11-6
SiO_2	0.09	0.26	1.35	1.66	1.38	0.76	0.57	0.62	1.66	1.41	1.65	0.22	0.59	0.55	1.04	0.23	2.23	0.55
P_2O_5	29.46	29.35	27.71	28.05	28.17	29.58	29.70	29.57	27.88	28.09	27.58	29.88	29.98	30.74	29.50	31.28	27.13	29.33
Al_2O_3	0.02	0.01	0.01	0.01	0.01	0.00	0.00	0.00	0.01	0.01	0.01	0.00	0.00	0.02	0.01	0.03	0.02	0.00
CaO	0.69	0.76	0.79	0.70	0.78	0.84	0.68	0.72	0.66	0.71	0.72	0.86	0.83	0.62	0.91	0.89	0.72	0.99
ThO_2	2.60	3.69	7.70	8.78	7.91	6.08	4.57	4.92	8.93	7.61	8.97	3.72	5.29	4.32	7.50	3.95	10.75	5.52
UO_2	0.25	0.24	0.24	0.24	0.24	0.13	0.16	0.16	0.07	0.25	0.10	0.31	0.20	0.22	0.16	0.31	0.27	0.29
PbO	0.29	0.37	0.70	0.79	0.71	0.53	0.42	0.46	0.75	0.68	0.74	0.41	0.48	0.43	0.66	0.41	0.93	0.53
La_2O_3	17.90	16.02	13.68	13.06	13.44	14.35	15.12	15.04	13.12	13.36	13.23	16.00	14.34	14.91	13.18	16.96	12.44	14.61
Ce_2O_3	29.54	28.80	28.22	28.75	28.43	27.63	28.86	28.44	28.41	29.09	28.15	29.22	28.43	29.45	27.29	29.73	28.05	27.65
Pr_2O_3	2.90	2.77	3.08	3.22	3.26	3.03	3.05	3.00	3.34	3.12	3.29	2.89	2.81	2.94	3.07	2.89	3.20	2.92
Nd_2O_3	10.28	10.19	12.31	12.86	12.45	11.12	11.08	11.11	13.27	12.41	12.87	10.03	11.07	10.86	11.63	9.90	12.61	10.96
Sm_2O_3	1.58	1.63	2.07	2.00	2.03	1.79	1.59	1.72	2.00	1.73	2.01	1.56	1.70	1.55	1.84	1.45	1.85	1.90
Eu_2O_3	1.03	0.00	0.00	0.00	0.00	0.05	0.06	0.08	0.00	0.00	0.00	0.00	0.11	0.00	0.04	0.02	0.00	0.07
Gd_2O_3	1.21	1.43	1.37	1.27	1.34	1.43	1.29	1.35	0.95	1.17	1.10	1.39	1.47	1.53	1.58	1.24	1.09	1.59
Dy_2O_3	0.39	0.74	0.09	0.08	0.07	0.69	0.60	0.62	0.01	0.05	0.08	0.70	0.65	0.74	0.67	0.60	0.06	0.72
Y_2O_3	0.95	2.22	0.29	0.24	0.25	2.68	2.48	2.46	0.17	0.27	0.38	2.04	2.71	2.52	2.30	1.84	0.20	2.26
Er_2O_3	0.04	0.14	0.00	0.00	0.00	0.14	0.15	0.16	0.00	0.01	0.01	0.16	0.20	0.15	0.13	0.10	0.00	0.08
Total	99.19	98.60	99.59	101.70	100.46	100.83	100.38	100.43	101.23	99.95	100.87	99.38	100.83	101.55	101.51	101.83	101.54	99.96
Si	0.003	0.010	0.054	0.066	0.055	0.030	0.022	0.024	0.066	0.056	0.066	0.008	0.023	0.021	0.040	0.009	0.089	0.022
P	0.990	0.987	0.944	0.937	0.949	0.973	0.980	0.977	0.937	0.949	0.932	0.993	0.982	0.992	0.967	1.004	0.915	0.976
Al	0.001	0.000	0.000	0.001	0.000	0.000	0.000	0.000	0.001	0.000	0.001	0.000	0.000	0.001	0.000	0.001	0.001	0.000
Ca	0.029	0.032	0.034	0.030	0.033	0.035	0.029	0.030	0.028	0.030	0.031	0.036	0.034	0.025	0.038	0.036	0.031	0.042
Th	0.023	0.033	0.071	0.079	0.072	0.054	0.041	0.044	0.081	0.069	0.082	0.033	0.047	0.037	0.066	0.034	0.098	0.049
U	0.002	0.002	0.002	0.002	0.002	0.001	0.001	0.001	0.001	0.002	0.001	0.003	0.002	0.002	0.001	0.003	0.002	0.003
Pb	0.003	0.004	0.008	0.008	0.008	0.006	0.004	0.005	0.008	0.007	0.008	0.004	0.005	0.004	0.007	0.004	0.010	0.006
La	0.262	0.235	0.203	0.190	0.197	0.206	0.217	0.217	0.192	0.197	0.195	0.232	0.205	0.210	0.188	0.237	0.183	0.212
Ce	0.429	0.419	0.416	0.415	0.414	0.393	0.412	0.406	0.413	0.425	0.411	0.420	0.403	0.411	0.387	0.413	0.409	0.398
Pr	0.042	0.040	0.045	0.046	0.047	0.043	0.043	0.043	0.048	0.045	0.048	0.041	0.040	0.041	0.043	0.040	0.046	0.042
Nd	0.146	0.145	0.177	0.181	0.177	0.154	0.154	0.155	0.188	0.177	0.184	0.141	0.153	0.148	0.161	0.134	0.179	0.154
Sm	0.022	0.022	0.029	0.027	0.028	0.024	0.021	0.023	0.027	0.024	0.028	0.021	0.023	0.020	0.025	0.019	0.025	0.026
Eu	0.014	0.000	0.000	0.000	0.000	0.001	0.001	0.001	0.000	0.000	0.000	0.000	0.002	0.000	0.001	0.000	0.000	0.001
Gd	0.016	0.019	0.018	0.017	0.018	0.018	0.017	0.017	0.013	0.016	0.015	0.018	0.019	0.019	0.020	0.016	0.014	0.021
Dy	0.005	0.009	0.001	0.001	0.001	0.009	0.008	0.008	0.000	0.001	0.001	0.009	0.008	0.009	0.008	0.007	0.001	0.009
Y	0.020	0.047	0.006	0.005	0.005	0.055	0.051	0.051	0.004	0.006	0.008	0.043	0.056	0.051	0.047	0.037	0.004	0.047
Er	0.000	0.002	0.000	0.000	0.000	0.002	0.002	0.002	0.000	0.000	0.000	0.002	0.002	0.002	0.002	0.001	0.000	0.001
Total	2.008	2.006	2.009	2.006	2.005	2.003	2.003	2.004	2.005	2.004	2.009	2.004	2.002	1.995	2.001	1.995	2.008	2.007
X_{LREE}	0.901	0.853	0.862	0.859	0.862	0.821	0.848	0.842	0.867	0.869	0.857	0.852	0.826	0.847	0.809	0.859	0.841	0.824
X_{HREE}	0.021	0.030	0.019	0.018	0.018	0.029	0.026	0.027	0.013	0.016	0.016	0.029	0.029	0.031	0.030	0.024	0.015	0.031
X_{Hut}	-0.001	0.007	0.046	0.059	0.048	0.026	0.018	0.020	0.061	0.049	0.059	0.004	0.019	0.019	0.037	0.005	0.079	0.016
X_{Brb}	0.059	0.064	0.068	0.059	0.066	0.070	0.057	0.060	0.056	0.060	0.061	0.072	0.069	0.051	0.076	0.074	0.061	0.082
X_{YPO4}	0.020	0.046	0.006	0.005	0.005	0.055	0.051	0.051	0.004	0.006	0.008	0.042	0.056	0.052	0.048	0.038	0.004	0.047
App. age (Ma)	1854.1	1861.6	1845.7	1852.9	1825.1	1846.9	1861.2	1875.7	1851.2	1823.9	1810.4	1886.7	1824.2	1891.0	1855.2	1839.0	1801.6	1833.6
2σ err. age (± , Ma)	101.4	81.3	49.9	45.5	48.7	60.3	73.3	69.6	47.1	46.5	46.4	69.8	55.4	63.4	44.5	63.5	34.4	61.5

Table 9 continued

Analysis No	52	53	54	54	55	56	57	58	58	59	59	60	60	62	63	64
Monazite	m11-7	m11-8	m2	m11-9	m11-10	m11-11	m3	m3	m11-13	m3	m11-14	m3	m11-15	m11-17	m11-18	m11-19
SiO_2	0.80	0.41	1.09	0.83	1.72	1.41	0.34	1.77	1.51	0.92	1.54	0.53	1.59	2.03	1.64	2.10
P_2O_5	28.68	29.52	29.28	28.57	27.20	27.10	30.18	27.98	27.25	29.36	28.18	30.36	27.77	27.08	27.94	27.06
Al_2O_3	0.00	0.00	0.01	0.01	0.02	0.01	0.00	0.01	0.01	0.00	0.01	0.00	0.00	0.01	0.01	0.01
CaO	0.93	1.24	0.81	0.95	0.72	0.68	0.58	0.69	0.69	0.95	0.70	0.55	0.71	0.71	0.73	0.73
ThO_2	6.23	6.16	7.10	6.47	8.91	7.63	3.27	8.92	8.08	6.89	8.33	3.94	8.59	10.16	8.79	10.41
UO_2	0.27	0.20	0.15	0.25	0.27	0.34	0.23	0.29	0.26	0.20	0.27	0.22	0.28	0.29	0.26	0.30
PbO	0.58	0.56	0.63	0.60	0.80	0.71	0.34	0.80	0.73	0.63	0.76	0.39	0.76	0.89	0.79	0.94
La_2O_3	13.50	14.59	13.80	13.68	13.11	12.58	15.82	12.49	12.86	13.13	13.51	15.06	12.93	12.74	12.81	12.45
Ce_2O_3	27.04	27.85	28.44	27.00	28.23	27.94	29.90	28.27	28.16	26.84	28.40	29.13	28.41	27.89	28.35	27.59
Pr_2O_3	2.92	2.97	3.01	2.98	3.33	3.12	2.94	3.12	3.13	2.88	3.10	3.00	3.18	3.36	3.23	3.21
Nd_2O_3	11.58	10.98	11.95	11.37	12.86	12.35	10.49	12.47	12.50	11.51	12.59	10.85	12.71	12.68	12.77	12.72
Sm_2O_3	1.95	1.76	1.79	1.93	2.13	2.17	1.59	1.98	2.15	1.79	2.06	1.69	2.12	2.03	2.12	1.97
Eu_2O_3	0.00	0.18	0.00	0.00	0.00	0.00	0.00	0.00	0.00	0.00	0.00	0.00	0.00	0.00	0.00	0.00
Gd_2O_3	1.66	1.48	1.43	1.64	1.22	1.57	1.53	1.37	1.34	1.69	1.18	1.67	1.24	1.16	1.25	1.17
Dy_2O_3	0.77	0.66	0.41	0.70	0.09	0.39	0.72	0.12	0.23	0.80	0.10	0.76	0.09	0.10	0.12	0.04
Y_2O_3	2.57	2.14	1.28	2.68	0.25	1.28	2.37	0.41	0.73	2.68	0.32	2.57	0.30	0.21	0.54	0.25
Er_2O_3	0.13	0.10	0.06	0.14	0.00	0.05	0.17	0.00	0.01	0.17	0.00	0.15	0.00	0.00	0.00	0.00
Total	99.61	100.79	101.24	99.79	100.86	99.30	100.46	100.68	99.63	100.44	101.04	100.86	100.66	101.33	101.34	100.94
Si	0.032	0.016	0.042	0.033	0.069	0.057	0.013	0.070	0.061	0.036	0.061	0.020	0.063	0.081	0.065	0.084
P	0.963	0.977	0.966	0.959	0.925	0.932	0.991	0.940	0.933	0.970	0.944	0.990	0.938	0.917	0.937	0.918
Al	0.000	0.000	0.000	0.000	0.001	0.000	0.000	0.000	0.001	0.000	0.001	0.000	0.000	0.000	0.000	0.000
Ca	0.040	0.052	0.034	0.040	0.031	0.030	0.024	0.030	0.030	0.040	0.030	0.023	0.030	0.031	0.031	0.032
Th	0.056	0.055	0.063	0.058	0.081	0.071	0.029	0.081	0.074	0.061	0.075	0.035	0.078	0.093	0.079	0.095
U	0.002	0.002	0.001	0.002	0.002	0.003	0.002	0.003	0.002	0.002	0.002	0.002	0.002	0.003	0.002	0.003
Pb	0.006	0.006	0.007	0.006	0.009	0.008	0.004	0.009	0.008	0.007	0.008	0.004	0.008	0.010	0.008	0.010
La	0.197	0.210	0.198	0.200	0.194	0.188	0.226	0.183	0.192	0.189	0.197	0.214	0.190	0.188	0.187	0.184
Ce	0.393	0.398	0.406	0.392	0.415	0.416	0.424	0.411	0.417	0.383	0.412	0.411	0.415	0.409	0.411	0.405
Pr	0.042	0.042	0.043	0.043	0.049	0.046	0.042	0.045	0.046	0.041	0.045	0.042	0.046	0.049	0.047	0.047
Nd	0.164	0.153	0.166	0.161	0.185	0.179	0.145	0.177	0.181	0.160	0.178	0.149	0.181	0.181	0.181	0.182
Sm	0.027	0.024	0.024	0.026	0.030	0.030	0.021	0.027	0.030	0.024	0.028	0.022	0.029	0.028	0.029	0.027
Eu	0.000	0.002	0.000	0.000	0.000	0.000	0.000	0.000	0.000	0.000	0.000	0.000	0.000	0.000	0.000	0.000
Gd	0.022	0.019	0.019	0.022	0.016	0.021	0.020	0.018	0.018	0.022	0.016	0.021	0.016	0.015	0.016	0.016
Dy	0.010	0.008	0.005	0.009	0.001	0.005	0.009	0.002	0.003	0.010	0.001	0.009	0.001	0.001	0.002	0.001
Y	0.054	0.045	0.027	0.057	0.005	0.028	0.049	0.009	0.016	0.056	0.007	0.053	0.006	0.004	0.011	0.005
Er	0.002	0.001	0.001	0.002	0.000	0.001	0.002	0.000	0.000	0.002	0.000	0.002	0.000	0.000	0.000	0.000
Total	2.010	2.011	2.001	2.012	2.013	2.014	2.001	2.002	2.011	2.003	2.004	1.997	2.006	2.010	2.007	2.008
X_{LREE}	0.811	0.815	0.843	0.807	0.857	0.839	0.862	0.849	0.851	0.800	0.861	0.850	0.858	0.845	0.850	0.840
X_{HREE}	0.033	0.028	0.025	0.032	0.017	0.026	0.031	0.020	0.021	0.034	0.017	0.033	0.017	0.016	0.018	0.016
X_{Hut}	0.025	0.010	0.037	0.026	0.060	0.050	0.010	0.063	0.054	0.030	0.056	0.018	0.058	0.073	0.059	0.076
X_{Brb}	0.078	0.102	0.068	0.079	0.061	0.058	0.048	0.059	0.059	0.080	0.059	0.046	0.061	0.061	0.062	0.063
X_{YPO4}	0.054	0.044	0.027	0.056	0.005	0.027	0.049	0.009	0.015	0.056	0.007	0.053	0.006	0.004	0.011	0.005
App. age (Ma)	1833.0	1829.7	1868.2	1859.8	1837.0	1813.8	1858.5	1821.6	1830.3	1876.6	1842.7	1837.5	1807.2	1807.6	1835.6	1845.8
2σ err. age (± , Ma)	56.9	58.8	46.1	56.3	45.2	48.4	74.2	38.3	47.7	46.7	46.8	66.3	45.7	41.1	45.5	40.6

Table 9 continued

Analysis No	65	66	69	70	71	72	73	74	75	76	79	80	81	83	84	85	86	88	89	90	91	92	151	153	155	156	157	160	161
Monazite	m5	m5	m4	m4	m4	m4	m11	m11	m11	m11	m17	m17	m17	m17	m16	m16	m16	Grt-m1-6	Grt-m1-7	Grt-m1-8	Grt-m1-9	Grt-m1-10	m6	m6	m5	m5	m5	m12	m12
SiO_2	0.23	1.58	0.40	0.92	0.94	0.76	2.02	0.37	1.00	1.80	0.97	1.94	1.25	1.44	1.73	2.03	1.44	1.08	1.18	0.84	1.24	0.70	1.46	1.33	0.56	0.42	1.21	0.89	0.85
P_2O_5	30.32	27.60	30.33	29.26	29.16	30.07	27.65	29.94	29.06	27.17	28.83	26.95	28.24	28.38	27.23	26.78	27.52	28.09	27.69	28.32	27.91	29.25	27.73	28.09	28.02	28.59	29.73	29.81	29.36
Al_2O_3	0.00	0.01	0.00	0.00	0.00	0.02	0.01	0.00	0.01	0.02	0.00	0.00	0.00	0.00	0.00	0.00	0.01	0.00	0.00	0.00	0.00	0.00	0.01	0.00	0.02	0.02	0.02	0.03	0.02
CaO	1.03	0.69	1.01	0.91	0.83	0.86	0.72	1.23	0.92	0.73	0.76	0.68	0.54	0.66	0.74	0.89	0.68	0.72	0.90	0.69	0.89	0.75	0.65	0.73	0.61	0.66	0.66	0.79	0.91
ThO_2	4.50	8.27	4.12	6.53	6.44	5.54	10.15	6.04	6.99	8.82	6.03	9.33	6.54	7.57	8.97	10.65	7.04	6.70	7.86	5.69	7.86	5.46	7.41	6.89	4.25	3.81	6.85	5.70	6.36
UO_2	0.35	0.34	0.85	0.30	0.22	0.38	0.33	0.23	0.25	0.26	0.27	0.31	0.22	0.38	0.26	0.33	0.42	0.17	0.20	0.20	0.22	0.17	0.29	0.27	0.24	0.22	0.39	0.24	0.22
PbO	0.48	0.76	0.59	0.61	0.58	0.55	0.91	0.56	0.64	0.79	0.58	0.83	0.59	0.74	0.80	0.96	0.69	0.59	0.71	0.52	0.71	0.48	0.68	0.62	0.41	0.38	0.69	0.55	0.59
La_2O_3	14.14	12.30	12.89	12.61	13.36	14.18	12.35	14.11	13.73	12.89	13.73	12.49	13.53	12.75	13.42	12.44	12.40	14.44	13.69	14.49	13.77	13.78	12.88	12.99	15.14	15.29	12.57	11.79	12.91
Ce_2O_3	28.61	27.95	25.83	26.94	28.01	28.30	28.28	27.62	28.42	28.75	28.95	28.79	29.91	28.20	28.31	27.02	26.60	29.16	27.86	29.08	27.90	27.52	28.72	28.74	28.77	28.29	27.12	27.39	28.06
Pr_2O_3	3.16	3.15	2.92	2.97	3.03	2.90	3.26	2.84	3.05	3.12	3.09	3.18	3.28	3.17	3.10	3.03	2.89	3.14	3.15	3.13	3.07	3.05	3.33	3.25	2.96	2.89	3.01	3.22	3.07
Nd_2O_3	11.96	12.22	10.54	11.53	11.88	11.27	12.21	10.88	11.88	12.40	12.13	12.50	12.50	12.12	11.72	11.76	11.57	12.33	11.83	12.26	11.79	11.78	12.90	12.73	10.66	10.36	11.79	12.87	11.84
Sm_2O_3	2.14	1.97	1.95	1.85	1.82	1.91	1.89	1.62	1.92	1.94	2.03	1.97	1.78	1.93	1.74	1.87	1.79	2.10	1.98	2.04	1.96	1.95	1.98	1.83	1.74	1.67	1.76	1.87	1.69
Eu_2O_3	0.00	0.00	0.31	0.14	0.06	0.06	0.00	0.22	0.00	0.00	0.01	0.00	0.00	0.00	0.00	0.00	0.00	0.00	0.00	0.00	0.00	0.00	0.00	0.00	0.00	0.00	0.00	0.00	0.00
Gd_2O_3	1.83	1.50	2.16	1.79	1.56	1.72	1.16	1.50	1.63	1.27	1.59	0.99	1.19	1.55	1.13	1.27	1.76	1.47	1.51	1.53	1.47	1.66	1.42	1.38	1.55	1.58	1.70	2.02	1.88
Dy_2O_3	0.42	0.33	1.34	0.76	0.52	0.59	0.05	0.68	0.36	0.04	0.33	0.03	0.13	0.42	0.07	0.13	0.85	0.13	0.30	0.19	0.29	0.76	0.14	0.16	0.68	0.70	0.68	0.77	0.71
Y_2O_3	1.40	0.94	5.01	2.73	1.58	1.78	0.20	2.22	0.96	0.27	0.88	0.22	0.44	1.27	0.29	0.36	2.70	0.34	0.76	0.56	0.72	2.75	0.43	0.48	2.17	2.23	2.59	2.01	1.89
Er_2O_3	0.03	0.03	0.30	0.12	0.05	0.02	0.00	0.10	0.02	0.00	0.00	0.00	0.00	0.06	0.00	0.01	0.17	0.00	0.00	0.01	0.00	0.16	0.00	0.02	0.15	0.17	0.12	0.13	0.06
Total	100.59	99.61	100.55	99.96	100.04	100.92	101.18	100.15	100.86	100.28	100.15	100.20	100.14	100.65	99.51	99.53	98.52	100.44	99.62	99.55	99.81	100.20	100.02	99.50	97.92	97.26	100.89	100.07	100.40
Si	0.009	0.063	0.015	0.036	0.037	0.029	0.080	0.015	0.039	0.073	0.038	0.078	0.050	0.057	0.070	0.082	0.058	0.043	0.048	0.034	0.050	0.027	0.059	0.053	0.023	0.017	0.047	0.035	0.033
P	0.996	0.939	0.987	0.970	0.971	0.983	0.929	0.988	0.965	0.926	0.965	0.921	0.952	0.949	0.932	0.920	0.940	0.950	0.945	0.961	0.947	0.972	0.941	0.952	0.963	0.978	0.972	0.982	0.972
Al	0.000	0.000	0.000	0.000	0.000	0.001	0.000	0.000	0.001	0.001	0.000	0.000	0.000	0.000	0.000	0.000	0.000	0.000	0.000	0.000	0.000	0.000	0.000	0.000	0.001	0.001	0.001	0.001	0.001
Ca	0.043	0.030	0.042	0.038	0.035	0.036	0.030	0.051	0.039	0.031	0.032	0.030	0.023	0.028	0.032	0.039	0.030	0.031	0.039	0.030	0.038	0.032	0.028	0.031	0.027	0.028	0.027	0.033	0.038
Th	0.040	0.076	0.036	0.058	0.058	0.049	0.092	0.054	0.062	0.081	0.054	0.086	0.059	0.068	0.083	0.098	0.065	0.061	0.072	0.052	0.072	0.049	0.068	0.063	0.039	0.035	0.060	0.051	0.057
U	0.003	0.003	0.007	0.003	0.002	0.003	0.003	0.002	0.002	0.002	0.002	0.003	0.002	0.003	0.002	0.003	0.004	0.002	0.002	0.002	0.002	0.002	0.003	0.002	0.002	0.002	0.003	0.002	0.002
Pb	0.005	0.008	0.006	0.006	0.006	0.006	0.010	0.006	0.007	0.009	0.006	0.009	0.006	0.008	0.009	0.011	0.008	0.006	0.008	0.006	0.008	0.005	0.007	0.007	0.005	0.004	0.007	0.006	0.006
La	0.202	0.182	0.183	0.182	0.194	0.202	0.181	0.203	0.199	0.191	0.200	0.186	0.199	0.186	0.200	0.186	0.185	0.213	0.204	0.214	0.204	0.199	0.190	0.192	0.227	0.228	0.179	0.169	0.186
Ce	0.407	0.411	0.364	0.386	0.403	0.400	0.411	0.394	0.408	0.424	0.419	0.425	0.436	0.408	0.419	0.401	0.393	0.427	0.411	0.427	0.410	0.395	0.422	0.421	0.428	0.419	0.383	0.390	0.402
Pr	0.045	0.046	0.041	0.042	0.043	0.041	0.047	0.040	0.044	0.046	0.045	0.047	0.048	0.046	0.046	0.045	0.042	0.046	0.046	0.046	0.045	0.044	0.049	0.047	0.044	0.043	0.042	0.046	0.044
Nd	0.166	0.175	0.145	0.161	0.167	0.156	0.173	0.151	0.166	0.178	0.171	0.180	0.178	0.171	0.169	0.170	0.167	0.176	0.170	0.176	0.169	0.165	0.185	0.182	0.155	0.150	0.163	0.179	0.165
Sm	0.029	0.027	0.026	0.025	0.025	0.025	0.026	0.022	0.026	0.027	0.028	0.027	0.025	0.026	0.024	0.026	0.025	0.029	0.027	0.028	0.027	0.026	0.027	0.025	0.024	0.023	0.024	0.025	0.023
Eu	0.000	0.000	0.004	0.002	0.001	0.001	0.000	0.003	0.000	0.000	0.000	0.000	0.000	0.000	0.000	0.000	0.000	0.000	0.000	0.000	0.000	0.000	0.000	0.000	0.000	0.000	0.000	0.000	0.000
Gd	0.024	0.020	0.028	0.023	0.020	0.022	0.015	0.019	0.021	0.017	0.021	0.013	0.016	0.020	0.015	0.017	0.024	0.019	0.020	0.020	0.020	0.022	0.019	0.018	0.021	0.021	0.022	0.026	0.024
Dy	0.005	0.004	0.017	0.010	0.007	0.007	0.001	0.009	0.005	0.001	0.004	0.000	0.002	0.005	0.001	0.002	0.011	0.002	0.004	0.002	0.004	0.010	0.002	0.002	0.009	0.009	0.008	0.010	0.009
Y	0.029	0.020	0.103	0.057	0.033	0.037	0.004	0.046	0.020	0.006	0.019	0.005	0.009	0.027	0.006	0.008	0.058	0.007	0.016	0.012	0.015	0.057	0.009	0.010	0.047	0.048	0.053	0.042	0.039
Er	0.000	0.000	0.004	0.001	0.001	0.000	0.000	0.001	0.000	0.000	0.000	0.000	0.000	0.001	0.000	0.000	0.002	0.000	0.000	0.000	0.000	0.002	0.000	0.000	0.002	0.002	0.001	0.002	0.001
Total	2.002	2.006	2.005	2.002	2.001	1.998	2.002	2.004	2.004	2.011	2.005	2.010	2.005	2.003	2.008	2.009	2.010	2.011	2.012	2.009	2.009	2.006	2.008	2.006	2.014	2.008	1.993	1.996	2.003
X_{LREE}	0.851	0.839	0.758	0.802	0.838	0.838	0.844	0.812	0.844	0.856	0.862	0.856	0.883	0.839	0.853	0.824	0.802	0.874	0.842	0.878	0.844	0.824	0.866	0.866	0.853	0.852	0.812	0.826	0.823
X_{HREE}	0.029	0.024	0.048	0.034	0.028	0.030	0.016	0.029	0.026	0.017	0.025	0.014	0.017	0.026	0.016	0.019	0.036	0.021	0.024	0.022	0.023	0.033	0.020	0.021	0.031	0.032	0.032	0.038	0.034
X_{Hut}	0.005	0.057	0.008	0.029	0.031	0.022	0.074	0.010	0.033	0.060	0.031	0.067	0.044	0.051	0.061	0.072	0.046	0.037	0.042	0.029	0.043	0.024	0.049	0.040	0.019	0.012	0.045	0.026	0.027
X_{Brb}	0.086	0.059	0.083	0.077	0.070	0.073	0.061	0.103	0.077	0.062	0.064	0.058	0.046	0.056	0.064	0.077	0.058	0.060	0.076	0.058	0.075	0.063	0.056	0.063	0.052	0.056	0.056	0.067	0.076
X_{YPO4}	0.029	0.020	0.103	0.057	0.033	0.037	0.004	0.046	0.020	0.006	0.019	0.005	0.009	0.027	0.006	0.008	0.057	0.007	0.016	0.012	0.015	0.057	0.009	0.010	0.046	0.047	0.055	0.042	0.040
App. age (Ma)	1878.1	1826.5	1844.5	1814.0	1806.8	1805.0	1814.7	1841.0	1838.1	1842.4	1853.6	1808.2	1817.4	1865.4	1840.0	1835.5	1815.7	1832.1	1869.6	1851.9	1862.9	1814.1	1830.9	1801.9	1837.7	1846.6	1881.8	1879.2	1862.1
2σ err. age (± , Ma)	58.1	39.8	50.5	46.6	47.6	49.8	35.2	50.0	45.4	39.0	49.3	37.1	47.3	41.9	38.5	34.5	43.3	55.4	49.6	61.8	49.2	64.5	52.1	52.1	71.7	76.4	50.3	59.4	54.9

Chapter 3

Table 1 Representative electron microprobe analyses of different minerals in metapelite, calc-silicate rock and metabasite

	Metapelite								Calc-silicate rock										Metabasite									
Mineral	Bt	Bt	Ms	Ms	Chl	Chl	Pl	Pl	Cpx	Cpx	Tr	Tr	Zo	Zo	Pl	Pl	Ms	Ms	Hbl	Hbl	Pl	Pl	Ep	Ep	Act	Act	Ms	Ms
Analysis #	865	867	579	583	960	962	918	920	605	626	25	618	750	751	73	74	766	768	308	310	356	362	364	366	425	426	328	333
SiO_2	35.64	35.34	45.17	45.42	26.04	28.22	60.13	60.51	55.08	54.95	57.02	56.28	39.77	39.46	66.59	67.00	47.08	47.18	44.32	44.25	53.98	54.52	38.28	38.31	44.56	44.25	47.69	48.23
TiO_2	2.72	2.60	0.87	0.72	0.00	0.00	0.00	0.00	0.01	0.07	0.07	0.08	n.d	n.d	0.00	0.00	n.d	n.d	1.06	0.96	0.00	0.00	0.04	0.13	0.78	0.81	0.00	0.01
Al_2O_3	18.49	18.47	34.24	34.19	21.32	20.48	25.50	24.96	0.55	0.52	3.22	2.74	34.50	34.68	20.94	20.58	34.45	34.46	10.60	10.55	29.27	28.59	25.49	26.23	10.43	10.48	31.55	32.12
Cr_2O_3	0.04	0.06	0.06	0.06	0.01	0.00	n.d	n.d	0.00	0.00	0.02	0.00	n.d	n.d	0.00	0.00	n.d	n.d	0.07	0.04	0.00	0.00	0.07	0.05	0.05	0.03	0.03	0.00
Fe_2O_3	n.c	n.c	n.c	n.c	n.c	n.c	0.07	0.13	n.c	n.c	n.c	n.c	0.06	0.10	n.c	n.c	n.c	n.c	n.c	n.c								
FeO	16.85	17.46	2.28	2.41	22.99	22.65	0.00	0.00	0.18	0.20	0.44	0.45	0.05	0.09	0.00	0.01	0.00	0.10	17.98	18.17	0.16	0.18	9.70	8.63	18.14	17.80	3.18	2.73
MnO	0.25	0.15	0.03	0.02	0.28	0.28	n.d	n.d	0.06	0.01	0.02	0.03	n.d	n.d	0.00	0.00	n.d	n.d	0.39	0.39	0.00	0.00	0.14	0.11	0.41	0.34	0.08	0.04
MgO	11.80	11.63	0.58	0.56	17.30	16.52	n.d	n.d	18.38	18.31	23.35	23.59	n.d	n.d	0.00	0.00	n.d	n.d	10.26	10.26	0.00	0.00	0.02	0.03	9.98	10.14	1.45	1.15
CaO	0.00	0.01	0.00	0.00	0.01	0.04	6.03	5.83	25.60	25.83	13.52	13.60	24.49	24.68	1.44	1.16	0.12	0.08	11.08	10.80	11.64	11.09	23.47	23.78	10.86	11.05	0.06	0.09
Na_2O	0.17	0.22	0.52	0.55	0.01	0.56	8.13	8.50	0.14	0.11	0.20	0.30	0.06	0.02	10.84	11.14	0.23	0.22	1.34	1.33	4.95	5.41	0.00	0.01	1.32	1.49	0.17	0.22
K_2O	10.34	9.99	11.23	11.05	0.00	0.00	0.12	0.09	0.00	0.00	0.11	0.11	0.01	0.00	0.11	0.10	11.85	11.79	0.70	0.72	0.02	0.03	0.01	0.00	0.67	0.68	11.11	11.17
Total	96.29	95.94	94.98	94.98	87.96	88.75	99.99	100.02	99.99	99.99	97.96	97.18	98.89	98.94	99.99	99.99	93.73	93.83	97.80	97.47	100.03	99.88	97.22	97.27	97.20	97.06	95.32	95.77
Structural formulae																												
Si	5.34	5.33	6.11	6.13	5.40	5.77	2.68	2.68	1.99	1.98	7.72	7.70	2.98	2.96	2.92	2.94	6.36	6.36	6.65	6.66	2.44	2.47	3.26	3.22	6.72	6.68	6.42	6.44
Ti	0.31	0.29	0.09	0.07	0.00	0.00	0.00	0.00	0.00	0.00	0.01	0.01	0.00	0.00	0.00	0.00	5.48	5.48	0.12	0.11	0.00	0.00	0.00	0.01	0.09	0.09	0.00	0.00
Al	3.27	3.28	5.46	5.44	5.21	4.93	1.32	1.34	0.02	0.02	0.51	0.44	3.05	3.06	1.08	1.06	0.00	0.00	1.87	1.87	1.56	1.52	2.55	2.60	1.85	1.87	5.01	5.06
Cr	0.00	0.01	0.01	0.01	0.00	0.00	n.d	n.d	0.00	0.00	0.00	0.00	n.d	n.d	0.00	0.00	n.d	n.d	0.01	0.00	0.00	0.00	n.d	n.d	0.01	0.00	0.00	0.00
Fe^{3+}	n.c	n.c	n.c	n.c	n.c	n.c	0.00	0.00	n.c	n.c	n.c	n.c	0.00	0.01	n.c	n.c	n.c	n.c	n.c	n.c	n.c	n.c	0.00	0.00	n.c	n.c	n.c	n.c
Fe^{2+}	2.11	2.20	0.26	0.27	3.99	3.87	n.c	n.c	0.01	0.01	0.05	0.05	n.c	n.c	0.00	0.00	0.00	0.01	2.26	2.29	0.01	0.01	n.c	n.c	2.29	2.25	0.36	0.30
Mn	0.03	0.02	0.00	0.00	0.05	0.05	n.d	n.d	0.00	0.00	0.00	0.00	n.d	n.d	0.00	0.00	n.d	n.d	0.05	0.05	0.00	0.00	0.01	0.01	0.05	0.04	0.01	0.00
Mg	2.64	2.61	0.12	0.11	5.35	5.03	n.d	n.d	0.99	0.99	4.71	4.81	n.d	n.d	0.00	0.00	n.d	n.d	2.29	2.30	0.00	0.00	0.00	0.00	2.24	2.28	0.29	0.23
Ca	0.00	0.00	0.00	0.00	0.00	0.01	0.29	0.29	0.99	1.00	1.96	1.99	1.97	1.98	0.07	0.05	0.02	0.01	1.78	1.74	0.56	0.54	2.14	2.14	1.75	1.79	0.01	0.01
Na	0.05	0.06	0.14	0.14	0.00	0.22	0.72	0.70	0.01	0.01	0.05	0.08	0.01	0.00	0.92	0.95	0.06	0.06	0.39	0.39	0.43	0.48	0.00	0.00	0.39	0.44	0.04	0.06
K	1.98	1.92	1.94	1.90	0.00	0.00	0.01	0.01	0.00	0.00	0.02	0.02	0.00	0.00	0.01	0.01	2.04	2.03	0.13	0.14	0.00	0.00	0.00	0.00	0.13	0.13	1.91	1.90
Total	15.73	15.73	18.11	18.09	20.00	19.88	5.02	5.01	4.01	4.01	15.05	15.12	8.00	8.01	5.00	5.01	13.96	13.94	15.55	15.56	5.00	5.01	7.96	7.98	15.52	15.57	14.05	14.01
Oxygen	22	22	22	22	28	28	8	8	6	6	23	23	8	8	8	8	22	22	23	23	8	8	8	8	23	23	22	22
X_{Mg}	0.56	0.54	0.31	0.29	0.57	0.57													0.56	0.57			0.00	0.01	0.55	0.55	0.43	0.43

n.c - not calculated, n.d - not determined

Table 2 Electron microprobe analyses of unaltered monazite cores

	Monazite cores																			
Analysis no.	79	139	149	151	157	158	161	169	170	172	175	176	182	183	185	189	192	195	196	225
P_2O_5	29.08	30.57	30.13	30.02	29.49	29.90	28.82	29.11	30.16	30.75	30.40	30.11	29.31	29.17	30.40	29.64	30.03	30.57	30.48	30.55
SiO_2	0.84	0.11	0.36	0.29	0.53	0.31	1.31	0.79	0.19	0.26	0.34	0.32	0.79	1.06	0.24	0.55	0.34	0.21	0.22	0.11
CaO	0.80	1.40	1.23	1.35	1.19	1.26	1.00	0.94	1.45	1.29	1.18	1.17	0.74	0.80	1.10	1.56	1.61	1.29	1.30	1.48
La_2O_3	13.75	13.37	12.64	12.03	12.91	12.73	12.46	12.01	13.51	12.50	12.60	12.98	12.29	12.17	12.63	12.47	12.85	13.16	13.11	12.44
Ce_2O_3	28.68	27.20	27.24	26.08	28.21	27.63	25.28	26.89	28.50	26.41	27.18	27.43	27.52	27.30	27.43	26.14	26.41	27.45	27.26	25.76
Pr_2O_3	3.06	2.91	3.01	2.92	3.14	2.98	2.72	2.88	3.08	2.90	2.95	2.92	3.06	3.08	3.02	2.89	2.87	2.98	2.93	2.99
Nd_2O_3	11.95	11.19	11.59	11.61	12.25	11.88	10.82	11.84	11.88	11.00	11.19	11.36	12.15	12.07	11.35	11.54	11.17	11.22	11.32	11.39
Sm_2O_3	2.05	1.87	1.90	2.03	2.13	2.18	1.39	2.18	1.98	2.07	1.87	1.82	2.01	1.98	2.06	1.84	1.81	1.83	2.00	2.11
Eu_2O_3	bd	0.21	0.24	0.31	bd	0.10	0.19	0.13	0.20	0.15	0.18	0.16	bd	bd	0.30	0.04	bd	0.30	0.29	0.29
Gd_2O_3	1.57	1.60	1.78	1.96	1.79	1.93	1.28	1.81	1.82	1.87	1.85	1.61	1.81	1.74	1.95	1.67	1.65	1.70	1.79	1.84
Dy_2O_3	0.35	0.73	0.80	0.95	0.56	0.73	1.19	0.83	0.55	1.08	1.13	0.96	0.82	0.79	0.92	0.72	0.79	0.86	0.90	0.85
Y_2O_3	1.19	3.05	3.67	4.11	1.90	2.76	5.61	3.84	1.92	4.90	4.51	4.23	3.52	3.52	4.00	3.20	3.43	3.81	3.78	3.32
Er_2O_3	0.02	0.21	0.27	0.26	0.08	0.12	0.45	0.25	0.05	0.34	0.28	0.31	0.25	0.26	0.28	0.21	0.24	0.27	0.28	0.27
PbO	0.56	0.50	0.46	0.53	0.48	0.51	0.62	0.49	0.43	0.43	0.42	0.43	0.43	0.48	0.44	0.62	0.55	0.40	0.41	0.57
ThO_2	5.86	4.70	4.80	5.00	5.10	4.48	6.78	5.46	3.96	4.35	4.16	4.17	4.88	5.37	3.86	6.54	5.71	3.64	3.71	5.48
UO_2	0.32	0.30	0.18	0.31	0.13	0.41	0.11	0.10	0.30	0.20	0.16	0.18	0.07	0.08	0.30	0.20	0.24	0.26	0.29	0.32
Al_2O_3	0.01	0.00	0.00	0.00	0.00	0.00	0.00	0.00	0.00	0.00	0.00	0.00	0.01	0.06	0.00	0.00	0.00	0.00	0.00	0.00
Total	100.08	99.91	100.31	99.77	99.88	99.90	100.03	99.54	99.99	100.50	100.40	100.13	99.64	99.93	100.28	99.83	99.68	99.96	100.06	99.77
P	0.971	1.000	0.986	0.987	0.979	0.987	0.950	0.968	0.993	0.994	0.989	0.986	0.972	0.964	0.992	0.979	0.988	0.996	0.994	1.001
Si	0.033	0.004	0.014	0.011	0.021	0.012	0.051	0.031	0.007	0.010	0.013	0.012	0.031	0.042	0.009	0.022	0.013	0.008	0.009	0.004
Ca	0.034	0.058	0.051	0.056	0.050	0.053	0.042	0.040	0.060	0.053	0.049	0.048	0.031	0.034	0.046	0.065	0.067	0.053	0.054	0.062
La	0.200	0.191	0.180	0.172	0.187	0.183	0.179	0.174	0.194	0.176	0.179	0.185	0.178	0.175	0.180	0.179	0.184	0.187	0.186	0.178
Ce	0.414	0.385	0.386	0.371	0.405	0.394	0.360	0.387	0.406	0.369	0.382	0.388	0.395	0.390	0.387	0.373	0.376	0.387	0.385	0.365
Pr	0.044	0.041	0.042	0.041	0.045	0.042	0.039	0.041	0.044	0.040	0.041	0.041	0.044	0.044	0.042	0.041	0.041	0.042	0.041	0.042
Nd	0.168	0.155	0.160	0.161	0.172	0.166	0.150	0.166	0.165	0.150	0.154	0.157	0.170	0.168	0.156	0.161	0.155	0.154	0.156	0.157
Sm	0.028	0.025	0.025	0.027	0.029	0.029	0.019	0.030	0.027	0.027	0.025	0.024	0.027	0.027	0.027	0.025	0.024	0.024	0.027	0.028
Eu	bd	0.003	0.003	0.004	bd	0.001	0.003	0.002	0.003	0.002	0.002	0.002	bd	bd	0.004	0.001	bd	0.004	0.004	0.004
Gd	0.021	0.020	0.023	0.025	0.023	0.025	0.017	0.024	0.023	0.024	0.024	0.021	0.023	0.023	0.025	0.022	0.021	0.022	0.023	0.024
Dy	0.005	0.009	0.010	0.012	0.007	0.009	0.015	0.010	0.007	0.013	0.014	0.012	0.010	0.010	0.012	0.009	0.010	0.011	0.011	0.011
Y	0.025	0.063	0.076	0.085	0.040	0.057	0.116	0.080	0.040	0.100	0.092	0.087	0.073	0.073	0.082	0.067	0.071	0.078	0.078	0.068
Er	0.000	0.003	0.003	0.003	0.001	0.002	0.006	0.003	0.001	0.004	0.003	0.004	0.003	0.003	0.003	0.003	0.003	0.003	0.003	0.003
Pb	0.006	0.005	0.005	0.006	0.005	0.005	0.007	0.005	0.005	0.005	0.004	0.004	0.005	0.005	0.005	0.007	0.006	0.004	0.004	0.006
Th	0.053	0.041	0.042	0.044	0.046	0.040	0.060	0.049	0.035	0.038	0.036	0.037	0.044	0.048	0.034	0.058	0.051	0.032	0.033	0.048
U	0.003	0.003	0.002	0.003	0.001	0.004	0.001	0.001	0.003	0.002	0.001	0.002	0.001	0.001	0.003	0.002	0.002	0.002	0.003	0.003
Al	0.000	0.000	0.000	0.000	0.000	0.000	0.000	0.000	0.000	0.000	0.000	0.000	0.000	0.003	0.000	0.000	0.000	0.000	0.000	0.000
Total	2.003	2.005	2.009	2.010	2.010	2.009	2.012	2.010	2.011	2.007	2.008	2.010	2.006	2.007	2.007	2.011	2.011	2.008	2.009	2.003
X_{LREE}	0.081	0.798	0.790	0.768	0.829	0.808	0.740	0.790	0.828	0.763	0.777	0.788	0.811	0.804	0.792	0.771	0.772	0.795	0.793	0.774
X_{HREE}	0.058	0.032	0.036	0.040	0.031	0.035	0.037	0.037	0.031	0.041	0.041	0.036	0.037	0.036	0.040	0.033	0.034	0.036	0.037	0.038
X_{Hut}	0.442	-0.009	-0.002	-0.004	0.002	-0.004	0.026	0.015	-0.018	-0.009	-0.007	-0.006	0.018	0.020	-0.005	0.001	-0.008	-0.015	-0.014	-0.005
X_{Brb}	0.414	0.116	0.102	0.112	0.099	0.104	0.083	0.078	0.120	0.106	0.097	0.096	0.062	0.067	0.091	0.129	0.132	0.106	0.107	0.124
X_{YPO4}	0.006	0.063	0.075	0.084	0.039	0.057	0.115	0.080	0.039	0.100	0.092	0.086	0.073	0.073	0.082	0.066	0.070	0.078	0.077	0.069
App. age (Ma)	1925.5	1931.0	1918.9	1943.9	1957.7	1924.7	1941.7	1905.3	1925.4	1933.8	2013.2	1993.0	1916.6	1919.2	1987.7	1937.5	1901.1	1946.2	1920.0	1932.7
2σ err. age (± , Ma)	78.7	87.9	68.1	63.4	66.0	63.9	55.2	63.6	72.4	71.6	76.9	76.2	69.6	64.3	74.8	54.9	59.2	78.2	75.9	59.8

Table 3 Electron microprobe analyses of unaltered monazite overgrowth zones

	Unaltered monazite rim overgrowth																			
Analysis no.	69	70	75	76	81	144	146	148	150	154	156	160	162	166	168	173	188	191	197	198
P_2O_5	30.12	28.95	28.60	27.49	28.19	0.84	29.11	30.32	29.28	30.38	30.15	30.26	29.53	29.49	28.92	29.63	29.81	30.25	29.48	28.69
SiO_2	0.34	0.91	1.02	1.67	1.27	28.97	0.79	0.13	0.71	0.16	0.34	0.28	0.61	0.80	1.04	0.83	0.54	0.13	0.88	1.07
CaO	0.92	0.86	0.87	0.72	0.54	13.48	0.68	1.20	0.70	1.88	0.61	1.75	0.73	0.69	0.67	0.67	1.52	1.43	0.69	1.08
La_2O_3	13.69	12.73	14.09	12.89	13.82	1.98	12.42	14.45	12.69	13.76	14.01	12.73	13.88	12.25	11.50	11.97	12.34	15.20	12.20	11.93
Ce_2O_3	27.06	27.40	29.04	28.73	30.06	0.00	27.80	28.02	27.84	27.49	29.35	26.37	28.65	27.60	27.00	27.13	26.49	27.45	27.64	26.42
Pr_2O_3	2.82	3.02	3.09	3.26	3.09	1.55	3.07	2.81	3.04	2.87	3.00	2.89	2.97	3.07	3.02	3.02	3.00	2.63	3.07	2.97
Nd_2O_3	10.23	11.85	12.03	12.24	12.26	0.36	12.27	10.78	11.99	10.76	11.62	11.18	11.25	12.50	12.40	12.40	11.78	10.15	12.38	11.80
Sm_2O_3	1.91	1.88	1.82	1.89	1.93	1.30	1.98	1.69	2.03	1.77	1.79	1.77	1.84	2.04	2.14	1.96	1.90	1.65	1.99	2.05
Eu_2O_3	0.24	0.12	bd	bd	bd	0.05	0.08	0.38	0.11	0.23	0.06	0.22	bd	bd	bd	bd	0.04	0.28	0.13	0.22
Gd_2O_3	1.87	1.71	1.49	1.19	1.22	6.16	1.83	1.50	1.75	1.53	1.54	1.66	1.52	1.70	1.81	1.91	1.61	1.52	1.73	1.76
Dy_2O_3	1.09	0.64	0.24	0.11	0.12	0.16	0.78	0.73	0.76	0.75	0.69	0.84	0.66	0.79	0.81	0.82	0.70	0.75	0.76	0.82
Y_2O_3	4.17	2.22	0.53	0.33	0.45	0.58	3.38	3.27	3.35	3.51	3.13	3.84	3.01	3.44	3.59	3.67	3.16	3.27	3.30	3.69
Er_2O_3	0.24	0.12	0.02	bd	bd	bd	0.27	0.23	0.23	0.25	0.23	0.28	0.20	0.22	0.25	0.25	0.21	0.24	0.24	0.25
PbO	0.53	0.59	0.63	0.75	0.57	11.88	0.43	0.37	0.40	0.35	0.28	0.45	0.39	0.45	0.52	0.44	0.60	0.43	0.46	0.54
ThO_2	3.69	6.46	6.80	8.50	6.49	28.51	5.07	3.39	4.92	3.81	2.91	5.05	4.37	5.17	6.04	5.26	6.56	4.13	5.48	6.64
UO_2	0.71	0.21	0.26	0.27	0.24	3.02	0.05	0.33	0.06	0.09	0.15	0.15	0.10	0.09	0.07	0.05	0.18	0.31	0.05	0.09
Al_2O_3	0.00	0.01	0.01	0.01	0.01	0.88	0.00	0.00	0.00	0.00	0.00	0.00	0.00	0.00	0.00	0.00	0.00	0.00	0.00	0.00
Total	99.62	99.67	100.55	100.06	100.25	99.73	100.01	99.58	99.84	99.60	99.85	99.72	99.70	100.29	99.77	100.00	100.42	99.84	100.46	100.04
P	0.990	0.968	0.959	0.934	0.951	0.036	0.967	0.996	0.972	0.993	0.991	0.990	0.978	0.972	0.962	0.976	0.979	0.993	0.971	0.954
Si	0.013	0.036	0.040	0.067	0.050	0.970	0.031	0.005	0.028	0.006	0.013	0.011	0.024	0.031	0.041	0.032	0.021	0.005	0.034	0.042
Ca	0.038	0.037	0.037	0.031	0.023	0.197	0.029	0.050	0.029	0.078	0.025	0.072	0.030	0.029	0.028	0.028	0.063	0.060	0.029	0.046
La	0.196	0.185	0.206	0.191	0.203	0.027	0.180	0.207	0.183	0.196	0.201	0.182	0.200	0.176	0.167	0.172	0.177	0.217	0.175	0.173
Ce	0.385	0.396	0.421	0.422	0.438	0.000	0.399	0.398	0.400	0.389	0.417	0.373	0.411	0.393	0.389	0.386	0.376	0.390	0.394	0.380
Pr	0.040	0.043	0.045	0.048	0.045	0.020	0.044	0.040	0.043	0.040	0.042	0.041	0.042	0.044	0.043	0.043	0.042	0.037	0.044	0.043
Nd	0.142	0.167	0.170	0.176	0.174	0.005	0.172	0.149	0.168	0.148	0.161	0.154	0.157	0.174	0.174	0.172	0.163	0.141	0.172	0.166
Sm	0.026	0.026	0.025	0.026	0.027	0.027	0.027	0.023	0.027	0.024	0.024	0.024	0.025	0.027	0.029	0.026	0.025	0.022	0.027	0.028
Eu	0.003	0.002	bd	bd	bd	0.001	0.001	0.005	0.002	0.003	0.001	0.003	bd	bd	bd	bd	0.001	0.004	0.002	0.003
Gd	0.024	0.022	0.020	0.016	0.016	0.055	0.024	0.019	0.023	0.020	0.020	0.021	0.020	0.022	0.024	0.025	0.021	0.020	0.022	0.023
Dy	0.014	0.008	0.003	0.001	0.002	0.001	0.010	0.009	0.010	0.009	0.009	0.010	0.008	0.010	0.010	0.010	0.009	0.009	0.010	0.010
Y	0.086	0.047	0.011	0.007	0.010	0.006	0.071	0.068	0.070	0.072	0.065	0.079	0.063	0.071	0.075	0.076	0.065	0.068	0.068	0.077
Er	0.003	0.002	0.000	bd	bd	bd	0.003	0.003	0.003	0.003	0.003	0.003	0.003	0.003	0.003	0.003	0.003	0.003	0.003	0.003
Pb	0.006	0.006	0.007	0.008	0.006	0.168	0.005	0.004	0.004	0.004	0.003	0.005	0.004	0.005	0.006	0.005	0.006	0.005	0.005	0.006
Th	0.033	0.058	0.061	0.078	0.059	0.413	0.045	0.030	0.044	0.033	0.026	0.044	0.039	0.046	0.054	0.047	0.058	0.036	0.049	0.059
U	0.006	0.002	0.002	0.002	0.002	0.043	0.000	0.003	0.001	0.001	0.001	0.001	0.001	0.001	0.001	0.001	0.002	0.003	0.000	0.001
Al	0.000	0.000	0.000	0.001	0.000	0.035	0.000	0.000	0.000	0.000	0.000	0.000	0.000	0.000	0.000	0.000	0.000	0.000	0.000	0.000
Total	2.004	2.004	2.008	2.008	2.005	2.004	2.007	2.008	2.006	2.019	2.002	2.014	2.005	2.004	2.005	2.001	2.011	2.011	2.003	2.014
X_{LREE}	0.159	0.108	0.060	0.052	0.055	0.082	0.815	0.815	0.818	0.784	0.848	0.765	0.833	0.814	0.800	0.805	0.776	0.799	0.814	0.778
X_{HREE}	0.040	0.063	0.066	0.083	0.062	0.059	0.037	0.031	0.035	0.031	0.031	0.035	0.030	0.035	0.037	0.038	0.032	0.032	0.035	0.036
X_{Hut}	0.386	0.438	0.443	0.466	0.463	0.444	0.022	-0.013	0.019	-0.039	0.005	-0.022	0.013	0.023	0.032	0.024	0.003	-0.016	0.025	0.020
X_{Brb}	0.409	0.385	0.424	0.391	0.414	0.408	0.057	0.099	0.059	0.153	0.051	0.143	0.061	0.057	0.056	0.056	0.125	0.118	0.058	0.090
X_{YPO4}	0.006	0.007	0.007	0.008	0.006	0.006	0.070	0.067	0.069	0.071	0.065	0.078	0.063	0.071	0.075	0.076	0.065	0.067	0.068	0.076
App. age (Ma)	1812.6	1847.3	1824.2	1897.7	1876.6	1760.0	1854.0	1822.4	1760.5	1894.4	1858.2	1816.0	1884.7	1857.7	1888.8	1825.0	1891.0	1868.3	1845.1	1768.2
2σ err. age (± , Ma)	48.3	54.3	70.6	73.7	66.8	45.3	68.0	78.0	68.9	81.8	94.7	65.0	74.2	65.9	59.7	65.2	54.7	70.1	63.8	54.4

Table 4 Electron microprobe analyses of hydrothermally altered monazite

	Hydrothermally altered monazite																		
Analysis no.	14	15	16	17	18	19	22	24	26	27	28	30	31	34	135	199	207	212	214
P_2O_5	29.39	29.85	29.96	30.00	29.04	29.52	28.96	27.85	29.38	28.50	28.52	29.56	29.56	29.05	29.74	29.79	30.22	29.72	28.10
SiO_2	0.84	0.37	0.33	0.32	0.99	0.54	0.63	1.28	0.56	0.76	0.88	0.42	0.71	0.87	0.31	0.57	0.43	0.52	1.30
CaO	0.19	0.23	0.32	0.32	0.44	0.57	0.44	0.17	0.39	0.51	0.27	0.48	0.13	0.14	0.40	0.22	0.58	0.41	0.32
La_2O_3	14.22	15.26	14.50	14.44	13.71	14.57	14.27	13.51	12.61	14.42	14.33	14.99	15.23	15.11	14.66	14.96	14.88	14.56	13.39
Ce_2O_3	29.33	31.13	30.35	30.67	29.32	29.72	29.60	29.66	29.95	29.26	29.98	30.39	31.16	30.32	30.93	31.42	30.69	30.18	28.88
Pr_2O_3	3.24	3.34	3.45	3.39	3.26	3.16	3.20	3.36	3.61	3.17	3.22	3.44	3.40	3.15	3.39	3.34	3.35	3.37	3.25
Nd_2O_3	13.05	13.65	13.30	13.40	12.83	12.83	12.84	13.15	14.63	12.24	12.88	12.83	13.77	12.88	13.22	13.22	13.08	12.76	12.92
Sm_2O_3	2.26	2.31	2.38	2.38	2.28	2.09	2.07	2.02	2.53	2.00	2.09	2.11	1.75	2.12	2.39	2.07	2.24	2.15	1.90
Eu_2O_3	0.09	0.10	0.18	0.12	0.04	bd	bd	bd	bd	bd	bd	0.09	bd	0.05	0.20	0.17	0.34	0.14	bd
Gd_2O_3	1.71	1.43	1.75	1.67	1.54	1.61	1.45	1.36	1.74	1.38	1.42	1.44	1.00	1.37	1.66	1.48	1.63	1.46	1.46
Dy_2O_3	0.41	0.11	0.34	0.27	0.28	0.39	0.31	0.22	0.25	0.34	0.22	0.16	0.12	0.17	0.20	0.26	0.27	0.25	0.28
Y_2O_3	1.27	0.51	0.91	0.63	1.12	1.31	1.31	0.88	0.71	1.22	1.02	0.67	0.71	0.74	0.54	0.77	0.77	0.68	1.10
Er_2O_3	0.04	bd	0.02	bd	0.05	0.06	0.04	0.02	0.02	0.07	0.03	0.03	bd	bd	bd	bd	bd	0.04	0.09
PbO	0.19	0.09	0.10	0.11	0.25	0.17	0.20	0.27	0.19	0.22	0.22	0.15	0.15	0.19	0.12	0.15	0.16	0.17	0.31
ThO_2	3.62	1.89	2.15	2.18	4.97	2.96	3.60	5.36	3.69	4.48	4.16	2.96	2.71	3.93	2.25	2.60	2.94	3.43	5.98
UO_2	0.03	0.02	0.02	0.01	0.00	0.03	0.05	0.02	0.00	0.03	0.01	0.02	0.00	0.01	0.02	0.02	0.03	0.00	0.02
Al_2O_3	0.00	0.00	0.00	0.00	0.01	0.00	0.00	0.01	0.00	0.02	0.00	0.00	0.01	0.00	0.00	0.00	0.00	0.00	0.00
Total	99.87	100.29	100.06	99.91	100.11	99.53	98.97	99.12	100.25	98.62	99.24	99.73	100.42	100.09	100.04	101.04	101.60	99.84	99.30
P	0.977	0.990	0.993	0.995	0.968	0.983	0.976	0.949	0.980	0.968	0.964	0.986	0.979	0.971	0.990	0.982	0.987	0.988	0.952
Si	0.033	0.015	0.013	0.012	0.039	0.021	0.025	0.051	0.022	0.030	0.035	0.017	0.028	0.034	0.012	0.022	0.016	0.020	0.052
Ca	0.008	0.010	0.013	0.013	0.019	0.024	0.019	0.008	0.016	0.022	0.011	0.020	0.006	0.006	0.017	0.009	0.024	0.017	0.014
La	0.206	0.220	0.209	0.209	0.199	0.211	0.210	0.201	0.183	0.213	0.211	0.218	0.220	0.220	0.213	0.215	0.212	0.211	0.198
Ce	0.422	0.446	0.435	0.440	0.423	0.428	0.431	0.437	0.432	0.430	0.439	0.438	0.446	0.438	0.445	0.448	0.434	0.434	0.423
Pr	0.046	0.048	0.049	0.048	0.047	0.045	0.046	0.049	0.052	0.046	0.047	0.049	0.049	0.045	0.049	0.047	0.047	0.048	0.047
Nd	0.183	0.191	0.186	0.188	0.180	0.180	0.183	0.189	0.206	0.175	0.184	0.181	0.192	0.182	0.186	0.184	0.180	0.179	0.185
Sm	0.031	0.031	0.032	0.032	0.031	0.028	0.028	0.028	0.034	0.028	0.029	0.029	0.024	0.029	0.032	0.028	0.030	0.029	0.026
Eu	0.001	0.001	0.002	0.002	0.001	bd	bd	bd	bd	bd	bd	0.001	bd	0.001	0.003	0.002	0.005	0.002	bd
Gd	0.022	0.019	0.023	0.022	0.020	0.021	0.019	0.018	0.023	0.018	0.019	0.019	0.013	0.018	0.022	0.019	0.021	0.019	0.019
Dy	0.005	0.001	0.004	0.003	0.004	0.005	0.004	0.003	0.003	0.004	0.003	0.002	0.002	0.002	0.003	0.003	0.003	0.003	0.004
Y	0.027	0.011	0.019	0.013	0.023	0.027	0.028	0.019	0.015	0.026	0.022	0.014	0.015	0.015	0.011	0.016	0.016	0.014	0.023
Er	0.001	bd	0.000	bd	0.001	0.001	0.000	0.000	0.000	0.001	0.000	0.000	bd	bd	bd	bd	bd	0.000	0.001
Pb	0.002	0.001	0.001	0.001	0.003	0.002	0.002	0.003	0.002	0.002	0.002	0.002	0.002	0.002	0.001	0.002	0.002	0.002	0.003
Th	0.032	0.017	0.019	0.019	0.045	0.027	0.033	0.049	0.033	0.041	0.038	0.027	0.024	0.035	0.020	0.023	0.026	0.031	0.054
U	0.000	0.000	0.000	0.000	0.000	0.000	0.000	0.000	0.000	0.000	0.000	0.000	0.000	0.000	0.000	0.000	0.000	0.000	0.000
Al	0.000	0.000	0.000	0.000	0.000	0.000	0.000	0.000	0.000	0.001	0.000	0.000	0.000	0.000	0.000	0.000	0.000	0.000	0.000
Total	1.997	2.000	1.999	1.998	2.001	2.004	2.004	2.004	2.001	2.006	2.004	2.002	1.999	1.999	2.002	2.001	2.003	1.997	2.002
X_{LREE}	0.900	0.939	0.916	0.924	0.885	0.893	0.895	0.901	0.907	0.885	0.905	0.914	0.939	0.920	0.926	0.927	0.908	0.913	0.881
X_{HREE}	0.053	0.032	0.046	0.038	0.046	0.050	0.048	0.038	0.039	0.045	0.042	0.035	0.029	0.035	0.024	0.023	0.024	0.023	0.024
X_{Hut}	0.042	0.027	0.034	0.034	0.065	0.052	0.053	0.058	0.051	0.064	0.051	0.048	0.030	0.043	0.005	0.016	0.004	0.016	0.045
X_{Brb}	0.000	0.000	0.000	0.000	0.000	0.000	0.000	0.001	0.000	0.002	0.000	0.000	0.001	0.000	0.034	0.019	0.048	0.035	0.027
X_{YPO4}	0.005	0.001	0.004	0.003	0.004	0.005	0.004	0.003	0.003	0.004	0.003	0.002	0.002	0.002	0.011	0.016	0.016	0.014	0.023
App. age (Ma)	1156.3	1088.9	1076.1	1153.8	1142.3	1262.3	1247.6	1149.4	1192.4	1130.3	1212.3	1105.4	1269.1	1117.9	1195.2	1277.8	1177.4	1126.8	1193.9
2σ err. age (±, Ma)	91.7	146.8	120.5	114.8	55.0	84.6	70.2	50.5	69.8	57.7	62.7	80.9	91.1	64.8	221.5	106.9	142.3	85.8	53.9

Curriculum Vitae

Personal particulars

Name	Emmanuel Owden Kazimoto
Address	Ludewig-Meyn Straße 10 24118 Kiel P. O. Box 35052, Dar es Salaam Tanzania
Email	kazimoto@min.uni-kiel.de / ekazimoto@udsm.ac.tz
Date of birth	30 November 1980
Nationality	Tanzanian

Education profile

University of Dar es Salaam	
2005 – 2008	Master of Science (Geology)
2001 – 2005	Bachelor of Science (Geology and Chemistry)
Tosamaganga High School	
1998 – 2000	Advanced Certificate for Secondary Education Examination (Advanced Secondary Education)

Kiel, 2-6-2014

Erklärung

Hiermit erkläre ich, Emmanuel Owden Kazimoto, dass die vorgelegte Abhandlung, abgesehen vor Beratung durch meinen akademischen Lehrer Professor Dr. Volker Schenk, nach Inhalt und Form meinen Arbeit ist und ausschließlich unter Verwendung der angegebenen Hilfsmittel entstanden ist.
Des Weiteren erkläre ich, dass ich weder diese noch eine ähnliche Arbeit an dieser oder einer anderen Hochschule im Rahmen eines Prüfüngsverfahrens vorgelegt oder veröffentlicht habe.

Kiel, den 2-6-2014 Emmanuel Owden Kazimoto